

QUANTIFYING THE TRANSLATION OF  
CELLULAR CONTRACTION MECHANISMS TO  
LEFT VENTRICULAR CONTRACTILE  
BEHAVIOUR USING COMPUTATIONAL  
MODELS OF CARDIAC MECHANICS AND  
THEIR PROBABILISTIC SURROGATES: THE  
ROLE OF CALCIUM AND SARCOMERE  
DYNAMICS IN RAT HEART FAILURE

AUTHOR

Stefano Longobardi

This dissertation is submitted for the degree of:

*Doctor of Philosophy*

SUPERVISORS

Prof. Steven A. Niederer  
Dr. Anna Sher

EXAMINERS

Prof. Peter Challenor  
Prof. Gary Miriams



School of Biomedical Engineering & Imaging Sciences  
Faculty of Life Sciences & Medicine  
King's College London

April 2022

## ABSTRACT

---

Heart failure (HF) affects nearly a million people in the UK alone and increases the risk of cardiovascular diseases, stroke and death. At the whole-organ level, HF often manifests as impaired left ventricular (LV) contractile function. At the cellular level, LV contractile dysfunction is associated with altered sarcomere kinetics and disrupted calcium ( $\text{Ca}^{2+}$ ) homeostasis. However, the link between cellular events and emerging pathological whole heart phenotypes is incompletely understood.

In this thesis, we aim to quantify the translation of cellular mechanisms to the LV contractile function and to elucidate the role of  $\text{Ca}^{2+}$  and sarcomere dynamics in rat HF, with emphasis on the disease with preserved ejection fraction phenotype (HFpEF). We employed (Chapter 3) a biophysically detailed 3D biventricular rat heart contraction mechanics model, which incorporated preload, afterload, fibre orientation, passive material properties, anatomy,  $\text{Ca}^{2+}$  transient and sarcomere dynamics. The model cell-level function was described using a set of parameters (key regulators of the ionic processes and sarcomere contraction). The model organ-level behaviour was described using a set of features characterising tissue and haemodynamics properties, and the LV volume and pressure transients and the corresponding pressure-volume (PV) loop.

We first (Chapter 4) fitted the model to real biventricular geometries, volumetric and functional data from a sham-operated (SHAM) and an aortic-banded (AB) 6-weeks-post-surgery rats, respectively representative of the healthy control and diseased rat cohorts from an experimental study on AB rats (diastolic HF animal model). We then characterised the LV features' sensitivity to model parameters. Model fitting was performed using the history matching (HM) technique, while uncertainty quantification was performed using Sobol' global sensitivity analysis (GSA). These normally require a large number of model evaluations to be performed. As the full forward model was too computationally expensive (~ 4 – 10 hours per single forward calculation), we made HM and GSA performance computationally feasible by replacing the input-to-output multi-scale map with fast-evaluating (~ 1 second per single forward calculation) probabilistic surrogates based on Gaussian process emulation (GPE). From now on, we will refer to the personalised (fitted) healthy SHAM rat model as "the model". The model constituted the starting point of the following three case studies.

In the first case study (Chapter 5), we used the model to show that it is possible to map pharmacological modulations from the sarcomere through to whole heart function and back again. As a case study, we validated the omecamtiv mecarbil (OM) mechanisms of action across scales in the healthy rat heart. Preclinical force-calcium (F-pCa) and LV haemodynamics data were used to constrain (using GPE + HM) the parameter space to represent *in silico* OM effects at the cellular level. The obtained spaces were then respectively mapped to features characterising the LV contractile function and to features of the F-pCa curve to show that the model predictions are in qualitative agreement with the experimentally observed OM effects at both the cell and whole-organ levels.

In the second case study (Chapter 6), we first performed a validation against pharmacological channel blocking experimental literature data using a number of compounds by showing that the model can predict the observed effects on the LV contractile function. Next (Chapter 7), we used the model to generate a pathological model, representing the 20-week-old obese ZSF1 rat (HFpEF animal model). This was done by perturbing specific model parameters according to experimental evidence from the available literature on ZSF1 rats. We then recovered the ZSF1 rat model back to the healthy state (using GPE + GSA + HM) by perturbing different sub-groups of parameters to represent different strategies of recovery to identify potential pharmacological, cellular targets for the treatment of HFpEF in rats.

In the third case study (Chapter 8), we used the model to demonstrate that changes in the F-pCa relationship do not uniquely map to observed changes in the LV function and vice versa. This result sheds new light on the assessment of myofilament  $\text{Ca}^{2+}$  sensitivity using F-pCa shifts and the corresponding predictions on the LV contractile function based on F-pCa shifts.

We have built a virtual platform that can be used to efficiently test different pharmacological interventions and provide an indication of/identify potential pharmaceutical, cellular targets for “virtually” treating HFpEF in rats. This was done by using computational models of cardiac mechanics and their probabilistic surrogates to quantify how normal/pathological cellular function is translated into normal/ altered whole heart function. We have demonstrated the feasibility of applying Bayesian probabilistic techniques to small mammalian (rat) healthy and diseased 3D models of cardiac mechanics. This thesis constitutes an important step towards applications to more complex systems (3D contractile human heart) for personalised medicine.

The 3D rat heart contraction mechanics model code and GPE, GSA, HM techniques’ implementations are available open access [140–142]. The scripts for generating the figures of all the main results of this thesis are available upon request.

## PUBLICATIONS

---

- [1] S. Longobardi, A. Sher, and S. A. Niederer. "In Silico Mapping of the Omecamtiv Mecarbil Effects from the Sarcomere to the Whole-Heart and Back Again." In: *Functional Imaging and Modeling of the Heart*. Ed. by Daniel B. Ennis, Luigi E. Perotti, and Vicky Y. Wang. Cham: Springer International Publishing, June 2021, pp. 406–415. ISBN: 978-3-030-78710-3. DOI: [10.1007/978-3-030-78710-3\\_39](https://doi.org/10.1007/978-3-030-78710-3_39).
- [2] S. Longobardi, A. Sher, and S. A. Niederer. "In silico identification of potential calcium dynamics and sarcomere targets for recovering left ventricular function in rat heart failure with preserved ejection fraction." In: *PLoS Comput. Biol.* 17.12 (Dec. 2021), pp. 1–22. DOI: [10.1371/journal.pcbi.1009646](https://doi.org/10.1371/journal.pcbi.1009646).
- [3] S. Longobardi, A. Sher, and S. A. Niederer. "Quantitative mapping of force-pCa curves to whole heart contraction and relaxation." In: *J. Physiol.* o (July 2022), pp. 1–20. DOI: [10.1113/jp283352](https://doi.org/10.1113/jp283352).
- [4] S. Longobardi, A. Lewalle, S. Coveney, I. Sjaastad, E. K.S. Espe, W. E. Louch, C. J. Musante, A. Sher, and S. A. Niederer. "Predicting left ventricular contractile function via Gaussian process emulation in aortic-banded rats." In: *Philos. Trans. A. Math. Phys. Eng. Sci.* 378.2173 (June 2020), p. 20190334. DOI: [10.1098/rsta.2019.0334](https://doi.org/10.1098/rsta.2019.0334).

*If I have seen further it is by standing on the shoulders of Giants.*

— Isaac Newton

## ACKNOWLEDGMENTS

---

Firstly, I would like to thank my supervisors Prof. Steven Niederer and Dr. Anna Sher, for helping me become the scientist I am today. Thank you, Steve, for showing me the way to do good research, for being humble and always straight to the point. Thank you, Anna, for always wanting me to aim for perfection, for caring about every little detail and for your precious advice on the world of pharma. You both have been of inspiration to me, and I will cherish the knowledge you have transmitted to me for years to come.

I would like to express my gratitude to my examiners Prof. Peter Challenor and Prof. Gary Miriams, for dedicating their time to improving this research's quality through their valuable expertise.

I would like to thank all my Cardiac Electromechanics Research Group colleagues, with whom I shared such good times and built a solid friendship. In particular, thank you, Marina, for having been in the right place at the right moment. Without you, I would have never started a PhD in London, and none of this would have ever happened. Also, thank you for your homemade pasta. Thank you, Cristobal, for being my first Spanish friend and sharing almost all our PhD "adventures" in and out of the office. Thank you, Alex, for helping me through the initial tough times of my PhD when I was lost and for your patience and wise pieces of advice. Thank you, Hugh, for improving my English communication skills by only talking to you – jokes apart – for your resourcefulness and sharp-wittedness and your espresso martinis. Thank you, Adelisa, for bringing joy to the office on rainy days (basically every day), for your incredible stories and your open-mindedness. Thank you, Damiano, for being my Italian buddy with whom I never missed a coffee at lunchtime or a beer at night. Thank you, Sofia, for your stubbornness, loyalty and kindness.

Special thanks go to Gianvito for showing me the art of computer programming. You indirectly helped me overcome crucial technical aspects of this research through your teachings, and I will always be grateful for that.

Lastly, I would like to thank my family for always believing in me and for their continuous support throughout all these years far from home, and Regina for supporting all my life choices and always standing by my side.

## CONTENTS

---

### I BACKGROUND

1	INTRODUCTION	2
1.1	Physiology of the heart	2
1.1.1	Cardiac electrophysiology	2
1.1.2	Cardiac cellular contraction	6
1.1.3	Cardiac physiologic anatomy	7
1.1.4	Cardiac cycle	8
1.2	Mathematical modelling of the heart	10
1.2.1	Cell electrophysiology	10
1.2.2	Cell contraction	12
1.2.3	Electromechanical coupling	13
1.2.4	Tissue electrophysiology	13
1.2.5	Tissue mechanics	15
1.2.6	Haemodynamics	16
1.3	Heart failure	17
1.3.1	HF with reduced ejection fraction	18
1.3.2	HF with preserved ejection fraction	19
1.4	Motivation and goals	20
1.4.1	Quantitatively linking cell, tissue and haemodynamic properties to whole heart function	20
1.4.2	In silico identification of potential pharmacological targets for HF treatment	21
1.5	Summary	21

### II METHODOLOGY

2	3D BIOPHYSICAL MODEL OF BIVENTRICULAR RAT HEART CONTRACTION MECHANICS	23
2.1	Ionic model	23
2.2	Contraction model	24
2.2.1	Length-dependence	27
2.2.2	Velocity-dependence	27
2.2.3	Uncoupling the binding and unbinding rates	28
2.2.4	The force-calcium relationship	29
2.3	Anatomy model	30
2.4	Tissue model	31
2.5	Electrical activation	31
2.6	Boundary conditions	32
2.7	Numerical solvers	32
2.8	Simulation protocol	33
2.9	Summary	33
3	MODEL EMULATION, FITTING AND UNCERTAINTY QUANTIFICATION	35

3.1	Model input parameters	35
3.2	Model output features	36
3.3	Multi-scale map	38
3.4	Gaussian process emulation	39
3.4.1	Regression accuracy	44
3.5	History matching	45
3.5.1	Refocusing	47
3.6	Global sensitivity analysis	49
3.6.1	Estimating Sobol' sensitivity indices	51
3.6.2	Emulator-based estimates	53
3.7	Summary	55
 III APPLICATION RESULTS		
4	IN SILICO PERSONALISED RAT HEART CONTRACTION MODELS: THE ROLE OF SARCOMERE DYNAMICS IN DIASTOLIC HEART FAILURE	57
4.1	Motivation	57
4.2	Rat data	58
4.3	Methods	59
4.3.1	Rat heart contraction model	59
4.3.2	Input parameter space	62
4.3.3	Training dataset and emulators	65
4.3.4	Global sensitivity analysis	66
4.3.5	History matching	67
4.4	Results	68
4.4.1	Model emulation	68
4.4.2	Model output sensitivity to model input	69
4.4.3	Model fitting	70
4.4.4	Fitted models	73
4.5	Discussion	75
4.5.1	Limitations	79
4.6	Summary	80
5	IN SILICO MAPPING OF SARCOMERE PHARMACOLOGICAL MODULATIONS TO WHOLE-ORGAN FUNCTION AND BACK AGAIN: THE OMECAMTIV MECARBIL CASE STUDY	81
5.1	Motivation	81
5.2	Preclinical data	82
5.2.1	Cell-level measurements	82
5.2.2	Whole-organ measurements	83
5.3	Methods	83
5.3.1	Rat heart contraction model	83
5.3.2	Input parameter space	84
5.3.3	Training dataset, emulators and global sensitivity analysis	85
5.3.4	Inferring OM effects on whole-organ function from in vitro F-pCa measurements	85

5.3.5	Inferring OM effects on the sarcomere from in vivo whole-organ measurements	86
5.4	Results	87
5.4.1	Model emulators and output sensitivities	87
5.4.2	Model predicted OM effects on the LV function	88
5.4.3	Model predicted OM effects on the F-pCa relationship	88
5.5	Discussion	89
5.5.1	Limitations	90
5.6	Summary	93
6	INTRODUCTION AND VALIDATION OF CALCIUM TRANSIENT VARIATIONS INTO THE WHOLE HEART MODEL	94
6.1	Motivation	94
6.2	Encoding $\text{Ca}^{2+}$ transient variations	95
6.3	Validating the personalised healthy rat heart model	97
6.3.1	Comprehensive in vitro Proarrhythmia Assay compounds	99
6.3.2	Compounds' effects on $\text{Ca}^{2+}$ transient	99
6.3.3	Compounds' effects on whole-organ function	101
6.3.4	Simulated compounds' effects on LV function comparison with experimental observations	103
6.4	Discussion	104
6.4.1	Limitations	104
6.5	Summary	105
7	IN SILICO IDENTIFICATION OF POTENTIAL CALCIUM DYNAMICS AND SARCOMERE TARGETS FOR RECOVERING LEFT VENTRICULAR FUNCTION IN RAT HEART FAILURE WITH PRESERVED EJECTION FRACTION	106
7.1	Motivation	106
7.2	Rat data	107
7.3	Methods	108
7.3.1	Rat heart contraction model	108
7.3.2	Input parameter space	110
7.3.3	Training dataset, emulators, global sensitivity analysis	112
7.3.4	Building a model of the 20-week-old obese ZSF1 rat	114
7.3.5	In silico recovering the ZSF1 rat towards healthy conditions	116
7.4	Results	117
7.4.1	Model emulators and output sensitivities	117
7.4.2	Personalised healthy rat heart model validation using emulators	119
7.4.3	The ZSF1 rat model	120
7.4.4	Recovered LV function in ZSF1 rats	123

7.5	Discussion	129
7.5.1	Limitations	133
7.6	Summary	135
8	IN SILICO QUANTITATIVE MAPPING OF FORCE-PCA CURVES TO WHOLE HEART CONTRACTION AND RELAXATION	136
8.1	Motivation	136
8.2	Methods	137
8.2.1	Cellular contraction model	137
8.2.2	Non-unique mapping of changes in $pCa_{50}$ to changes in sarcomere properties	138
8.2.3	The relationship between sarcomere properties and LV function	139
8.2.4	Non-unique mapping of changes in LV function to changes in sarcomere properties	140
8.2.5	Non-unique mapping of F-pCa curve to LV function and of LV function to F-pCa curve	140
8.3	Results	140
8.3.1	Non-monotonic relationship between sarcomere parameters and LV function	140
8.3.2	$pCa_{50}$ changes are non-uniquely explained by sarcomere alterations: the one-parameter case	142
8.3.3	$pCa_{50}$ changes are non-uniquely explained by sarcomere alterations: the two-parameter case	143
8.3.4	LV function changes are non-uniquely explained by sarcomere alterations	144
8.3.5	Non-unique mapping from/to F-pCa curve to/from LV function	145
8.4	Discussion	146
8.4.1	Limitations	149
8.5	Summary	149
<b>IV THE END</b>		
9	CONCLUSION	152
9.1	Contribution	152
9.2	Limitations	152
9.2.1	Rat heart model	152
9.2.2	Experimental data	155
9.2.3	Model emulation, fitting and uncertainty quantification	156
9.3	Next steps	158
9.4	Final remarks	159
<b>V APPENDIX</b>		
A	VALIDATION OF GPE-BASED GSA AND HM TECHNIQUES	161
A.1	GPE-based GSA technique validation using analytic solutions for Sobol' indices of test functions	161
A.1.1	Ishigami function	161

A.1.2	G*-function	162
A.1.3	Simulator estimates	163
A.1.4	Emulator estimates	166
A.2	HM validation using synthetic data	169
BIBLIOGRAPHY		172

## LIST OF FIGURES

---

- Figure 1.1 The heart and its conduction system. Adapted from [73], Unit III, Chapter 10, Page 128, Figure 10-1. Copyright © 2021 by Elsevier, Inc. 3
- Figure 1.2 The five phases of an action potential in left ventricular myocytes. 5
- Figure 1.3 Proteins' organisation within the sarcomere. Adapted from [73], Unit II, Chapter 6, Page 81, Figure 6-3. Copyright © 2021 by Elsevier, Inc. 6
- Figure 1.4 The sliding filament mechanisms at the basis of sarcomere contraction. Adapted from [73], Unit II, Chapter 6, Page 84, Figure 6-8. Copyright © 2021 by Elsevier, Inc. 7
- Figure 1.5 Wiggers diagram representing the four main phases of the cardiac cycle in the left heart. 9
- Figure 2.1 The full 3D biophysical model of biventricular rat heart contraction mechanics is a multi-scale framework of integrated sub-models describing the main mechanisms which regulate the heart contraction and relaxation at the cell, tissue and body scales. 23
- Figure 2.2 Main ion channels and pumps included in the Gattoni et al. [68] model. 25
- Figure 2.3 Fraction of bound  $\text{Ca}^{2+}$ -TnC complexes (TRPN) and of bound cross-bridges (XB) as a function of time. The intracellular  $\text{Ca}^{2+}$  concentration variation over time is also displayed on a different scale (blue). 26
- Figure 2.4 Land et al. [119] cell contraction model schematic.  $\text{Ca}^{2+}$  binds to TnC, and when the fraction of bound complexes (TRPN) reaches  $\text{TRPN}_{50}$ , half of the maximum number of cross-bridges has passed from the non-permissive state (N) to the actively cycling state (XB). Generated active force, which directly depends on the fraction of formed cross-bridges, causes tissue contraction, which backwards modulates the force generation itself in a length- and velocity-dependent manner. 28

- Figure 3.1 Multi-scale 3D biventricular rat heart contraction model. Given a fixed calcium transient (a) and mesh with fibres (b), parameters representing cell, tissue and haemodynamics properties (left grey column, described in Table 3.1) constitute the input for the model. LV volume and pressure transients and PV loop are obtained after a four-beats model run. The LV features (right grey column, described in Table 3.2), extracted from the 4th-beat curves (c1-c2), constitute the output for the model. 36
- Figure 3.2 Rat heart contraction mechanics model 4-beat simulation output. LVV and LVP transients (left panel) are drawn with a thin blue line, and their last-beat parts, along with the corresponding PV loop (right panel), are drawn with a thick blue line. 37
- Figure 3.3 The 12 LV features of interest are extracted from the LV volume and pressure curves (EF feature not showed as it is a derived quantity). 38
- Figure 4.1 Rat representative MR Images. 59
- Figure 4.2 LV volume transients obtained by segmenting the LV blood pool of 47 consecutive time frames images for the SHAM (blue) and the AB (red) reference rat images. Dashed lines indicate approximately diastasis time during the cardiac cycle. 60
- Figure 4.3 Rat representative MRI scans segmentations. LV and RV blood pools and myocardium are tagged with red, green and blue colours, respectively. 61
- Figure 4.4 Rat representative cubic Hermite finite element meshes. 62
- Figure 4.5 SHAM (blue) and AB (red) rats characteristic action potentials and calcium transients simulated using the Gattoni et al. [69] model of rat left ventricular myocyte electrophysiology at 6 Hz pacing frequency and 37 °C. 62

- Figure 4.6 Building the surrogate model. Input points (a) are sampled in the parameter space using a Latin hypercube design (b). The model (simulator) is run using these points. The simulator output is composed of features extracted from the LV volume and pressure transients and PV loop (c). The initial simulator input matrix and the corresponding output matrix represent the training dataset for the surrogate model (emulator) based on Gaussian processes. The trained emulator (d) is used to predict the simulator output at new points in the input parameter space. 66
- Figure 4.7 For each LV feature, the GPE with the highest  $R^2$  split test score is used to make predictions at the respective left-out subset of test points. Predictions are sorted in ascending order for the sake of better visualisation and joined with a thick blue line, and the respective observations (empty dots) are sorted accordingly. 2 STD confidence intervals (shaded regions) are also plotted around predicted mean lines. 70
- Figure 4.8 For each LV feature, the GPE with the highest  $R^2$  split test score is used to make predictions at the respective left-out subset of test points. Predictions are sorted in ascending order for the sake of better visualisation and joined with a thick blue line, and the respective observations (empty dots) are sorted accordingly. 2 STD confidence intervals (shaded regions) are also plotted around predicted mean lines. 71
- Figure 4.9 The impact of the cell, tissue and boundary conditions properties on organ-scale LV features in the SHAM rat model. The contribution of each parameter is represented by the sum of its first- and (when present) second-order effects. For each LV feature, higher-order interactions (coloured in grey) are represented by the sum of total effects minus the sum of all first- and second-order effects. 72

- Figure 4.10 The impact of cell, tissue and boundary conditions properties on organ-scale LV features in the AB rat model. The contribution of each parameter is represented by the sum of its first- and (when present) second-order effects. For each LV feature, higher-order interactions (coloured in grey) are represented by the sum of total effects minus the sum of all first- and second-order effects. 73
- Figure 4.11 High-dimensional input parameter space reduction during SHAM history matching. SHAM HM completed within eight waves. 74
- Figure 4.12 High-dimensional input parameter space reduction during AB history matching. AB HM completed within nine waves. 75
- Figure 4.13 Input parameters' one-dimensional ranges after completing HM procedure. Comparison between SHAM (blue) and AB (red) rat models' fittings. For each input parameter, the displayed intervals are scaled according to the initial range for that specific parameter. When SHAM and AB intervals' intersection is non-empty, this is also displayed with dotted lines. 75
- Figure 4.14 Simulator runs using the HM last wave's  $X_{NIMP}$  points as an input. (A) Obtained LV features' (empty, coloured dots) distributions around experimental mean values (filled, black dots) for SHAM (.1) and AB (.2). 2 standard deviations confidence intervals are shown as vertical straight lines centred in their respective mean value. All the displayed values (including confidence intervals) are normalised by the respective experimental mean values. (B) Simulated LV volume (.1) and pressure (.2) curves which the features in (A) were extracted from, for SHAM (blue) and AB (red). The average curves are displayed in darker colour variant. (C) Resulting SHAM (.1) and AB (.2) pressure-volume loops with EDV, ESV, PeakP features' ~ 95 % experimental confidence intervals. 76

- Figure 5.1 For each LV feature, the GPE with the highest  $R^2$  split test score is used to make predictions at the respective left-out subset of test points. Predictions are sorted in ascending order for the sake of better visualisation and joined with a thick blue line, and the respective observations (empty dots) are sorted accordingly. 2 STD confidence intervals (shaded regions) are also plotted around predicted mean lines. 89
- Figure 5.2 The impact of cross-bridge related sarcomere parameters on organ-scale LV features in the healthy rat. The contribution of each parameter is represented by its Sobol' main effect. For each LV feature, higher-order interactions (coloured in grey) are represented by the sum of all total effects minus the sum of all main effects. 90
- Figure 5.3 OM-compatible sarcomere space encoded by the  $n_{xb}$  and  $TRPN_{50}$  parameters, inferred from *in vitro* rat F-pCa data. A LHD of 100,000 points in the ranges of experimental variability of the F-pCa curve (left panel) is projected into the corresponding plausible 2D sarcomere parameter space (right panel). The reference parameter set is represented by a black dot, while reference dashed black lines divide the plane in four parts to highlight the quadrant of OM action. 91
- Figure 5.4 Predicted *in silico* OM effects on whole-heart function as percentage changes of LV features' values from control values. Experimental uncertainty ranges are displayed as shaded regions using percentage-from-control mean  $\pm$  standard deviation values for both the healthy (grey) and +OM (orange) cases. 91
- Figure 5.5 OM-compatible sarcomere space encoded by the  $k_{xb}$ ,  $n_{xb}$ ,  $TRPN_{50}$  and  $T_{ref}$  parameters, inferred from *in vivo* pig haemodynamic data. This space is obtained by running one iteration of HM which constrains the full parameter space according to an implausibility criterion that evaluates how plausible is a point to yield model predictions that are matching experimental observations. 92

- Figure 5.6 Predicted *in silico* OM effects on the sarcomere as described by F-pCa curves calculated from the constrained, OM-compatible sarcomere parameter space and by the related percentage changes of  $p\text{Ca}_{50}$  and  $h$  values from control values. Experimental uncertainty ranges are displayed (the middle and far right panels) as shaded regions using percentage-from-control mean  $\pm$  standard deviation values for both the healthy (grey) and +OM (orange) cases. 92
- Figure 6.1 A 4-feature parametric representation of the calcium transient. (A.1) The calcium transient is described by four relevant quantities: diastolic concentration (DCA), amplitude (AMPL), time to peak concentration (TP) and time to half-relaxation from peak concentration (RT50). (B.1–4) Each of the 4 calcium features can be scaled independently to produce a new calcium transient. (A.2) All the features can be scaled at the same time to produce many different new calcium transients. 97
- Figure 6.2 Calcium transient features linearly scale with their respective scaling coefficients. Example showing perturbations in the range [50 %, 150 %] from control values for all the calcium features but RT50, which undergoes perturbation in the range [50 %, 110 %]. 97

- Figure 6.3 Model validation workflow. (1) The pore block model is used to calculate the fraction of blocked ion channel at a given compound concentration for each channel. The same channels' conductances are scaled to reflect this compound effect, and (2) the rat myocyte electrophysiological model is run to generate perturbed calcium transients for different compound concentrations. (3) The calcium transients are used as an input for the 3D biventricular rat heart contraction model, and as many LV features' perturbed values are obtained as the number of input curves, which corresponds to the number of tested compound concentrations. (4) LV feature' values are plotted against the tested compound concentrations to obtain dose-response curves. (5) The qualitative trend of the LV features after *in silico* compound "administration" is compared with literature experimentally measured same compound effects on the same LV features for all the compounds under study. 98
- Figure 6.4 The effect of verapamil on the intracellular calcium transient. The Gattoni et al. [69] model is run using different ion channels' conductances' scaling coefficients to simulate the effect of different concentrations (blue colour variants) of the example compound considered. 101
- Figure 6.5 Calcium transient features' dose-response curves. Calcium transient features are extracted from perturbed calcium transients and plotted against the respective simulated compound concentrations. 101
- Figure 6.6 LV and RV pressure features' dose-response curves for the eight CiPA compounds. Simulated PeakP, maxdP and mindP features' values are given as percentages of the respective control values and are represented as dots in blue and orange variants, colour-coded with the compound doses for the left and right ventricles, respectively. Black dots indicate the control values when no compound is present. Experimental data of compounds' effects on the LV (when available) is also displayed as red dots. 102

- Figure 6.7 Model validation against known CiPA compounds effects on whole-organ function. Eight CiPA compounds effects (“experiment” columns) on PeakP, maxdP and mindP are compared with model same compounds’ predicted effects on the same features (“model” columns). Compounds’ effects are colour-coded as orange (feature unchanged) and green (feature decreased). None of the compounds caused an increase in the considered LV features. White/empty space means that the specific effect could not be retrieved from the examined literature studies. The model predicted effects are in agreement with the experimentally observed effects for 6 out of 8 compounds. [104](#)
- Figure 7.1 3D biventricular rat heart contraction model multi-scale map. Chosen 16 input parameters are calcium transient and sarcomere properties (green), haemodynamics properties (red) and tissue properties (blue). The output features of interest are 14 indexes (yellow) characterising the LV function and are extracted from the LV pressure and volume curves. The input parameters (Table 7.2) can be quantitatively be mapped to the output features (Tables 3.2–7.3) either by running the full model or by making predictions using trained GPEs. [110](#)
- Figure 7.2 Calcium transient parameters’ experimental percentage variations’ distributions in heart failure rat models (blue boxes). The chosen *in silico* variability for the same parameters is also shown as blue shaded areas. [112](#)
- Figure 7.3 Training dataset visual exploration. The GPEs’ training dataset 16D input parameter space is plotted as a 2D projection for each pair of parameters (orange dots). The initial space (blue dots) simulated for building the training dataset is plotted in the same manner to highlight regions which are not covered by the training dataset. [113](#)

- Figure 7.4 ZSF1 rat model recovery towards SHAM rat model. ZSF1 rat (red) and SHAM rat (blue) models' LV pressure and volume transients and PV loops are plotted with dashed lines. SHAM model *in silico* variability is also represented by a cloud of thin blue full lines. Black arrow represents the direction of recovery. [117](#)
- Figure 7.5 For each LV feature, the GPE with the highest  $R^2$  split test score is used to make predictions at the respective left-out subset of test points. Predictions are sorted in ascending order for the sake of better visualisation and joined with a thick blue line, and the respective observations (empty dots) are sorted accordingly. 2 STD confidence intervals (shaded regions) are also plotted around predicted mean lines. [119](#)
- Figure 7.6 The impact of calcium dynamics, sarcomere, tissue and boundary conditions properties on organ-scale LV features in the healthy rat. The contribution of each parameter is represented by its Sobol' main effect. For each LV feature, higher-order interactions (coloured in grey) are represented by the sum of all total effects minus the sum of all main effects. [120](#)
- Figure 7.7 LV pressure features' dose-response curves for the eight CiPA compounds. Simulated (dots in blue variants, colour-coded with the compound doses), emulated (full lines and shaded areas in blue) and experimentally observed (dots in red) PeakP, maxdP and mindP features' values are given as percentages of the respective control values. Experimental data taken from [5] (bepridil and verapamil – PeakP), [122] (chlorpromazine, PeakP), [109] (diltiazem – PeakP and maxdP), [206] (nifedipine – PeakP), [241] (ranolazine – PeakP, maxdP and mindP), [108] (verapamil – maxdP). [122](#)
- Figure 7.8 First wave of history matching. The space represented by the parameters selected for optimisation is constrained according to an implausibility criterion which evaluates how plausible is a point to yield model predictions that are matching experimental observations. [122](#)

- Figure 7.9 Matching experimental LV features' values. Simulator runs at input parameter points from the HM first (and also last) wave's non-implausible space. Obtained LV features' (empty, blue dots) distributions around experimental mean values (filled, black dots) are all within  $3$  STD confidence intervals (vertical straight lines centred in their respective mean value). The best fit in weighted  $L_1$  norm is also displayed (black cross). All the values including confidence intervals have been normalised by the respective experimental mean values. [123](#)
- Figure 7.10 Representative SHAM and ZSF1 rat models calcium transients and pressure-volume loops. The ZSF1 rat model is created by perturbing the SHAM (healthy) state. LV features which significantly changed from control to diseased animal are highlighted at the centre of the PV loops sub-plot. EF showed no significant change. [124](#)
- Figure 7.11 History matching waves progression. At each wave, 128 points are simulated from the current non-implausible parameter region and the features' values from the converging simulations are plotted as box plots coloured in blue variants for different consecutive waves. The median trend of these distributions is represented by a dashed blue line. Mean  $\pm 3$  standard deviations target intervals are represented in light red-coloured shaded areas for each LV feature. [129](#)
- Figure 7.12 Best fit recovered rat heart models. For each parameter group, the last wave fitted models are compared against the target mean, which the history matching aimed to match, and the best-fit model is selected according to the  $L_2$ -norm. This best-fit rat model (RECOV, black thick line) is compared with the reference ZSF1 rat model (red dashed line) and with the reference SHAM rat model (blue dashed line). [130](#)

Figure 7.13 Parameter distributions across progressing waves for the four different parameter groups. Each parameter distribution is represented as a grey box plot at each wave. Its median trend during multiple waves is highlighted in a solid black line and is compared with the ZSF1 rat model reference value for the same parameter highlighted in a dashed red line. All the plotted RECOV parameter values are given as percentages of the respective baseline ZSF1 parameter values. [131](#)

Figure 7.14 Isometric force-calcium relationship and generated active tension properties from the recovered rat model parameter space. (A) Calcium sensitivity ( $pCa_{50}$ ) and Hill coefficient ( $h$ ) features are extracted from the F-pCa curve, while peak tension ( $T_{max}$ ) and maximum rates of tension development ( $dT/dt_{max}$ ) and decay ( $dT/dt_{min}$ ) are extracted from the twitch transient. (B) Distributions of extracted  $pCa_{50}$  (blue),  $h$  (orange),  $T_{max}$  (green),  $dT/dt_{max}$  (red),  $dT/dt_{min}$  (purple) values are compared with the respective ZSF1 rat model baseline values (dashed lines). [133](#)

Figure 7.15 Personalised healthy rat heart contraction model LV volume features' response to model parameters' one-at-a-time variation. Both input parameters and output features are given as percentages of their baseline values (vertical and horizontal red dashed lines, respectively). Simulated features' values are displayed as open blue dots. A linear regression (LR) model with second-order degree polynomials is fitted to the data (blue lines) to facilitate the visualisation of non-linear and non-monotonic relationships between the features and each parameter. [134](#)

- Figure 8.1 The full 3D biventricular rat heart contraction model is run at a fixed parameter set with only one parameter taking equally-spaced values in the  $\pm 50\%$  range of perturbation from its baseline value (vertical red dashed lines). The converging mechanics simulations' output PV loops are analysed to extract the corresponding EDV, ESV, SV and EF features' values (open blue dots), given as percentages from their baseline values (horizontal red dashed lines). The process is repeated separately for each parameter regulating the  $pCa_{50}$  feature of the F-pCa curve. A linear regression (LR) model with second-order degree polynomials is fitted to the data (blue lines) to facilitate the visualisation of non-linear and non-monotonic relationships between the features and each of the parameters considered. [141](#)
- Figure 8.2 The full 3D biventricular rat heart contraction model is run at a fixed parameter set with only one parameter varying around its baseline value. The resulting LV volume and pressure transients and corresponding PV loops are plotted for some of the parameter values (full lines in blue variants) and compared to the reference parameter set mechanics solution (dashed black line). Example showing  $k_{off}$  parameter variation in the range obtained as a  $\pm 40\%$  perturbation of its baseline value. [142](#)
- Figure 8.3 The impact of  $pCa_{50}$ -modulating, sarcomere parameters on EDV, ESV, SV and EF organ-scale LV feature. The contribution of each parameter is represented by the sum of its first- and second-order effects. For each LV feature, higher-order interactions (up to the fourth order) are represented by the sum of all total effects minus the sum of all first- and second-order effects. [142](#)

- Figure 8.4      Different parameters can be individually perturbed to achieve the very same shift in the force-calcium relationship. Example showing 2 % leftwards (upper plot) and rightwards (bottom plot) shifts of the reference  $p\text{Ca}_{50}$  value. As  $\text{TRPN}_{50}$  and  $n_{\text{trpn}}$  also regulate the F-pCa curve's Hill coefficient (equation (2.19)), notice that for these two parameters the shift in the  $p\text{Ca}_{50}$  value is also affecting the curve's slope. [144](#)
- Figure 8.5      For each pair of parameters regulating the  $p\text{Ca}_{50}$  feature of the F-pCa curve, a 2D uniform grid is constructed using a  $\pm 50\%$  perturbation around the reference parameter set values (black dots). (A) The cell contraction model is then used to calculate the  $p\text{Ca}_{50}$  feature value at every parameter point of the grid, and each grid is plotted as a heat map with values given as percentages from the control  $p\text{Ca}_{50}$  value. Contour plots are finally added to highlight the presence of isolines, whose many different parameter sets induce the same shift ( $-2\%$  dotted,  $0\%$  full,  $+2\%$  dashed black lines) in the control  $p\text{Ca}_{50}$  value. (B) Parameter points from the obtained isolines are mapped by the emulator into EF feature values. These values (given as percentages of the control EF value) are represented by different colour intensities used to colour each parameter point in the isolines, showing that parameters that share the same  $p\text{Ca}_{50}$  values are linked to different EF values. [145](#)

- Figure 8.6 For each pair of parameters regulating the  $pCa_{50}$  feature of the F-pCa curve, a 2D uniform grid is constructed using a  $\pm 50\%$  perturbation around the reference parameter set values (black dots). (A) A trained emulator is then used to predict the EF feature value at every parameter point of the grid, and each grid is plotted as a heat map with values given as percentages from the control EF value. Contour plots are finally added to highlight the presence of isolines (full black lines), whose many different parameter sets induce the same 0% shift in the control EF value. (B) Parameter points from the obtained isolines are mapped by the cell contraction model into  $pCa_{50}$  feature values. These values (given as percentages of the control  $pCa_{50}$  value) are represented by different colour intensities used to colour each parameter point in the isolines, showing that parameters that share the same EF values are linked to different  $pCa_{50}$  values. [146](#)
- Figure 8.7 The same IVRT value (A) can be linked to different  $pCa_{50}$  values (B) (i.e. to differently shifted F-pCa curves). [147](#)
- Figure 8.8 The same PeakP value (A) can be linked to different  $pCa_{50}$  values (B) (i.e. to differently shifted F-pCa curves). [148](#)
- Figure 8.9 Force-LV volume curves at the end-diastolic and end-systolic pressures (top right, orange and green lines) can be separately manipulated to modulate the LV contractile function. However, interventions on calcium transient (bottom left, blue line) and sarcomeric generated force (top left, orange and green full lines) both manifest as modifications of the former curves, which in turn causes modification of the PV loop (bottom right, blue full line). In addition, pharmacological modulations on the sarcomere might cause a shift of the force-calcium relationship (top left, orange and green dashed lines). However, this will preserve the EF (bottom right, blue dashed line) without improving LV contractile function, which was the desired outcome of the performed sarcomeric intervention. [150](#)

- Figure 9.1 Non-implausible parameter space visual exploration for the SHAM rat model. The 8D simulated input parameter space is plotted as a 2D projection for each pair of parameters (light blue dots). The specific parameter sets leading to a converging mechanics simulation are further highlighted (dark blue dots) to spot regions of non-convergence. 1D slices of the full space where a single parameter might have independently led to model failure are additionally marked with a black rectangular box. [154](#)
- Figure 9.2 Non-implausible parameter space visual exploration for the AB rat model. The 8D simulated input parameter space is plotted as a 2D projection for each pair of parameters (light red dots). The specific parameter sets leading to a converging mechanics simulation are further highlighted (dark red dots) to spot regions of non-convergence. 1D slices of the full space where a single parameter might have independently led to model failure are additionally marked with a black rectangular box. [155](#)
- Figure A.1 Ishigami function Sobol' first-order (main) and total sensitivity indices estimated using the simulator. Indices are given as pointwise estimates with bootstrap 95 % confidence intervals. [164](#)
- Figure A.2 G\*-function Sobol' first-order (main) and total sensitivity indices estimated using the simulator. Indices are given as pointwise estimates with bootstrap 95 % confidence intervals. [165](#)
- Figure A.3 Ishigami function Sobol' first-order (main) and total sensitivity indices estimated using the emulator. Indices are given as different estimates (forming entire distributions) corresponding to different samples from the full emulators' posterior distributions. [167](#)
- Figure A.4 G\*-function Sobol' first-order (main) and total sensitivity indices estimated using the emulator. Indices are given as different estimates (forming entire distributions) corresponding to different samples from the full emulators' posterior distributions. [168](#)

- Figure A.5 Simulated LV features' distributions around synthetic mean values. These are obtained by evaluating the simulator at input parameter points belonging to the first (w1) up to the last (w9) waves of HM performed on synthetic data. Simulated features are shown as empty dots, while the related synthetic mean values are displayed as full dots. 2 STD confidence intervals are also shown as vertical straight lines centred around synthetic mean values. All the displayed values (including confidence intervals) are normalised by their respective synthetic mean values. [170](#)
- Figure A.6 Input parameters' ranges at each wave during SHAM rat heart model HM on synthetic data (blue). The parameters' ranges where the synthetic data were sampled from are also shown (red). [170](#)
- Figure A.7 The process of points' selection for synthetic data generation to be used for HM technique validation. [171](#)

## LIST OF TABLES

---

Table 2.1	Gattoni et al. [69] model's ionic currents.	<a href="#">24</a>
Table 3.1	Model parameters and their definitions.	<a href="#">36</a>
Table 3.2	Indexes of LV systolic and diastolic functions.	<a href="#">39</a>
Table 4.1	MRI characteristics.	<a href="#">60</a>
Table 4.2	Segmentation tags volume estimates based on voxels size/count.	<a href="#">61</a>
Table 4.3	SHAM rat model input parameters' values from experimental and modelling studies.	<a href="#">63</a>
Table 4.4	AB rat model input parameters' values from experimental and modelling studies.	<a href="#">64</a>
Table 4.5	Parameters' ranges used for describing both the SHAM and AB rat models' 8D input parameter space.	<a href="#">65</a>
Table 4.6	Left ventricular features' target mean and standard deviation values. One asterisk (*) features values come directly from the available MRI data. Two asterisks (**) features values come from literature experimental studies.	<a href="#">68</a>

Table 4.7	The SHAM rat GPEs' accuracy. The GPEs' accuracy was evaluated using the average $R^2$ score and $ISE_2$ obtained with a 5-fold cross-validation. Values are reported as mean±std.	<a href="#">69</a>
Table 4.8	The AB rat GPEs' accuracy. The GPEs' accuracy was evaluated using the average $R^2$ score and $ISE_2$ obtained with a 5-fold cross-validation. Values are reported as mean±std.	<a href="#">69</a>
Table 4.9	Details of history matching progression for the SHAM and AB rat models' fitting. At each wave, parameter points are tested against an implausibility criterion using the reported cut-off values ( $I_{cutoff}$ ), and only a percentage of these points (NIMP) out of the total tested points resulted to be non-implausible.	<a href="#">74</a>
Table 4.10	Representative SHAM and AB rat models' input parameters' values. Parameter bounds of all non-implausible models are also provided.	<a href="#">77</a>
Table 4.11	Representative SHAM and AB rat models' output LV features' values. Feature bounds of all non-implausible models are also provided.	<a href="#">78</a>
Table 5.1	F-pCa curve features' fractions of change experimental variability in OM-containing solution-exposed healthy rat skinned muscles. Values are given as ranges of minimum and maximum fractions of change from control experimental mean values.	<a href="#">82</a>
Table 5.2	Left ventricular features' experimental variability in healthy pigs after OM administration. Values are given as mean±std percentage change from control experimental mean values. Asterisked ( $\cdot$ )* features' changes were reported to be statistically significant.	<a href="#">83</a>
Table 5.3	Model parameters and their definitions.	<a href="#">84</a>
Table 5.4	Additional LV features of interest.	<a href="#">84</a>
Table 5.5	Parameters' ranges used for describing the healthy rat model 4D input parameter space.	<a href="#">85</a>
Table 5.6	GPEs' accuracy. The GPEs' accuracy was evaluated using the average $R^2$ score and $ISE_2$ obtained with a 5-fold cross-validation. Values are reported as mean±std.	<a href="#">88</a>
Table 6.1	Features encoding the calcium transient shape.	<a href="#">95</a>

Table 6.2	IC <sub>50</sub> and Hill coefficient values describing the affinity of eight CiPA compounds with the I <sub>Na</sub> , I <sub>to</sub> , I <sub>K1</sub> and I <sub>CaL</sub> ion channels. The dash symbol indicates that the specific compound has no inhibitory effect on the respective ion channel. Values taken from [38, 131]. 100
Table 6.3	Qualitative change in three LV pressure features observed in literature rat experiments for eight different CiPA compounds. Down-facing arrow means that the specific LV feature decreases from its control value with the specific compound; left-right arrow means that the compound has no effect on that feature; dash symbol means that the specific information could not be retrieved from literature. 103
Table 7.1	Experimental ZSF1 obese rat haemodynamic data. For each LV feature of interest, mean and standard deviation values are given as percentages of the related control mean values. Asterisked (·)* features' changes were reported to be statistically significant. 108
Table 7.2	Model parameters and their definitions. 109
Table 7.3	Indexes of LV systolic and diastolic functions. 109
Table 7.4	Calcium transient parameters' experimental variability in heart failure rat models. 111
Table 7.5	Parameters' ranges used for describing the healthy rat model 16D input parameter space. 113
Table 7.6	SHAM rat model <i>in silico</i> variability for the LV features used as targets for ZSF1 rat model recovery. Target mean and standard deviation LV features' values to be matched for recovering the ZSF1 rat. 116
Table 7.7	GPEs' accuracy. The GPEs' accuracy was evaluated using the average R <sup>2</sup> score and ISE <sub>2</sub> obtained with a 5-fold cross-validation. Values are reported as mean±std. 118
Table 7.8	Parameters ranking according to their influence on the model output total variance. A rank is assigned to each parameter according to how much it impacts the model output total variance. Parameter groups are assigned a score given by the sum of the ranks of their member parameters. This score reflects the importance of the group as an input for the multi-scale model. 121

Table 7.9	Representative SHAM and ZSF1 rat models' input parameters' values. <a href="#">125</a>
Table 7.10	Representative SHAM and ZSF1 rat models' output LV features' values. <a href="#">126</a>
Table 7.11	GPEs' accuracy for the Ca parameter group. <a href="#">126</a>
Table 7.12	GPEs' accuracy for the TNF parameter group. <a href="#">126</a>
Table 7.13	GPEs' accuracy for the TKF parameter group. <a href="#">127</a>
Table 7.14	GPEs' accuracy for the CaMYO parameter group. <a href="#">127</a>
Table 7.15	Details of history matching progression. HM is run for each parameter group in order to re-fit the specific parameters within the group. Parameter points (400,000 at Wave 1 and 100,000 at the next Waves) are tested against an implausibility criterion using the reported cutoff values, and only a percentage of these points resulted to be non-implausible (NIMP). <a href="#">128</a>
Table 7.16	LV features' percentages of recovery. For each LV feature we aimed to recover, the distance between its median recovered value and the respective healthy value is divided by the distance between the initial, diseased value and the healthy value. This ratio describes the percentage of recovery for the examined feature. <a href="#">128</a>
Table 7.17	Percentage perturbations of cardiac cellular properties resulting from the last waves' parameter spaces. For each parameter last wave distribution, its median value is given as a $\pm$ percentage perturbation from the corresponding ZSF1 reference value. $\text{Ca}^{2+}$ transient parameters are reported as coefficients used to scale the corresponding SHAM rat baseline real parameter values. <a href="#">132</a>
Table 8.1	The mapping of sarcomere properties to $F_{\text{pCa}}$ variations is non-unique. By scaling each parameter $p_i$ by the corresponding $\alpha_i$ coefficient, the cellular contraction model simulates a $p\text{Ca}_{50}$ value which is shifted by exactly $\Delta$ units from the reference value. <a href="#">143</a>
Table A.1	Ishigami function Sobol' first-order and total effects' theoretical values for $a = 7$ , $b = 0.1$ . <a href="#">164</a>
Table A.2	$G^*$ -function Sobol' first-order and total effects' theoretical values for $D = 10$ and $\alpha_i = 1$ , $\delta_i \sim \mathcal{U}([0, 1])$ , $a_i = i - 1$ , for $i = 1, \dots, D$ . <a href="#">165</a>

Table A.3 Ishigami function emulators' predictivity as described by the  $R^2$  score. Predictivity is tested against the same set of points for each of emulators trained on differently large training datasets. [167](#)

Table A.4  $G^*$ -function emulators' predictivity as described by the  $R^2$  score. Predictivity is tested against the same set of points for each of emulators trained on differently large training datasets. [168](#)

Table A.5 Synthetic data LV features' variability given as mean  $\pm$  standard deviation values to match for HM validation. Only the LV features with an asterisk (\*)<sup>\*</sup> were used as targets for HM. [169](#)

## ACRONYMS

---

SA	Sino-atrial (node)
AV	Atrio-ventricular (node/bundle/valves)
AP	Action potential
EC	Excitation-contraction (coupling)
$\text{Na}^+$	Sodium
$\text{K}^+$	Potassium
$\text{Cl}^-$	Chloride
$\text{Ca}^{2+}$	Calcium
NAK	Sodium/potassium pump
ATP	Adenosine triphosphate
NCX	Sodium/calcium exchanger
Tm	Tropomyosin
Tn	Troponin
TnC	Troponin C
SR	Sarco(endo)plasmic reticulum
T	Transverse (tubules)
RyR	Ryanodine receptor

PMCA	Plasma membrane $\text{Ca}^{2+}$ ATPase
SERCA	Sarcoplasmic $\text{Ca}^{2+}$ ATPase
RV	Right ventricle
LV	Left ventricle
RA	Right atrium
LA	Left atrium
EDV	End-diastolic volume
EDP	End-diastolic pressure
IVC	Isovolumetric contraction
SV	Stroke volume
ESV	End-systolic volume
EF	Ejection fraction
ESP	End-systolic pressure
IVR	Isovolumetric relaxation
HH	Hodgkin-Huxley (model)
MM	Markov (chain) model
ODE	Ordinary differential equation
HF	Heart failure
HFrEF	Heart failure with reduced ejection fraction
HFpEF	Heart failure with preserved ejection fraction
LoD	(Mesh personalisation) level of detail
AB	Aortic-banded (rat)
SHAM	Sham-operated (rat)
MRI	Magnetic resonance imaging
LVV	Left ventricular volume
LVP	Left ventricular pressure
PV	Pressure-volume (loop)
F-pCa	Force-pCa (curve)
GPE	Gaussian process emulation/emulator

GP	Gaussian process
SE	Squared exponential (kernel)
ISE	Independent standard error
HM	History matching (technique)
GSA	Global sensitivity analysis
LHD	Latin hypercube design
MC	Monte Carlo
MCMC	Markov chain Monte Carlo
OM	Omecamtiv mecarbil
CiPA	Comprehensive in vitro proarrhythmia assay

## Part I

### BACKGROUND

## INTRODUCTION

---

### OUTLINE

In this chapter, we describe the heart and how it functions, from single-cell excitation through to whole-organ contraction and relaxation (Section 1.1). We then present how the key physiological mechanisms at different biological scales can be modelled using equations of bio-electro-mechanics (Section 1.2). Heart failure pathology is then introduced, with emphasis on the two most common phenotypes of the disease, namely when the ejection fraction is reduced and when it is preserved (Section 1.3). We continue by stating the motivation for the research carried out within this thesis (Section 1.4), and we conclude with a brief summary (Section 1.5).

### 1.1 PHYSIOLOGY OF THE HEART

During each heartbeat, the chambers of the heart are activated by an electrical impulse that propagates across the entire tissue. The activation wave is initiated by a group of pacemaking cells, making up the *sino-atrial (SA) node* and located in the right atrium, and immediately starts activating the atria before reaching the *atrio-ventricular (AV) node*. The AV node slows down the activation signal before it passes to the *atrio-ventricular bundle*. This allows the atria to fully contract to fill the ventricles with blood before the latter are activated. The activation signal through the AV bundle (which branches in two) spreads throughout the ventricles via the specialised, fast *His-Purkinje* conduction system. The arrival of the activation wave at each cardiac muscle cell causes a depolarisation of the cell membrane that initiates an *action potential (AP)*. This cellular electrical signal gives rise to a calcium transient that activates the tension generating proteins inside the cell through a process called *excitation-contraction (EC) coupling*. This causes the heart walls to contract, pumping blood in and out of the heart and around the body and to the lungs.

The biological facts and definitions we present in this chapter mainly follow the standard textbooks of medical physiology by Guyton and Hall [73] and of cardiovascular physiology by Levick [128].

#### 1.1.1 Cardiac electrophysiology

The surface membrane of a cardiac cell is called the *sarcolemma*. On either side of the sarcolemma, the intracellular and the extracellular

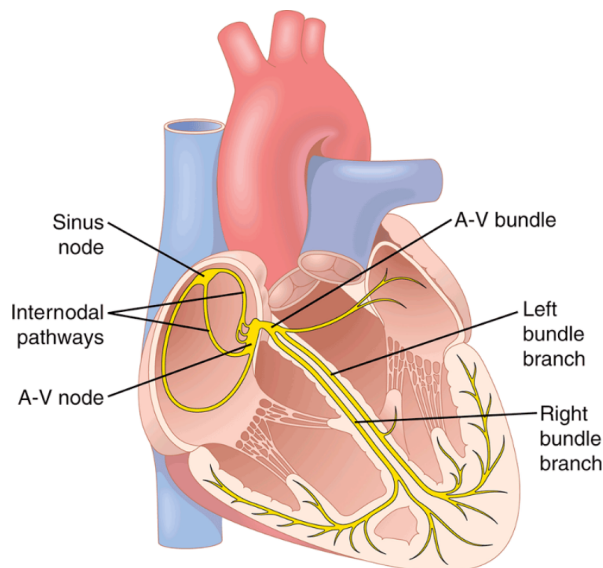


Figure 1.1: The heart and its conduction system. Adapted from [73], Unit III, Chapter 10, Page 128, Figure 10-1. Copyright © 2021 by Elsevier, Inc.

environments consist of ionic solutions. For cardiac electrophysiology the major ion species are sodium ( $\text{Na}^+$ ), potassium ( $\text{K}^+$ ), chloride ( $\text{Cl}^-$ ) and calcium ( $\text{Ca}^{2+}$ ). An important property of the sarcolemma is its ability to maintain concentration gradients, such that each ion species is unevenly distributed between the intracellular and extracellular space, resulting in concentration gradients across the membrane. As ions are charged particles, their uneven distribution across the sarcolemma also creates an electrical gradient. The resulting electrochemical gradient provides a driving force to move ions across the cell membrane.

Another crucial property of the sarcolemma is its capacity to respond to electrical stimulation through the brief dynamic opening and closing of highly specific ion channels and electrogenic transporters to produce changes in its transmembrane potential. With each heartbeat, the cell membrane is depolarised, and an AP is initiated as a result of a complex interplay of multiple ion channels, exchangers and transporters in the myocardium. A typical AP consists of five phases, each one associated with the opening of specific sarcolemma ion channels. The main ionic events at each AP phase can be summarised as follows.

**PHASE 0.** The initial depolarisation is due to the opening of voltage-gated fast  $\text{Na}^+$  channels ( $I_{\text{Na}}$ ) when the transmembrane voltage reaches the activation threshold of the channel between  $-70$  and  $-60$  mV. Positive charged  $\text{Na}^+$  current flows rapidly into the cell due to the large  $\text{Na}^+$  concentration gradient and the negative transmembrane potential, leading to further depolarisation.

**PHASE 1.** The early repolarisation of the AP is primarily caused by the rapidly activating and inactivating transient outward K<sup>+</sup> current ( $I_{to}$ ).

**PHASE 2.** A plateau phase follows, resulting from a prolonged influx of Ca<sup>2+</sup> ions, as the voltage-gated L-type Ca<sup>2+</sup> channels ( $I_{CaL}$ ) open upon depolarisation. This flow of Ca<sup>2+</sup> ions plays a crucial role in cardiac EC coupling, as it initiates a series of intracellular events that ultimately lead to myocardial contraction. Another current that contributes to the late Phase 2 plateau is the net inward current through the Na<sup>+</sup>/Ca<sup>2+</sup> exchanger (**NCX**) in Ca<sup>2+</sup> extrusion mode. This exchanger is a reversible counter-transport system that, when in forward (Ca<sup>2+</sup> extrusion) mode, uses the energy provided by the inward flux of Na<sup>+</sup> ions down their electrochemical gradient to extrude Ca<sup>2+</sup> ions with a generally accepted stoichiometry of 3: 1, thus moving one net charge into the cell. These two inward currents that determine the AP plateau are balanced by a reduced outward K<sup>+</sup> current due to the membrane K<sup>+</sup> conductance falling upon depolarisation. This phenomenon is called *inward rectification*, caused by the obstruction of the inner mouth of K<sup>+</sup> channels at higher voltages.

**PHASE 3.** The outward flow of K<sup>+</sup> ions is the major factor causing repolarisation that determines the duration of the AP. The large number of K<sup>+</sup> channels can be divided into two molecular families: the voltage-gated channels and the inward rectifier channels. The voltage-gated outward K<sup>+</sup> channels are the rapidly ( $I_{Kr}$ ) and slowly ( $I_{Ks}$ ) activating delayed rectifiers, and are responsible for repolarisation, fully activated at around -10 mV and deactivated by full repolarisation. The inward rectifier K<sup>+</sup> channels, such as the time-independent K<sup>+</sup> current  $I_{K1}$ , help regulate the resting membrane potential and contribute to late Phase 3 repolarisation.

**PHASE 4.**  $I_{K1}$  closes upon depolarisation and reopens during repolarisation to help terminate the AP and reset the membrane potential to the resting state, which for non-pacemaker cardiac cells such as the ventricular myocytes is around -90 mV. An important contribution to maintain resting membrane potential ionic homeostasis is given by the Na<sup>+</sup>/K<sup>+</sup> ATPase (**NAK**). This is a key transporter and uses energy (in the form of *adenosine triphosphate (ATP)*) to establish a low intracellular Na<sup>+</sup> concentration and a high intracellular K<sup>+</sup> concentration by moving 3 Na<sup>+</sup> ions out and 2 K<sup>+</sup> ions into the cell by hydrolysis of 1 ATP molecule. This transport is *electrogenic*, meaning that it results in the extrusion of 1 net charge per cycle.

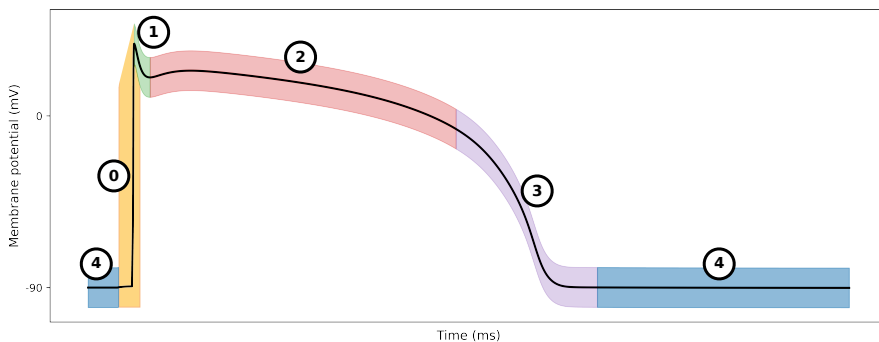


Figure 1.2: The five phases of an action potential in left ventricular myocytes.

Every ventricular myocyte is in general not excitable (*refractory*) between Phase 0 through to halfway through Phase 3, meaning that the cell cannot produce another AP. This is due to all the  $\text{Na}^+$  channels moving to the *inactivated* state after the initial Phase 0 depolarisation. The period of time since the cell was last activated and it is unable to initiate another activation is called *absolute refractory period*. However, cell *hyperpolarisation* due to  $\text{K}^+$  ions leak, which makes the membrane potential being more negative than the resting configuration, makes the  $\text{Na}^+$  channels reset to the still closed but not inactivated state. At this moment (*relative refractory period*), the cell can potentially evoke a new AP, although needing a larger-than-normal excitatory stimulus.

#### 1.1.1.1 The role of calcium in sarcomere contraction

Calcium plays a key role in signalling the cardiac cell to contract. The variation of  $\text{Ca}^{2+}$  levels observed inside the cell during each heartbeat is referred to as the *calcium transient* or *calcium signal*. To understand the  $\text{Ca}^{2+}$  dynamics that give rise to the characteristic  $[\text{Ca}^{2+}]_i$  transient shape, we need to introduce other important structural and functional myocyte components.

Cardiac myocytes have a long cylindrical shape. The sarcolemma encapsulating the cell invaginates and forms an extensive tubular network called *transverse (T) tubules* which allows the AP to penetrate rapidly to the interior of the cell. Next to the T-tubules inside the cell lies the terminal cisternae of the *sarco(endo)plasmic reticulum (SR)*, forming a closely coupled structure called a *dyad*. Within the dyad,  $\text{Ca}^{2+}$  ions movement takes place via the L-type  $\text{Ca}^{2+}$  channels located on the T-tubules and via the *ryanodine receptors (RyRs)*, which are  $\text{Ca}^{2+}$  release channels located on the SR. The SR contains a store of  $\text{Ca}^{2+}$  ions, which are partially released into the *sarcoplasm* (another name for the cytoplasm within the sarcolemma) when the cell is excited. As the AP travels along the sarcolemma and along the T-tubules,  $\text{Ca}^{2+}$  enters the cell through the L-type  $\text{Ca}^{2+}$  channels during Phase 2 of the action potential.  $\text{Ca}^{2+}$  then binds to and activates the RyRs,

triggering the further release of a much greater number of  $\text{Ca}^{2+}$  ions from the SR. This process is termed *calcium-induced calcium release*.  $\text{Ca}^{2+}$  diffuses from the dyadic space into the cytosol and then on the sarcomeric proteins, which make up the contractile machinery, activating contraction.

As  $\text{Ca}^{2+}$  is removed from the cytosol,  $[\text{Ca}^{2+}]_i$  decreases so that  $\text{Ca}^{2+}$  dissociates from the sarcomeric proteins, causing the sarcomere to relax.  $\text{Ca}^{2+}$  removal is achieved either via  $\text{Ca}^{2+}$  extrusion from the cell or  $\text{Ca}^{2+}$  uptake into intracellular  $\text{Ca}^{2+}$  stores. Two mechanisms are known to be responsible for the extrusion of  $\text{Ca}^{2+}$  from the cell: NCX and the *plasma membrane  $\text{Ca}^{2+}$  ATPase* (PMCA). The majority of the  $\text{Ca}^{2+}$  entering the cytosol during a  $[\text{Ca}^{2+}]_i$  transient is taken up back into the SR via the *sarcoplasmic  $\text{Ca}^{2+}$  ATPase* (SERCA), with 2  $\text{Ca}^{2+}$  ions transported into the SR for every 1 ATP molecule consumed, returning the cardiac myocyte to its resting state.

### 1.1.2 Cardiac cellular contraction

The basic contractile unit of each myocyte is called the *sarcomere* and is mainly composed of filamentous proteins (*myofilaments*) between thin partitions called *Z disks*. The two principal interdigitating myofilaments are predominantly composed, respectively, of *myosin* protein (*thick filament*) and of *actin* protein (*thin filament*). The thin filament consists of two actin strings arranged as a two-stranded helix. The groove between the actin strands contains two regulatory proteins: *tropomyosin* (Tn) and *troponin* (Tm). The sarcomere also contains spring-like filaments of *titin*, connecting Z disks. They ensure that myosin filaments stay aligned and they confer elasticity to the heart wall along with the extracellular *collagen*.

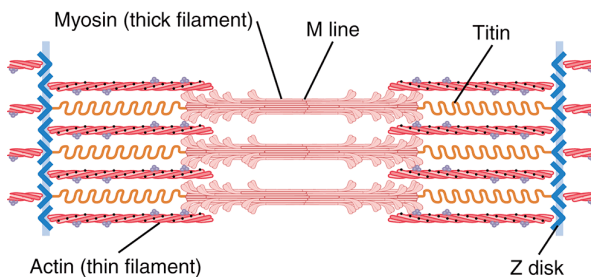


Figure 1.3: Proteins' organisation within the sarcomere. Adapted from [73], Unit II, Chapter 6, Page 81, Figure 6-3. Copyright © 2021 by Elsevier, Inc.

In the heart, contraction is initiated by a rise in  $[\text{Ca}^{2+}]_i$ .  $\text{Ca}^{2+}$  binds to the calcium-binding subunit of Tn, namely *troponin C* (TnC), on the thin filament, which causes Tm to move out of the actin groove, exposing actin binding sites. The thick filament, made of many myosin molecules, has its main body composed of centrally aligned myosin

tails and with protruding myosin heads exposed: these myosin heads now bind to the exposed actin binding sites. Contraction then follows as described by the *sliding filament theory*. The attached myosin heads rotate in the *power stroke*, pulling the thick filaments past the thin filaments, causing the sarcomere to contract. The myosin heads then unbind and can reattach to actin to further contract the sarcomere. The acto-myosin bond, which is formed through the attachment of myosin heads on the actin filament, is called a *cross-bridge* and constitutes an independent generator of force: the force generated within the entire sarcomere is therefore proportional to the number of attached myosin heads. Coordinated myocyte contraction in the heart is responsible for the rhythmic pumping of blood.

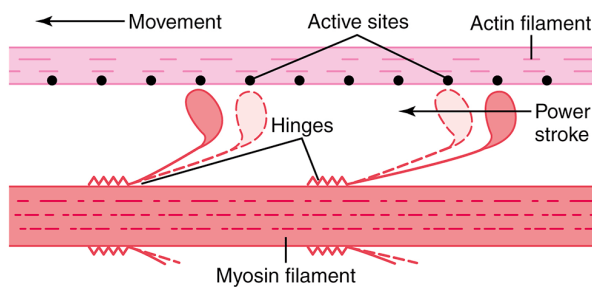


Figure 1.4: The sliding filament mechanisms at the basis of sarcomere contraction. Adapted from [73], Unit II, Chapter 6, Page 84, Figure 6-8. Copyright © 2021 by Elsevier, Inc.

### 1.1.3 Cardiac physiologic anatomy

The heart is composed of two muscular pumps, the right and left ventricles (RV, LV), each one filled from a contractile reservoir, respectively the right and left atria (RA, LA). Atrial and ventricular cells are the two major types of cardiac muscle along with His-Purkinje system cells, although the latter is mainly responsible for controlling the rhythmical beating of the heart rather than generating tension. Cardiac muscle cells take the name of *cardiomyocytes*. In this thesis, we will not deal with the skeletal muscle, so that we will refer to cardiomyocytes as simply *myocytes* with no ambiguities.

In the heart, myocytes are joined together at their ends by *intercalated discs*. At the intercalated discs, each myocyte effectively connects to a network of electrochemically coupled cells (*syncytium*). This is due to the presence of *gap junctions* where the membranes of two interfacing cells almost fuse with one another, allowing rapid diffusion of ions. Myocytes are arranged with a preferred direction. Groups of aligned myocytes are generally referred to as *fibres*. The aligned myocytes are then formed into *sheets*, and many sheets form the main layer of the heart walls, namely the *myocardium*, encapsulated within the *endocardium* (internal layer) and the *epicardium* (external layer). The

sheets spread within the myocardium in many different and specific directions resulting in the heart contracting in a twisting motion, thereby maximising the amount of blood ejected from the ventricles. The epicardium is the visceral layer of a more complex structure called *pericardium*, which surrounds the heart, conferring both structural and mechanical stability and lubrication.

The atria and the ventricles are two distinct functional syncytia, meaning that activation in the atria does not directly pass to the ventricles: this is mediated by the AV bundle (Section 1.1). The two syncytia are, in fact, separated by fibrous, non-conductive tissue surrounding two openings called *atrio-ventricular valves*. AV valves physically connect the *blood pools* or *chambers* in the left and the right heart enclosed within the atrial and ventricular syncytia. The heart chambers are further connected to the arterial *pulmonary circulation* and *systemic circulation* through the *pulmonary* and *aortic valves*, respectively, and to the venous pulmonary and systemic circulation via four *pulmonary veins* and via the *inferior* and *superior vena cavae* and *coronary sinus*, respectively. The LV chamber is further connected to the heart muscle itself through *coronary arteries*, which transport oxygen-rich blood to the heart to function as for all the other tissues and organs in the body.

The series of cardiac events that occur in the time frame that goes from the beginning of one heartbeat until the beginning of the next is called *cardiac cycle*.

#### 1.1.4 Cardiac cycle

The cardiac cycle consists of a period of relaxation called *diastole*, during which the ventricles are filled with blood from the atria, followed by a period of contraction called *systole* when the blood is ejected from the ventricles to the lungs, the heart tissue itself and the rest of the body. At each moment of the cardiac cycle, the amount of blood in the heart remains approximately constant, although differently distributed among the four chambers.

Venous blood flows through the systemic and pulmonary venous system major vessels (Section 1.1.3) to the RA and LA, respectively. Following spontaneous depolarisation of the SA node myocytes, atria are activated and start contracting, pumping blood into the ventricles. Atrial contraction thus serves as primer pump to ventricular *filling*. The volume of blood in a ventricle at the end of its filling is called *end-diastolic volume (EDV)*, while the corresponding chamber pressure is called *end-diastolic pressure (EDP)*. Atrial systole is followed by ventricular systole. A sharp rise in ventricular pressure above the atrial pressure makes the AV valves close by a reversed pressure gradient, preventing retrograde blood flow. The ventricles are activated with the aortic valve closed. The myocardium begins to generate tension

but must raise the ventricle pressure to be high enough to overcome the aortic pressure. During this time, the ventricle pressure rapidly increases, but the volume remains constant and is referred to as the *isovolumetric contraction (IVC)* period. When the ventricular pressure exceeds the arterial pressure, this makes the aortic and pulmonary valves open, causing *ejection* of blood from the ventricles. The ejected blood volume also called *stroke volume (SV)* is only about two-thirds of the available EDV of blood: a residual blood volume, namely the *end-systolic volume (ESV)*, remains. The proportion of ejected blood, i.e. SV divided by EDV, takes the name of *ejection fraction (EF)*. The rate of ventricular blood ejection is initially rapid and then progressively slows down. Since the rate at which the aortic blood is draining away into the peripheral circulation now exceeds ventricular ejection, ventricular pressure also begins to fall until reaching the *end-systolic pressure (ESP)* when the outflow valves close. At this point, both the ventricles become closed chambers again, and a rapid pressure fall occurs driven by the elastic recoil of the deformed and relaxing myocardium. This process takes place at constant blood volumes and is called *isovolumetric relaxation (IVR)*. When the intraventricular pressures decrease back to their low diastolic levels, the AV valves open and blood floods in from the atria (which have themselves been filling up during ventricular systole), and the next cardiac cycle begins.

To summarise, isovolumetric contraction, ejection, isovolumetric relaxation, and filling are the 4 main phases of the cardiac cycle (Figure 1.5).

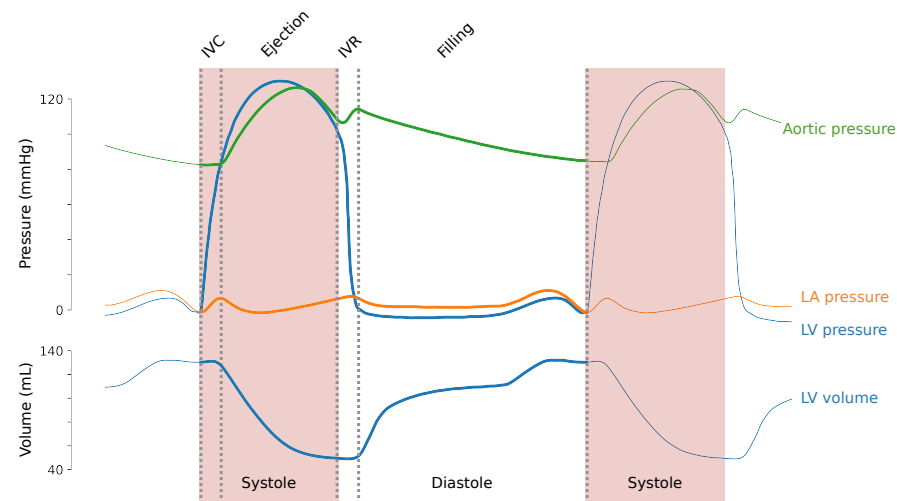


Figure 1.5: Wiggers diagram representing the four main phases of the cardiac cycle in the left heart.

## 1.2 MATHEMATICAL MODELLING OF THE HEART

Biophysically detailed mathematical models of cardiac physiology have been developed to reproduce *in silico* the cardiac function at different biological scales, from the cell up to the whole organ. These models can provide insight into the pathophysiology of complex cardiovascular diseases and help interpret clinical observations to improve patients' treatment.

### 1.2.1 Cell electrophysiology

Models of cardiac cells' electrophysiology began with the work of Noble in 1962 [167], who created the first computational model of the long-lasting action and pace-maker potentials of Purkinje fibres of the heart. He continued on the pioneering work of Hodgkin and Huxley [81], who in 1952 modelled  $\text{Na}^+$ ,  $\text{K}^+$  and leakage currents that give rise to dynamic changes in membrane potential and hence the AP across the surface membrane of a squid giant nerve fibre.

Hodgkin and Huxley, and then Noble, modelled the sarcolemma as an electrical circuit (*equivalent circuit model*), comprised of a capacitor in parallel with resistors that represented ionic currents. The total membrane current was given as the sum of the capacitive current and the ionic current:

$$I_m = C_m \frac{dV_m}{dt} + I_i, \quad \text{with} \quad I_i = \sum_{\text{ion}} I_{\text{ion}} \quad (1.1)$$

where

$I_m$  total membrane current

$I_i$  total ionic current, i.e. sum of all ionic currents  $I_{\text{ion}}$  with sign (negative, positive for inward, outward currents, respectively)

$C_m$  cell membrane capacitance per unit area

$V_m$  transmembrane voltage

and for each ion species the corresponding transmembrane current  $I_{\text{ion}}$  was described by the *Ohm's law* as:

$$I_{\text{ion}} = g_{\text{ion}} (V_m - E_{\text{ion}}) \quad (1.2)$$

where

$g_{\text{ion}}$  average channel conductance

$E_{\text{ion}}$  equilibrium potential of the ion

The equilibrium potential of a given ion species is the electric potential that would be required to maintain a zero net ion flux if the ion was allowed to diffuse down to its concentration gradient, assuming the cell membrane is permeable to only that ion species. The *Nernst*

equation expresses the equilibrium potential of an ion as a function of the ion concentrations inside and outside the cell:

$$E_{\text{ion}} = \frac{RT}{Fz} \ln \frac{[\text{ion}]_e}{[\text{ion}]_i} \quad (1.3)$$

where

R	gas constant
T	absolute temperature
F	Faraday's constant
z	ion valency
$[\text{ion}]_i$	ion intracellular concentration
$[\text{ion}]_e$	ion extracellular concentration

Since Noble's initial work, many ionic cell models have been developed to represent the baseline physiology of both atrial, ventricular, and SA node myocytes [49]. These models all share the same cell membrane modelling strategy by viewing it as an electric circuit (equation (1.1)) and mostly differ in single ion channels' kinetics representation.

The current  $I_{\text{ion}}$  introduced in equation (1.1) is the result of ions moving across the cell membrane through an ion channel, which is made of pore-forming proteins that span the membrane lipid bilayer. Ion channels are regulated by one or more *gates*, which allow ions to pass according to whether they are in an open or closed state. Changes in an ion channel conformation take place in response to chemical or electrical signals, temperature, or mechanical stress. Cardiac cells ion channels are mostly *voltage-gated*, meaning that they change conformation with varying transmembrane voltage. Two approaches are commonly being used to represent ionic channels kinetics: the first uses the Hodgkin-Huxley (HH) formulation [81] while the second (a generalisation of the first) uses continuous-time Markov chain models (MM) [62].

In the HH characterisation of channels, the conductance  $g_{\text{ion}}$  (equation (1.2)) is given by the product of a maximal conductance term and one or more separate *gating variables* that represent the probability of finding the channel open:

$$g_{\text{ion}} = g_{\text{ion}}^{\max} \times y_1 \times \dots \times y_N \quad (1.4)$$

where each gating variable  $y := y_i$  can be formulated using the equation:

$$\frac{dy}{dt} = \frac{y_\infty - y}{\tau_y} \quad (1.5)$$

where

$y_\infty$  voltage-dependent steady-state function of the gate

$\tau_y$  voltage-dependent time constant

The gating variables described in the HH formulation do not represent specific kinetic states of the ion channel. Moreover, they are assumed to be independent.

To explicitly describe the dependence of a given transition on the occupancy of different states for a given channel, MMs are used [62]. In this case, a discrete number of states represent the possible configurations a channel has. Transitions from one state to the other can occur at different rates, and the rate zero is used by convention when no direct switching between two given states is possible. Gating variables will then simply represent the probability of finding the channel in the respective states (*state variables*). An example of the MM approach to model an ion channel which can be either in the open, closed or inactivated configuration, includes 3 state variables to represent the three possible configurations and 6 transition rates. Variation of state  $y_i$  is given as a function of the other state variables  $y_j$  for  $j \in \{1, 2, 3\} \setminus \{i\}$ :

$$\frac{dy_i}{dt} = \sum_{\substack{j=1 \\ j \neq i}}^3 (k_{ji} y_j - k_{ij} y_i) \quad (1.6)$$

where  $k_{ji} \in \mathbb{R}$  is the rate at which transition from state  $y_j$  to state  $y_i$  occurs.

It is worth mentioning that the two presented HH and MM modelling frameworks are not mutually exclusive but are very frequently used in combination to represent the many different ion channels within the cell.

### 1.2.2 Cell contraction

Cardiac contraction models are used to simulate active tension generation at the sarcomere level arising from the thin and thick filaments. The development of these models has proceeded over the years in parallel with key experimental discoveries about striated and cardiac muscle physiology [164]. As a result, contraction models have transitioned from simple phenomenological models aiming to represent the average sarcomere dynamics to very complex, spatially detailed models trying to capture the exact positions of individual molecules. However, in the view of incorporating these models within whole-organ computational frameworks, currently adopted sarcomere contraction models have achieved a balance between recapitulating the main mechanistic phenomena while still being represented by a tractable number of ordinary differential equations (ODEs) to remain computationally efficient to solve. Fundamental mechanisms that are desirable to recapitulate in these multi-scale sarcomere contraction

models include force dependence on sarcomere length (*Frank-Starling mechanism*), myofilament cooperative activation by  $\text{Ca}^{2+}$ , acto-myosin cooperative interaction in cross-bridges formation and force dependence on sarcomere length variation (velocity) [164].

### 1.2.3 Electromechanical coupling

In biophysically detailed models of cardiac electromechanics, the active tension along the muscle fibres direction is calculated using sarcomere contraction models, introduced in Section 1.2.2. This calculation is normally performed in two steps. The first step consists in solving a system of ODEs of the form:

$$\frac{dy}{dt} = f(t, \lambda, \dot{\lambda}, y) \quad (1.7)$$

where  $f$  is a non-linear function and

- $t$  time
- $\lambda$  fibre strain
- $\dot{\lambda}$  fibre strain rate ( $= d\lambda/dt$ )
- $y$  vector of state variables

In the second step, active tension ( $T_a$ ) is calculated as a function of time, fibre strain and strain rate and state variables which are varying over time, via a non-linear function  $g$ :

$$T_a = g(t, \lambda, \dot{\lambda}, y) \quad (1.8)$$

The coupling between the electrical and mechanical components of the model resides in the definition of the vector of state variables  $y$ . This is in part given by cell electrophysiology model components (e.g. gate and/or state variables) and in part given by cell contraction model components (e.g. variables representing sarcomeric proteins kinetics). The variation in the second set of  $y$  vector components can depend on the current state of the first set of components via the action of function  $f$ . Furthermore, the electromechanical coupling takes place when the solution of equation (1.7) ( $y$ ) enters the calculation of the active tension in equation (1.8) through the function  $g$ .

### 1.2.4 Tissue electrophysiology

A tissue model of cardiac electrophysiology is required to link cellular excitation through to whole organ electrical activation.

When a single cardiac myocyte undergoes depolarisation, the evoked AP travels in the form of a depolarisation wave which is able to activate the neighbouring cells. We have seen that cardiac myocytes are microscopically organised into fibres and further organised into

sheets (Section 1.1.3). This spatial arrangement causes an anisotropic propagation of the depolarisation wavefront, which is faster along the principal axis of the fibre and slower in the other directions. Different factors can affect propagation, including the shape of the myocytes, the curvature of the wavefront, the relative positions of the gap junctions within the fibres, the extracellular matrix composition and the local vasculature [43]. In the 3-dimensional ventricular tissue, the AP depolarisation wave propagation is mainly orthogonal, with the fibre, sheet, and sheet-normal being the three principal directions.

Cardiac tissue electrophysiology can be mathematically described [43] by first considering the tissue as a syncytium of electrically coupled cells and successively homogenising it to treat it as a smooth, continuous space. In the *bidomain model*, both the intracellular (subscript i) and the extracellular (subscript e) spaces are considered as smooth and overlapping domains, separated by the cell membrane. The electric current densities in the two domains are described by Ohm's law as:

$$\mathbf{J}_d = -\mathbf{G}_d \nabla \phi_d, \quad \text{with } d = i, e \quad (1.9)$$

where

- $\mathbf{J}_d$  current density
- $\mathbf{G}_d$  conductivity tensor
- $\phi_d$  electric potential

Conservation of current and charge is then enforced:

$$\begin{aligned} \nabla \cdot \mathbf{J}_i &= -I_m \\ \nabla \cdot \mathbf{J}_e &= I_m \end{aligned} \Rightarrow \nabla \cdot (\mathbf{J}_i + \mathbf{J}_e) = 0 \quad (1.10)$$

where  $I_m$  is the cell membrane current calculated as in equation (1.1) using an ionic cellular model (Section 1.2.1), and additionally scaled by a factor  $\beta_m$  to match the domains' 3-dimensional nature:

$$I_m = \beta_m \left( C_m \frac{dV_m}{dt} + I_i \right) \quad (1.11)$$

The transmembrane voltage can be expressed in terms of electric potentials as

$$V_m = \phi_i - \phi_e \quad (1.12)$$

so that the final set of equations describing the bidomain model takes the following form:

$$\nabla \cdot (\mathbf{G}_i(\nabla V_m + \nabla \phi_e)) = \beta_m \left( C_m \frac{dV_m}{dt} + I_i \right) \quad (1.13)$$

$$\nabla \cdot ((\mathbf{G}_i + \mathbf{G}_e)\nabla \phi_e) = -\nabla \cdot (\mathbf{G}_i \nabla V_m) \quad (1.14)$$

The system is solved using the finite element method with no-flux conditions at the computational domain boundaries (*Neumann boundary conditions*).  $\mathbf{G}_i$  and  $\mathbf{G}_e$  conductivity tensors' components are taken to reflect the anisotropy of the cardiac tissue.

### 1.2.5 Tissue mechanics

A tissue model of cardiac mechanics is required to link cellular active contraction models through to whole organ pump function. For the modelling of the mechanical properties of cardiac tissue, nonlinear solid mechanics is used. The mathematical formalism adopted in this section follows the standard textbook of nonlinear continuum mechanics by Bonet and Wood [26].

Like electrical properties, tissue mechanical properties depend on the orientation of cardiac tissue microstructure. Therefore, to mathematically describe cardiac tissue deformations, tensors are commonly given in terms of a coordinate system locally aligned with the muscle fibre ( $\mathbf{f}$ ), sheet ( $\mathbf{s}$ ) and sheet-normal directions ( $\mathbf{n}$ ) in the reference configuration, determining the orthonormal matrix  $\mathbf{L} = [\mathbf{f} \ \mathbf{s} \ \mathbf{n}]$ . In the finite elastic deformation theory, the transformation from undeformed ( $\mathbf{X}$ ) configuration to deformed ( $\mathbf{x}$ ) configuration is described through the deformation gradient tensor:

$$\mathbf{F} = \frac{\partial \mathbf{x}}{\partial \mathbf{X}} \quad (1.15)$$

The determinant of the deformation gradient  $J := \det(\mathbf{F})$  measures the volume variation as the material undergoes deformation. Large deformation mechanics equations for an incompressible solid enforce the stress equilibrium with an incompressibility constraint:

$$\nabla \cdot (\mathbf{J}^{-1} \mathbf{F} \mathbf{T} \mathbf{F}^T) = 0, \quad \text{with constraint} \quad J = 1 \quad (1.16)$$

where  $\mathbf{T}$  is the second Piola-Kirchhoff stress tensor. The solution to the mechanics problem requires a description of the material behaviour known as the *constitutive law*, which gives the stress tensor  $\mathbf{T}$  as a function of the Green strain tensor  $\mathbf{E}$  and the Cauchy strain tensor  $\mathbf{C}$  for the material. The Green strain tensor is given as a function of the deformation gradient tensor:

$$\mathbf{E} = \frac{1}{2} (\mathbf{C} - \mathbf{I}), \quad \text{with} \quad \mathbf{C} = \mathbf{F}^T \mathbf{F} \quad (1.17)$$

and is transformed to a fibre-aligned coordinate system using  $\mathbf{E}^{fsn} = \mathbf{L}^T \mathbf{E} \mathbf{L}$ . The stress tensor  $\mathbf{T}^{fsn}$  is determined from the constitutive law, which is generally expressed as a *strain energy function*  $W$ :

$$\mathbf{T}^{fsn} = \frac{\partial W}{\partial \mathbf{E}^{fsn}} \quad (1.18)$$

The stress tensor  $\mathbf{T}^{fsn}$  is then transformed back using  $\mathbf{L} \mathbf{T}^{fsn} \mathbf{L}^T$ . The final second Piola-Kirchhoff stress tensor is obtained from the strain energy function by adding an active tension component  $T_a$  (Section 1.2.2) along the fibres direction  $\mathbf{f}$ :

$$\mathbf{T} = \mathbf{L} \frac{\partial W}{\partial \mathbf{E}^{fsn}} \mathbf{L}^T + T_a \mathbf{f} \mathbf{f}^T \quad (1.19)$$

$T$  expresses the stresses in actively contracting incompressible cardiac tissue in terms of its strain and completes the set of equations required to model actively contracting cardiac tissue. The resulting system of equations is solved using the finite element method. A given displacement can be used to prescribe the position of the nodes at the computational domain boundaries (*Dirichlet boundary conditions*).

### 1.2.6 Haemodynamics

The blood pumped by the heart appears in electromechanical models as a mechanical boundary condition for the cavity pressure. During ejection, the change in pressure can be simulated using a windkessel model [198]. In this framework, the aorta is modelled as a compliant vessel, which obeys

$$p_{ao} = \frac{v_{ao}}{C} \quad (1.20)$$

where

$C$  total arterial compliance

$p_{ao}$  aortic blood pressure

$v_{ao}$  aortic blood volume

Blood flow to the body is modelled using the simple *Darcy's law of flow* which gives the flow as being proportional to the pressure drop between inlet and outlet pressures:

$$I_{out} = \frac{p_{ao} - p_{out}}{R} \quad (1.21)$$

where

$R$  peripheral body vessels resistance

$I_{out}$  blood flow to the body

$p_{out}$  external pressure

The external pressure  $p_{out}$  is assumed to be approximately equal to zero. Equations (1.20)–(1.21) make up the *two-element windkessel model*. However, more realistic aortic pressure waves can be obtained by introducing a second resistance for the aortic valve, making up the *three-element windkessel model* [245]:

$$\frac{dv_{LV}}{dt} = \frac{1}{Z} (p_{ao} - p_{LV}) \quad (1.22)$$

$$\frac{dv_{ao}}{dt} = -I_{out} - \frac{dv_{LV}}{dt} \quad (1.23)$$

$$I_{out} = \frac{1}{R} p_{ao} \quad (1.24)$$

$$p_{ao} = \frac{1}{C} v_{ao} \quad (1.25)$$

where

- $Z$  aortic characteristic impedance
- $p_{LV}$  left-ventricular pressure
- $v_{LV}$  left-ventricular volume

The three-element windkessel model equations can also be re-written more concisely as:

$$\frac{d^2v_{LV}}{dt^2} = - \left( \frac{1}{CZ} + \frac{1}{RC} \right) \frac{dv_{LV}}{dt} - \frac{1}{CZR} p_{LV} - \frac{1}{Z} \frac{dp_{LV}}{dt} \quad (1.26)$$

Equation (1.26) can be further generalised as done in [119] to model simple haemodynamic boundary conditions during the other cardiac cycle phases as well, namely, preload filling (to initialise the heart to a prescribed end-diastolic pressure), isovolumetric contraction, isovolumetric relaxation and diastolic filling:

$$m_1 \frac{d^2v_{LV}}{dt^2} + m_2 \frac{dv_{LV}}{dt} + m_3 \frac{dp_{LV}}{dt} + m_4 v_{LV} + m_5 p_{LV} + m_6 = 0 \quad (1.27)$$

This is done by solving (1.27) with coefficients  $\mathbf{m} := (m_1, \dots, m_6) \in \mathbb{R}^6$  adjusted according to the phase in the cardiac cycle as follows:

$$\mathbf{m} = \begin{cases} (0, 0, 1, 0, 0, 0) & \rightarrow \text{phase 0: preload filling} \\ (0, 1, 0, 0, 0, 0) & \rightarrow \text{phase 4: isovolumetric contraction} \\ (ZC, 1 + Z/R, C, 0, 1/R, 0) & \rightarrow \text{phase 1: systolic ejection (equation (1.26))} \\ (0, 1, 0, 0, 0, 0) & \rightarrow \text{phase 2: isovolumetric relaxation} \\ (0, 0, 1, 0, \kappa_{diast}, -p \cdot \kappa_{diast}) & \rightarrow \text{phase 3: diastolic filling} \end{cases} \quad (1.28)$$

Briefly, the heart is inflated to a prescribed end-diastolic pressure ( $p$ ) and stays in the diastolic phase ( $dp_{LV}/dt = 0$ ) until volume flow reverses. Next, isovolumetric contraction is simulated ( $dv_{LV}/dt = 0$ ) until the cavity pressure is high enough to open the aortic valve (prescribed  $p_{ao}$  pressure). Ejection is simulated using the three-element windkessel model (1.26). When flow reverses once again, the constraint for isovolumetric relaxation is set ( $dv_{LV}/dt = 0$ ). When pressure finally relaxes below the prescribed  $p$ , a simple phenomenological model is used for diastole at a fixed  $\kappa_{diast}$  inflation speed ( $dp_{LV}/dt = \kappa_{diast} (p - p_{LV})$ ).

### 1.3 HEART FAILURE

Heart failure (HF) is a chronic condition that occurs when the heart is unable to pump blood to meet the demands of the body. HF affects

nearly a million people in the UK alone [21], and increases the risk of cardiovascular diseases, stroke and death [4, 76]. HF patients are most commonly divided into two macro-categories according to distinct LV EF phenotypes. When HF is accompanied by systolic dysfunction, the ventricular myocytes cannot contract properly due to insufficiently oxygenated or damaged tissue. This condition often manifests as a lower than normal EF (normal is from 50 % to 70 %) and is referred to as *heart failure with reduced ejection fraction (HFrEF)*. When HF is accompanied by diastolic dysfunction, the ventricular myocytes retain the ability to contract but cannot relax properly due to thickened and stiff tissue. This condition often presents a normal or even elevated EF and is referred to as *heart failure with preserved ejection fraction (HFpEF)*. Although LV EF value can be useful as an initial screening tool (e.g. EF < 50 % or EF > 50 %), it cannot provide an accurate assessment of the whole cardiac function on its own [73] as systolic and diastolic dysfunction can each present as HFrEF or HFpEF. HF is, in fact, a heterogeneous syndrome rather than a specific disease, and HF patients can exhibit multiple pathological conditions, which are common in both the HFrEF and HFpEF diseases. Nevertheless, HFrEF and HFpEF patients often present distinct traits, medical history and co-morbidities. Current pharmacological treatments for HF patients vary according to the EF phenotype. These are discussed in the next two sections.

Importantly, improved treatment strategies are constantly being sought for, and the Food and Drug Administration has stated [59] recently that an improvement in symptoms and/or physical function, even without a documented favourable effect on the primary endpoints (e.g. an urgent heart failure visit/hospitalisation or cardiovascular death), can be the basis for a drug to be approved as HF treatment [64]. For this reason, physiopathologic or “explanatory” endpoints [252] have been regaining attention in the initial drug assessment phase and as secondary endpoints in later phases of clinical trials. For instance, non-invasive measurements of the LV function such as cardiac output fall within these categories as targets for improvement (e.g. increased SV / EF) [252].

### 1.3.1 HF with reduced ejection fraction

The most common causes of HFrEF are decreased coronary blood flow due to ischaemic heart disease, damaged heart valves and primary cardiac muscle disease. The gold standard pharmacotherapies are beta-blockers, angiotensin receptor/neprilysin inhibitors, sodium-glucose co-transporter inhibitors, beta-blockers and mineralocorticoid receptor antagonists. These were all shown to improve the primary endpoint composite of cardiovascular death and HF hospitalisation in breakthrough clinical trials [55].

Novel strategies of HF treatment are being developed that tend to differ from the above-mentioned pharmacotherapies that focus on the neurohormonal modulation paradigm. Among novel strategies, the direct sarcomere modulators are an important compound class in this direction [233]. Sarcomere modulators' mechanism of action relies on the fact that sarcomeric proteins dynamics are the basis of myocardial contraction and relaxation [220]. The two new compounds omecamtiv mecarbil [229] and mavacamten [172] provide new sarcomere modulators that can increase and decrease sarcomere activation by cardiac myosin stimulation and inhibition, respectively. Both these compounds alter myofilament  $\text{Ca}^{2+}$  sensitivity, and knowing when and why this will result in improved cardiac function is an important question.

### 1.3.2 *HF with preserved ejection fraction*

HFpEF is a heterogeneous disease and is sometimes attributed to LV diastolic dysfunction. Diastolic function worsens as part of normal ageing [7], and this partially explains the age association with increasing HFpEF risk. Other potentially prominent risk factors for HFpEF include obesity, metabolic syndrome, hypertension, sedentary state, coronary disease, kidney disease [184]. Hypertension is the dominant substrate upon which HFpEF develops, being present in 80 % – 90 % of patients in community-based studies e.g. [28].

In HFpEF diseased heart, there is often an inability to enhance early diastolic relaxation and suction with exercise, contributing to increased filling pressures. There is also an increase in passive LV chamber stiffness in HFpEF so that even if relaxation and suction were adequate, a higher filling pressure would be required to distend the chamber to an adequate preload volume. This increase in LV passive stiffness can be related to changes in the extracellular matrix due to deposition of collagen (*fibrosis*) [34], as well as changes within the cardiac myocyte, e.g. in  $\text{Ca}^{2+}$  handling and the phosphorylation status of titin. Typical structural changes associated with HFpEF are LA enlargement and LV hypertrophy, characterised by an enlargement or thickening of the heart muscle [253]. However, investigations in broader HFpEF samples have established a much more heterogeneous cardiac phenotype, characterised by many patterns of cardiac remodelling, including no remodelling at all [213].

There are limited evidence-based pharmacotherapies for HFpEF. This may be due to the disparateness of the disease as well as its multi-factorial pathophysiology. Patients currently receive either angiotensin-converting enzyme inhibitors/aldosterone receptor blockers,  $\text{Ca}^{2+}$  channel blockers or beta-blockers, but the mortality and the morbidity associated with the disease have so far remained high [3]. Therefore,

patients with HFpEF are currently considered the largest unmet need in cardiology [174].

Previously, HFpEF was thought to result from solely diastolic dysfunction and LV hypertrophy [180]. However, therapies within this conceptual framework were not successful [44]. Recently, a combination of immune dysregulation and inflammation that leads to systemic microvascular endothelial dysfunction in various organ systems has been proposed as the cause of HFpEF. There are now ~ 20 pharmacotherapeutic clinical trials targeting signalling mechanisms along this cascade. Two examples of these clinical trials aim to block IL-1, a pro-inflammatory cytokine that inhibits the L-type  $\text{Ca}^{2+}$  channels, and inhibit the late inward  $\text{Na}^+$  current, respectively. Both therapies are expected to prevent cytosolic  $\text{Ca}^{2+}$  overload, which may, in turn, improve LV relaxation (or *lusitropy*). Targeting  $\text{Ca}^{2+}$  handling is already the subject of different clinical trials. On the other hand, the possibility to target the sarcomere to treat different cardiovascular pathologies, including HFpEF, by dynamically modulating its constituent proteins is an ongoing investigation [180].

## 1.4 MOTIVATION AND GOALS

### 1.4.1 Quantitatively linking cell, tissue and haemodynamic properties to whole heart function

The whole heart contraction is the result of complex molecular mechanisms and electromechanical events at the cellular level. The organ-scale function is thus strongly dependent on and can be manipulated by cellular manipulations, yet quantitatively mapping changes in one part of this system to another to understand their role in disease or predicting how changing a single protein's function may affect whole-organ function is complex and is not susceptible to intuitive analysis. For this reason, the main purpose of this thesis is to develop a computational framework to quantitatively link pathological and pharmacological manipulations across scales and physics in the heart, from single-cell up to the whole-organ contractile function. By improving our understanding of the transduction of the calcium dynamics and sarcomere function through to whole-organ contractile function in healthy and diseased states, we hope to provide a virtual platform to test hypotheses and possibly identify potential targets for treating HF.

#### 1.4.2 *In silico identification of potential pharmacological targets for HF treatment*

The currently available mathematical models of the heart have to be tuned to experimental measurements of the real world biological system they aim to represent in order to build a robust virtual platform. Another important issue is assessing how variability in a model input can impact our confidence in model predictions. Calibrating detailed models to biological data with uncertainty and then propagating this uncertainty into model predictions represents a significant methodological and computational challenge, which we aim to address with this thesis work.

#### 1.5 SUMMARY

The heart is a complex system where many different sub-cellular, cellular, tissue and whole-organ scales' mechanisms interplay to yield a coordinated contraction and relaxation. We have described the heart physiology at each of these scales, and we have shown how current biophysically-detailed computational bio-electro-mechanics models are able to capture the main biological phenomena to represent the heart function *in silico*. We have introduced the HF syndrome, which encompasses a large variety of diseases, empathising the need to have a virtual platform to reproduce the heart characteristic pathophysiological mechanisms to guide preclinical research towards better HF pharmacological treatments.

Part II  
METHODOLOGY

# 2

## 3D BIOPHYSICAL MODEL OF BIVENTRICULAR RAT HEART CONTRACTION MECHANICS

### OUTLINE

In this chapter, we systematically build a mathematical model of 3D biventricular rat heart contraction mechanics. We start with modelling ion fluxes across each cell membrane using an ionic model for left ventricular myocytes at physiological temperature and pacing rate (Section 2.1). We then model active tension generation at the cellular level using a model of sarcomere contraction, which includes length- and velocity-tension dependencies (Section 2.2). We present the framework to build a 3D computer representation (mesh) of rat biventricular anatomies from experimental data (Section 2.3). We finally describe passive material properties (Section 2.4), myocardial electrical activation (Section 2.5) and spatial and haemodynamic boundary conditions (Section 2.6). We conclude with a brief summary (Section 2.9).

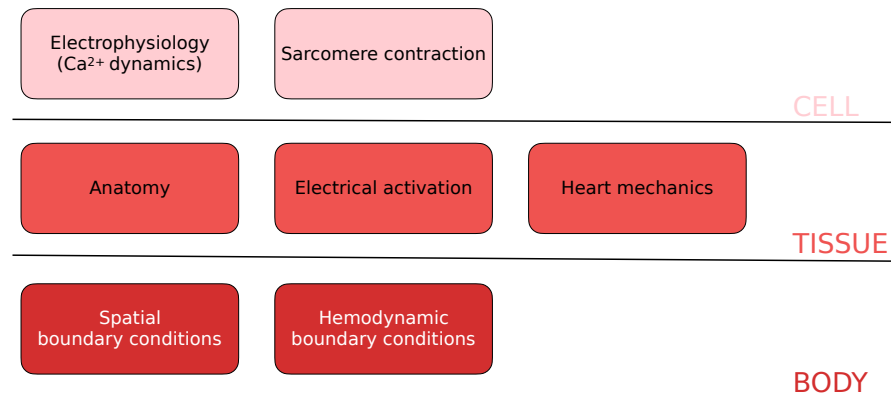


Figure 2.1: The full 3D biophysical model of biventricular rat heart contraction mechanics is a multi-scale framework of integrated sub-models describing the main mechanisms which regulate the heart contraction and relaxation at the cell, tissue and body scales.

### 2.1 IONIC MODEL

We employed the Gattoni et al. [68] model to simulate rat left ventricular myocytes electrophysiology and calcium dynamics at physiological pacing rate (6 Hz) and temperature (37 °C). This model was selected as two variants of it exist [69], where the model was specifically tailored

to represent the LV myocyte electrophysiology of a healthy control rat and a rat model of heart failure. In Chapter 4, we will use magnetic resonance images to derive heart anatomies (meshes) for the same kind of animal models, and we were in a unique spot since the experiments used to create the two ionic models in [69] were performed on the very same cohort of rats from which the medical images were obtained.

All the currents present in the Gattoni et al. [68] model are summarised in Table 2.1, while the main ion channels, transporters and pumps are depicted in Figure 2.2.

LABEL	DEFINITION
$I_{LCC}$	L-type $\text{Ca}^{2+}$ current
$I_{RyR}$	ryanodine receptor current
$I_{TRPN}$	troponin buffering current
$I_{SERCA}$	sarcoplasmic $\text{Ca}^{2+}$ pump current
$I_{SR\ell}$	sarcoplasmic reticulum leakage current
$I_{NCX}$	$\text{Na}^+/\text{Ca}^{2+}$ exchanger current
$I_{PMCa}$	plasma membrane $\text{Ca}^{2+}$ pump current
$I_{Ca b}$	$\text{Ca}^{2+}$ leak current
$I_{NaK}$	$\text{Na}^+/\text{K}^+$ pump current
$I_{Na}$	$\text{Na}^+$ current
$I_{K1}$	inwardly rectifying $\text{K}^+$ current
$I_{to}$	transient outward $\text{K}^+$ current
$I_{ss}$	steady-state outward $\text{K}^+$ current
$I_f$	hyperpolarisation-activated current
$I_{BNa}$	$\text{Na}^+$ background current
$I_{BK}$	$\text{K}^+$ background current

Table 2.1: Gattoni et al. [69] model's ionic currents.

## 2.2 CONTRACTION MODEL

We employed the Land et al. [119] myocyte contraction model to simulate both dynamic force generation at the sarcomere level in response to a calcium transient and the steady-state force-calcium relationship in the rat heart. This model describes the cooperative binding of  $\text{Ca}^{2+}$  to TnC, which causes unblocking of the actin sites for myosin cross-bridge cycling. We selected this specific model because it is regulated by only 4 ODEs, which makes it computationally inexpensive to be run. This was a desired feature, as we aim at incorporating the model

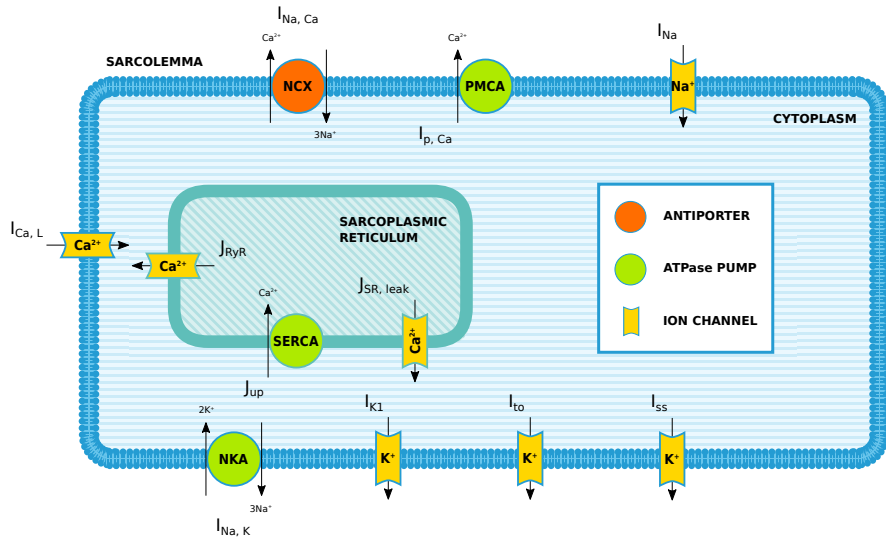


Figure 2.2: Main ion channels and pumps included in the Gattoni et al. [68] model.

within a larger multi-scale, whole-organ contraction mechanics model where general performances can be heavily affected by their cellular sub-unit model. Despite the low number of equations, the Land et al. [119] model is still able capture all the key mechanisms regulating sarcomeric function (previously discussed in Section 1.2.2), including active tension generation dependence on sarcomere length (Section 2.2.1) and velocity (Section 2.2.2). At the same time, this model was previously shown to be suitable for being incorporated within whole-heart computational frameworks [119, 130].

The process of  $\text{Ca}^{2+}$  binding to TnC is described via the following equation:

$$\frac{d\text{TRPN}}{dt} = k_{\text{trpn}} \left[ \left( \frac{[\text{Ca}^{2+}]_i}{\text{Ca}_{T50}} \right)^{n_{\text{trpn}}} (1 - \text{TRPN}) - \text{TRPN} \right] \quad (2.1)$$

where

TRPN	proportion of bound $\text{Ca}^{2+}$ -TnC complexes
$k_{\text{trpn}}$	unbinding rate of $\text{Ca}^{2+}$ from TnC
$[\text{Ca}^{2+}]_i$	representative $\text{Ca}^{2+}$ transient
$\text{Ca}_{T50}$	$\text{Ca}^{2+}$ thin filament sensitivity
$n_{\text{trpn}}$	$\text{Ca}^{2+}$ -TnC binding degree of cooperativity

Tropomyosin kinetics and the cross-bridge cycle are represented by a two-state model. One state is the *cross-bridge state* (XB), where the cross-bridge is actively cycling and includes both the weakly, strongly, and unbound states all collapsed into one state, while the other state

is the *non-permissive state* ( $N = 1 - XB$ ). The transition between these two states is described via the following equation:

$$\frac{dXB}{dt} = k_{xb} \left[ \text{permtot}(1 - XB) - \frac{1}{\text{permtot}} XB \right], \quad \text{with} \quad (2.2)$$

$$\text{permtot} := \sqrt{\left( \frac{\text{TRPN}}{\text{TRPN}_{50}} \right)^{n_{xb}}}$$

where

- $XB$  proportion of formed cross-bridges
- $k_{xb}$  cross-bridges cycling rate
- $\text{TRPN}_{50}$  fraction of  $\text{Ca}^{2+}$ -TnC bounds for half-maximal cross-bridges activation
- $n_{xb}$  cross-bridge formation degree of cooperativity

TRPN and XB variation over time within one cardiac cycle is shown in Figure 2.3, where the representative calcium transient from healthy, 6 Hz-paced rat left ventricular myocytes at 37 °C which was used to run the simulation is also displayed.

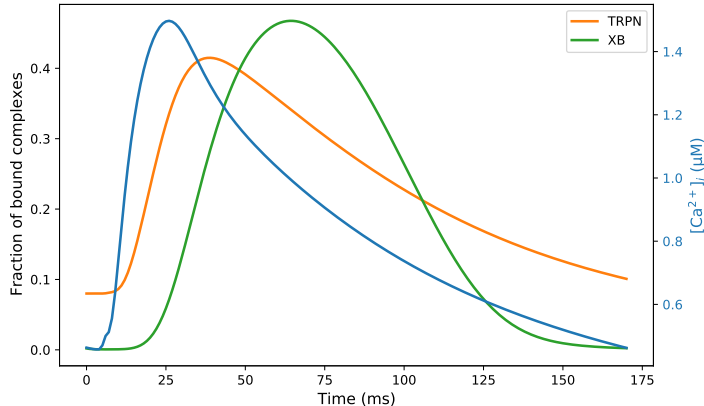


Figure 2.3: Fraction of bound  $\text{Ca}^{2+}$ -TnC complexes (TRPN) and of bound cross-bridges (XB) as a function of time. The intracellular  $\text{Ca}^{2+}$  concentration variation over time is also displayed on a different scale (blue).

In the Land et al. [119] model, normalised active force is defined as:

$$F_n = g(Q) \cdot h(\lambda) \cdot XB \quad (2.3)$$

where

- $h(\lambda)$  length-dependence factor
- $g(Q)$  velocity-dependence factor

Normalised force (equation (2.3)) is then scaled to actual tension using a reference tension  $T_{ref}$  scaling coefficient that encapsulates the total number of cross-bridges and the fraction of cycling cross-bridges in the force-generating state for any given time:

$$T = T_{ref} \cdot F_n \quad (2.4)$$

### 2.2.1 Length-dependence

The active tension dependence on sarcomere length was based on filament overlap modelling:

$$h'(\lambda) = 1 + \beta_0 [\lambda + \min(\lambda, 0.87) - 1.87] \quad (2.5)$$

$$h(\lambda) = \max(0, h'(\min(\lambda, 1.2))) \quad (2.6)$$

where

$\beta_0$  phenomenological tension length-dependence scaling factor

This results in a linear length dependence near resting sarcomere length and a twice as steep decrease in tension when the sarcomere length falls below the thick filament length (at  $\lambda = 0.87$ ).

A phenomenological representation of the thin filament calcium sensitivity shift in a length-dependent manner is also included as an important mechanism of tension length-dependence. This is implemented by  $Ca_{T50}$  in equation (2.1), which is further taken to be:

$$Ca_{T50} := Ca_{50}[1 + \beta_1(\lambda - 1)] \quad (2.7)$$

where

$Ca_{50}$  reference  $Ca^{2+}$  thin filament sensitivity

$\beta_1$  phenomenological tension length-dependence scaling factor

$\lambda$  extension ratio along the fibre direction

At the resting sarcomere configuration ( $\lambda = 1$ ), length-dependence effects are not present, and no consequent shift in the calcium sensitivity is observed ( $Ca_{T50} = Ca_{50}$ ).

### 2.2.2 Velocity-dependence

To phenomenologically represent the tension development dependence on cross-bridge kinetics, the *fading memory model* was employed as previously done in [163], describing the velocity response as several strain-rate-dependent variables that decay with time. In particular, this model describes the relationship between tension and sarcomere sliding velocity by separating tension development into a non-linear static component and a linear time-dependent component, as described by the following two equations:

$$\frac{dQ_i}{dt} = A_i \frac{d\lambda}{dt} - \alpha_i Q_i, \quad i = 1, 2 \quad (2.8)$$

where

$A_i, i = 1, 2$  parameters related to the viscous and elastic moduli

$\alpha_i, i = 1, 2$  parameters related to the frequencies

The effect  $g(Q)$  seen in equation (2.3) on tension is given by an equation derived from the Hill force-velocity curve extended to model stretch and shortening in a symmetric way as done in [163]:

$$g(Q) = \begin{cases} \frac{\alpha Q + 1}{1 - Q} & Q \leq 0 \\ \frac{1 + (\alpha + 2)Q}{1 + Q} & Q > 0 \end{cases}, \quad \text{with } Q := \sum_{i=1}^2 Q_i \quad (2.9)$$

where

$\alpha$  slope of the Hill force-velocity relationship

Land et al. [119] cell contraction model's main mechanisms are summarised in the schematic provided in Figure 2.4.

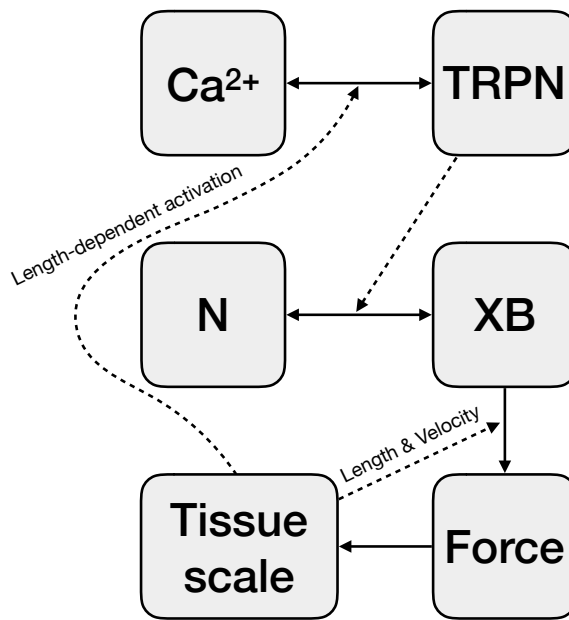


Figure 2.4: Land et al. [119] cell contraction model schematic.  $\text{Ca}^{2+}$  binds to TnC, and when the fraction of bound complexes (TRPN) reaches  $\text{TRPN}_{50}$ , half of the maximum number of cross-bridges has passed from the non-permissive state (N) to the actively cycling state (XB). Generated active force, which directly depends on the fraction of formed cross-bridges, causes tissue contraction, which backwards modulates the force generation itself in a length- and velocity-dependent manner.

### 2.2.3 Uncoupling the binding and unbinding rates

We wanted to uncouple the unbinding rate from the binding rate in the  $\text{Ca}^{2+}$ -TnC relationship. This was achieved by assigning a different

function to parameter  $k_{trpn}$  according to whether this was multiplying the first term or the second term in equation (2.1):

$$\frac{dTRPN}{dt} = k_{trpn} \left[ \left( \frac{[Ca^{2+}]_i}{Ca_{T50}} \right)^{n_{trpn}} (1 - TRPN) - TRPN \right] \quad (2.10)$$

$$= \underbrace{k_{trpn}}_{k_{on}} \left( \frac{[Ca^{2+}]_i}{Ca_{T50}} \right)^{n_{trpn}} (1 - TRPN) - \underbrace{k_{trpn}}_{k_{off}} TRPN \quad (2.11)$$

$$= k_{on} \left( \frac{[Ca^{2+}]_i}{Ca_{T50}} \right)^{n_{trpn}} (1 - TRPN) - k_{off} TRPN \quad (2.12)$$

Both the  $Ca^{2+}$ -independent part ( $k_{on}$ ) of the binding rate and the unbinding rate ( $k_{off}$ ) were set to the same model baseline  $k_{trpn}$  value, although now it is possible to treat them as two different parameters. This will serve the purpose of understanding the individual contribution of each of them in the active tension generation.

#### 2.2.4 The force-calcium relationship

The steady-state solutions of Equations (2.12)–(2.2) are:

$$TRPN_{ss} = \frac{\left( \frac{[Ca^{2+}]_i}{Ca_{T50}} \right)^{n_{trpn}}}{\frac{k_{off}}{k_{on}} + \left( \frac{[Ca^{2+}]_i}{Ca_{T50}} \right)^{n_{trpn}}} \quad (2.13)$$

$$XB_{ss} = \frac{(TRPN)^{n_{xb}}}{(TRPN_{50})^{n_{xb}} + (TRPN)^{n_{xb}}} \quad (2.14)$$

In the case of isometric force studies, the length- ( $h(\lambda)$ ) and velocity- ( $g(Q)$ ) dependence terms equal to 1, and the steady-state force is given by:

$$F = T_{ref} \cdot XB_{ss} \quad (2.15)$$

Equation (2.15) can be re-written in a more classical form as

$$\frac{F}{F_0} = \frac{x^{h(x)}}{1 + x^{h(x)}}, \quad \text{with } x := \frac{[Ca^{2+}]_i}{EC_{50}} \quad (2.16)$$

where

$F_0$  reference force ( $= T_{ref}$ )

$h(x)$  Hill coefficient

$EC_{50}$  half-maximal effective concentration

The Hill coefficient  $h(x)$  has the following form:

$$h(x) = n_{xb} [n_{trpn} - \log_x (1 - TRPN_{50}(1 - x^{n_{trpn}}))] \quad (2.17)$$

while the half-maximal effective concentration  $EC_{50}$  is given as a function of five model parameters:

$$EC_{50} = Ca_{T50} \left( \frac{k_{off}}{k_{on}} \frac{TRPN_{50}}{1 - TRPN_{50}} \right)^{1/n_{trpn}} \quad (2.18)$$

By construction, the Land et al. [119] model has a biphasic Hill coefficient. To simplify the analysis, we approximated the steady-state force by characterising  $F$  using a single Hill coefficient value  $h$  defined as the slope at half-maximal activation:

$$h := \lim_{x \rightarrow 1} h(x) = n_{xb} n_{trpn} (1 - TRPN_{50}) \quad (2.19)$$

As a result, the Hill coefficient does not depend on  $[Ca^{2+}]_i$  and is a function of three model parameters. Using logarithmically-spaced calcium values, equation (2.16) becomes

$$\frac{F}{F_0} = \frac{1}{1 + 10^{h(pCa_{50} - pCa)}} , \quad \text{with} \quad (2.20)$$

$$pCa := -\log [Ca^{2+}]_i \quad (2.21)$$

$$pCa_{50} := -\log EC_{50} \quad (2.22)$$

Equation (2.20) takes the name of *force-pCa (F-pCa) curve*.

### 2.3 ANATOMY MODEL

Rat biventricular anatomy was represented *in silico* by a *cubic Hermite* finite element mesh. This was generated using an automatic service for ventricular cardiac meshes personalisation developed by Lamata et al. [114, 115].

The mesh customisation pipeline starts from a binary image, which in general corresponds to a segmentation obtained from heart medical images (e.g. magnetic resonance images). An idealised template mesh composed of truncated ellipsoids is then tailored to the binary mask provided, and image registration is performed to assess the deformation field from template to real anatomy. During this step, the user can choose the so-called *level of detail (LoD)*, which gives a trade-off between fitting accuracy and numerical stability. The LoD ranges from 1 (coarse and most stable) to 5 (accurate but less likely to be stable). After having calculated the warping function by image registration, this is used to map the template mesh to the deformed space using a variational technique. The last step of the pipeline involves enhancing the quality of the mesh by improving the regularity of each element

by linearising internal nodes transmural positions with no loss of accuracy.

Rule-based fibres [18], along with the generated meshes, complemented the anatomical description of the rat heart. We used a transmural variation of  $-60^\circ$  to  $80^\circ$  from epicardium to endocardium.

## 2.4 TISSUE MODEL

We modelled passive material properties using the transversely isotropic cardiac strain energy function proposed by Guccione et al. [72]:

$$W = W_g(\mathbf{E}), \quad \text{with} \quad (2.23)$$

$$W_g(\mathbf{E}) := \frac{1}{2} C_1 (e^{Q(\mathbf{E})} - 1) \quad (2.24)$$

$$Q(\mathbf{E}) := b_f E_{ff}^2 + b_{ft}(2E_{fs}^2 + 2E_{fn}^2) + b_t(E_{ss}^2 + E_{nn}^2 + 2E_{sn}^2) \quad (2.25)$$

where

$\mathbf{E}$  Green strain tensor (introduced in Section 1.2.5)

$C_1$  scaling coefficient (representing an overall tissue stiffness)

$b_f, b_{ft}, b_t$  tissue mechanical response in the fibre,

fibre-transverse shear and transverse planes

We adopted this formulation since it is widely used in the cardiac modelling community [121] and most importantly because it is regulated by a few parameters, with one ( $C_1$ ) being particularly interesting for modelling purposes as it can be scaled to directly impact the whole tissue stiffness.

Cardiac tissue was further assumed to be fully incompressible. This was enforced by expanding the strain-energy function in equation (2.23) with a *Lagrange multiplier scheme*, in combination with an *incompressibility penalty* to improve stability of mechanics simulations [120]:

$$W = W_g(\mathbf{E}) - p(J - 1) + \frac{\kappa}{2}(J - 1)^2, \quad \text{with} \quad J := \det(\mathbf{F}) \quad (2.26)$$

$$\text{and with constraint: } J = 1 \quad (2.27)$$

where

$p$  hydrostatic pressure

$\kappa$  penalty parameter

$\mathbf{F}$  deformation gradient tensor (introduced in Section 1.2.5)

## 2.5 ELECTRICAL ACTIVATION

The calcium transient was assumed not to vary spatially, and it homogeneously activated contraction throughout the ventricular walls.

Previous heart models have shown that heterogeneous activation patterns have negligible impact in the small rat heart [119], and so activation was assumed instantaneous for simplicity and to improve computational tractability.

## 2.6 BOUNDARY CONDITIONS

We applied spatial boundary conditions to the mesh throughout the mechanics solution process. Specifically, we constrained all the ventricles basal plane mesh nodes along the apex-base axis and allowed no movement along any direction for one node on the interior LV wall. This constraint prevented free rotation and translation without limiting the deformation [119].

We also set haemodynamic boundary conditions to control blood flow and pressures at the computational domain boundaries, thereby coupling the biventricular heart with the rest of the body circulatory system. We used a *three-element windkessel model* [245] to regulate ejection, and we used the windkessel model generalised formulation (equation (1.27)) to regulate the other phases of the cardiac cycle, namely initial preload filling, isovolumetric contraction, isovolumetric relaxation and diastolic filling, as described in Section 1.2.6. The RV boundary condition pressures (atrial and pulmonary artery) were set to be 1/3 of the equivalent LV values and the RV windkessel parameters were scaled to be equal to  $R/3$ ,  $Z/3$ ,  $3C$  from the reference LV windkessel parameter set ( $R$ ,  $Z$ ,  $C$ ) as done in [120], based on typical pressure differences between the ventricles [215].

## 2.7 NUMERICAL SOLVERS

We solved the whole-ventricles mechanics problem using `elecmec` [118, 120], an in-house software package developed at King's College London. This uses the standard *Galerkin finite element method* to numerically solve the partial differential equations describing the solid mechanics problem. In particular, trilinear basis functions are used for the incompressibility constraint weak form, while tricubic Hermite basis functions are used for the weak form associated to the balance of stress to ensure continuity of the stresses and strains in the solution. In short, `elecmec` uses a Q3 – Q1 formulation with Lagrange multiplier and penalty term [121]. The weak form integrals are approximated using *Gaussian quadrature* at  $4 \times 4 \times 4$  points, and the resulting non-linear system is solved for displacements and pressures using the *Newton method* combined with a simple *line search method* which repeatedly halves the search step to prevent the residual from increasing too much. The ODE system associated to the cell contraction model is solved using a standard *fixed-point iterations* on a *Crank-Nicolson scheme*, with

an adaptive time stepping scheme which decreases the time step temporarily when slow convergence is detected. The default time step for the mechanics problem (when not adaptively changing) is 0.1 ms. Cubic Hermite finite-element meshes are used as the computational domain for elecmech. In this thesis, the two used biventricular meshes (Chapter 4) were derived from magnetic resonance images with dimension of  $128 \times 128 \times 9$  voxels and spacing of  $0.39 \times 0.39 \times 1.5 \text{ mm}^3$ . The meshes' resolution was 2, 12 and 6 elements in the radial, circumferential and longitudinal directions, respectively. The meshes had 108 elements and 174/177 nodes, and collapsed elements were used in the apex of the left ventricle.

## 2.8 SIMULATION PROTOCOL

The whole-organ complete cardiac cycle was simulated using the protocol described in [119, 130]. Briefly, dynamic changes in the LV and RV cavities' boundary conditions were cyclically applied. During diastole, a fixed atrial preload pressure and filling resistance was applied. At activation, the cavity boundary conditions were switched to an isovolumetric constraint in both chambers. When each chamber reached pre-set aortic and pulmonary artery pressures, a three-element windkessel model boundary condition was applied to each chamber to represent the aortic and pulmonary artery afterload. Once each chamber stopped ejecting, an isovolumetric boundary condition was applied to represent isovolumetric relaxation. Once the cavity pressure fell below its respective atrial pressure, the heart returned to the diastolic cavity boundary conditions to complete the PV loop.

## 2.9 SUMMARY

We modelled the rat heart using a 3D biventricular contraction mechanics model. Cellular electrophysiology was simulated using the Gattoni et al. [68] model of rat LV myocytes at  $37^\circ\text{C}$  and 6 Hz pacing frequency. Active tension generation was described using the Land et al. [119] model of sarcomere contraction. LV and RV anatomy was represented by a cubic Hermite finite element mesh [114]. Rule-based fibres [18] were included with a transmural variation of  $-60^\circ$  to  $80^\circ$  from epicardium to endocardium. Passive material properties were modelled using the Guccione transversely isotropic cardiac strain energy function [72], combined with a Lagrange multiplier scheme and a penalty term [120]. The  $\text{Ca}^{2+}$  transient was assumed not to vary spatially, and it homogeneously activated contraction throughout the ventricular walls. Spatial boundary conditions were applied by constraining the movement of specific mesh nodes, and haemodynamic boundary conditions were described by a generalised three-element windkessel

model [244]. The resulting multi-scale model of coupled electromechanics was simulated using elecmech software package [118].

## MODEL EMULATION, FITTING AND UNCERTAINTY QUANTIFICATION

### OUTLINE

In this chapter, we describe the methods we used for model emulation, fitting and uncertainty quantification. First, the full multi-scale 3D biventricular rat heart contraction model is represented as a nonlinear mapping between selected input parameters and scalar output features of interest (Section 3.3). Second, the nonlinear mapping is emulated using probabilistic surrogates based on Gaussian process emulation (Section 3.4). Finally, two applications of emulators are presented: the Bayesian history matching technique for model fitting (Section 3.5) and the emulation-based Sobol' global sensitivity analysis for model uncertainty quantification (Section 3.6). We conclude with a brief summary (Section 3.7).

We want to create a quantitative link of the cell, tissue and haemodynamic properties to whole heart function. To do this, we first need to define quantities of interest that will vary to reflect model properties and quantities of interest that will consequently vary to reflect model behaviour. The quantitative mapping that will result from this work is summarised in Figure 3.1, and it is progressively constructed in Sections 3.1–3.2–3.3.

### 3.1 MODEL INPUT PARAMETERS

The presented multi-scale rat heart contraction model (Chapter 2) is regulated by 71, 17, 18 parameters for the ionic, cell contraction, tissue + boundary components, respectively. We selected specific parameters as representative regulators of each of these three sub-models for a total of 8 parameters. Specifically, 2 parameters ( $Ca_{50}$ ,  $k_{off}$ ) described the thin filament kinetics, 2 parameters ( $k_{xb}$ ,  $T_{ref}$ ) described the thick filament kinetics, and 4 parameters ( $p$ ,  $p_{ao}$ ,  $Z$ ,  $C_1$ ) described boundary conditions and tissue properties. The 8 parameters considered are described in Table 3.1. A fixed calcium transient simulated using the adopted ionic model was used as the sarcomere activation signal for the whole heart.

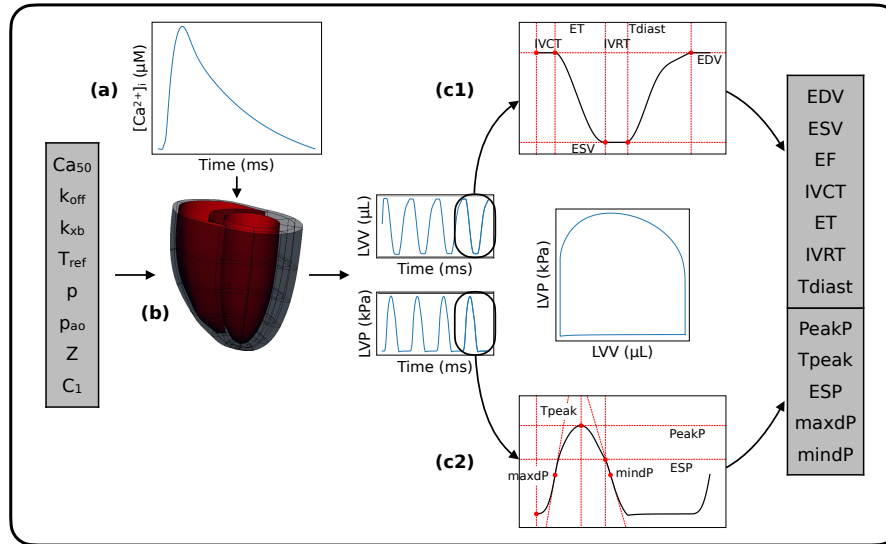


Figure 3.1: Multi-scale 3D biventricular rat heart contraction model. Given a fixed calcium transient (a) and mesh with fibres (b), parameters representing cell, tissue and haemodynamics properties (left grey column, described in Table 3.1) constitute the input for the model. LV volume and pressure transients and PV loop are obtained after a four-beats model run. The LV features (right grey column, described in Table 3.2), extracted from the 4th-beat curves (c1-c2), constitute the output for the model.

PARAMETER	UNITS	DEFINITION
$\text{Ca}_{50}$	$\mu\text{M}$	reference $\text{Ca}^{2+}$ thin filament sensitivity
$k_{\text{off}}$	$\text{ms}^{-1}$	unbinding rate of $\text{Ca}^{2+}$ from TnC
$k_{\text{xb}}$	$\text{ms}^{-1}$	cross-bridges cycling rate
$T_{\text{ref}}$	$\text{kPa}$	maximal reference tension
$p$	$\text{kPa}$	end-diastolic pressure
$p_{\text{ao}}$	$\text{kPa}$	aortic systolic pressure
$Z$	$\text{mmHg s mL}^{-1}$	aortic characteristic impedance
$C_1$	$\text{kPa}$	tissue stiffness

Table 3.1: Model parameters and their definitions.

### 3.2 MODEL OUTPUT FEATURES

We are interested in characterising the LV contractile function in the rat model. A typical full rat heart contraction mechanics model output consists in LV volume (**lVV**) and LV pressure (**LVP**) transients (i.e. the blood volume and pressure variations within the LV chamber during time), along with the corresponding *pressure-volume* (**PV**) loop. Multiple-beats simulations are commonly run to reach a more numeri-

cally stable *limit cycle*, and only the last-beat curves are analysed. In Figure 3.2, an example 4-beat simulation is shown with the limit cycle curves highlighted.

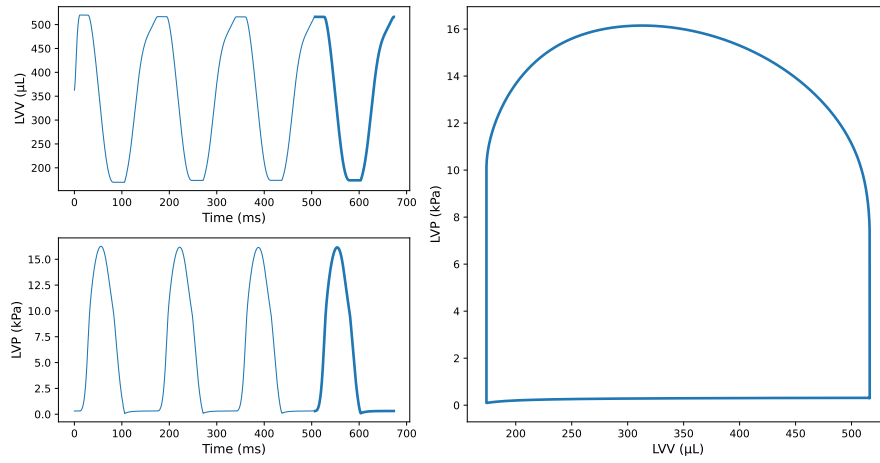


Figure 3.2: Rat heart contraction mechanics model 4-beat simulation output. LVV and LVP transients (left panel) are drawn with a thin blue line, and their last-beat parts, along with the corresponding PV loop (right panel), are drawn with a thick blue line.

To quantitatively describe the LV behaviour, we extracted from the last-beat curves 12 scalar features of clinical interest and commonly used to characterise the LV systolic and diastolic functions:

$$\text{EDV} = \max_{t>0} v_{\text{LV}}(t) \quad (3.1)$$

$$\text{ESV} = \min_{t>0} v_{\text{LV}}(t) \quad (3.2)$$

$$\text{EF} = 100 \times \frac{\text{EDV} - \text{ESV}}{\text{EDV}} \quad (3.3)$$

$$\text{IVCT} = t_1 - t_0 \quad (3.4)$$

$$\text{ET} = t_2 - t_1 \quad (3.5)$$

$$\text{IVRT} = t_3 - t_2 \quad (3.6)$$

$$\text{Tdiast} = t_4 - t_2 \quad (3.7)$$

$$\text{PeakP} = \max_{t>0} p_{\text{LV}}(t) = p_{\text{LV}}(t_5) \quad (3.8)$$

$$\text{Tpeak} = \arg \max_{t>0} p_{\text{LV}}(t) = t_5 \quad (3.9)$$

$$\text{ESP} = p_{\text{LV}}(t_2) \quad (3.10)$$

$$\text{maxdP} = \max_{t>0} \frac{dp_{\text{LV}}(t)}{dt} \quad (3.11)$$

$$\text{mindP} = \min_{t>t_2} \frac{dp_{\text{LV}}(t)}{dt} \quad (3.12)$$

where

$t_i$ , for $i = 0, \dots, 5$	positive time points (explained in Figure 3.3)
$v_{LV}(t)$	LV volume transient
$p_{LV}(t)$	LV pressure transient

The process of LV output features extraction is illustrated in Figure 3.3, while features' definitions are provided in Table 3.2.

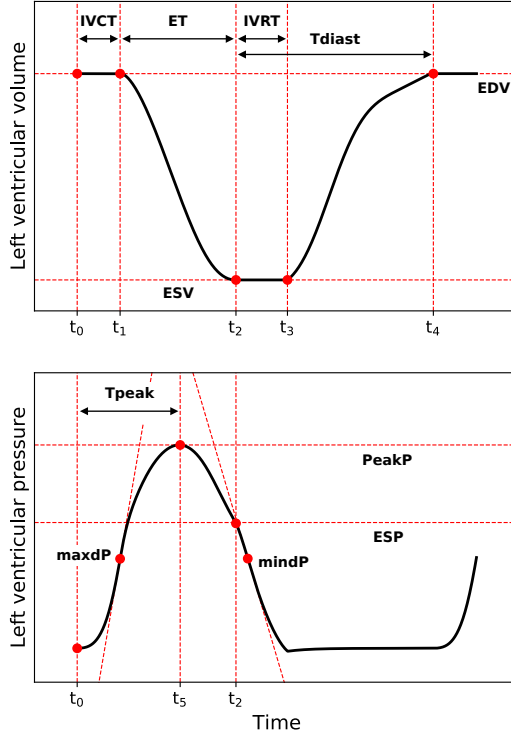


Figure 3.3: The 12 LV features of interest are extracted from the LV volume and pressure curves (EF feature not showed as it is a derived quantity).

### 3.3 MULTI-SCALE MAP

For a given fixed  $\text{Ca}^{2+}$  transient, cubic-Hermite finite element heart mesh and fibre orientation, we can use the cardiac mathematical model described above, solved using the nonlinear finite element method, to map every set of 8 input parameters  $\mathbf{x}$  used to initialise the model to a set of 12 scalar output LV features ( $y_1, \dots, y_{12}$ ):

$$f_{\text{simul}}: \mathbb{R}^8 \rightarrow \underbrace{\mathbb{R} \times \dots \times \mathbb{R}}_{12 \text{ times}} \quad (3.13)$$

$$\mathbf{x} \mapsto (y_1, \dots, y_{12})$$

Equation (8.7) effectively constitutes a quantitative link between cellular, tissue and haemodynamic properties to whole-organ function. The multi-scale mapping  $f_{\text{simul}}$  takes the name of *simulator*.

LV FEATURE	UNITS	DEFINITION
EDV	$\mu\text{L}$	end-diastolic volume
ESV	$\mu\text{L}$	end-systolic volume
EF	%	ejection fraction
IVCT	ms	isovolumetric contraction time
ET	ms	systolic ejection time
IVRT	ms	isovolumetric relaxation time
Tdiast	ms	diastolic filling time
PeakP	kPa	peak systolic pressure
Tpeak	ms	time to peak systolic pressure
ESP	kPa	end-systolic pressure
maxdP	$\text{kPa ms}^{-1}$	maximum pressure rise rate
mindP	$\text{kPa ms}^{-1}$	maximum pressure decay rate

Table 3.2: Indexes of LV systolic and diastolic functions.

One simulator evaluation at a new input parameter set requires the full-forward model of rat heart contraction mechanics to be run. However, this is computationally expensive ( $\sim 4\text{-}10$  CPU hours per evaluation). We overcome the computational burden of running such a complex model by replacing it with a probabilistic surrogate based on *Gaussian process emulation*, as we shall see in the next section. We will adopt the mathematical formalism of the standard textbook of Gaussian processes for machine learning by Rasmussen and Williams [187].

### 3.4 GAUSSIAN PROCESS EMULATION

Let's consider  $N$  realisations  $y^{(i)}$ ,  $i = 1, \dots, N$  of a computer code  $f$  ( $= f_{\text{simul}}$ ) for  $N$  different input parameter points  $x^{(i)}$ ,  $i = 1, \dots, N$  each one with dimension  $D$ :  $x^{(i)} = (x_1^{(i)}, \dots, x_D^{(i)})^T$ . More concisely, this can be written as  $f(X)$  (or  $f$ ) where  $X = (x^{(1)}, \dots, x^{(N)})$  is the input matrix. The pair  $(X, f(X))$  is called the *learning sample*. A *Gaussian process emulator* (GPE) treats the deterministic response  $f(x)$  as a realisation of a random function  $f(x, \omega)$  which can be written as the sum of a regression model and a stochastic process [175]:

$$f(x, \omega) = h(x) + Z(x, \omega), \quad (x, \omega) \in \mathbb{R}^D \times \Omega \quad (3.14)$$

where  $\Omega$  is a probability sample space, commonly the Lebesgue-measurable set of real numbers.

The regression part  $h(x)$  provides a mean approximation to the computer code. We will only consider the parametric case where  $h$  is

given as a linear combination of elementary basis functions, namely  $(D + 1)$  one-degree polynomials:

$$h(x) := \sum_{i=0}^D \beta_i h_i(x) = h(x)^T \beta \quad (3.15)$$

where  $\beta = (\beta_0, \dots, \beta_d)^T$  is the regression parameter vector and  $h(x) = (h_0(x), \dots, h_d(x))$  is the basis function vector with

$$h_i(x) := \begin{cases} 1 & \text{if } i = 0 \\ x_i & \text{if } i = 1, \dots, D \end{cases} \quad (3.16)$$

The stochastic part  $Z(x, \omega)$  is a centred (zero-mean) Gaussian process (GP), completely and uniquely determined by its covariance function (or *kernel*)  $k$ :

$$Z(x, \omega) := \mathcal{GP}(\mathbf{o}, k(x, x')) \quad (3.17)$$

The covariance function specifies the covariance between pairs of random variables:

$$k: \mathbb{R}^D \times \mathbb{R}^D \rightarrow \mathbb{R}, \quad \text{with} \quad (3.18)$$

$$(x, x') \mapsto k(x, x') = \text{Cov}(Z(x, \omega), Z(x', \omega)) \quad (3.19)$$

We can notice that the covariance between the outputs is written as a function of the inputs. We will only consider the case of a *stationary* stochastic process, where the covariance is a function of the difference  $x - x'$  and is thus invariant to translations in the input space. We will adopt the infinitely differentiable, stationary *squared exponential* (SE) kernel defined as:

$$k_{\text{SE}}(d(x, x')) := \sigma_f^2 e^{-\frac{1}{2} d(x, x')} \quad (3.20)$$

$$d(x, x') := (x - x')^T \Lambda (x - x')$$

where  $\sigma_f^2 \in \mathbb{R}_+$  is the noise-free signal variance and  $\Lambda = \text{diag}(\ell_1^2, \dots, \ell_D^2)$ ,  $\ell_i \in \mathbb{R}_+$  for  $i = 1, \dots, D$  are the *characteristic length-scales* of the process. This formulation of the covariance function implements an *automatic relevance determination*, since the inverse of each length-scale determines how relevant the corresponding input component is: if the length-scale has a very large value, the covariance will become almost independent of that component, effectively removing it from the inference.

Choosing the GP covariance structure which best captures the nature of the underlying data is important because, by the principle of *similarity*, it is assumed that the target value  $f(x)$  of a point  $x$  can be informative on the prediction for a test point close to it. In the context of Gaussian processes, the selection of the covariance function

can formally be achieved through the process of *model selection*. The smoothness of the squared exponential kernel we have adopted could represent a very strong assumption as some argue it is unrealistic for modelling many physical processes. However, a preliminary model selection through *k-fold cross-validation* was run on data generated by our cardiac mechanics forward model, and estimated a similar to SE kernel generalisation error for other different, rougher kernels such as Matérn<sub>v=3/2</sub> (once differentiable) and Matérn<sub>v=5/2</sub> (twice differentiable).

Under the assumption of a GP model, the learning sample follows a multivariate normal distribution:

$$\mathbf{f} | \mathbf{X} \sim \mathcal{N}(\mathbf{H}_X \boldsymbol{\beta}, \Sigma_{XX}) \quad (3.22)$$

where  $\mathbf{H}_X := (\mathbf{h}(\mathbf{x}^{(1)})^\top, \dots, \mathbf{h}(\mathbf{x}^{(N)})^\top)$  is the regression matrix and  $\Sigma_{XX}$  is the *Gram covariance matrix* obtained by evaluating the covariance function at all the pairs of input points in  $\mathbf{X}$ :

$$\mathbf{X} \xrightarrow{k_{SE}(\cdot, \cdot)} \Sigma_{XX}, \quad (\Sigma_{XX})_{ij} = k_{SE}(\mathbf{x}_i, \mathbf{x}_j) \quad \text{for } i, j = 1, \dots, N \quad (3.23)$$

Let's suppose we have a new set of points  $\mathbf{X}_* = (\mathbf{x}_*^{(1)}, \dots, \mathbf{x}_*^{(M)})$ . We do not know  $\mathbf{f}(\mathbf{X}_*)$  (or  $\mathbf{f}_*$ ) values because we have not observed them yet. However, we can put a *prior distribution* on  $\mathbf{f}_*$  of the same type as the learning sample's one:

$$\mathbf{f}_* | \mathbf{X}_* \sim \mathcal{N}(\mathbf{H}_{X_*} \boldsymbol{\beta}, \Sigma_{X_* X_*}) \quad (3.24)$$

Their joint probability distribution will be:

$$\begin{bmatrix} \mathbf{f} \\ \mathbf{f}_* \end{bmatrix} | \mathbf{X}, \mathbf{X}_* \sim \mathcal{N}\left([\mathbf{H}_X \boldsymbol{\beta}, \mathbf{H}_{X_*} \boldsymbol{\beta}], \begin{bmatrix} \Sigma_{XX} & \Sigma_{XX_*} \\ \Sigma_{X_* X} & \Sigma_{X_* X_*} \end{bmatrix}\right) \quad (3.25)$$

To incorporate the knowledge that the observations provide about the function  $\mathbf{f}$ , we condition this distribution on the learning sample. Because multivariate Gaussian distributions are closed under conditioning, the conditional distribution (also called *posterior distribution*) we get is again normally distributed:

$$\mathbf{f}_* | \mathbf{X}_*, \mathbf{X}, \mathbf{f} \sim \mathcal{N}(\boldsymbol{\mu}, \Sigma) \quad (3.26)$$

where

$$\boldsymbol{\mu} := \mathbf{H}_{X_*} \boldsymbol{\beta} + \Sigma_{X_* X} \Sigma_{XX}^{-1} (\mathbf{f} - \mathbf{H}_X \boldsymbol{\beta}) \quad (3.27)$$

$$\Sigma := \Sigma_{X_* X_*} - \Sigma_{X_* X} \Sigma_{XX}^{-1} \Sigma_{X X_*} \quad (3.28)$$

We will additionally model the learning sample observations to be affected by noise:

$$\mathbf{y}^{(i)} := \mathbf{f}(\mathbf{x}^{(i)}) + \varepsilon, \quad \varepsilon \sim \mathcal{N}(0, \sigma_n^2) \quad (3.29)$$

where  $\sigma_n^2 \in \mathbb{R}^+$  is the noise variance, and the noise is assumed to be additive, independent and identically distributed. The use of a noise term (or *nugget*) might seem counter-intuitive as the learning sample is the result of a deterministic model run (i.e., for the same input you always get the same output). However, it has been previously shown [8] that it is beneficial to include it even when emulating deterministic models. From a technical point of view, having a noisy representation of the learning sample results in adding a diagonal matrix to the latent function  $\mathbf{f}$  covariance matrix:

$$k_{SE}(\mathbf{x}, \mathbf{x}') = k_{SE}(\mathbf{x}, \mathbf{x}') + \sigma_n^2 \delta_{\mathbf{x}, \mathbf{x}'} \Rightarrow \text{Cov}(\mathbf{y}) = \Sigma_{XX} + \sigma_n^2 I \quad (3.30)$$

where  $\delta_{\mathbf{x}, \mathbf{x}'}$  is the *Kronecker delta* (equals 1 when  $\mathbf{x} = \mathbf{x}'$  and 0 when otherwise). This in turn ensures that the GP covariance matrix is always invertible, even in the case when the latent function covariance matrix ( $\Sigma_{XX}$ ) is ill-conditioned. Apart from the numerical stabilisation purpose, the use of the nugget can account for discrepancies between the GP emulator and the simulator and, since it modifies the shape of the GP model likelihood, it corresponds to modelling the variability which is not explained by the simulator inputs.

The joint probability distribution associated to the noisy formulation becomes:

$$\begin{bmatrix} \mathbf{y} \\ \mathbf{f}_* \end{bmatrix} | X, X_* \sim \mathcal{N}\left([\mathbf{H}_X \boldsymbol{\beta}, \mathbf{H}_{X_*} \boldsymbol{\beta}], \begin{bmatrix} \Sigma_{XX} + \sigma_n^2 I & \Sigma_{XX_*} \\ \Sigma_{X_* X} & \Sigma_{X_* X_*} \end{bmatrix}\right) \quad (3.31)$$

and the GPE posterior distribution is therefore:

$$\mathbf{f}_* | X_*, X, \mathbf{y} \sim \mathcal{N}(\boldsymbol{\mu}, \boldsymbol{\Sigma}) \quad (3.32)$$

where

$$\boldsymbol{\mu} := \mathbf{H}_{X_*} \boldsymbol{\beta} + \Sigma_{X_* X} (\Sigma_{XX} + \sigma_n^2)^{-1} (\mathbf{y} - \mathbf{H}_X \boldsymbol{\beta}) \quad (3.33)$$

$$\boldsymbol{\Sigma} := \Sigma_{X_* X_*} - \Sigma_{X_* X} (\Sigma_{XX} + \sigma_n^2)^{-1} \Sigma_{X_* X} \quad (3.34)$$

It is worth noticing that the most computational expensive operation that needs to be performed when assembling the posterior distribution (both the noise-free (3.26) and the noisy (3.32) ones) is the inversion of a symmetric, positive definite  $N \times N$  matrix (the kernel-induced covariance matrices  $\Sigma_{XX}$  and  $\Sigma_{XX} + \sigma_n^2$ , respectively). This operation is commonly performed by using a *Cholesky factorisation* of the matrix to be inverted, with a total cost  $\mathcal{O}(N^3)$ , and by solving the resulting triangular system given by the obtained Cholesky factor, with a total cost  $\mathcal{O}(N^2)$  [187]. From an algorithmic viewpoint, if the learning sample does not change (matrix  $X$  used to assemble the covariance matrix  $\Sigma_{XX}$ ), its Cholesky factor can be stored so that making inference on many different new sets of test points  $X_*$  will every time only cost  $\mathcal{O}(N^2)$ . This feature of Gaussian process emulators being fast to be

evaluated will prove crucial for the applications we shall present in the next two sections.

So far we have introduced many free-parameters which belong to the non-parametric part of the model. They can be summarised in the so-called vector of *hyperparameters*:

$$\boldsymbol{\theta} := (\{\Lambda\}, \sigma_f^2, \sigma_n^2) \quad (3.35)$$

where  $\{\Lambda\}$  denotes the elements of matrix  $\Lambda$  (all the length-scales). In order to make the GPE a practical tool in an application, we need to specify values for the otherwise unspecified hyperparameters: this is done through a process of *fitting* also known as *training*.

We will use a Bayesian approach to model training, where inference is performed by applying rules of probability theory. A Gaussian process model is non-parametric; however, the latent function  $\mathbf{f}$  values at the training points can be considered as model parameters: the more training points, the more parameters. We start from the Bayes' rule to model the posterior distribution of model parameters  $\mathbf{f}$ :

$$p(\mathbf{f} | \mathbf{y}, \mathbf{X}, \boldsymbol{\theta}) = \frac{p(\mathbf{y} | \mathbf{X}, \mathbf{f}) p(\mathbf{f} | \mathbf{X}, \boldsymbol{\theta})}{p(\mathbf{y} | \mathbf{X}, \boldsymbol{\theta})} \quad (3.36)$$

where  $p(\mathbf{y} | \mathbf{X}, \mathbf{f})$  is the *likelihood* and  $p(\mathbf{f} | \mathbf{X}, \boldsymbol{\theta})$  is the parameters *prior*. The term at the denominator is a normalisation constant and is called *marginal likelihood*. It does not depend on parameters  $\mathbf{f}$  and is defined as:

$$p(\mathbf{y} | \mathbf{X}, \boldsymbol{\theta}) := \int p(\mathbf{y} | \mathbf{X}, \mathbf{f}) p(\mathbf{f} | \mathbf{X}, \boldsymbol{\theta}) d\mathbf{f} \quad (3.37)$$

Under the assumption of Gaussian noise this integral can be solved analytically. By recalling that

$$\mathbf{y} | \mathbf{X}, \mathbf{f} \sim \mathcal{N}(\mathbf{f}, \sigma_n^2 \mathbf{I}) \quad (3.38)$$

$$\mathbf{f} | \mathbf{X}, \boldsymbol{\theta} \sim \mathcal{N}(\mathbf{H}_X \boldsymbol{\beta}, \Sigma_{XX}) \quad (3.39)$$

we obtain:

$$\mathbf{y} | \mathbf{X}, \boldsymbol{\theta} \sim \mathcal{N}(\mathbf{H}_X \boldsymbol{\beta}, \Sigma_{XX} + \sigma_n^2 \mathbf{I}) \quad (3.40)$$

We can notice that the convolution of two Gaussian distributions is still Gaussian. It is common to take the logarithm of the obtained distribution: this is the *log marginal likelihood*

$$\begin{aligned} \log p(\mathbf{y} | \mathbf{X}, \boldsymbol{\theta}) &= -\frac{1}{2}(\mathbf{y} - \mathbf{H}_X \boldsymbol{\beta})^\top (\Sigma_{XX} + \sigma_n^2 \mathbf{I})^{-1} (\mathbf{y} - \mathbf{H}_X \boldsymbol{\beta}) + \\ &\quad -\frac{1}{2} \log |\Sigma_{XX} + \sigma_n^2 \mathbf{I}| - \frac{N}{2} \log 2\pi \end{aligned} \quad (3.41)$$

This equation has three terms which can be interpreted as follows. The first term is large when the data fit the model well; the second

term is a complexity penalty and is large when the model is simple; the last term is a normalisation constant.

At this point, a fully Bayesian approach would involve assigning a prior distribution to the hyperparameters and deriving a posterior distribution in the same manner as done in equation (3.36), using the marginal likelihood of equation (3.37) as likelihood. However, as the resulting integrals cannot be solved analytically and require numerical strategies to be estimated, to maintain computational tractability we opt for a simpler approach where a single value is estimated for each hyperparameter and considered as the true value. A drawback to this technique is a possible underestimation of the simulator variability, but this is outweighed by savings in the computational effort. This approach takes the name of *maximum likelihood-II* type of inference, and consists in maximising the log marginal likelihood with respect to the model hyperparameters:

$$\hat{\theta} := \arg \max_{\theta \in \mathbb{R}} \log p(\mathbf{y} | \mathbf{X}, \theta) \quad (3.42)$$

Gradient descent optimisation algorithms are commonly used [194] to minimise an objective function (or *loss function*), which in this case is simply the log marginal likelihood with inverted sign:

$$J(\theta) := -\log p(\mathbf{y} | \mathbf{X}, \theta) \quad (3.43)$$

This is done iteratively by updating at every step (or *epoch*) the parameters in the opposite direction of the gradient of the objective function with respect to the parameters ( $\nabla_{\theta} J(\theta)$ ).

### 3.4.1 Regression accuracy

The accuracy of each *univariate* GPE for regression tasks is evaluated using a k-fold cross-validation process. At each split, a GPE is trained on the current  $(k-1)/k$  fraction of the entire dataset, and it is then evaluated in all the points  $\mathbf{x}_i$ ,  $i = 1, \dots, M$  of the held-out  $1/k$  fraction of the dataset, with dimensions  $M \times D$ . The obtained point-wise predictions  $y_i^{\text{mean}}$   $i = 1, \dots, M$  (corresponding to the posterior distribution mean values) are then compared with the true function output values  $y_i^{\text{true}}$   $i = 1, \dots, M$ . We use the *coefficient of determination* (or  $R^2$ -score) to measure how well the regression predictions approximate the real data points. This is defined as:

$$R^2 := 1 - \frac{\sum_{i=1}^M (y_i^{\text{true}} - y_i^{\text{mean}})^2}{\sum_{i=1}^M (y_i^{\text{true}} - \bar{y})^2}, \quad \text{with} \quad (3.44)$$

$$\bar{y} := \frac{1}{M} \sum_{i=1}^M y_i^{\text{true}} \quad (3.45)$$

We additionally use the GPE predicted posterior variance values  $y_i^{\text{var}}$ ,  $i = 1, \dots, M$  to calculate the percentage of points which have an

*independent standard error* (ISE) smaller than 2. This quantity, which we call  $\text{ISE}_2$ , is a diagnostic used to assess the emulator's adequacy as a surrogate of the true deterministic function [17], as it measures how well the emulator uncertainty is accounting for the mean predictions' departure from the observed data and is defined as:

$$\text{ISE}_2 := \frac{100}{M} \cdot \sum_{i=1}^M \left( \frac{|y_i^{\text{true}} - y_i^{\text{mean}}|}{\sqrt{y_i^{\text{var}}}} < 2 \right) \quad (3.46)$$

The Boolean result inside the parentheses is encoded with either 0 (false) or 1 (true). The GPE accuracy can be finally described by the  $R^2$ -score and  $\text{ISE}_2$  obtained by averaging the same metrics calculated when testing the emulator on the respective left-out parts of each dataset splitting during cross-validation.

For each scalar feature of interest  $y_j$  we will train one univariate GPE  $f_{\text{emul},j}$  as a surrogate of the simulator restricted map:

$$\begin{aligned} f_{\text{simul},j} : \mathbb{R}^D &\rightarrow \mathbb{R} \\ x &\mapsto y_j \end{aligned} \quad (3.47)$$

Having available trained  $f_{\text{emul},j}$  emulators is powerful as they enable performing model exploration, fitting and uncertainty quantification. These tasks, in fact, normally require a large number of model evaluations, which is prohibitive when the simulator is computationally intensive to be solved.

### 3.5 HISTORY MATCHING

A first application of emulators is in the *history matching* (HM) technique. In the case where real system observations are available, HM can be used to learn about the input space characterising the simulator  $f_{\text{simul}}$ , which is being used to describe the real system.

Let  $y$  be a scalar, *real system value*. First, we can assume that the *observation*  $z$  that we make of the real system value is affected by a *measurement error*  $e$ :

$$z = y + e \quad (3.48)$$

We also assume that the measurement error is uncorrelated with  $y$ . As the simulator is only an *in silico* representation of the real system, for each given input  $x$  such that the corresponding simulator output  $f_{\text{simul}}(x)$  is at its closest to the real system value, a *model discrepancy* will still exist between the simulator output and the real system value:

$$y = f_{\text{simul}}(x) + d \quad (3.49)$$

so that:

$$z = f_{\text{simul}}(\mathbf{x}) + d + e \quad (3.50)$$

The model discrepancy term  $d$  was formally introduced in [102] as an additional source of uncertainty in simulator predictions (referred to as *model inadequacy*) and the correct characterisation of it often requires experts' knowledge. Here we assume that  $d$  is independent of  $\mathbf{x}$  and uncorrelated with  $f$ .

HM is an iterative process that allows to thoroughly explore the input space by discarding regions of input points that are unlikely to yield a simulator output match with real system observations. In order to do that, it makes use of emulators  $f_{\text{emul}}$  to approximate the simulator output at many input points where the simulator would be too computationally expensive to be run. HM relies on the so-called *implausibility measure*, which is calculated for each test point  $\mathbf{x}$  in the input space:

$$I(\mathbf{x}) := \frac{|\mathbb{E}[f_{\text{emul}}(\mathbf{x})] - z|}{\sqrt{\mathbb{V}[\mathbb{E}[f_{\text{emul}}(\mathbf{x})] - z]}} = \frac{|\mathbb{E}[f_{\text{emul}}(\mathbf{x})] - z|}{\sqrt{\mathbb{V}[f_{\text{emul}}(\mathbf{x})] + \mathbb{V}[d] + \mathbb{V}[e]}} \quad (3.51)$$

The implausibility measure is then compared against a pre-defined cutoff value  $I_{\text{cutoff}}$  to assess whether the corresponding input point will be likely to produce an acceptable match to the real system observation. A common choice (e.g. [9, 50, 235]) is to take a cutoff value of 3, by following the Pukelsheim's 3-sigma rule [185]. By assuming the distribution ( $\mathbb{E}[f_{\text{emul}}(\mathbf{x})] - z$ ) to be unimodal, the rule states that the probability of  $I(\mathbf{x}) > 3$  is at most  $\sim 5\%$ . In HM context, large implausibility measures (i.e. values above the chosen cutoff) will deem the associated points *implausible*, while points with an implausibility measure below the cutoff value will be deemed *non-implausible*.

As one might have available observations  $z_j$  for more than one feature of interest  $y_j$ , the implausibility measure can be naturally extended to take into account individual implausibility measures  $I_j(\mathbf{x})$ , each one obtained using the corresponding univariate emulator  $f_{\text{emul},j}$  of feature  $y_j$ . A simple way to do this is to take the maximum across all the implausibility measures:

$$I_M(\mathbf{x}) := \max_{j \in \{1, \dots, \# \text{features}\}} I_j(\mathbf{x}) \quad (3.52)$$

It follows that the parameter space will be constrained according to the worst (in terms of high implausibility value) observation match predicted by one of the emulators. As a wrong prediction from one emulator can lead to rejecting points that would have otherwise been kept according to their other individual implausibility measures, the joint implausibility measure  $I_M$  can be modified to take the second to last or the third to last highest implausibility measure value to be compared against the cutoff value.

### 3.5.1 Refocusing

After having evaluated the first initial set of test points (sampled in the high-dimensional input parameter space) with consequent space reduction according to the implausibility criterion, we do not have to stop immediately. Instead, we can continue performing the same operation iteratively where now the initial space where we sample test points is the obtained non-implausible space from the first or previous iteration (or *wave*). In the context of HM, this operation is called *refocusing*.

At each HM wave, we will perform the following operations.

**STEP 1.** If this is the first wave, sample many points from the input parameter space  $X$ ; if this is not the first wave, sample many points from the current non-implausible space  $X_{NIMP}$ . Points are commonly sampled using a space-filling design and constitute the so-called *not-ruled-out-yet* (NROY) space:

$$NROY \subset \begin{cases} X & \text{if } \text{wave} = 1 \\ X_{NIMP} & \text{if } \text{wave} > 1 \end{cases}$$

**STEP 2.** Calculate the implausibility measure for each point in the NROY space and test it against the chosen cutoff value  $I_{cutoff}$  to rule-out the NROY space into implausible  $X_{IMP}$  and non-implausible  $X_{NIMP}$  spaces:

$$\begin{aligned} X_{IMP} &:= \{x \in NROY \mid I_M(x) > I_{cutoff}\} \\ X_{NIMP} &:= \{x \in NROY \mid I_M(x) \leq I_{cutoff}\} \end{aligned}$$

**STEP 3.** Determine the non-implausible part  $T_{NIMP}$  of the training dataset  $T$  and augment it with newly simulated points  $T^+$  from the current  $X_{NIMP}$  space:

$$\begin{aligned} T_{NIMP} &:= \{(x, f_{\text{simul}}(x)) \in T \mid I_M(x) \leq I_{cutoff}\} \\ T^+ &:= \{(x, f_{\text{simul}}(x)), x \in X_{NIMP}\} \\ T &= T_{NIMP} \cup T^+ \end{aligned}$$

**STEP 4.** Cut the  $X_{IMP}$  space out of the investigated parameter space and retain only the  $X_{NIMP}$  space.

**STEP 5.** Unless a stopping criterion has been reached, refocus on the  $X_{NIMP}$  space, i.e. repeat from STEP 1 using emulators trained on the new training dataset  $T$ , being these now more accurate in the non-implausible parameter region.

In STEP 1, we have seen that NROY points are sampled such that they uniformly cover the high-dimensional input parameter space. This is a relatively trivial task for the first wave's space where, for example, a Latin hypercube design (LHD) [88] can be used. In fact, the initial space is normally given as a D-dimensional hypercube, i.e. given as the Cartesian product of D 1-dimensional intervals. However, the situation is more complicated starting from wave 2, as this time NROY points are to be sampled such that they uniformly cover the  $X_{NIMP}$  space, which in general has a not well defined topological structure. Let's suppose that the number of NROY points we want to sample over the current  $X_{NIMP}$  space is  $m$ , and that the number of  $X_{NIMP}$  points defining the  $X_{NIMP}$  space is  $n$ . Then, for wave 2 and successive waves we will perform the following operations.

(I) If  $m > n$ :

1. Build a multivariate normal distribution centred in all  $X_{NIMP}$  points and scaled by the current *min-max* range of the known  $X_{NIMP}$  space. The spread of this distribution can be further scaled by a factor (e.g. 10% of the initial standard deviation) in order to sample closer to the mean values ( $X_{NIMP}$  points).
2. Sample points from the built multivariate normal distribution, test them against the implausibility condition using the emulators of the current wave, and retain only the points that are deemed non-implausible.
3. Append the newly generated non-implausible points to the current  $X_{NIMP}$  set and re-calculate  $n = |X_{NIMP}|$ .
4. Repeat block (I) until  $m < n$ .

(II) Select  $m$  well-spread points from the set of  $n$  candidate  $X_{NIMP}$  points to be the best representatives of the  $X_{NIMP}$  space and thus the new NROY points.

The operations described in block (I) are known as the *cloud technique*, previously adopted in [50]. For what concerns the operation in (II), we employed the *part-and-select* algorithm [201] to tackle the point selection problem. Briefly, the  $n$  candidate points are partitioned into  $m$  clusters, and the most representative point of each cluster is returned.  $m - 1$  divisions of a single set into two sets are iteratively performed to obtain the  $m$  clusters. At each step, the set with the greatest dissimilarity among its members is the one that is divided, where the dissimilarity is computed as the set diameter in the Cheby-shev metric. To finally select the most representative member of a set, the point which is closest in Euclidean metric to the centre of the hyper-rectangle circumscribing the set itself is chosen.

In STEP 5, refocusing on the  $X_{NIMP}$  space will not take place if a stopping criterion is reached. The HM process can be stopped by observing at each wave the proportion of volumes of space that are cut-out of/retained in the current NROY space. If the percentage of  $X_{NIMP}$  space volume out of the total NROY space volume does not decrease in consecutive waves, this means that we have reached *convergence of the non-imausible space*, and we can stop. A more advanced stopping criterion consists in looking at the emulator variance for each  $X_{NIMP}$  point and comparing it with the sum of the observation error and model discrepancy variances: if the former is significantly smaller than this sum, and the same trend is observed throughout the entire  $X_{NIMP}$  space, this means that increasing the accuracy of the emulators for the next wave will not be of any use and the space will not be cut, so that we can stop. Finally, a combination of the percentage of  $X_{NIMP}$  space's volume reduction analysis and of variance analysis can be used to create arbitrarily complex stopping criteria.

### 3.6 GLOBAL SENSITIVITY ANALYSIS

In order to assess the contribution of the model input parameters' uncertainty into explaining the model output features' total variance, a global sensitivity analysis ([GSA](#)) can be performed. In the next paragraphs, we shall see how having fast-evaluating trained emulators enable characterisation of model sensitivities even for complex, computationally expensive simulators.

By assuming that for our specific biophysical system model  $f (=f_{\text{simul}})$  only low order correlations between input variables  $\mathbf{X} := (X_1, \dots, X_D)$  have an impact on the output ( $Y = f(\mathbf{X})$ ) variance, we can make use of the *high-dimensional model representation* [[186](#)] to introduce a functional decomposition of our simulator of the form:

$$f(\mathbf{X}) := f_0 + \sum_i f_i(X_i) + \sum_i \sum_{j>i} f_{ij}(X_i, X_j) + \dots + f_{i...D}(X_1, \dots, X_D) \quad (3.53)$$

If  $f$  is square integrable over the unit hypercube  $\Omega := [0, 1]^D$ , the decomposition (3.53) is unique given that [[219](#)]:

$$\int_0^1 f_{i_1, i_2, \dots, i_s}(X_{i_1}, X_{i_2}, \dots, X_{i_s}) dX_{i_w} = 0, \quad \text{with} \quad (3.54)$$

$$1 \leq i_1 < i_2 < \dots < i_s \leq D \quad (3.55)$$

$$i_w \in \{i_1, i_2, \dots, i_s\} \quad (3.56)$$

Now, let's assume  $\mathbf{X} = (X_1, \dots, X_D)$  to be a random vector of independent and uniformly distributed random variables over  $\Omega$ , then

using the integrals in equation (3.54), we can express each element in equation (3.53) as:

$$f_0 = \mathbb{E}[Y] \quad (3.57)$$

$$f_i = \mathbb{E}_{X_{\sim i}}[Y|X_i] - \mathbb{E}[Y] \quad (3.58)$$

$$f_{ij} = \mathbb{E}_{X_{\sim ij}}[Y|(X_i, X_j)] - f_i - f_j - f_0 \quad (3.59)$$

$$\dots \quad (3.60)$$

and so forth for higher orders, where  $X_{\sim i}$  indicates all components of  $\mathbf{X}$  but the  $i$ -th component. As  $f$  is square-integrable, we can apply the variance operator to every element of (3.53)

$$V_i = \mathbb{V}[f_i] = \mathbb{V}_{X_i}[\mathbb{E}_{X_{\sim i}}[Y|X_i]] \quad (3.61)$$

$$V_{ij} = \mathbb{V}[f_{ij}] = \mathbb{V}_{X_i X_j}[\mathbb{E}_{X_{\sim ij}}[Y|(X_i, X_j)]] + \quad (3.62)$$

$$- \mathbb{V}_{X_i}[\mathbb{E}_{X_{\sim i}}[Y|X_i]] - \mathbb{V}_{X_j}[\mathbb{E}_{X_{\sim j}}[Y|X_j]] \quad (3.63)$$

$$\dots \quad (3.63)$$

and so forth for higher orders, giving:

$$\mathbb{V}[Y] = \sum_i V_i + \sum_i \sum_{j>i} V_{ij} + \dots + V_{i\dots D} \quad (3.64)$$

Equation (3.64) takes the name of *ANOVA decomposition* of the variance. Dividing both sides by  $\mathbb{V}[Y]$  yields the relationship existing between the so-called *Sobol' sensitivity indices*:

$$1 = \sum_i S_i + \sum_i \sum_{j>i} S_{ij} + \dots + S_{i\dots D} \quad (3.65)$$

The Sobol' *main effect* (first-order sensitivity index) is defined as:

$$S_i := \frac{\mathbb{V}_{X_i}[\mathbb{E}_{X_{\sim i}}[Y|X_i]]}{\mathbb{V}[Y]}, \quad \text{for } i = 1, \dots, D \quad (3.66)$$

and it is a global sensitivity measure representing the amount of model output variance reduction that we would obtain if parameter  $X_i$  were to be fixed. Another important global sensitivity measure is the Sobol' *total effect*, defined as:

$$S_{Ti} := \frac{\mathbb{E}_{X_{\sim i}}[\mathbb{V}_{X_i}[Y|X_{\sim i}]]}{\mathbb{V}[Y]} = 1 - \frac{\mathbb{V}_{X_{\sim i}}[\mathbb{E}_{X_i}[Y|X_{\sim i}]]}{\mathbb{V}[Y]}, \quad (3.67)$$

$$\text{for } i = 1, \dots, D \quad (3.68)$$

and represents the total contribution of parameter  $X_i$  and all its higher-order interactions to the model output variance reduction. An intuitive description of the total effect index can be obtained from equation (3.67), by regarding  $\mathbb{V}_{X_{\sim i}}[\mathbb{E}_{X_i}[Y|X_{\sim i}]] / \mathbb{V}[Y]$  as the main effect of  $X_{\sim i}$ . Therefore, because of equation (3.65), subtraction of this term from 1 must leave only all the terms that include  $X_i$  component.

### 3.6.1 Estimating Sobol' sensitivity indices

*Monte Carlo* (MC) simulations can be used to estimate both the main and the total effects directly. However, a simple brute force approach that uses two nested “for” loops to calculate the conditional variance and expectation appearing in both equations (3.66)–(3.67) would cost  $N^2$  model evaluations per Sobol' index, which will become prohibitively expensive as  $N$  is typically taken to be between  $10^2$  and  $10^4$  for reliable estimates. For this reason, several integral estimators have been developed to reduce as much as possible the number of model runs needed to calculate Sobol' sensitivity indices. Here, we discuss the particular approach followed by Saltelli et al. [204].

Because of the known identity  $V[Y] = E[Y^2] - E^2[Y]$ , the numerator in equations (3.66) can be written as:

$$V_{X_i}[E_{X_{\sim i}}[Y|X_i]] = \int E_{X_{\sim i}}^2[Y|X_i]dX_i - \left( \int E_{X_{\sim i}}[Y|X_i]dX_i \right)^2 \quad (3.69)$$

where the second term is equal to  $E^2[Y]$ , while the first term can be rewritten by expressing the integral argument as an integral in  $2(D - 1)$  dimensions:

$$E_{X_{\sim i}}^2[Y|X_i] = \int f(X_{\sim i}, X_i)dX_{\sim i} \cdot \int f(X_{\sim i}, X_i)dX_{\sim i} \quad (3.70)$$

$$= \int \int f(X_{\sim i}, X_i)f(X'_{\sim i}, X_i)dX_{\sim i}dX'_{\sim i} \quad (3.71)$$

so that

$$\int E_{X_{\sim i}}^2[Y|X_i]dX_i = \int \int f(X_{\sim i}, X_i)f(X'_{\sim i}, X_i)dXdX'_{\sim i} \quad (3.72)$$

is an integral in  $2D - 1$  dimensions. The integral form of the main effect is therefore given by:

$$S_i = \frac{\int \int f(X_{\sim i}, X_i)f(X'_{\sim i}, X_i)dXdX'_{\sim i} - E^2[Y]}{V[Y]} \quad (3.73)$$

Similarly, an integral form for the total effect can be obtained:

$$S_{Ti} = \frac{E[Y^2] - \int \int f(X_{\sim i}, X_i)f(X_{\sim i}, X'_i)dXdX'}{V[Y]} \quad (3.74)$$

Estimators that have been developed to replace the brute force MC estimator commonly make use of the so-called *sampling and resampling approach* to generate the input space where to evaluate the model to eventually estimate the Sobol' sensitivity indices. This consists in generating a random matrix  $\mathbf{M}$  of size  $N \times 2D$ , uniformly sampled in the unit hypercube  $\Omega$ . Matrices  $\mathbf{A}$  and  $\mathbf{B}$ , each one of size  $N \times D$ ,

are then extracted from the first and second halves of the matrix  $\mathbf{M}$ , respectively:

$$\mathbf{M} = [\mathbf{A} \mid \mathbf{B}] \in [0, 1]^{N \times 2D} \quad (3.75)$$

Finally, additional  $D$  matrices of size  $N \times D$  are also built starting from matrix  $\mathbf{A}$ , by replacing each time a different  $i$ -th column with the  $i$ -th column from matrix  $\mathbf{B}$ :

$$\mathbf{A}_\mathbf{B}^{(i)} := [A_1, \dots, A_{i-1}, B_i, A_{i+1}, \dots, A_D], \quad (3.76)$$

$$\text{for } i = 1, \dots, D \quad (3.77)$$

In total, only  $N \times (D + 2)$  model evaluations, corresponding to  $f(\mathbf{A})$ ,  $f(\mathbf{B})$  and  $f(\mathbf{A}_\mathbf{B}^{(i)})$ ,  $i = 1, \dots, D$ , will be needed to estimate the Sobol' sensitivity indices, compared to the  $2 \times D \times N^2$  for the brute force approach. In fact, the two integrals appearing in the numerator of equations (3.73)–(3.74) can be approximated by:

$$(S_i) \quad \int \int f(\mathbf{X}_{-i}, X_i) f(\mathbf{X}'_{-i}, X'_i) d\mathbf{X} d\mathbf{X}' \approx \frac{1}{N} \sum_{j=1}^N f(\mathbf{B})_j f(\mathbf{A}_\mathbf{B}^{(i)})_j \quad (3.78)$$

$$(S_{Ti}) \quad \int \int f(\mathbf{X}_{-i}, X_i) f(\mathbf{X}_{-i}, X'_i) d\mathbf{X} d\mathbf{X}' \approx \frac{1}{N} \sum_{j=1}^N f(\mathbf{A})_j f(\mathbf{A}_\mathbf{B}^{(i)})_j \quad (3.79)$$

We will make use of the Sobol'-Saltelli [204] estimator for the main effect's and of the Jansen [92] estimator for the total effect's numerators calculation:

$$\mathbb{V}_{X_i} [\mathbb{E}_{\mathbf{X}_{-i}} [Y | \mathbf{X}_i]] \approx \frac{1}{N} \sum_{j=1}^N f(\mathbf{B})_j (f(\mathbf{A}_\mathbf{B}^{(i)})_j - f(\mathbf{A})_j) \quad (3.80)$$

$$\mathbb{E}_{\mathbf{X}_{-i}} [\mathbb{V}_{X_i} [Y | \mathbf{X}_{-i}]] \approx \frac{1}{2N} \sum_{j=1}^N (f(\mathbf{A})_j - f(\mathbf{A}_\mathbf{B}^{(i)})_j)^2 \quad (3.81)$$

$$\text{for } i = 1, \dots, D \quad (3.82)$$

while for both the effects' denominators, we will use the following estimate:

$$\mathbb{V}[Y] \approx \frac{1}{2N} \sum_{j=1}^{2N} f([\mathbf{A}^\top \mid \mathbf{B}^\top]^\top)_j \quad (3.83)$$

In addition, the initial matrix  $\mathbf{M}$  will not be sampled uniformly in the unit hypercube  $\Omega$ , but it will be sampled in the same space using a low-discrepancy, quasi-random Sobol' sequence [217], in order to obtain better estimates as described in [204]. It is worth mentioning that every column of the obtained matrices  $\mathbf{A}$  and  $\mathbf{B}$  will be rescaled

to the respective original interval  $[p_i^{\inf}, p_i^{\sup}]$  of the component  $X_i$  it represents, before calculating  $f(\mathbf{A})$ ,  $f(\mathbf{B})$  and  $f(\mathbf{A}_B^{(i)})$ s. This is done by using the simple bijection:

$$b: [0, 1] \rightarrow [p_i^{\inf}, p_i^{\sup}] \quad (3.84)$$

$$X_i \mapsto (1 - X_i) p_i^{\inf} + X_i p_i^{\sup} \quad (3.85)$$

Model components' second-order interactions are often of interest as well. These can be analysed by calculating Sobol' second-order effects, which, by recalling equation (3.62), are defined as:

$$S_{ij} := \frac{V_{ij}}{\mathbb{V}[Y]}, \quad \text{for } i, j = 1, \dots, D \quad (3.86)$$

The numerator in (3.86) will be calculated using the Saltelli estimator proposed in [202]:

$$V_{ij} \approx \frac{1}{N} \sum_k^N f(\mathbf{B}_A^{(i)})_k f(\mathbf{A}_B^{(j)})_k - f(\mathbf{A})_k f(\mathbf{B})_k \quad (3.87)$$

while the denominator will be estimated using again (3.83). Notice that the cost for calculating Sobol' second-order sensitivity indices is  $N \times (2D + 2)$  model evaluations, as we additionally need to calculate  $f(\mathbf{B}_A^{(i)})$  for  $i = 1, \dots, D$ .

### 3.6.2 Emulator-based estimates

Let's suppose that the considered estimators for Sobol' first- and second-order and total effects (3.80)–(3.83)–(3.87) can all be recapitulated in a single function  $\mathcal{S}$  that takes as an input simulator  $f_{\text{simul}}$  evaluations  $Y$  at specific points  $X$  ( $Y = f_{\text{simul}}(X)$ ) and gives as an output the Sobol' sensitivity indices  $S_i$ ,  $S_{ij}$ ,  $S_T$ :

$$Y \xrightarrow{\mathcal{S}(\cdot)} S_i, S_{ij}, S_T \quad (3.88)$$

In this study, we use the full GPE posterior distribution  $f_{\text{emul}}(X)$  as given in equation (3.32) to replace  $f_{\text{simul}}$  for Sobol' indices estimates calculation. In particular, we will adopt two approaches. The first (and simpler) one consists in using the point-wise predictions given by the GPE posterior distribution expectation for estimating the Sobol' indices:

$$\mathbb{E}[f_{\text{emul}}(X)] \xrightarrow{\mathcal{S}(\cdot)} S_i, S_{ij}, S_T \quad (3.89)$$

The second approach instead consists in randomly sampling points  $\hat{Y}$  from  $f_{\text{emul}}(X)$ , which is a multivariate normal distribution, and use them to obtain many estimates of the Sobol' indices. This operation will take into account also the GPE posterior distribution covariance

structure, and the resulting Sobol' sensitivity indices will be given as random variables:

$$\left. \begin{array}{l} f_{\text{emul}}(X) \sim \hat{Y}_1 \xrightarrow{\mathcal{S}(\cdot)} S_i^1, S_{ij}^1, S_{Ti}^1 \\ f_{\text{emul}}(X) \sim \hat{Y}_2 \xrightarrow{\mathcal{S}(\cdot)} S_i^2, S_{ij}^2, S_{Ti}^2 \\ \vdots \end{array} \right\} S_i(\omega), S_{ij}(\omega), S_{Ti}(\omega) \quad (3.90)$$

with sample space  $\omega \in [0, 1]$ . We can finally use the expectation of these random variables as a sensitivity index in its common definition:

$$S_i = \mathbb{E}[S_i(\omega)], \quad S_{ij} = \mathbb{E}[S_{ij}(\omega)], \quad S_{Ti} = \mathbb{E}[S_{Ti}(\omega)] \quad (3.91)$$

and the variance (and more generally the entire distribution) as an indicator of the sensitivity index accuracy [153].

So far, we have considered Sobol' indices estimates without taking into account the numerical error which is present when expectation and variance integrals are approximated using quadrature formulae. This uncertainty in the Sobol' indices estimates is commonly quantified using the *bootstrapping* technique [10]. This consists in resampling (i.e. sampling with replacement) a number of times the MC points from the unit hypercube  $\Omega$ , and each time re-calculating the Sobol' indices. A *moment method* is then used to construct confidence intervals from the bootstrap distribution, giving a symmetric distribution around the mean estimate of the Sobol' index value. It is worth noticing that the number of resamples used can be easily increased to improve the accuracy of bootstrap confidence intervals since the most expensive part will still reside in the model evaluation process rather than in the resampling process.

In the case when either full simulator evaluations (equation (3.88)) or emulator posterior distribution mean point-wise predictions (equation (3.89)) are used to estimate the Sobol' indices, the bootstrapping approach can be easily applied to derive estimates' confidence intervals. The situation changes when we make use of emulator posterior distribution samples to estimate the Sobol' indices (equation (3.90)). In fact, quantifying how the uncertainty of the emulator predictions propagates into the uncertainty of the integral estimates is a non-trivial task and also an actively researched topic of probabilistic numerics [45, 63, 77, 170]. As further analyses on the topic are out of the scope for this project, we neglected the uncertainty arising from the integral estimates and only considered the uncertainty arising from the fact that we are using an emulator to replace the true forward model. This choice is consistent with the assumption that as the number of MC samples  $N$  grows, the numerical error of the quadrature formulae will converge to 0, and what is left will be only the uncertainty of the emulator, which does not change with  $N$  for a fixed learning sample (training dataset).

### 3.7 SUMMARY

We have shown how the complex 3D biophysically-detailed model of rat heart contraction mechanics can be seen as a multi-scale function that maps a multi-dimensional input parameter vector to a one-dimensional output feature scalar. We have presented the main probabilistic tools to replace this map with a fast-evaluating surrogate model, which in turn enables the performance of expensive analysis such as model fitting through HM technique and uncertainty quantification through Sobol' GSA.

Part III  
APPLICATION RESULTS

## IN SILICO PERSONALISED RAT HEART CONTRACTION MODELS: THE ROLE OF SARCOMERE DYNAMICS IN DIASTOLIC HEART FAILURE

### OUTLINE

In this chapter, we personalise the 3D biventricular rat heart contraction mechanics mathematical model to clinical data obtained from a cohort of sham-operated and 6-weeks-post-surgery aortic banded rats. We specifically build one representative model for each cohort (control and diseased ones). For this purpose, we first personalise the rat anatomy to magnetic resonance images (Section 4.3.1.1). We then adopt an ionic model which was specifically fitted to patch-clamp measurements in intact LV myocytes of rats from the same two animal cohorts (Section 4.3.1.2). We then build a surrogate model of both the sham-operated and the aortic banding rat heart models (Section 4.3.3). Global sensitivities are then characterised for both models (Section 4.3.4). Models are further fitted to volumetric and functional data from the available medical images and literature experimental studies (Section 4.3.5). We then provide a discussion and address specific limitations (Section 4.5), and we conclude with a brief summary (Section 4.6).

### 4.1 MOTIVATION

With each beat, cardiac myocytes generate tension and relax. Cellular tension is transduced into a coordinated, global whole-heart deformation resulting in an effective, system-level pump function. The integration of cellular, tissue and organ-scale mechanisms is essential for achieving efficient transduction of work into concerted myocardial contraction and relaxation. The breakdown of this system of integrated mechanisms can give rise to HF.

Cardiac biophysical models provide a useful tool for studying whole-organ contraction [164] by simulation and can therefore be used to understand how impaired cell level function is linked with impaired organ level activity. Building a virtual representation of the real system requires tuning the cardiac model properties and boundary conditions to experimental data. GSA studies are also needed to determine the role of cellular, tissue and haemodynamics properties on whole-organ function.

However, the high simulation cost and the multi-scale nature of the cardiac system have limited the formal parameter estimation and sensitivity analysis for this type of model. Different techniques have been employed for global parameter inference on cardiac cell models, including gradient descent [57], genetic algorithms [71], multivariate regression [207] and Markov chain MC (MCMC) [93]. Most of these approaches are computationally intensive, and the computation burden is even higher when going from single to multiple scales.

Surrogate models (emulators) can be used to replace the computationally expensive real model with a statistical representation of it, allowing rapid predictions of the model output. Using emulators, we can thus perform the high number of model evaluations required to estimate global sensitivities. In this study, we use GPEs, which provide confidence bounds on predictions and can therefore be used for HM. Previously employed for fitting models of galaxy formation [235], infectious disease transmission [9] and, more recently, human atrial cell [50], HM has shown to be a valuable tool for global parameter inference.

To demonstrate the capacity of GPE and HM to fit a virtual heart model, we tune model mechanics-related parameters to literature experimental data from control and LV hypertrophied rat hearts. LV hypertrophy is induced surgically by constricting the ascending aorta over 4 to 6 weeks and represents a common pathway to HF development. Aortic-banded rats are commonly used as an experimental animal model for HF pathology [36].

We also seek to quantitatively characterise the diseased rat impaired LV contractile function. Therefore, we first compare the parameter spaces obtained after fitting both the control and diseased rat heart models. We then perform a GSA to understand how model properties differently affect the LV function across the two rat phenotypes.

This work, which incorporates our previous publication [139], confirms that impaired whole-organ function in rat HF is linked to altered properties at the sarcomere level.

## 4.2 RAT DATA

We used healthy control and diseased rat data from experimental studies conducted by Røe et al. [190]. Briefly, *aortic banding* (AB) was performed in male Wistar rats ( $n = 29$ ), while *sham-operated* (SHAM) rats ( $n = 23$ ) served as controls. *In vivo* cardiac function was characterised by echocardiography six weeks after surgery. The criterion for inclusion in the AB group was posterior wall thickening ( $> 1.9$  mm). A cohort of rats ( $n = 8$ ,  $n = 15$  from SHAM, AB groups, respectively) underwent an examination with *magnetic resonance imaging* (MRI). Rats in the AB cohort showed a preserved systolic function (ejection frac-

tion and fractional shortening). Concentric LV hypertrophy arose, as appraised by increased LV mass and wall thickness. Moreover, evidence of reduced peak early diastolic velocity ( $e'$ ) and increased early mitral inflow velocity / mitral annular early diastolic velocity ( $E/e'$ ) confirmed an impaired diastolic function in the rats.

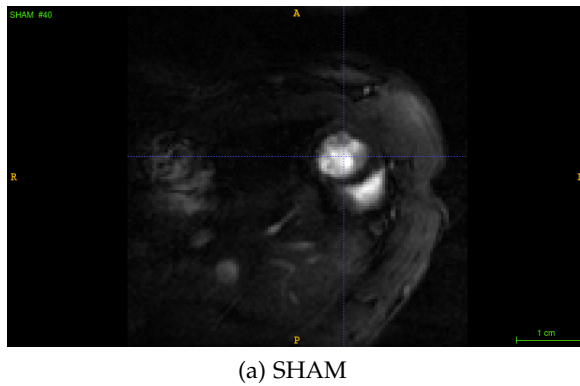
### 4.3 METHODS

#### 4.3.1 Rat heart contraction model

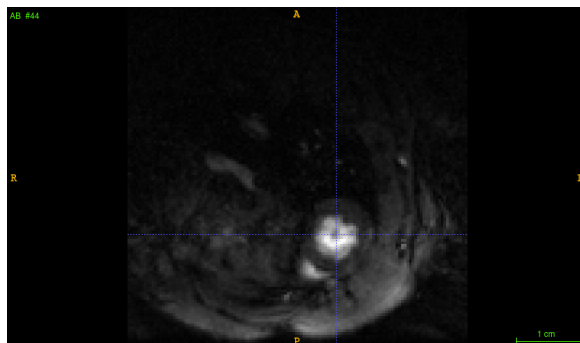
We modelled both the healthy and the diseased rat heart contraction mechanics using the multi-scale mathematical model presented in Chapter 2. Rat phenotype-specific anatomy and calcium dynamics descriptions were used, as described in the following two sections.

##### 4.3.1.1 Mesh generation

One representative cine MRI scan was obtained for both the SHAM and the AB rat cohorts. Each image set consisted of 47 equally, 2.779 ms-spaced time frames. Example apicobasal slices are shown in Figure A.7, while MRI characteristics are reported in Table 4.1.



(a) SHAM



(b) AB

Figure 4.1: Rat representative MR Images.

RAT	MRI CHARACTERISTICS	
	SIZE (#VOXELS)	VOXEL SIZE (mm <sup>3</sup> )
SHAM	128 × 128 × 9	0.39 × 0.39 × 1.5
AB	128 × 128 × 9	0.39 × 0.39 × 1.5

Table 4.1: MRI characteristics.

For each rat, we segmented the LV blood pool at each time frame and collected the corresponding volume estimates based on voxels size/count. This allowed extracting LV volume transient for each rat, displayed in Figure 4.2.

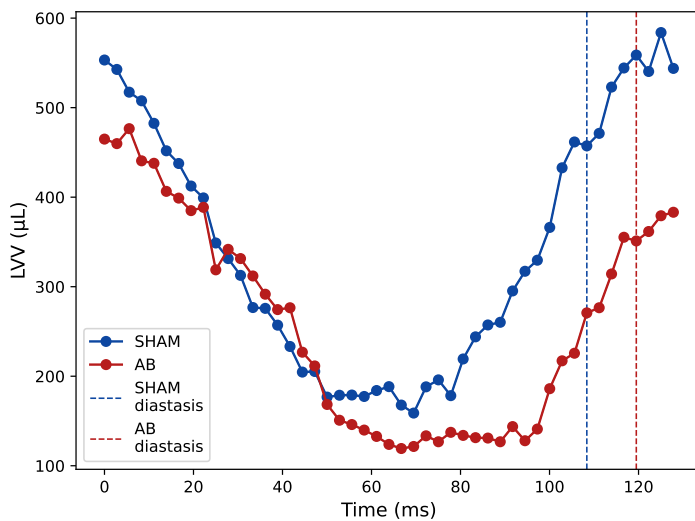
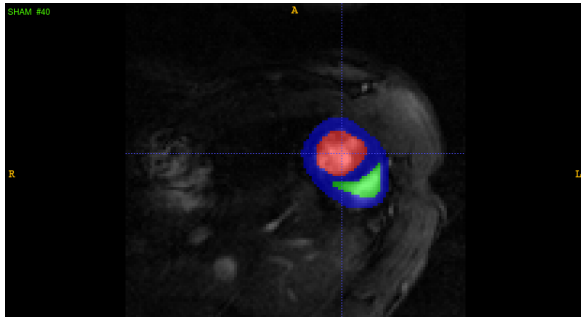


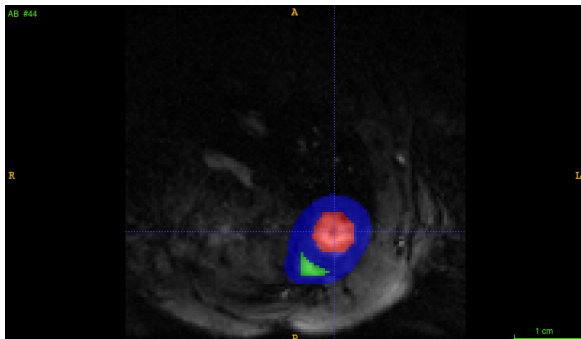
Figure 4.2: LV volume transients obtained by segmenting the LV blood pool of 47 consecutive time frames images for the SHAM (blue) and the AB (red) reference rat images. Dashed lines indicate approximately diastasis time during the cardiac cycle.

Time frames were numbered from 1 to 47. Frame #1 was assumed to be the moment the heart enters the ejection phase of the cardiac cycle. In order to approximate the stress-free configuration for mechanics simulations, we selected a time frame halfway through diastole, which could represent cardiac diastasis (specifically frame #40 and #44 for the SHAM and AB rats, respectively). We segmented the entire biventricular anatomy at these time frames, comprising three main tags: the LV and RV blood pools and the surrounding myocardium. All the segmentations were performed manually using ITK-SNAP (v.3.6.0) [251]. Obtained segmentations are displayed in Figure 4.3 and estimated volumes are summarised in Table 4.2.

Rat meshes with fibres were generated from the representative MRI scans segmentations using the approach described in Section 2.3. We



(a) SHAM



(b) AB

Figure 4.3: Rat representative MRI scans segmentations. LV and RV blood pools and myocardium are tagged with red, green and blue colours, respectively.

RAT	SEGMENTATION CHARACTERISTICS		
	LV ( $\text{mm}^3$ )	RV ( $\text{mm}^3$ )	MYOCARDIUM ( $\text{mm}^3$ )
SHAM	459.14	417.94	1127.93
AB	357.97	212.17	1181.72

Table 4.2: Segmentation tags volume estimates based on voxels size/count.

opted for an LoD of 2 for both the SHAM and the AB mesh generation, as we prioritised stability for mechanics simulations over accuracy. The generated meshes are shown in Figure 4.4.

#### 4.3.1.2 Ionic model

We employed two variants [69] of the original ionic model [68] the same authors developed in order to describe the control SHAM and the diseased AB rats specific calcium dynamics. The experimental data the authors used to re-fit the original model comes from exactly the same experimental study ([190]) from which we obtained the MRI scans. For this reason, we were able to have both sham-operated and aortic-banded rat cohorts-specific anatomy and electrophysiology

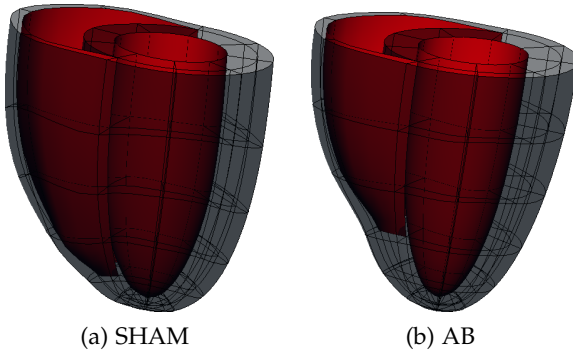


Figure 4.4: Rat representative cubic Hermite finite element meshes.

mathematical descriptions at the same time. Simulated action potentials and calcium transients from the two different models are shown in Figure 4.5.

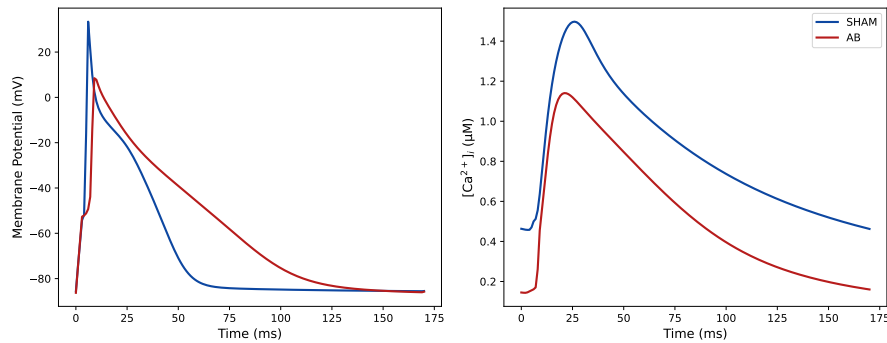


Figure 4.5: SHAM (blue) and AB (red) rats characteristic action potentials and calcium transients simulated using the Gattoni et al. [69] model of rat left ventricular myocyte electrophysiology at 6 Hz pacing frequency and 37 °C.

#### 4.3.2 Input parameter space

The input parameter space  $X \subset \mathbb{R}^8$  of the simulator map  $f_{\text{simul}}$  introduced in equation (8.7) was defined as the Cartesian product of 8 one-dimensional parameter ranges. These ranges were determined using prior information collected from both experimental and modelling literature studies, summarised in Tables 4.3–4.4. The finally adopted parameter ranges are reported in Table 4.5. To avoid bias, we used the same input parameter space  $X$  for both the SHAM and AB rat models over which points were sampled for simulation. Features from the simulated PV loops were then used to build the emulators' training datasets.

PARAMETER	UNITS	VALUE FROM EXPERIMENTAL STUDIES		VALUE FROM MODELLING STUDIES	
		RANGE	REFERENCE	RANGE	REFERENCE
$C_{a50}$	$\mu M$	—	—	[0.8, 1.56]	[14, 66, 118, 130, 163, 243]
$k_{off}$	$ms^{-1}$	[0.0013, 1.2]	[54, 191, 231]	[0.05, 0.2]	[118, 130, 163]
$k_{xb}$	$ms^{-1}$	0.1	[23, 225]	[0.008, 0.2]	[118, 130]
$T_{ref}$	$kPa$	—	—	[20, 160]	[23, 29, 111, 118, 130, 165, 176, 188, 226]
$p$	$kPa$	[0.2, 1.4]	[112, 133, 143, 161, 195, 196, 208, 211, 212]	1.0	[118, 130]
$p_{ao}$	$kPa$	[12, 21]	[110, 112, 123, 161, 171, 195, 196, 232]	[8, 9]	[118, 130]
$Z$	$mmHg\ s\ ml^{-1}$	[1.5, 16]	[40, 89, 107, 129, 132, 249, 254]	[6, 20]	[118, 130, 244]
$C_1$	$kPa$	[0.1, 3.0]	[168] (review paper)	[0.4, 1.]	[118, 130, 165, 173]

Table 4.3: SHAM rat model input parameters' values from experimental and modelling studies.

PARAMETER	UNITS	VALUE FROM EXPERIMENTAL STUDIES		VALUE FROM MODELLING STUDIES	
		RANGE	REFERENCE	RANGE	REFERENCE
$C_{a50}$	$\mu M$	—	—	[0.8, 1.0]	[130]
$k_{off}$	$ms^{-1}$	—	—	0.1	[130]
$k_{xb}$	$ms^{-1}$	—	—	0.02	[130]
$T_{ref}$	$kPa$	—	—	120	[130]
$p$	$kPa$	[0.3, 1.6]	[112, 133, 143, 161, 195, 196, 208, 211, 212]	1.0	[130]
$p_{a0}$	$kPa$	[21, 26]	[112, 161, 195, 196]	[7, 20]	[130]
$Z$	$mmHg\ s\ ml^{-1}$	[5.5, 23]	[89, 107, 249]	9.5	[130]
$C_1$	$kPa$	—	—	[0.2, 1.6]	[130]

Table 4.4: AB rat model input parameters' values from experimental and modelling studies.

PARAMETER	UNITS	RANGE
$C_{a50}$	$\mu\text{m}$	[0.25, 3.25]
$k_{\text{off}}$	$\text{ms}^{-1}$	[0.05, 0.2]
$k_{\text{xb}}$	$\text{ms}^{-1}$	[0.008, 0.2]
$T_{\text{ref}}$	$\text{kPa}$	[80, 160]
$p$	$\text{kPa}$	[0.3, 1.4]
$p_{\text{ao}}$	$\text{kPa}$	[6, 21]
$Z$	$\text{mmHg s ml}^{-1}$	[5.5, 20]
$C_1$	$\text{kPa}$	[0.1, 3]

Table 4.5: Parameters' ranges used for describing both the SHAM and AB rat models' 8D input parameter space.

#### 4.3.3 *Training dataset and emulators*

We trained GPEs on model simulations to replace the simulator multi-scale map (Section 3.3) with a fast-evaluating map. GPEs were defined as the sum of a linear regression model and a zero-mean GP, as described in Section 3.4, although for this study, the linear regression model polynomials were of the third degree. The chosen polynomials' degree resulted from a grid-search of integers from 1 to 4 with 5-fold cross-validation, which prevented the regression model from either under/over fitting. The learning sample was modelled not to be noisy. The GPE training was performed in two steps as described previously [235, 236]. Firstly, the linear regression model coefficients were fitted to the data by minimising the residual sum of squares; secondly, the GP hyperparameters were fitted to the residuals (data minus predicted mean) by maximisation of the log-marginal likelihood function (equation (3.41) with  $H_X\beta = 0$  and  $\sigma_n^2 = 0$ ). The GPE implementation and training were performed using routines of the `scikit-learn` Python library [183].

The emulation framework is outlined in Figure 4.6. Briefly, 8 LHDs of 1,024 input parameter points each were simulated, and the successfully completed simulations were collected to form the training dataset, with a final size of 825 and 850 points for the SHAM and AB models, respectively. The low number of successful runs relates to a combination of the failure of mechanics simulations converging or completing a full cardiac cycle, which may happen if the contraction is insufficient to reach the aortic pressure. One GPE was then trained for each LV output feature (Table 3.2), for a total of 12 GPEs.

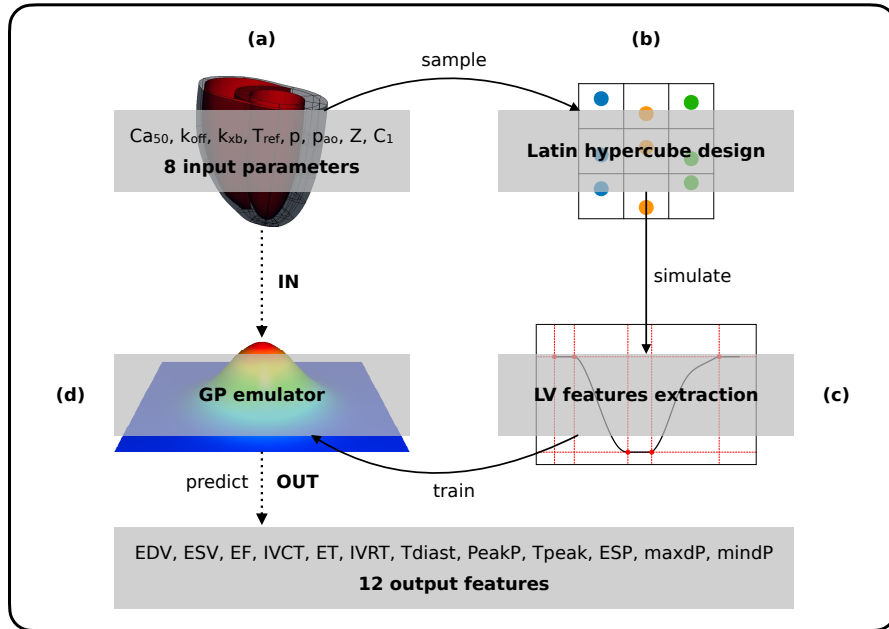


Figure 4.6: Building the surrogate model. Input points (a) are sampled in the parameter space using a Latin hypercube design (b). The model (simulator) is run using these points. The simulator output is composed of features extracted from the LV volume and pressure transients and PV loop (c). The initial simulator input matrix and the corresponding output matrix represent the training dataset for the surrogate model (emulator) based on Gaussian processes. The trained emulator (d) is used to predict the simulator output at new points in the input parameter space.

The trained GPEs were firstly employed to perform a global sensitivity analysis. A subset of them was then used in combination with the experimental target values to fit the rat models.

#### 4.3.4 Global sensitivity analysis

To assess how uncertainty in the model output can be attributed to different sources of uncertainty in the model input factors, we performed a variance-based sensitivity analysis. Variance-based methods of probabilistic sensitivity analysis quantify the sensitivity of the output to the model inputs in terms of a reduction in the variance of the output. We measured this reduction by estimating the Sobol' sensitivity indices [218] as described in Section 3.6.1.

Sobol' sensitivity indices were estimated using the SALib Python library [78], integrated with GPEs' posterior mean point-wise predictions, according to the first emulation-based approach of equation (3.89), presented in Section 3.6.2. Parameters whose Sobol' indices' value was below the threshold 0.01 were determined to have negligible effects.

### 4.3.5 History matching

The *in silico* rat heart biophysical model should aim to achieve the best representation of the real system. This requires tuning the model input parameters such that the model output features reflect the available experimental data.

We constrained the model parameters based on model read-outs that describe key features in the LV volume and pressure transients and PV loop (Table 3.2). For this purpose, we adopted the HM approach described in Section 3.5. The maximum implausibility measure (equation (3.52)) across multiple target features was used, with the model discrepancy term (and its corresponding variance) set to zero in equation (3.51). The real system observation  $z$  and the related observation error  $V[e]$  were taken to be equal to the mean  $\mu_j$  and the square of the standard deviation  $\sigma_j$  characterising the experimental variability  $\mu_j \pm \sigma_j \in \mathbb{R}$  of each given  $j$ -th feature. The Historia Python tool [140] was used for the HM implementation.

Target features' mean and standard deviation experimental values that we aimed to match using the model came from two different sources. Specific organ-scale features unavailable in the MRI data [190] were deduced from literature experimental studies all performed on male rats at body temperature with abdominal/ascending aortic banding [112, 133, 143, 161, 195, 196, 208, 211, 212]. In particular, EDV, ESV, ET and IVRT features were immediately available from the MRI data, while information about PeakP, maxdP and mindP features was collected from the literature. We did not have specific values for IVCT, Tdiast, Tpeak and ESP, and we chose not to match EF explicitly as this is derived from EDV and ESV. This gave us 7 organ-scale features to constrain our model parameters. Their experimental variability is reported in Table 4.6.

The HM was performed as follows. We started with 400,000 NROY points for wave 1, sampled using a LHD in the input parameter space  $X$  (defined in Section 4.3.2). For the next waves, 50,000 NROY points were sampled using the cloud technique in the corresponding previous waves' non-implausible space  $X_{NIMP}$ . At each wave, 256 points were selected from the current  $X_{NIMP}$  space using the part-and-select algorithm and simulated to enrich the training dataset for the emulators to be used in the next wave.

The cutoff value  $I_{cutoff}$  was initialised to 3.0, and incremented by 0.5 units until we achieved a non-empty non-implausible set after applying the implausibility criterion using the first wave's emulators. This gave initial  $I_{cutoff}$  values of 5.5 and 5.0 for the SHAM and AB rat models' fitting, respectively.  $I_{cutoff}$  was then decremented by 0.5 units with each HM wave down to the commonly used value of 3.0 (see Section 3.5). The decrement rate of 0.5 was selected to ensure that we

LV FEATURE	EXP. VARIABILITY		REFERENCE
	SHAM	AB	
EDV*	$508.80 \pm 39.01$	$466.50 \pm 37.10$	[190]
ESV*	$154.60 \pm 16.53$	$125.60 \pm 23.40$	[190]
ET*	$51.21 \pm 1.85$	$54.72 \pm 1.85$	[190]
IVRT*	$20.55 \pm 1.85$	$41.11 \pm 1.85$	[190]
PeakP**	$16.66 \pm 1.02$	$21.66 \pm 0.69$	[112, 133, 143, 161, 195, 196, 208, 211, 212]
maxdP**	$1.14 \pm 0.25$	$1.24 \pm 0.24$	[112, 133, 143, 161, 195, 196, 208, 211, 212]
mindP**	$-1.00 \pm 0.23$	$-1.16 \pm 0.23$	[112, 133, 143, 161, 195, 196, 208, 211, 212]

Table 4.6: Left ventricular features' target mean and standard deviation values. One asterisk (\*) features values come directly from the available MRI data. Two asterisks (\*\*) features values come from literature experimental studies.

reached the desired final value of 3.0 within a reasonable number of waves and maintain computational tractability while allowing us to initialise the HM over a sufficient large search space. The final waves were run with  $I_{\text{cutoff}} = 3.0$ .

## 4.4 RESULTS

### 4.4.1 Model emulation

The obtained cross-validation GPEs' test scores used as a measure of accuracy as described in Section 3.4 are reported in Tables 4.7–4.8 for the SHAM and AB models' emulators, respectively. The mean  $R^2$  score was  $> 0.9$  for all the 12 features but mindP, which had an  $R^2$  score of 0.74 in both the SHAM and AB models, and IVRT, which had an  $R^2$  score of 0.85 in the AB model. The  $ISE_2$  was  $> 0.8$  for all the features for both the rat models. Each emulator evaluation at a new input parameter point took  $\sim 1.2$  seconds against a full simulator single-core run of  $\sim 4$  hours, for a total gained speed-up of 12,000 fold per evaluation. An example illustration of emulators making inference on a test set from the cross-validation process is provided in Figures 4.7–4.8 for the SHAM and AB models' emulators, respectively.

LV FEATURE	R <sup>2</sup>	ISE <sub>2</sub> (%)
EDV	0.9712 ± 0.0046	87.75 ± 1.17
ESV	0.9736 ± 0.0023	86.42 ± 2.53
EF	0.9342 ± 0.0155	87.63 ± 2.44
IVCT	0.9658 ± 0.0122	88.00 ± 4.50
ET	0.9408 ± 0.0054	88.24 ± 1.65
IVRT	0.9135 ± 0.0128	87.63 ± 4.38
Tdiast	0.9412 ± 0.0056	86.66 ± 1.99
PeakP	0.9867 ± 0.0027	86.78 ± 1.04
Tpeak	0.9659 ± 0.0117	85.69 ± 5.82
ESP	0.9973 ± 0.0004	86.66 ± 2.23
maxdP	0.9792 ± 0.0064	86.66 ± 4.89
mindP	0.7437 ± 0.0283	93.45 ± 1.64

Table 4.7: The SHAM rat GPEs' accuracy. The GPEs' accuracy was evaluated using the average R<sup>2</sup> score and ISE<sub>2</sub> obtained with a 5-fold cross-validation. Values are reported as mean±std.

LV FEATURE	R <sup>2</sup>	ISE <sub>2</sub> (%)
EDV	0.9461 ± 0.0273	87.88 ± 4.05
ESV	0.9714 ± 0.0050	87.29 ± 2.37
EF	0.9661 ± 0.0101	86.23 ± 3.63
IVCT	0.9906 ± 0.0021	84.47 ± 2.51
ET	0.9593 ± 0.0159	89.29 ± 3.49
IVRT	0.8559 ± 0.0165	85.88 ± 1.78
Tdiast	0.9473 ± 0.0197	88.11 ± 4.06
PeakP	0.9871 ± 0.0077	85.29 ± 2.13
Tpeak	0.9542 ± 0.0150	86.00 ± 7.70
ESP	0.9959 ± 0.0024	86.23 ± 2.59
maxdP	0.9860 ± 0.0039	87.41 ± 3.08
mindP	0.7474 ± 0.0687	89.76 ± 2.37

Table 4.8: The AB rat GPEs' accuracy. The GPEs' accuracy was evaluated using the average R<sup>2</sup> score and ISE<sub>2</sub> obtained with a 5-fold cross-validation. Values are reported as mean±std.

#### 4.4.2 Model output sensitivity to model input

Figures 4.9–4.10 show how input parameters contribute to explaining each LV feature's total variance in the SHAM and AB models.

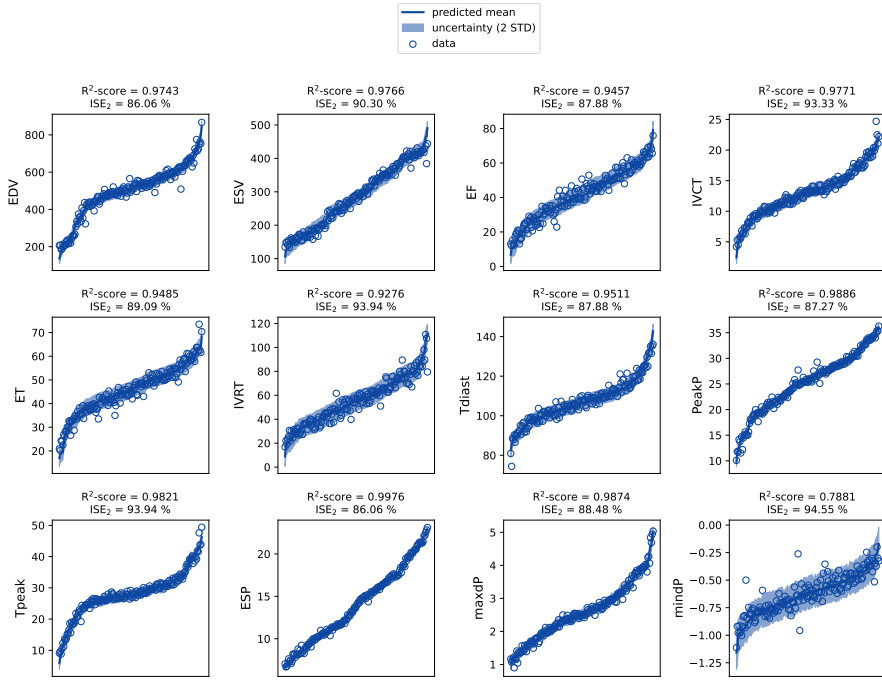


Figure 4.7: For each LV feature, the GPE with the highest  $R^2$  split test score is used to make predictions at the respective left-out subset of test points. Predictions are sorted in ascending order for the sake of better visualisation and joined with a thick blue line, and the respective observations (empty dots) are sorted accordingly. 2 STD confidence intervals (shaded regions) are also plotted around predicted mean lines.

The  $C_{50}$  parameter is the most influential across all the LV features. The  $k_{off}$ ,  $T_{ref}$  and  $p_{ao}$  parameters also play a key role. All these statements are true for both rat phenotypes. In contrast,  $C_1$  is more important for AB than for SHAM, explaining a fraction of the total variance of 9 out of 12 LV features (in SHAM,  $C_1$  is important for only 5 features). In particular, this parameter has an important contribution in explaining end-diastolic volume in AB (and not in SHAM). The  $k_{xb}$  parameter affects the AB more than the SHAM features, albeit only moderately (5 out of 12 against 4 out of 12, respectively). Finally, we observe an increased contribution of  $p_{ao}$  in explaining end-systolic pressure when going from SHAM to AB.

#### 4.4.3 Model fitting

The HM process is illustrated in Figures 4.11–4.12 for the SHAM and AB rat models. The input parameter points in 8D are plotted as a 2D projection for each pair of parameters. The initial  $X$  space (lightest colour variants) became progressively constrained to smaller  $X_{NIMP}$  regions (darker colour variants) as the HM process went forward.

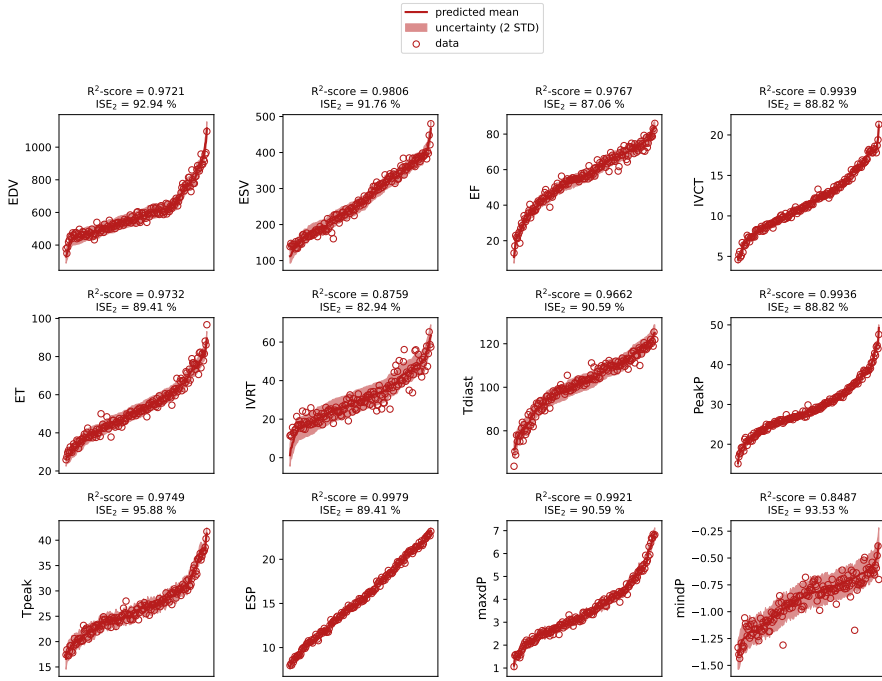


Figure 4.8: For each LV feature, the GPE with the highest  $R^2$  split test score is used to make predictions at the respective left-out subset of test points. Predictions are sorted in ascending order for the sake of better visualisation and joined with a thick blue line, and the respective observations (empty dots) are sorted accordingly. 2 STD confidence intervals (shaded regions) are also plotted around predicted mean lines.

During the last waves, as we continued to observe a decrease in the  $X_{NIMP}$  space volume, we stopped the process when the percentage of  $X_{NIMP}$  points out of the total testing NROY points fell below 5 %. This prevented exhaustion of computational resources, although convergence of the  $X_{NIMP}$  space had not yet been reached, completing SHAM and AB models' fitting in 8 and 9 waves, respectively. Details of HM progression, including cutoff values and percentages of space reduction, are given in Table 4.9.

Although HM does not ensure the reduction in individual parameters' ranges but rather a whole high-dimensional space reduction [50], the diagonal plots in Figures 4.11–4.12 suggest that all the parameters underwent reduction (to different degrees) across their 1D domain, both in the SHAM and AB models. Therefore, we analysed whether these parameters had been constrained to lie in spaces that differ according to the rat phenotype. This phenomenon was observed in 5 of the 8 total parameters, as highlighted in Figure 4.13. We can see that  $z$ ,  $Ca_{50}$ ,  $k_{xb}$ ,  $k_{off}$  and  $T_{ref}$  take values in completely separated spaces for the SHAM and AB models. The most extensive space separation is observed for  $Ca_{50}$  and  $T_{ref}$ .



Figure 4.9: The impact of the cell, tissue and boundary conditions properties on organ-scale LV features in the SHAM rat model. The contribution of each parameter is represented by the sum of its first- and (when present) second-order effects. For each LV feature, higher-order interactions (coloured in grey) are represented by the sum of total effects minus the sum of all first- and second-order effects.

We finally investigated whether the constrained input parameter space was mapped by the simulator into model read-outs that matched experimental observations. For this purpose, we sampled using the cloud technique and simulated 1,024 points in the HM final wave  $X_{NIMP}$  parameter space of both the SHAM and AB models. Of these, only 264 and 178 points led to a successfully completed simulation for SHAM and AB models, respectively. After extracting the LV features from the simulator outputs, we examined their distributions and compared them to the same features' experimentally observed variability (Table 4.6). This is summarised in Figure 4.14.

Figures 4.14A.1–2 show that points belonging to the reduced input parameter space reproduce the majority of the emerging organ-scale LV features except for ESV, maxdP and mindP which distribute far from the experimentally observed mean values. The simulated LV volume and pressure transients from which the features were extracted are also reported (Figures 4.14B.1–2). The resulting pressure-volume loops are provided in Figures 4.14C.1–2. By comparing the highlighted average curves, we can notice smaller end-diastolic and end-systolic volumes for AB, which still preserve the ejection fraction observed in



Figure 4.10: The impact of cell, tissue and boundary conditions properties on organ-scale LV features in the AB rat model. The contribution of each parameter is represented by the sum of its first- and (when present) second-order effects. For each LV feature, higher-order interactions (coloured in grey) are represented by the sum of total effects minus the sum of all first- and second-order effects.

the control rat. Diastolic time is increased in AB due to an increase in IVRT. LV peak pressure is visibly higher in AB.

#### 4.4.4 Fitted models

Unlike classical optimisation algorithms that converge to a single set of parameters possibly representing a global minimum of the chosen loss function, the HM procedure proposes an entire cloud of points (belonging to the last wave non-imausible, restricted parameter space) which are all possible candidates to yield a model features' match to experimental observation within experimental uncertainty. In order to have one representative model for the SHAM rat and one for the AB rat to be used as the baseline, reference models of healthy and diseased rat hearts, respectively, we selected one candidate represented by the best-fit according to the  $L_2$  norm of the difference between the simulated features' values vector and the corresponding experimental mean values vector. The complete sets of fitted model parameters and corresponding LV features for both the reference SHAM and AB rat models are reported in Tables 4.10–4.11.

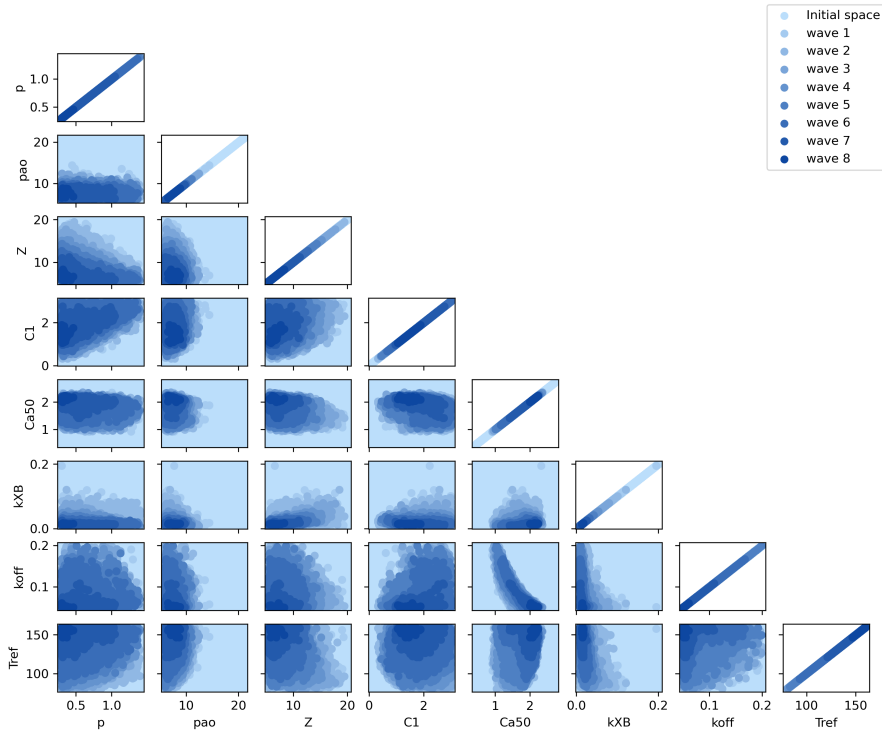


Figure 4.11: High-dimensional input parameter space reduction during SHAM history matching. SHAM HM completed within eight waves.

WAVE	RAT			
	SHAM		AB	
	$I_{\text{cutoff}}$	NIMP (%)	$I_{\text{cutoff}}$	NIMP (%)
1	5.5	0.09	5.0	0.08
2	5.0	41.79	4.5	65.66
3	4.5	25.63	4.0	59.89
4	4.0	49.47	3.5	61.29
5	3.5	28.22	3.0	43.46
6	3.0	12.05	3.0	30.59
7	3.0	8.56	3.0	21.33
8	3.0	0.09	3.0	12.93
9	—	—	3.0	1.15

Table 4.9: Details of history matching progression for the SHAM and AB rat models' fitting. At each wave, parameter points are tested against an implausibility criterion using the reported cutoff values ( $I_{\text{cutoff}}$ ), and only a percentage of these points (NIMP) out of the total tested points resulted to be non-imausible.

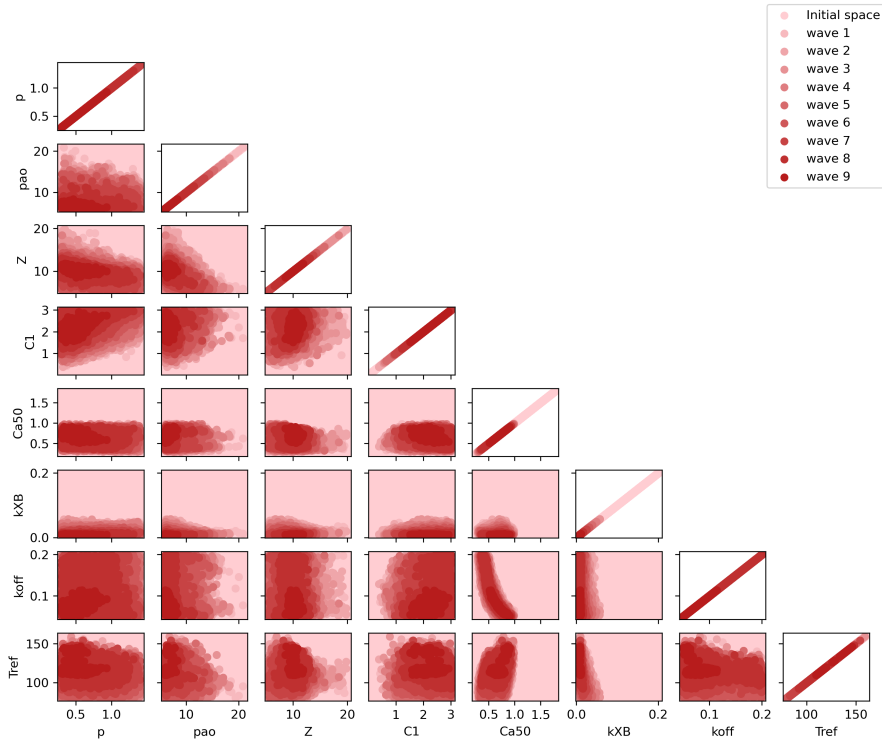


Figure 4.12: High-dimensional input parameter space reduction during AB history matching. AB HM completed within nine waves.

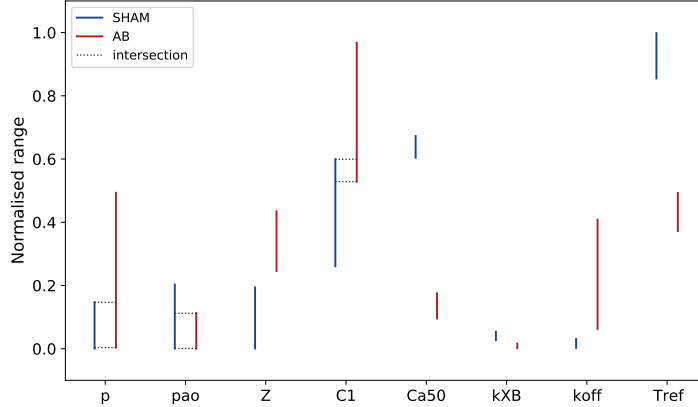


Figure 4.13: Input parameters' one-dimensional ranges after completing HM procedure. Comparison between SHAM (blue) and AB (red) rat models' fittings. For each input parameter, the displayed intervals are scaled according to the initial range for that specific parameter. When SHAM and AB intervals' intersection is non-empty, this is also displayed with dotted lines.

#### 4.5 DISCUSSION

We have shown how GPEs can be used to rapidly and robustly tune a multi-scale rat heart model to organ-scale functional measurements and characterise the global sensitivity of the model. To the best of

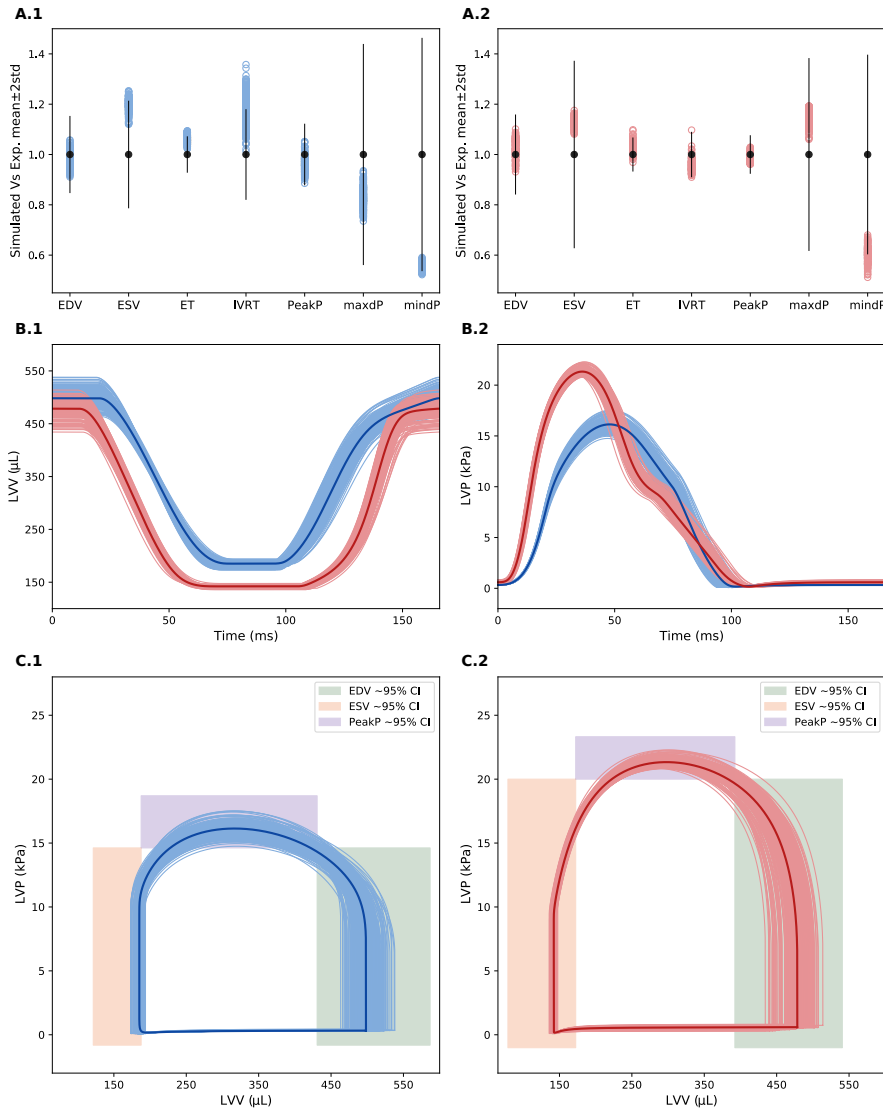


Figure 4.14: Simulator runs using the HM last wave's  $X_{NIMP}$  points as an input. (A) Obtained LV features' (empty, coloured dots) distributions around experimental mean values (filled, black dots) for SHAM (.1) and AB (.2). 2 standard deviations confidence intervals are shown as vertical straight lines centred in their respective mean value. All the displayed values (including confidence intervals) are normalised by the respective experimental mean values. (B) Simulated LV volume (.1) and pressure (.2) curves which the features in (A) were extracted from, for SHAM (blue) and AB (red). The average curves are displayed in darker colour variant. (C) Resulting SHAM (.1) and AB (.2) pressure-volume loops with EDV, ESV, PeakP features' ~ 95 % experimental confidence intervals.

our knowledge, this is the first example of the use of HM to constrain multi-scale cardiac mechanics models. Previous attempts to tune cardiac mechanics model parameters have sequentially fitted

PARAMETER	UNITS	VALUE	
		SHAM	AB
$C_{a50}$	$\mu\text{M}$	2.1723 [2.06, 2.27]	0.7087 [0.54, 0.77]
$k_{off}$	$\text{ms}^{-1}$	0.0515 [0.05, 0.06]	0.0686 [0.06, 0.11]
$k_{xb}$	$\text{ms}^{-1}$	0.0172 [0.01, 0.02]	0.0090 [0.01, 0.02]
$T_{ref}$	$\text{kPa}$	156.067 [148.38, 159.83]	112.582 [109.80, 119.41]
$p$	$\text{kPa}$	0.3122 [0.30, 0.46]	0.3914 [0.30, 0.84]
$p_{ao}$	$\text{kPa}$	7.1136 [6.01, 9.04]	7.0047 [6.01, 7.68]
$Z$	$\text{mmHg s mL}^{-1}$	5.6234 [5.51, 8.31]	9.9301 [9.06, 11.80]
$C_1$	$\text{kPa}$	0.9141 [0.86, 1.84]	1.6725 [1.63, 2.91]

Table 4.10: Representative SHAM and AB rat models' input parameters' values. Parameter bounds of all non-imausible models are also provided.

parameters [242] or fitted a maximum of 2–4 parameters using deterministic approaches [130]. Here we fitted 8 parameters concurrently. This means that error is evenly distributed across parameters and does not accumulate in the latter parameters as it occurs in sequential fitting techniques. We showed that active and passive parameters could be fitted simultaneously, avoiding potential confounding effects of slow relaxation, as occurs in heart failure models [248]. In addition, by providing bounds on model parameters (therefore an estimate of parameter uncertainty), the HM technique is compatible with verification, validation and uncertainty quantification (VVUQ) methods [182] supported by the ASME V&V40 standards and the FDA [11].

HM produced different constraints for the SHAM and AB models, even if starting from the same hypercube in the input parameter space (Section 4.3.2). Interestingly, the separation across the two rat phenotypes in the 1D parameters' ranges occurs mainly for parameters describing active tension development at the cellular level. We interpret this result as a confirmation that impaired whole-organ function in the AB rat is linked to altered properties at the sarcomere level.

LV FEATURE	UNITS	VALUE	
		SHAM	AB
EDV	$\mu\text{L}$	516.23 [463.33, 538.12]	467.88 [434.30, 513.83]
ESV	$\mu\text{L}$	173.82 [173.23, 193.67]	137.88 [135.76, 147.62]
EF	%	66.33 [58.87, 66.85]	70.53 [66.83, 73.22]
IVCT	ms	19.3 [18.60, 22.30]	13.2 [10.20, 13.80]
ET	ms	52.9 [52.40, 56.00]	57.7 [53.00, 60.10]
IVRT	ms	23.8 [20.80, 27.90]	40.0 [32.20, 45.10]
Tdiast	ms	93.5 [87.60, 94.30]	94.8 [93.20, 101.70]
PeakP	kPa	16.15 [14.75, 17.52]	20.94 [20.82, 22.28]
Tpeak	ms	46.6 [46.10, 50.40]	38.3 [32.80, 38.50]
ESP	kPa	10.04 [8.77, 11.45]	9.79 [8.76, 10.41]
maxdP	$\text{kPa ms}^{-1}$	0.9973 [0.84, 1.07]	1.4462 [1.32, 1.48]
mindP	$\text{kPa ms}^{-1}$	-0.5712 [-0.59, -0.52]	-0.3306 [-0.72, -0.26]

Table 4.11: Representative SHAM and AB rat models' output LV features' values. Feature bounds of all non-imausible models are also provided.

We have performed the first GSA of cardiac mechanics. Previous models have performed local sensitivity analysis [214], or attempted GSA on simplified cardiac cell models [181]. Our GSA approach highlighted that LV function is mostly influenced by cellular properties, consistent with our HM results.

#### 4.5.1 Limitations

The first limitation is the heterogeneity of the data used to constrain the models. Specifically, pressure measurements were not available from the used rat experimental data, so they were collected and averaged over similar experimental literature studies. Furthermore, we used only one representative anatomy for the SHAM rats' cohort and one representative anatomy for the AB rats' cohort. To use as many features as possible to personalise the two models, single measurements coming from these two anatomies' segmentations were used as the HM target mean values for the ET and IVRT features. Specifically, mean ET and IVRT values were extracted from a non-linear fit to the experimental LVV transients presented in Figure 4.2). Moreover, the respective HM target standard deviation values were empirically derived during the extraction process of features' mean values and not referred to population-based statistics.

Another important limitation concerns the GPEs' implementation. In Section 4.3.3, we have fitted the GPE mean function separately and then trained the GP part on the residuals, following a GPE-HM approach applied previously [205, 236]. However, different emulation strategies exist (see e.g. [50, 169], where the linear regression model parameters and the GP hyperparameters are jointly optimised). Furthermore, the degree of the GPE mean function polynomials was taken to be equal to 3, which might have made the regression model perform most of the fit to the data while leaving little room to the GP part for improvement/learning the data structure. Moreover, in this study, the learning sample was assumed not to be noisy. All these modelling choices might have led to underestimating the predictions' uncertainty, which might have also impacted the implausibility measure calculation, as pointed out by the reviewers of this study during the peer-review process. By looking at the obtained mean cross-validation  $ISE_2$  testing scores for both the SHAM and AB rat models' emulators, we can see that they were never above 90 %, while the same models'  $R^2$  scores were very high ( $> 90\%$ ). This could be an indication of uncertainty underestimation coupled with high accuracy in the mean point-wise predictions. From an HM perspective, the possible underestimation of the uncertainty might have prevented reaching convergence of the non-implausible space within a few waves. However, the high accuracy in the predictions proved to be crucial in matching the target features, thereby fitting the two rats model. In the next studies, we shall see that we cherished the reviewers' important advice, and we improved the emulation framework, although the optimal choice of GPE training strategy for fitting cardiac models still requires further research.

Finally, global sensitivity indices were estimated using the available emulator means, ignoring the emulator predicted uncertainty. In the

next studies, this was further improved by making use of GPEs full posterior distribution samples to calculate the Sobol' indices.

More general limitations of the adopted modelling framework can be found in Chapter 9, Section 9.2.

#### 4.6 SUMMARY

We have shown that GPE can effectively be used to robustly and rapidly constrain multi-scale cardiac models from organ-scale measurements. The obtained virtual biventricular rat hearts are a valuable system to be used for further investigation of heart failure. Moreover, we demonstrated that our GPE-based GSA approach enables the computationally efficient identification of key components in 3D ventricular mechanics, giving a deeper insight into the link between cell, tissue, shape and boundary conditions properties and organ-scale function.

## IN SILICO MAPPING OF SARCOMERE PHARMACOLOGICAL MODULATIONS TO WHOLE-ORGAN FUNCTION AND BACK AGAIN: THE OMECAMTIV MECARBIL CASE STUDY

### OUTLINE

In this chapter, we use the personalised SHAM rat heart contraction model as a reference model of a healthy rat heart to show that it is possible to quantitatively map pharmacological interventions at the sarcomere level through to the whole-organ function. Moreover, we show that we can infer cell-level pharmacological effects from whole-organ observations, demonstrating the feasibility of the inverse mapping. We apply this framework to an example drug, namely omecamtiv mecarbil, which has been proposed as a possible treatment of HF. We first present the variability observed in the drug effects from preclinical data, namely from (1) *in vivo* whole-heart haemodynamics measurements and (2) *in vitro* steady-state F-pCa measurements (Section 5.2). We then model the drug mechanism of action using 4 model parameters (Section 5.3.2), and we use emulators to map these to the LV features and to characterise the latter global sensitivities (Section 5.3.3). We then constrain the 4-parameter space using the preclinical data (Sections 5.3.4–5.3.5). The constrained parameter space from case (1) is then mapped to F-pCa curves (Section 5.4.3), while the one resulting from case (2) is mapped to the LV features (Section 5.4.2). We then include a discussion of the results and address specific limitations (Section 5.5), and we conclude with a brief summary (Section 5.6).

### 5.1 MOTIVATION

HF is a leading cause of hospitalisation worldwide, with more than one million admissions annually in the US and Europe [19]. However, the treatment options are limited, and, therefore, new pharmacotherapies are continuously sought. HF pathways can involve impaired cellular function and propagate up to the whole-organ dysfunction. Multi-scale contraction modelling represents a valuable tool for understanding the underlying mechanisms and possibly identifying targets in these pathways.

Building on the developed rat heart contraction modelling framework (Chapter 4), we can investigate mechanisms of drug action and better understand the mechanistic processes linking cellular and

whole-heart contraction. For this case study, we chose omecamtiv mecarbil (OM), a novel drug currently in Phase 3 clinical trial [230] for treating HF. OM is a selective allosteric cardiac myosin modulator. It increases the rate of cross-bridge cycling by accelerating phosphate release [150] without disrupting intracellular calcium dynamics [84]. Recently, OM was shown to enhance the duty ratio, resulting in increased calcium sensitivity and slowed force development [98, 227].

This chapter outlines our methodology of incorporating OM into our model, which consists of calibrating the cellular model using *in vitro* data from skinned cellular and trabecular preparations in OM-containing solutions [98, 103, 160], and validating the biventricular multi-scale contraction model using pressure-volume measurements from *in vivo* whole-heart studies in healthy animals with OM [16]. Our simulation results are consistent with the available experimental data on OM and, importantly, support the hypothesis (e.g. [227]) that OM affects the thin filament (in addition to the expected effect on thick filaments due to OM being the selective cardiac myosin activator).

This work, incorporating our previous publication [136], demonstrates how quantitative mapping from cellular to whole-organ level can be used to improve our understanding of drug action mechanisms.

## 5.2 PRECLINICAL DATA

### 5.2.1 Cell-level measurements

*In vitro* measurements of the OM effects on the sarcomere in healthy rats were taken from literature experimental studies performed on skinned myocytes' preparations. OM effects were given in terms of alterations of the  $p\text{Ca}_{50}$  and  $h$  features of the F-pCa curve (introduced in Section 2.2.4, equation (2.20)). To map these effects from skinned to intact/*in vivo* results, we used percentages of F-pCa features' change from the control muscle to the OM-containing solution-exposed muscle. These values are summarised in Table 5.1.

FRACTION OF CHANGE	EXP. VARIABILITY	REFERENCE
$P_{\text{shift}}$ (for $p\text{Ca}_{50}$ )	[0.0085, 0.0833]	[98, 103, 160]
$P_{\text{slope}}$ (for $h$ )	[-0.7282, -0.2470]	[98, 103, 160]

Table 5.1: F-pCa curve features' fractions of change experimental variability in OM-containing solution-exposed healthy rat skinned muscles. Values are given as ranges of minimum and maximum fractions of change from control experimental mean values.

### 5.2.2 Whole-organ measurements

We did not have *in vivo* measurements of the OM effects on the whole-organ function in healthy rats, so qualitative observations from a healthy pig study were used [16]. Again, we used percentage changes in LV features from baseline values after OM administration. In particular, we focused on the features whose change from control was reported to be statistically significant. These values are summarised in Table 5.2.

LV FEATURE	EXP. VARIABILITY (%)	REFERENCE
EDV*	$87.14 \pm 17.14$	[16]
ESV*	$76.92 \pm 20.51$	[16]
SV	$100.00 \pm 25.81$	[16]
EF	$115.91 \pm 18.18$	[16]
ET*	$116.16 \pm 9.61$	[16]
Tdiast*	$88.24 \pm 16.97$	[16]
maxdP*	$121.66 \pm 35.53$	[16]
mindP	$108.96 \pm 31.01$	[16]

Table 5.2: Left ventricular features' experimental variability in healthy pigs after OM administration. Values are given as mean $\pm$ std percentage change from control experimental mean values. Asterisked ( $\cdot^*$ ) features' changes were reported to be statistically significant.

## 5.3 METHODS

### 5.3.1 Rat heart contraction model

To quantitatively link sarcomere properties to whole-organ function, we used the personalised SHAM rat heart contraction model derived in Section 4.4.4. Again, this model (or simulator) can be seen as a multi-scale map from input parameters to output features.

With the simulator input, we aimed at modelling the OM effect at the sarcomere level. As OM increases the rate of cross-bridge formation [150], we considered parameters that are specifically responsible for cross-bridge dynamics in the Land et al. [119] cell contraction sub-model, namely  $k_{xb}$ ,  $n_{xb}$ , TRPN<sub>50</sub> and  $T_{ref}$ . These parameters, introduced in Section 2.2 and again reported in Table 5.3, constituted the simulator 4-dimensional input.

The simulator output described the LV function using a set of scalar features. These were the same 12 features used in the previous analysis

PARAMETER	UNITS	DEFINITION
$k_{xb}$	$\text{ms}^{-1}$	cross-bridges cycling rate
$n_{xb}$	—	cross-bridge formation degree of cooperativity
TRPN <sub>50</sub>	—	fraction of $\text{Ca}^{2+}$ -TnC bounds for half-maximal cross-bridges activation
$T_{\text{ref}}$	kPa	maximal reference tension

Table 5.3: Model parameters and their definitions.

(Table 3.2) with the addition of other 2 features (Table 5.4), for a total of 14 features.

LV FEATURE	UNITS	DEFINITION
SV	$\mu\text{L}$	stroke volume
ET/Tdiast	—	systolic ejection time over diastolic filling time

Table 5.4: Additional LV features of interest.

The obtained simulator map had thus the following form:

$$\begin{aligned} f_{\text{simul}}: \mathbb{R}^4 &\rightarrow \underbrace{\mathbb{R} \times \cdots \times \mathbb{R}}_{14 \text{ times}} \\ x &\mapsto (y_1, \dots, y_{14}) \end{aligned} \tag{5.1}$$

When running the simulator at a new parameter point, we fixed all the parameters not included in the set of simulator inputs to the personalised SHAM rat model baseline parameter values (Table 4.10) when applicable, or to the Land et al. [119] model baseline values when otherwise.

### 5.3.2 Input parameter space

The input parameter space  $X \subset \mathbb{R}^4$  of the simulator map  $f_{\text{simul}}$  introduced in equation (5.1) was defined as the hypercube obtained by the Cartesian product of 4 one-dimensional parameter ranges. Each of these ranges was given as the combination of bounds inferred from the *in vitro* F-pCa data presented in Section 5.2.1 (further details are provided in Section 5.3.4) and a  $\pm 50\%$  ( $\pm 30\%$  for  $T_{\text{ref}}$ ) perturbation around the related parameter reference value. Adopted ranges are reported in Table 5.5.

PARAMETER	UNITS	RANGE
$k_{xb}$	$\text{ms}^{-1}$	[0.0086, 0.0258]
$n_{xb}$	—	[0.90, 7.05]
$\text{TRPN}_{50}$	—	[0.05, 0.50]
$T_{\text{ref}}$	$\text{kPa}$	[109.25, 202.89]

Table 5.5: Parameters' ranges used for describing the healthy rat model 4D input parameter space.

### 5.3.3 Training dataset, emulators and global sensitivity analysis

We sampled 4096 points from a LHD over the input parameter space  $X$  defined in Section 5.3.2. The simulator was run at these points, and the successfully completed simulations were collected to form the training dataset (1189 points).

Univariate GPEs, defined as in Section 3.4, were used to predict each of the 14 LV output features, and all the GPE model hyperparameters (both from the mean function and from the zero-mean GP) were jointly optimised during training by maximisation of the model log marginal likelihood (equation (3.41)). For each of the 14 trained GPEs, we used the  $R^2$ -score to check the regression accuracy and the  $\text{ISE}_2$  to assess the adequacy of being used as a surrogate model (Section 3.4.1). The GPE implementation and training were performed using GPERks emulation tool [142] based on GPyTorch Python library [67].

To study the input parameters' impact on the output LV features' total variance, we performed a GSA using the trained GPEs. Model outputs' sensitivity to model inputs was characterised by Sobol' first-order and total effects. These were estimated using SALib Python library [78]. GPERks tool [142] was used to incorporate GPEs' full posterior distribution samples to account for emulators' uncertainty in Sobol' indices' estimates, by following the second emulation-based approach of equations (3.90)–(3.91), presented in Section 3.6.2. Parameters whose Sobol' indices' distributions' expectation was below the threshold 0.01 were determined to have negligible effects.

### 5.3.4 Inferring OM effects on whole-organ function from *in vitro* F-pCa measurements

We wanted to investigate whether it is possible to validate OM mechanisms of action by using the built quantitative link between sarcomere properties and whole-organ function.

By recalling equations (2.18)–(2.19):

$$pCa_{50} = -\log \left[ Ca_{T50} \left( \frac{k_{off}}{k_{on}} \frac{TRPN_{50}}{1 - TRPN_{50}} \right)^{1/n_{trpn}} \right] \quad (5.2)$$

$$h = n_{xb} n_{trpn} (1 - TRPN_{50}) \quad (5.3)$$

we can notice that among the 4 chosen input parameters (Section 5.3.1) there are 2 parameters, namely  $TRPN_{50}$  and  $n_{xb}$ , that can be used to tune both the  $pCa_{50}$  and  $h$  at the same time. Given a set of changes  $(\Delta pCa_{50}, \Delta h)$  in these two features of the F-pCa curve, it is possible to scale the 2 parameters' reference values such that the F-pCa curve undergoes a perturbation of exactly  $(\Delta pCa_{50}, \Delta h)$ . This can be accomplished by solving for the set of scaling coefficients  $(\alpha, \beta) \in \mathbb{R} \times \mathbb{R}$  the following equations:

$$pCa_{50}(p_{new}) - pCa_{50}(p) = \Delta pCa_{50} \quad (5.4)$$

$$h(p_{new}) - h(p) = \Delta h \quad (5.5)$$

where  $pCa_{50}(\cdot)$  and  $h(\cdot)$  are now seen as functions of the reference  $p = (TRPN_{50}, n_{xb})$  and the new  $p_{new} = (\alpha \cdot TRPN_{50}, \beta \cdot n_{xb})$  parameter vectors.

The resulting 2-dimensional space, given by all the possible  $p_{new}$  vectors obtained by solving equations 5.4–5.5 for all the viable  $(\Delta pCa_{50}, \Delta h)$  according to the experimentally observed variability for the F-pCa curve (Table 5.1), will constitute an OM-compatible sarcomere space encoded by the  $TRPN_{50}$  and  $n_{xb}$  parameters. To obtain the OM-compatible sarcomere space, we first generated a LHD of 100,000 points over the 2D space of F-pCa curve's features experimental variability (expressed as fractions of control/no-drug values) (Table 5.1). We then projected this space into the corresponding 2D sarcomere parameter space as described above.

We finally mapped the obtained 2D sarcomere parameter space to EDV, ESV, ET/Tdiast and maxdP using the corresponding GPEs, in order to see if these features were moving in the direction of change experimentally observed in the *in vivo* pig haemodynamics after OM administration (Section 5.2.2). The mapping was performed while keeping  $k_{xb}$  and  $T_{ref}$  parameters, for which we had no data, fixed to their reference values.

### 5.3.5 Inferring OM effects on the sarcomere from *in vivo* whole-organ measurements

We wanted to understand what the experimental *in vivo* pig data of altered LV function with OM administration could tell us about the sarcomere parameter space of the model. To do this, we used a single

iteration of the HM technique. This was done as described in Section 3.5, using the maximum implausibility measure (equation (3.52)) across multiple target features, with the model discrepancy term (and its corresponding variance) set to zero in equation (3.51). Historia tool [140] was used to run the HM procedure.

For the target features, we aimed at matching the experimental variability observed in the LV features that showed a significant change from baseline after OM administration (asterisked features of Table 5.2). At the same time, we wanted the model to preserve the “control state” for those features that did not show significant change from baseline. For this purpose, we matched for these features an experimental percentage variability of  $100\% \pm 0\%$  (i.e. no change). We sampled 400,000 NROY points from a LHD in the input parameter space  $X$  (derived in Section 5.3.2). As the GPEs had very high accuracy and very low variance for the predictions (shown in the results Section 5.4.1), the HM single iteration was performed with half the common value for the implausibility cutoff, i.e.  $I_{\text{cutoff}} = 1.5$ . This allowed to cut most of the space while still retaining few  $X_{\text{NIMP}}$  points, as we shall see in Section 5.4.3.

The obtained  $X_{\text{NIMP}}$  space constituted an OM-compatible sarcomere space encoded by the  $k_{\text{xb}}$ ,  $n_{\text{xb}}$ ,  $\text{TRPN}_{50}$  and  $T_{\text{ref}}$  parameters. The points from this space were finally mapped using the Land et al. [119] model of cellular contraction to F-pCa curves in order to see if the corresponding  $\text{pCa}_{50}$  and  $h$  features were moving in the direction of change experimentally observed in rats’ skinned muscle preparations in OM-containing solutions (Section 5.2.1).

## 5.4 RESULTS

### 5.4.1 Model emulators and output sensitivities

All the trained GPEs had a cross-validation mean accuracy  $> 0.99$  and  $> 0.97$  for the  $R^2$  score and  $\text{ISE}_2$ , respectively. These are reported in Table 5.6. An example illustration of emulators making inference on a test set from the cross-validation process is provided in Figure 5.1.

The performed GSA (Figure 5.2) showed that  $\text{TRPN}_{50}$  was the most important parameter in explaining the LV features’ total variance in the model. The second most important parameter was  $n_{\text{xb}}$ , followed by  $T_{\text{ref}}$  and  $k_{\text{xb}}$  parameters. It is worth noticing that the two cross-bridge formation-regulating parameters that affect the LV function the most are also the ones that regulate the force-calcium relationship in the rat model.

LV FEATURE	R <sup>2</sup>	ISE <sub>2</sub> (%)
EDV	0.9967 ± 0.0011	99.07 ± 0.61
ESV	0.9997 ± 0.0000	99.57 ± 0.26
EF	0.9990 ± 0.0002	98.90 ± 0.90
IVCT	0.9932 ± 0.0020	98.23 ± 0.72
ET	0.9955 ± 0.0010	99.15 ± 0.59
IVRT	0.9971 ± 0.0009	98.73 ± 0.59
Tdiast	0.9971 ± 0.0005	99.74 ± 0.33
PeakP	0.9991 ± 0.0002	97.14 ± 0.85
Tpeak	0.9952 ± 0.0013	98.90 ± 0.77
ESP	0.9983 ± 0.0003	98.48 ± 0.50
maxdP	0.9959 ± 0.0044	99.49 ± 0.61
mindP	0.9961 ± 0.0019	99.24 ± 0.31
SV	0.9991 ± 0.0001	98.99 ± 0.77
ET/Tdiast	0.9969 ± 0.0006	99.66 ± 0.31

Table 5.6: GPEs' accuracy. The GPEs' accuracy was evaluated using the average R<sup>2</sup> score and ISE<sub>2</sub> obtained with a 5-fold cross-validation. Values are reported as mean±std.

#### 5.4.2 Model predicted OM effects on the LV function

The OM-compatible 2D sarcomere parameter space inferred from *in vitro* rat F-pCa data is shown in Figure 5.3.

Figure 5.4 shows that the corresponding inferred median effects of these changes to pCa<sub>50</sub> and h due to OM on whole-organ function show a qualitative agreement in the direction of change for all the 4 LV features reported to be significantly altered by OM in the pig study [16].

#### 5.4.3 Model predicted OM effects on the F-pCa relationship

The HM first wave identified 3,469 points (corresponding to 0.8672 % of the initial space) as non-imausible for replicating the organ-scale effects of OM administration. The resulting OM-compatible 4D sarcomere parameter space inferred from *in vivo* pig haemodynamic data is shown in Figure 5.5.

Figure 5.6 shows that the corresponding inferred median effects of these changes to the LV function due to OM on the intact F-pCa curve show a qualitative agreement in the direction of change for both the pCa<sub>50</sub> and h features reported to be altered by OM in the rat skinned muscle studies [98, 103, 160].

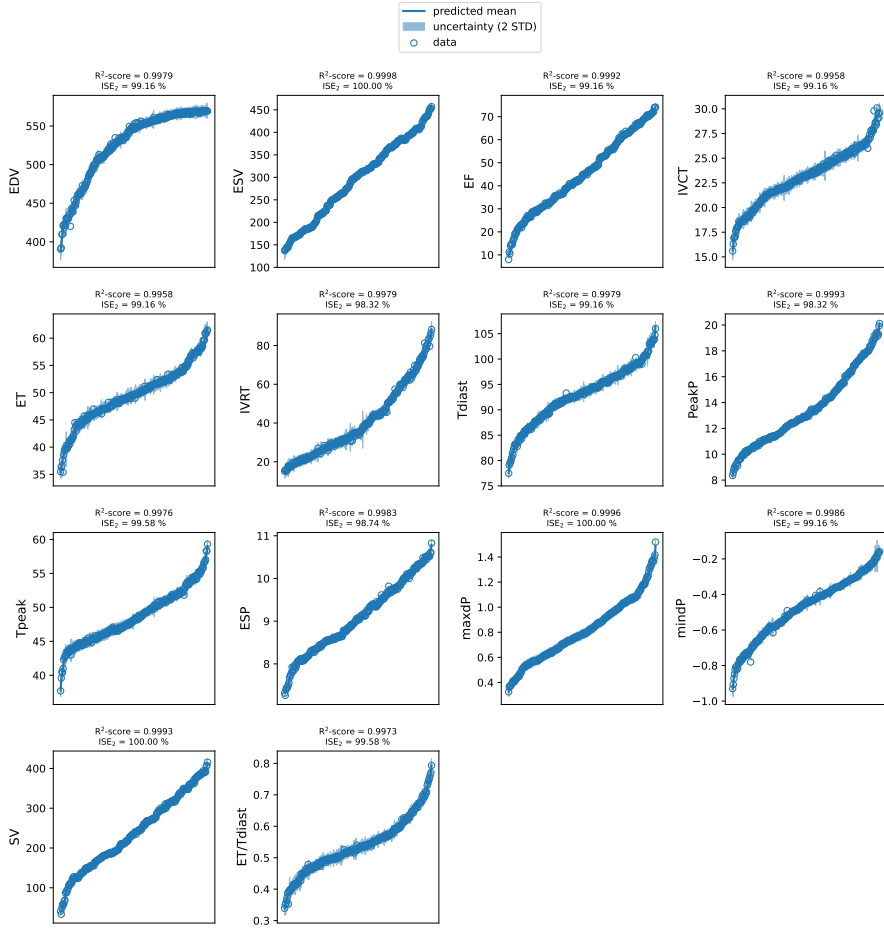


Figure 5.1: For each LV feature, the GPE with the highest  $R^2$  split test score is used to make predictions at the respective left-out subset of test points. Predictions are sorted in ascending order for the sake of better visualisation and joined with a thick blue line, and the respective observations (empty dots) are sorted accordingly. 2 STD confidence intervals (shaded regions) are also plotted around predicted mean lines.

## 5.5 DISCUSSION

We have demonstrated that the personalised, virtual rat heart framework (Section 4.4.4) can recapitulate the effects of OM on cardiac contraction and that multi-scale cardiac mechanics models can be used to infer the impact of drugs on cellular function from whole-organ observations. Calibration of model parameters to both cellular and whole-organ data on OM gives us additional insight into the mechanistic processes that link cellular and whole-heart contraction. Our results demonstrate that in order to reproduce available data, OM requires altering the function of both thick and thin filaments. The OM effect on thick filament (the direct site of action of OM) is essential to reproduce the OM effect on tension in whole-heart. Simulations

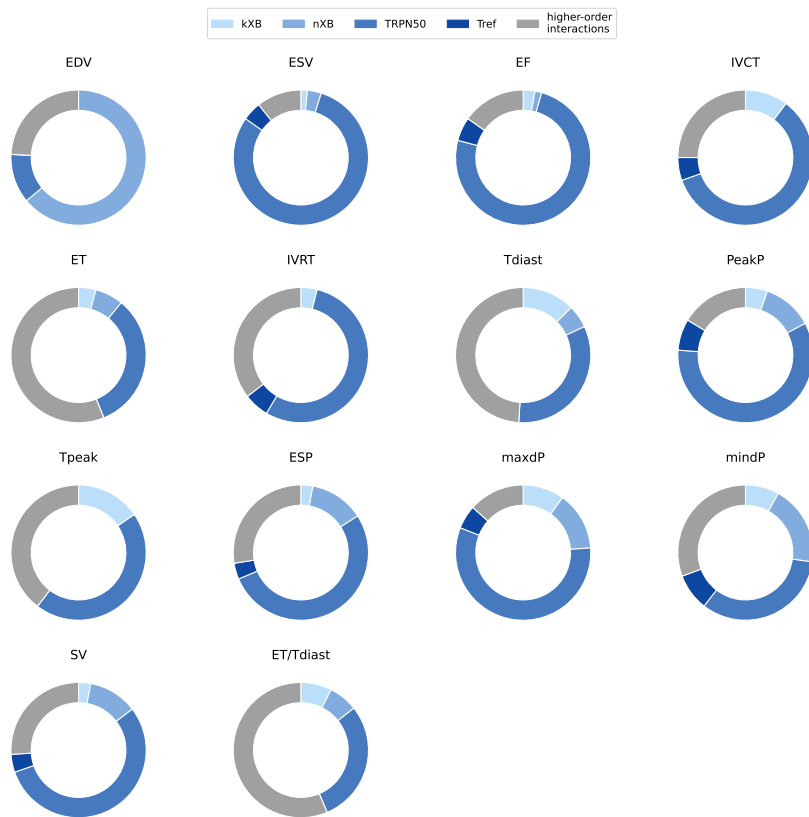


Figure 5.2: The impact of cross-bridge related sarcomere parameters on organ-scale LV features in the healthy rat. The contribution of each parameter is represented by its Sobol' main effect. For each LV feature, higher-order interactions (coloured in grey) are represented by the sum of all total effects minus the sum of all main effects.

show that the OM effect on F-pCa curves involves changes in thin filament function, namely by altering calcium myofilament sensitivity, which supports the recent hypothesis of the effect of OM on thin filaments [227].

### 5.5.1 Limitations

As a result of the adopted simplified approach for sarcomere contraction modelling (Section 2.2), the OM effect is modelled using 2- to 4-parameters linked to the cross-bridge cycling but not directly incorporating the OM mechanism of action (which is to increase the rate of myosin-head attachment to actin [150]).

OM whole-organ data in healthy animals is limited. To the best of our knowledge, the *in vivo* pig haemodynamics data [16] used to constrain the model parameters is the only available non-human study of OM effect on LV function with therapeutic doses in healthy animals.

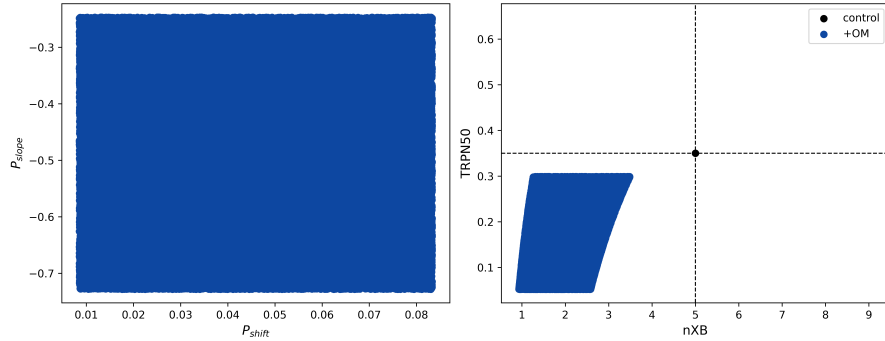


Figure 5.3: OM-compatible sarcomere space encoded by the  $n_{xb}$  and TRPN<sub>50</sub> parameters, inferred from *in vitro* rat F-pCa data. A LHD of 100,000 points in the ranges of experimental variability of the F-pCa curve (left panel) is projected into the corresponding plausible 2D sarcomere parameter space (right panel). The reference parameter set is represented by a black dot, while reference dashed black lines divide the plane in four parts to highlight the quadrant of OM action.

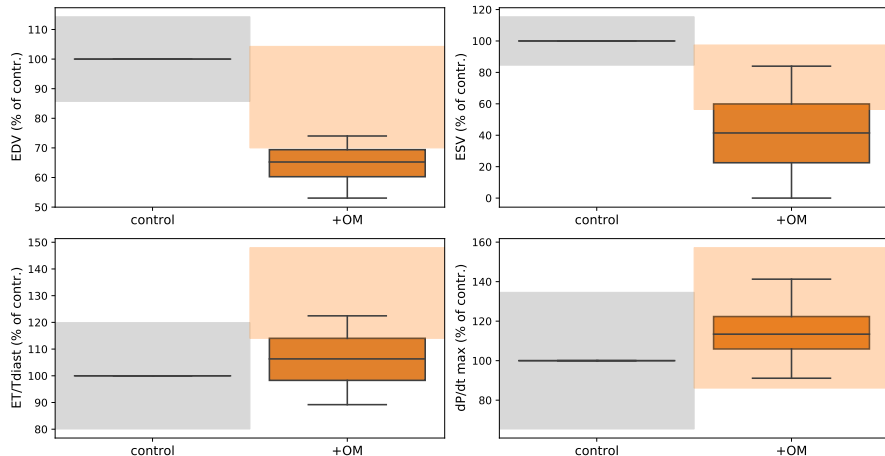


Figure 5.4: Predicted *in silico* OM effects on whole-heart function as percentage changes of LV features' values from control values. Experimental uncertainty ranges are displayed as shaded regions using percentage-from-control mean  $\pm$  standard deviation values for both the healthy (grey) and +OM (orange) cases.

Furthermore, differences across species and in acute vs chronic OM administration are not explored. For example, studies in healthy volunteers [228] suggest an increase in SV and EF following OM treatment as a result of the overall systolic function improvement. However, we only mapped LV features' values that were reported to significantly change from control after OM administration [16], and our results excluded cases when a change in SV and EF features was observed. Additional studies are needed to investigate species differences and chronic effects of OM.

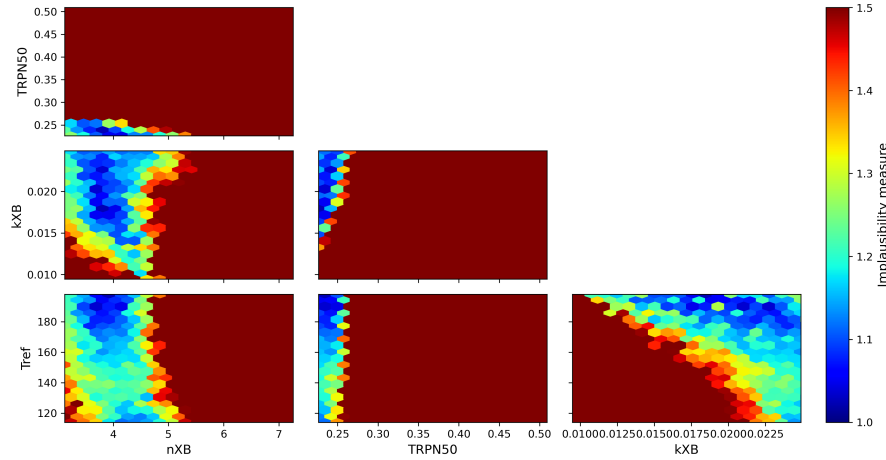


Figure 5.5: OM-compatible sarcomere space encoded by the  $k_{xb}$ ,  $n_{xb}$ ,  $TRPN_{50}$  and  $T_{ref}$  parameters, inferred from *in vivo* pig haemodynamic data. This space is obtained by running one iteration of HM which constrains the full parameter space according to an implausibility criterion that evaluates how plausible is a point to yield model predictions that are matching experimental observations.

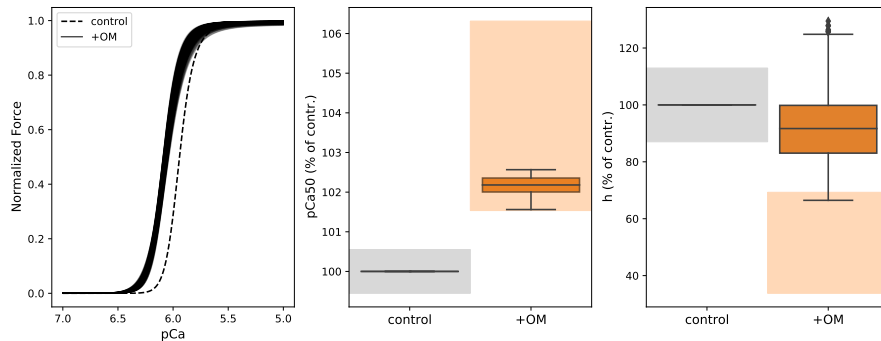


Figure 5.6: Predicted *in silico* OM effects on the sarcomere as described by F-pCa curves calculated from the constrained, OM-compatible sarcomere parameter space and by the related percentage changes of  $pCa_{50}$  and  $h$  values from control values. Experimental uncertainty ranges are displayed (the middle and far right panels) as shaded regions using percentage-from-control mean  $\pm$  standard deviation values for both the healthy (grey) and +OM (orange) cases.

We have shown that the median model predictions qualitatively match the observed changes due to OM at the tissue and whole-organ scale. However, the model does not quantitatively match experimental observations. Specifically, there are some non-implausible Hill coefficients in Figure 5.6 that are increased and do not qualitatively match the experimentally observed changes. Similarly, in some cases ET/Tdiast is predicted to decrease in Figure 5.4, in contrast to the experimental observations. There are four potential contributors to this discrepancy. First, the tissue and organ drug effects are taken

from different species. Second, the reference model parameters and anatomy are determined from a distinct set of experiments from the OM measurements. Third, the model is a simplification and may be missing some features. Fourth, the experiments are performed in skinned preparations, while the model replicates intact tissue. This likely explains the discrepancy in the predicted change in the Hill coefficient, which is sensitive to the skinning process. A self-consistent multi-scale data of the effects of OM on cell, tissue and organ scales would allow us to identify better and address the source of these discrepancies.

More general limitations of the adopted modelling framework can be found in Chapter 9, Section 9.2.

## 5.6 SUMMARY

We demonstrated how multi-scale heart contraction models can aid our understanding of the mechanistic links between cellular and whole-organ function and can help in interpreting skinned experimental preparations in the context of *in vivo* whole-heart function. We have also shown that the same models can be used to map pharmacological effects on the sarcomere through to whole heart function and back again.

## INTRODUCTION AND VALIDATION OF CALCIUM TRANSIENT VARIATIONS INTO THE WHOLE HEART MODEL

### OUTLINE

In this chapter, we investigate how  $\text{Ca}^{2+}$  transient variations can be mapped to the rat whole heart function. When using the full-forward model, it suffices to change the fixed  $\text{Ca}^{2+}$  transient curve (used as the sarcomere activation signal for the whole heart) with a different curve to test its impact on the LV function. When using the developed emulation framework instead, we propose to encode the shape of the  $\text{Ca}^{2+}$  transient curve using a set of scalar features of clinical interest (Section 6.2), allowing these to be quantitatively mapped to the LV features as an additional component to the emulator input parameter set. In the second part of this study, we validate the personalised SHAM rat heart contraction model against known pharmacological channel blocking experimental data (Section 6.3). This is done by plugging into the full-forward model  $\text{Ca}^{2+}$  transient curves resulting from different ionic models obtained by perturbing the reference ionic model under the action of pharmacological compounds at multiple doses. We then provide a discussion and address specific limitations (Section 6.4), and we conclude with a brief summary (Section 6.5).

### 6.1 MOTIVATION

$\text{Ca}^{2+}$  dynamics plays a key role in cardiac contraction and relaxation. We have seen that mapping sarcomere properties to the LV function quantitatively can predict the mechanisms that are behind pathological conditions of the heart (Chapter 4) and validate pharmacological compounds' mechanisms of action (Chapter 5). Building upon this concept, the possibility to quantitatively map also  $\text{Ca}^{2+}$  dynamics alterations to the whole heart behaviour is desirable. In Chapter 4, we derived a personalised model of the SHAM rat heart contraction using a fixed  $\text{Ca}^{2+}$  transient as a stimulus. In this chapter, we aim at incorporating  $\text{Ca}^{2+}$  transient variations in the full simulator map (equation 8.7) in order to understand how different, physiological and possibly more pathological variations in  $\text{Ca}^{2+}$  transient phenotypes can impact the LV function.

## 6.2 ENCODING $\text{Ca}^{2+}$ TRANSIENT VARIATIONS

We used a 4-feature parametric representation of the  $\text{Ca}^{2+}$  transient that maps to common experimentally measured features. The 4 features encode the shape of the  $\text{Ca}^{2+}$  transient and are summarised in Table 6.1.

$\text{Ca}^{2+}$ FEATURE	UNITS	DEFINITION
DCA	$\mu\text{M}$	diastolic $\text{Ca}^{2+}$ concentration
AMPL	$\mu\text{M}$	$\text{Ca}^{2+}$ concentration signal amplitude
TP	ms	time to peak $\text{Ca}^{2+}$ concentration
RT <sub>50</sub>	ms	time to half-maximal relaxation from peak $\text{Ca}^{2+}$ concentration

Table 6.1: Features encoding the calcium transient shape.

We wish to sample random sets of these features so that the final samples will uniformly cover the feature space to possibly cover both healthy and pathological  $\text{Ca}^{2+}$  transient phenotypes. For this purpose, we used linear weights to scale each of the four features from a representative  $\text{Ca}^{2+}$  transient. This parametric encoding of  $\text{Ca}^{2+}$  transient variation ensured that all transients maintained a characteristic  $\text{Ca}^{2+}$  transient morphology.

The specific implementation of this scaling strategy is presented in Algorithm 1. Note that the `features` function returns the set of four features given an input  $\text{Ca}^{2+}$  transient; the `concatenate` function returns a 1D array obtained by concatenating all the given input 1D arrays of different sizes; the `linear_interpolator` function returns a function whose call method uses 1D linear interpolation to find the value of new points.

Figure 6.1 shows how the algorithm works and how new random  $\text{Ca}^{2+}$  transients can be generated.

An essential property of this  $\text{Ca}^{2+}$  scaling strategy is that the features scale linearly with the scaling coefficient used, as shown in Figure 6.2. This allows us to randomly sample the scalar parameters that encode the  $\text{Ca}^{2+}$  transient from a space-filling design (e.g. an LHD) while generating samples that cover the full feature space. Having a training dataset with input parameters that uniformly cover the high-dimensional parameter space also helps GP emulators training while at the same time improving their predictions' accuracy.

The employed Gattoni et al. [69] ionic model simulates a  $\text{Ca}^{2+}$  transient for a fixed pacing rate (6 Hz) so that it occurs within a fixed time span. At physiological pacing rates, the rat  $\text{Ca}^{2+}$  transient never

---

**Algorithm 1:** Scaling a representative calcium transient ( $y := [\text{Ca}^{2+}]_i(t)$ ) using linear interpolation.

---

**Require:**  $t = (t_1, \dots, t_N)$ ,  $y = (y_1, \dots, y_N)$ , with  $t_i, y_i \geq 0 \forall i = 1, \dots, N$   
 $p = (p_1, \dots, p_4)$ , with  $p_i \geq 0 \forall i = 1, \dots, 4$

**Ensure:**

$y_{\text{new}} \mid (\text{features}(t, y_{\text{new}}))_i = p_i \cdot (\text{features}(t, y))_i \quad \forall i = 1, \dots, 4$   
where  $\text{features}(t, y) = (\text{DCA}, \text{AMPL}, \text{TP}, \text{RT50})$

```

DCA ← (features(t, y))_1
y_new ← p_1 · DCA + p_2 · (y - DCA)
i_max ← arg maxi=1,...,N y
T ← t_N
if p_3 · (t_{i_max} - t_1) + p_4 · (t_N - t_{i_max}) ≤ T then
    s ← (p_3 - p_4) · t_{i_max}
    t_tmp ← concatenate(p_3 · (t_1, ..., t_{i_max}), (p_4 · t_{i_max+1} +
    s, ..., p_4 · t_{N-1} + s), (t_N))
    f ← linear_interpolator(t_tmp, y_new)
    y_new ← f(t)
else
    print "Not a valid scaling! Returning original calcium curve."
    y_new ← y
end if
return y_new

```

---

reaches an equilibrium in diastole so that, during a  $\text{Ca}^{2+}$  transient, time is spent rising or relaxing. As the cell is paced at a fixed cycle length, the sum of time to peak and relaxation time is capped. This means that one cannot increase without the other decreasing, and independent perturbation of TP and RT50 can only decrease. In this framework, slowing of relaxation at a fixed cycle length means that the cell does not have enough time to relax, causing DCA to rise while AMPL decreases. From an algorithmic viewpoint, not all the randomly picked  $\text{Ca}^{2+}$  features' scaling coefficient sets will thus be viable. The "if" statement in Algorithm 1 controls this behaviour by discarding all those curves that decay outside the fixed time interval without fully repolarising. The existing coupling between TP and RT50  $\text{Ca}^{2+}$  features manifests as regions of the feature space that can not be captured by our  $\text{Ca}^{2+}$  transient scaling strategy. These are indicated by the blank triangles in the  $p_3$ -vs-RT50 and  $p_4$ -vs-TP subplots, visible in Figure 6.2.

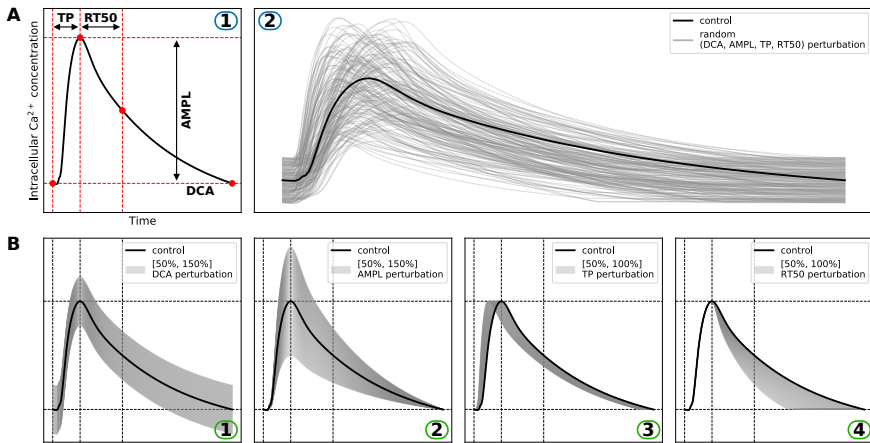


Figure 6.1: A 4-feature parametric representation of the calcium transient.  
(A.1) The calcium transient is described by four relevant quantities: diastolic concentration (DCA), amplitude (AMPL), time to peak concentration (TP) and time to half-relaxation from peak concentration (RT<sub>50</sub>). (B.1–4) Each of the 4 calcium features can be scaled independently to produce a new calcium transient. (A.2) All the features can be scaled at the same time to produce many different new calcium transients.

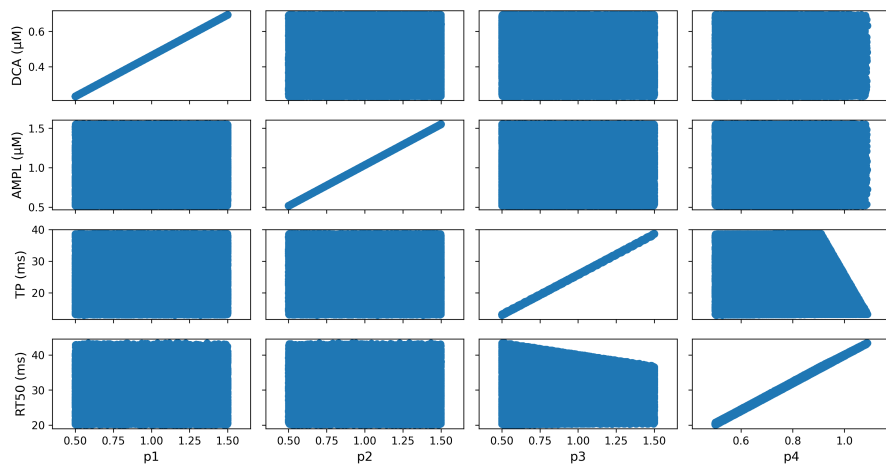


Figure 6.2: Calcium transient features linearly scale with their respective scaling coefficients. Example showing perturbations in the range [50 %, 150 %] from control values for all the calcium features but RT<sub>50</sub>, which undergoes perturbation in the range [50 %, 110 %].

### 6.3 VALIDATING THE PERSONALISED HEALTHY RAT HEART MODEL

To test if the rat heart contraction model can predict how changes in  $\text{Ca}^{2+}$  transients impact the whole heart function, we validated the computational framework by comparing qualitative and quantitative measurements and predictions of changes in cardiac mechanics in the presence of compounds that manipulate the  $\text{Ca}^{2+}$  transient. This provides a multi-scale test on the ability of the model to map from

changes in ion channels conductances to changes in  $\text{Ca}^{2+}$  transient and the resulting changes in whole heart function.

A schematic of the adopted validation workflow is provided in Figure 6.3.

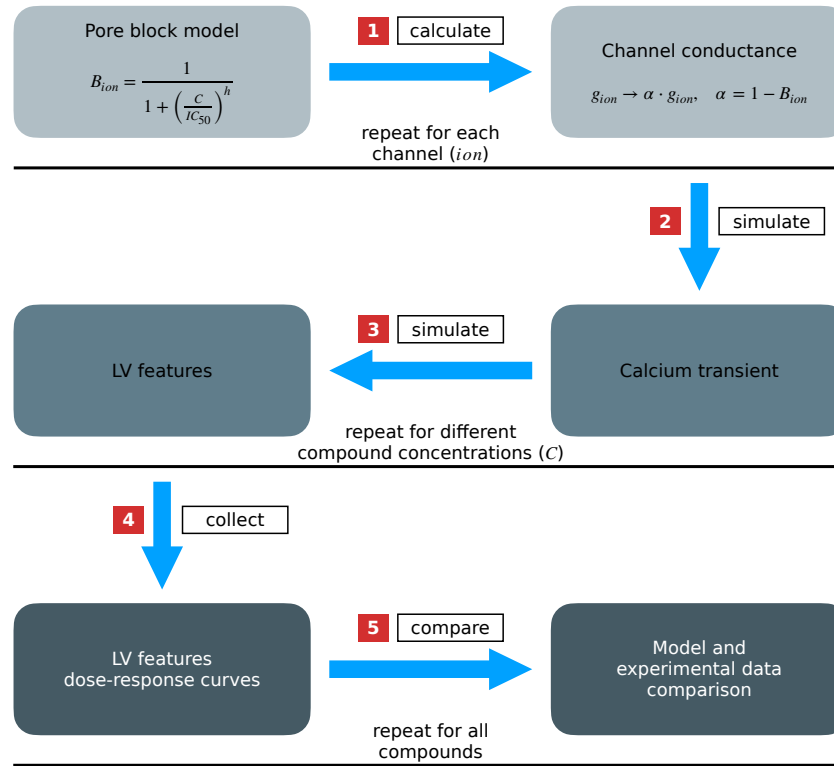


Figure 6.3: Model validation workflow. (1) The pore block model is used to calculate the fraction of blocked ion channel at a given compound concentration for each channel. The same channels' conductances are scaled to reflect this compound effect, and (2) the rat myocyte electrophysiological model is run to generate perturbed calcium transients for different compound concentrations. (3) The calcium transients are used as an input for the 3D biventricular rat heart contraction model, and as many LV features' perturbed values are obtained as the number of input curves, which corresponds to the number of tested compound concentrations. (4) LV feature' values are plotted against the tested compound concentrations to obtain dose-response curves. (5) The qualitative trend of the LV features after *in silico* compound "administration" is compared with literature experimentally measured same compound effects on the same LV features for all the compounds under study.

### 6.3.1 Comprehensive *in vitro Proarrhythmia Assay* compounds

We selected 8 compounds, which were well characterised for multiple ion channels and for which we could find whole organ measurements from literature, from the *comprehensive in vitro proarrhythmia assay* (CiPA) [177] official list, namely bepridil, chlorpromazine, diltiazem, mexiletine, nifedipine, ranolazine, sotalol and verapamil, and we described their action at the cellular level using a 4-channel description, namely  $I_{Na}$ ,  $I_{to}$ ,  $I_{K1}$  and  $I_{CaL}$ .  $I_{Kr}$  channel was not included as the related current has a small amplitude in rat cardiomyocytes [247], and so was not included in the employed rat cell ionic model [69].

The affinity of each compound for each ion channel was taken from CiPA project datasets [38, 131], summarised in Table 6.2.

The affinity of each compound for each ion channel is described by the Hill coefficient  $h$  and the half-maximal inhibitory concentration  $IC_{50}$  values of a Hill-type relationship which gives the fraction of blocked current  $B$  as a function of the compound concentration  $C$ , also known as the *pore block model*:

$$B = \frac{1}{1 + \left(\frac{C}{IC_{50}}\right)^h} \quad (6.1)$$

### 6.3.2 Compounds' effects on $Ca^{2+}$ transient

For each compound, we calculated  $B$  for each channel when  $C$  was set to equally-spaced values in a log-molar space. By subtracting the obtained  $B$  values from 1, we obtained a matrix of scaling coefficients for the channels' conductances, representing the fractions of active channels in the presence of the compounds at different concentrations. We tested 13 equally-spaced values (in  $-\log M$  units) in the range [4, 10] (extremes included), which corresponded to compounds' concentrations between  $10^{-10} M$  and  $10^{-4} M$ . We then run the Gattoni et al. [69] model by scaling the ion channels' conductances to simulate the action of different concentrations of each compound at the cellular level and collected the resulting  $Ca^{2+}$  transients (last beat curves of limit cycle, 5000 beats simulations). An example of  $Ca^{2+}$  transients obtained after simulating the effect of verapamil is provided in Figure 6.4.

As the  $Ca^{2+}$  transients obtained in the presence of the compound at different concentrations can be encoded by DCA, AMPL, TP and RT50 features (Section 6.2), we can visualise how these features are varying in a dose-dependent manner. The  $Ca^{2+}$  transient features' dose-response curves are shown in Figure 6.5 for verapamil.

We can notice that for the TP and RT50 features, the response is not following a fully logistic trend on the right branches. This is because,

COMPOUND	ION CHANNEL			
	$I_{Na}$	$I_{To}$	$I_{K1}$	$I_{CaL}$
<b>BEPRIDIL</b>				
$IC_{50}$ (nM)	$2.93 \cdot 10^3$	$8.59 \cdot 10^3$	-	$2.81 \cdot 10^3$
h	1.16	3.54	-	0.65
<b>CHLORPROMAZINE</b>				
$IC_{50}$ (nM)	$4.54 \cdot 10^3$	$1.76 \cdot 10^7$	$9.27 \cdot 10^3$	$8.19 \cdot 10^3$
h	2.00	0.37	0.69	0.84
<b>DILTIAZEM</b>				
$IC_{50}$ (nM)	$1.11 \cdot 10^5$	$2.82 \cdot 10^9$	-	$1.12 \cdot 10^2$
h	0.70	0.17	-	0.71
<b>MEXILETINE</b>				
$IC_{50}$ (nM)	-	-	-	$3.82 \cdot 10^4$
h	-	-	-	1.03
<b>NIFEDIPINE</b>				
$IC_{50}$ (nM)	$2.84 \cdot 10^4$	-	-	$1.15 \cdot 10^1$
h	1.11	-	-	0.67
<b>RANOLAZINE</b>				
$IC_{50}$ (nM)	$6.88 \cdot 10^4$	-	-	-
h	1.42	-	-	-
<b>SOTALOL</b>				
$IC_{50}$ (nM)	$1.14 \cdot 10^9$	$4.31 \cdot 10^7$	$3.05 \cdot 10^6$	$7.06 \cdot 10^6$
h	0.51	0.66	1.20	0.87
<b>VERAPAMIL</b>				
$IC_{50}$ (nM)	-	$1.34 \cdot 10^4$	$3.49 \cdot 10^8$	$2.02 \cdot 10^2$
h	-	0.82	0.27	1.10

Table 6.2:  $IC_{50}$  and Hill coefficient values describing the affinity of eight CiPA compounds with the  $I_{Na}$ ,  $I_{To}$ ,  $I_{K1}$  and  $I_{CaL}$  ion channels. The dash symbol indicates that the specific compound has no inhibitory effect on the respective ion channel. Values taken from [38, 131].

for high compound concentrations, we have seen (Figure 6.4) that the  $\text{Ca}^{2+}$  signal had almost vanished, making the analysis of these curves challenging.

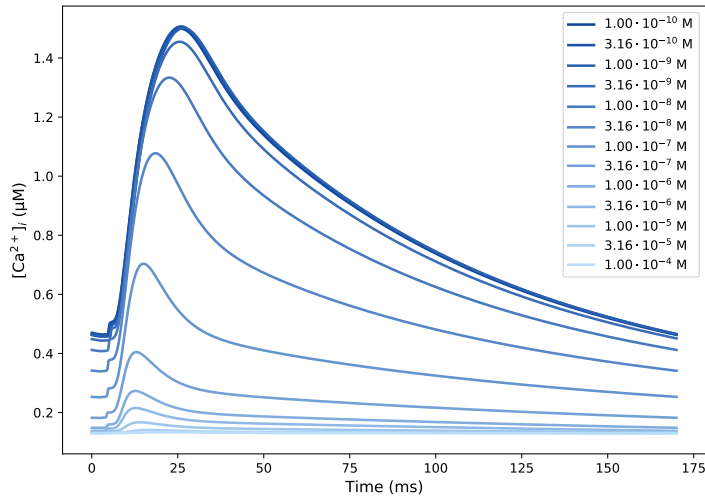


Figure 6.4: The effect of verapamil on the intracellular calcium transient. The Gattoni et al. [69] model is run using different ion channels' conductances' scaling coefficients to simulate the effect of different concentrations (blue colour variants) of the example compound considered.

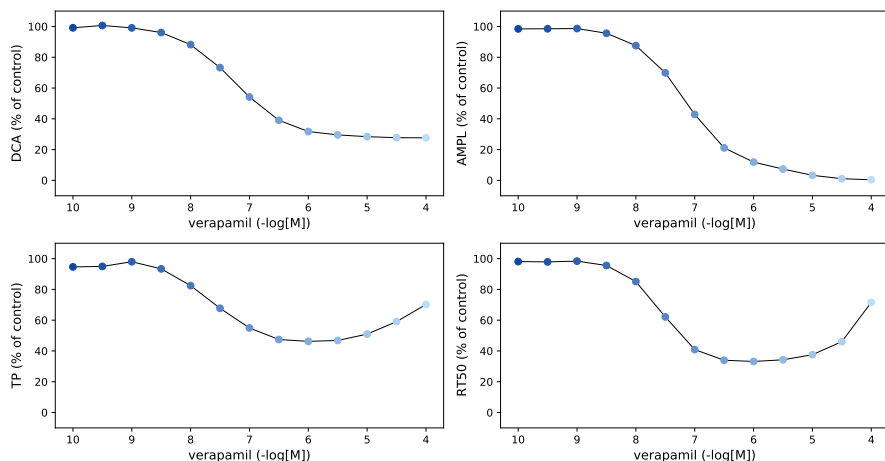


Figure 6.5: Calcium transient features' dose-response curves. Calcium transient features are extracted from perturbed calcium transients and plotted against the respective simulated compound concentrations.

### 6.3.3 Compounds' effects on whole-organ function

We finally used the personalised healthy (SHAM) rat model (Section 4.4.4) to simulate the LV features' values using as an input the obtained  $Ca^{2+}$  transients and the remaining parameters fixed to the reference values (Table 4.10). This allowed us to obtain the LV features' change from baseline values in a dose-dependent manner. PeakP, maxdP and mindP features' simulated responses to different doses of all the tested compounds are reported in Figure 6.6. We additionally

extracted the same features' values from the RV limit cycle solution to see if the compound-induced variations were consistent with what observed for the LV. These are provided in the same figure. Moreover, the simulated LV features' percentage changes were compared with quantitative experimental measurements [5, 108, 109, 122, 206, 241] of compounds' effects when these were available from literature (Section 6.3.4, Table 6.3). In particular, in the same figure we report experimental observations for bepridil and verapamil – PeakP [5], chlorpromazine – PeakP [122], diltiazem – PeakP and maxdP [109], nifedipine – PeakP [206], ranolazine – PeakP, maxdP and mindP [241], and verapamil – maxdP [108].

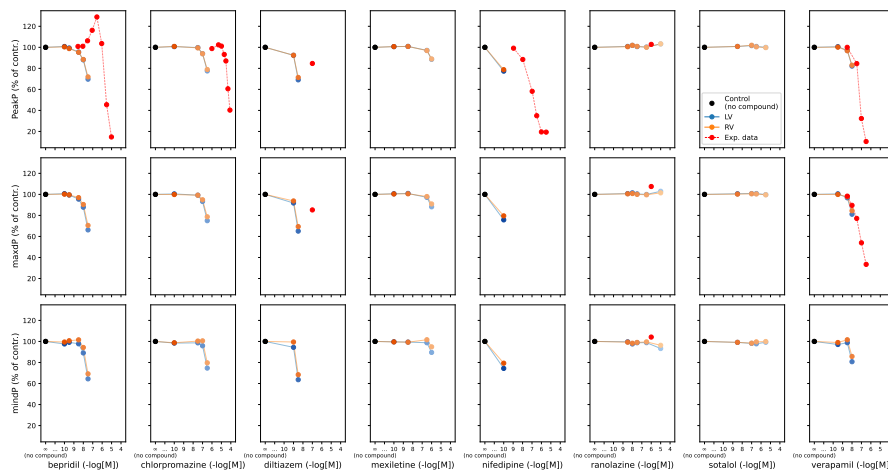


Figure 6.6: LV and RV pressure features' dose-response curves for the eight CiPA compounds. Simulated PeakP, maxdP and mindP features' values are given as percentages of the respective control values and are represented as dots in blue and orange variants, colour-coded with the compound doses for the left and right ventricles, respectively. Black dots indicate the control values when no compound is present. Experimental data of compounds' effects on the LV (when available) is also displayed as red dots.

The *in silico* obtained compounds' effects on the considered pressure features were consistent in both the LV and RV and showed either a decreasing or unchanged trend from baseline values with increasing compounds' concentrations. Experimental data (highlighted in red in Figure 6.6) confirmed the trend simulated by the simulator, although with a non-negligible mismatch in the absolute values (see Section 6.4 for discussion) for bepridil, chlorpromazine, diltiazem and nifedipine compounds (more pronounced) and ranolazine and verapamil compounds (mild).

### 6.3.4 Simulated compounds' effects on LV function comparison with experimental observations

The LV pressure features' qualitative responses after *in silico* compound "administration" were compared to qualitative changes in the same LV features observed after compounds administration in literature experimental studies performed on either conscious or Langendorff-perfused or working healthy rat heart preparations. These experimental changes were either recorded after a single dose in the pre-ischaemic phase of an ischaemia-reperfusion experiment or in a dose-dependent manner and are summarised in Table 6.3. The qualitative LV features' response to compounds observed experimentally was given by either the trend of percentage change from reference values (data displayed in red in Figure 6.6) or by a reported significant change with compound administration.

COMPOUND	LV FEATURE			REFERENCES
	PeakP	maxdP	mindP	
bepridil	↓	—	—	[5, 86, 124]
chlorpromazine	↓	—	—	[100, 122, 199]
diltiazem	↓	↓	↓	[58, 65, 109]
mexiletine	↔	↓	—	[80, 97, 154]
nifedipine	↓	↓	↓	[58, 166, 206]
ranolazine	↔	↔	↔	[87, 239, 241]
sotalol	↓	↓	↔	[82, 116, 148]
verapamil	↓	↓	↓	[108, 216, 222]

Table 6.3: Qualitative change in three LV pressure features observed in literature rat experiments for eight different CiPA compounds. Down-facing arrow means that the specific LV feature decreases from its control value with the specific compound; left-right arrow means that the compound has no effect on that feature; dash symbol means that the specific information could not be retrieved from literature.

The comparison of qualitative model predictions to experimental observations is shown in Figure 6.7. The model correctly predicted 16 out of 19 (84 %) experimental observations, with 5 observations missing data, matching 6 out of 8 compounds. Model predictions were never opposite to observations, with either the model or observations reporting no-change when the model failed.

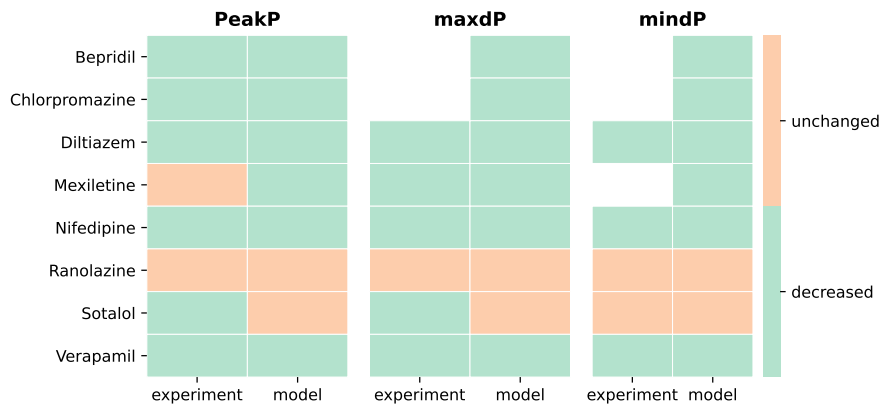


Figure 6.7: Model validation against known CiPA compounds effects on whole-organ function. Eight CiPA compounds effects (“experiment” columns) on PeakP, maxdP and mindP are compared with model same compounds’ predicted effects on the same features (“model” columns). Compounds’ effects are colour-coded as orange (feature unchanged) and green (feature decreased). None of the compounds caused an increase in the considered LV features. White/empty space means that the specific effect could not be retrieved from the examined literature studies. The model predicted effects are in agreement with the experimentally observed effects for 6 out of 8 compounds.

## 6.4 DISCUSSION

We have encoded the shape of the  $\text{Ca}^{2+}$  transient using 4 clinically relevant features. This will prove crucial for assessing the impact of different, more pathological  $\text{Ca}^{2+}$  transient morphologies on the LV function. By following this approach, we will be able to employ emulators that can map these  $\text{Ca}^{2+}$  features to characterise their relative impact on the whole heart function via GPE-based GSA, as we shall see in the next chapter, Section 7.4.1.

The used approach for model validation simulates the compound-induced changes in the  $\text{Ca}^{2+}$  transient starting from single ion channels’ perturbations. This allows overcoming the issue when no directly recorded  $\text{Ca}^{2+}$  transients under the action of compounds are available. In so doing, we created a fully simulated map from compound properties to whole organ function.

### 6.4.1 Limitations

Most of the compounds we tested were  $\text{Ca}^{2+}$  channel blockers, which are known to reduce the heart rate. However, secondary effects such as a reflex increase in beta-adrenergic tone in response to systemic vascular dilation can neutralise this negative chronotropic effect. For this reason, the level of reflex beta-adrenergic discharge could balance

out the net effect on heart rate [144]. Nevertheless, our model does not account for heart rate variations, so the validation was performed by evaluating the effects of compounds at a fixed, physiological rate. The negative chronotropic effect, coupled with the impact  $\text{Ca}^{2+}$  channel blockers have on muscle sympathetic nerve activity [22], can also partially explain the mismatch observed (Figure 6.6) when quantitatively comparing compounds' effects onto LV pressure features with the model simulations. Another source of mismatch can be linked to the fixed LV volume setup typically used in the considered experimental studies to evaluate the compounds' effects, which differ from our rat heart model.

More general limitations of the adopted modelling framework can be found in Chapter 9, Section 9.2.

## 6.5 SUMMARY

Having a validated, personalised model of rat heart contraction is powerful as it can be trusted when this is used to predict compounds' mechanisms of action or for identifying *in silico* pharmacological cellular targets, as we shall see in the next chapter.

## IN SILICO IDENTIFICATION OF POTENTIAL CALCIUM DYNAMICS AND SARCOMERE TARGETS FOR RECOVERING LEFT VENTRICULAR FUNCTION IN RAT HEART FAILURE WITH PRESERVED EJECTION FRACTION

### OUTLINE

In this chapter, we build an emulator that can map both calcium dynamics, sarcomere, tissue and haemodynamics properties to the LV function, using the personalised SHAM rat heart contraction model as the simulator (Section 7.3.3). We first characterise the model outputs' global sensitivities to model inputs (Section 7.4.1). We then start from the healthy reference rat model and we create a model of the 20-week-old obese ZSF1 rat, a well-established animal model of HFpEF, by manipulating specific model input parameter based on available ZSF1 rat literature data (Section 7.3.4). We then use different sub-groups of input parameters as targets of a re-fitting, history matching procedure, with the aim of recovering the ZSF1 rat model back to the healthy state (Section 7.3.5). The selected groups of parameters mimic the action of possible calcium-, thin filament-, thick filament-, whole sarcomere-targeting compounds. We show that using the implemented framework it is possible to *in silico* efficiently identify possible pharmacological interventions on the sarcomere to treat HFpEF in rats (Section 7.4.4). We then provide a discussion and address specific limitations (Section 7.5), and we conclude with a brief summary (Section 7.6).

### 7.1 MOTIVATION

HFpEF disease currently constitutes an unmet clinical need [3]. Animal models can be a valuable research tools to investigate HFpEF, as co-morbidities and other confounding factors can be more precisely controlled than in the clinical setting. However, there are no perfect animal models for HFpEF, and this is partly because it is difficult to fulfil all the features observed in human disease at the same time in animals. The currently available animal models of HFpEF have attempted to reproduce the dominant factors typically documented to cause diastolic dysfunction and HFpEF. They fall across the following macro-categories: aortic banding and systemic hypertension, diabetes mellitus and obesity, cardiometabolic syndrome and ageing. All of these animal models have been successfully established in rodents [46].

For instance, the 20-week-old obese ZSF1 rat presents many features of a cardiometabolic syndrome such as hypertension, obesity, type 2 diabetes mellitus, insulin resistance and HF, developing a diastolic dysfunction in parallel with LV hypertrophy and LA dilation. As this animal model also presents exercise intolerance, an important feature diagnosed in humans, it currently constitutes a well-established [46] animal model of HFpEF. From now on, we will refer to the “20-week-old obese ZSF1 rat” as the “ZSF1 rat” for brevity. However, regardless of the animal model used in the process of drug discovery and development at preclinical stages, identifying pharmacological interventions that recover physiological function in the HFpEF diseased animal remains a challenge.

In this case study, which incorporates our previous publication [137], we aim to predict changes in myocyte function that recovers whole heart function. First, we develop a multi-scale mathematical model that maps ion channel and sarcomere function through to whole organ pump function in an HFpEF rat heart. Specifically, we build an *in silico* representation of the ZSF1 rat HFpEF animal model. This model can then be used to identify the cellular function that can be manipulated to recover whole heart function. We next use this animal model to propose potential pharmacological targets by simulating and testing their different mechanisms of action.

## 7.2 RAT DATA

In order to create a mathematical model of the ZSF1 rat, we first needed to characterise its LV systolic and diastolic functions. For this purpose, we performed a literature search on PubMed (date 09/03/2021) with the query: “(rat) AND (ZSF1) AND (haemodynamic)”. The search gave 32 results, and we analysed them all. Of these, 19 contained information about LV haemodynamic measurements. All the 19 studies [1, 30–32, 51, 53, 74, 83, 113, 125–127, 162, 178, 200, 209, 223, 234, 240] had been conducted on male rats at the age of 20 weeks, and diastolic dysfunction was confirmed by echocardiographic measurements (decreased E/A, increased E/E', increased LA area). We identified common phenotypes in these obese ZSF1 rats' haemodynamics compared to their respective control (lean ZSF1 rat) as described by 4 LV features, namely EF (no change), PeakP (increased), maxdP (increased), Tau (increased). To regularise observed changes in ZSF1 rats from multiple labs, we considered the average percentage changes between ZSF1 rats and local control animals. These are summarised in Table 7.1.

LV FEATURE	EXP. VARIABILITY (%)	REFERENCE
EF	$103.95 \pm 7.62$	[30, 51, 74, 125–127, 200, 209, 223]
PeakP*	$119.26 \pm 6.07$	[126, 127]
maxdP*	$125.46 \pm 5.26$	[30, 74, 125, 126, 209]
Tau*	$141.97 \pm 13.67$	[30, 51, 74, 126, 127, 200, 223]

Table 7.1: Experimental ZSF1 obese rat haemodynamic data. For each LV feature of interest, mean and standard deviation values are given as percentages of the related control mean values. Asterisked (·)\* features' changes were reported to be statistically significant.

## 7.3 METHODS

### 7.3.1 Rat heart contraction model

We modelled the healthy rat heart using the personalised SHAM rat heart contraction model derived in Section 4.4.4. This rat model will be referred to as “SHAM” throughout the next sections. Again, this model (or simulator) can be seen as a multi-scale map from input parameters to output features.

We augmented the list of parameters used previously (Sections 4.3.1–5.3.1) in order to have a more comprehensive description of both the calcium and sarcomere dynamics, tissue and haemodynamic boundary conditions' properties by considering a total of 16 parameters. Specifically, 4 parameters encoded the shape of the  $\text{Ca}^{2+}$  transient (Section 6.2), 8 parameters described the sarcomere dynamics (4 parameters were thin filament-related and 4 were thick filament-related), and 4 parameters described tissue and boundary conditions' properties. The full list of parameters considered is reported in Table 7.2.

As for the simulator output, we characterised the LV function using the same 12 scalar features used in the previous analysis (Table 3.2) with the addition of other 2 features (Table 7.3), for a total of 14 features.

The obtained simulator map had thus the following form:

$$\begin{aligned} f_{\text{simul}}: \mathbb{R}^{16} &\rightarrow \underbrace{\mathbb{R} \times \cdots \times \mathbb{R}}_{14 \text{ times}} \\ x &\mapsto (y_1, \dots, y_{14}) \end{aligned} \tag{7.1}$$

When running the simulator at a new parameter point, as we were using the personalised SHAM rat model, all the other parameters were kept fixed to its reference parameter values (Table 4.10) when

PARAMETER	UNITS	DEFINITION
DCA	$\mu\text{M}$	diastolic $\text{Ca}^{2+}$ concentration
AMPL	$\mu\text{M}$	$\text{Ca}^{2+}$ concentration signal amplitude
TP	ms	time to peak $\text{Ca}^{2+}$ concentration
RT <sub>50</sub>	ms	time to half-maximal relaxation from peak $\text{Ca}^{2+}$ concentration
Ca <sub>50</sub>	$\mu\text{M}$	reference $\text{Ca}^{2+}$ thin filament sensitivity
$\beta_1$	—	phenomenological tension length-dependence scaling factor
k <sub>off</sub>	$\text{ms}^{-1}$	unbinding rate of $\text{Ca}^{2+}$ from TnC
n <sub>trpn</sub>	—	$\text{Ca}^{2+}$ -TnC binding degree of cooperativity
k <sub>xb</sub>	$\text{ms}^{-1}$	cross-bridges cycling rate
n <sub>xb</sub>	—	cross-bridge formation degree of cooperativity
TRPN <sub>50</sub>	—	fraction of $\text{Ca}^{2+}$ -TnC bounds for half-maximal cross-bridges activation
T <sub>ref</sub>	kPa	maximal reference tension
p	kPa	end-diastolic pressure
p <sub>ao</sub>	kPa	aortic systolic pressure
Z	$\text{mmHg s mL}^{-1}$	aortic characteristic impedance
C <sub>1</sub>	kPa	tissue stiffness

Table 7.2: Model parameters and their definitions.

LV FEATURE	UNITS	DEFINITION
SV	$\mu\text{L}$	stroke volume
Tau	ms	isovolumetric pressure relaxation time constant

Table 7.3: Indexes of LV systolic and diastolic functions.

applicable, or to the Land et al. [119] model baseline values when otherwise.

To reduce computational costs, we will again train low-cost emulators to be a surrogate for the full model. This will allow mapping input parameters to output LV features both in a deterministic (using the

simulator) and in a probabilistic (using the emulator) way, as shown in Figure 7.1.

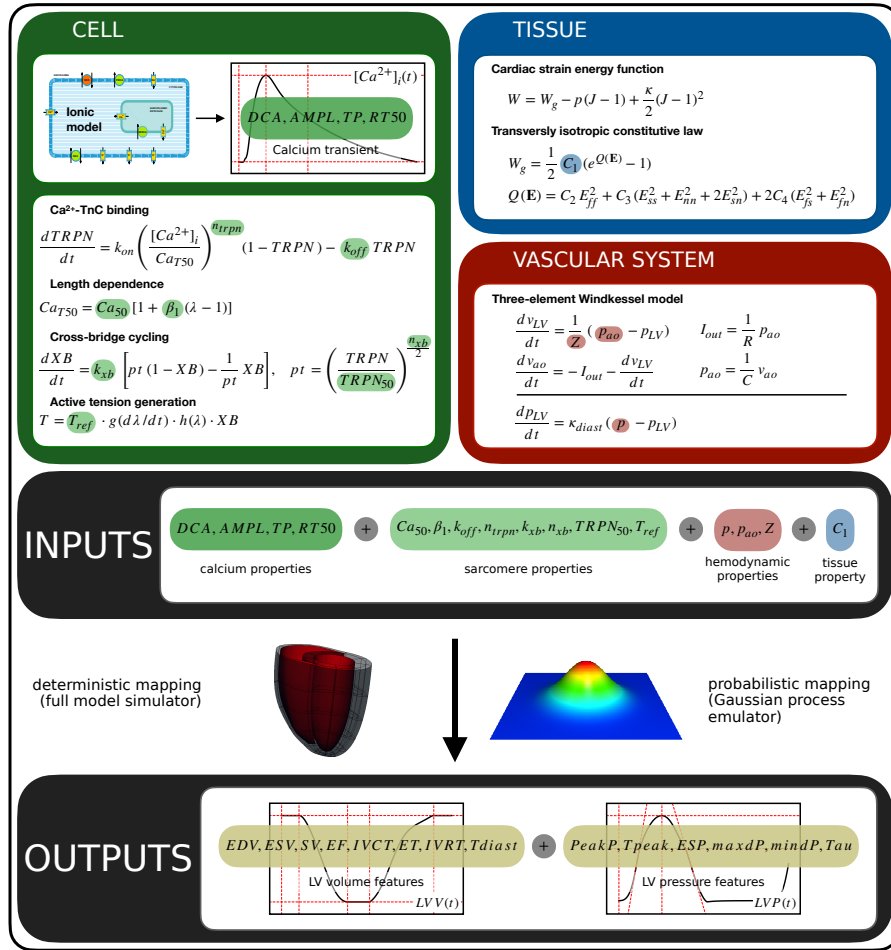


Figure 7.1: 3D biventricular rat heart contraction model multi-scale map. Chosen 16 input parameters are calcium transient and sarcomere properties (green), haemodynamics properties (red) and tissue properties (blue). The output features of interest are 14 indexes (yellow) characterising the LV function and are extracted from the LV pressure and volume curves. The input parameters (Table 7.2) can be quantitatively be mapped to the output features (Tables 3.2–7.3) either by running the full model or by making predictions using trained GPEs.

### 7.3.2 Input parameter space

The input parameter space  $X \subset \mathbb{R}^{16}$  of the simulator map  $f_{\text{simul}}$ , introduced in equation (7.1), was defined as the hypercube obtained by the Cartesian product of 16 one-dimensional parameter ranges. Each parameter interval was constructed with lower and upper bounds given as percentages of the SHAM rat heart model reference parame-

ter values (Table 4.10), based on a literature search and preliminary sensitivity analysis studies.

Specifically, for the  $\text{Ca}^{2+}$  transient parameters/features (AMPL, DCA, TP and RT<sub>50</sub>), we performed a literature search to understand how these values could change when going from diseased to control animal in rat HF. We collected experimental observations from 30 experimental studies [2, 6, 20, 24, 25, 35, 39, 41, 52, 56, 69, 83, 85, 91, 95, 96, 101, 104, 105, 134, 135, 145–147, 149, 156, 158, 159, 193, 197] on both HFrEF and HFpEF animal models, including AB (aortic-banded rat), TAC (transverse aortic constricted rat), CHF (rat with chronic heart failure), MI (rat with myocardial infarction), ZSF1 (Zucker diabetic fatty rat) DSS (Dhal salt-sensitive rat). To normalise observations across studies with different animal models and different pacing frequencies used for  $\text{Ca}^{2+}$  transients' recording (0.5, 0.333, 1, 3, 4, 6, 7 Hz), we averaged mean percentage variations from control to diseased animals for each of the four  $\text{Ca}^{2+}$  transient parameters. Minimum and maximum percentage variations observed experimentally are reported as ranges in Table 7.4.

PARAMETER	EXP. VARIABILITY (%)	REFERENCE
DCA	[38.00, 200.0]	[2, 6, 20, 24, 25, 35, 39, 41, 52, 56, 69, 83, 85, 91, 95, 96, 101, 104, 105, 134, 135, 145–147, 149, 156, 158, 159, 193, 197]
AMPL	[30.41, 203.23]	same as above
TP	[100.00, 151.26]	same as above
RT <sub>50</sub>	[59.56, 176.27]	same as above

Table 7.4: Calcium transient parameters' experimental variability in heart failure rat models.

The adopted range for the  $\text{Ca}^{2+}$  transient parameters was [10 %, 200 %] of the respective control values, which achieved a full coverage of the experimentally observed variability (Table 7.4) while being nearly symmetric around the baseline value (100 %). The range for RT<sub>50</sub> parameter was further adjusted to [10 %, 110 %] in order to limit the generation of implausible  $\text{Ca}^{2+}$  transients (where the sum of the time to peak and the relaxation time exceed the cycle length) when randomly scaling the reference  $\text{Ca}^{2+}$  transient (Algorithm 1, Section 6.2). Although the upper bound of this range seems not to cover the experimental observations fully, it is important to note that most heart failure studies are performed at non-physiological pacing rates (0.3–1 Hz), which allow much longer relaxation times that will not be seen at physiological (6 Hz) pacing rates. We summarise the experimental

variability of the  $\text{Ca}^{2+}$  transient parameters and the adopted *in silico* variability in Figure 7.2.

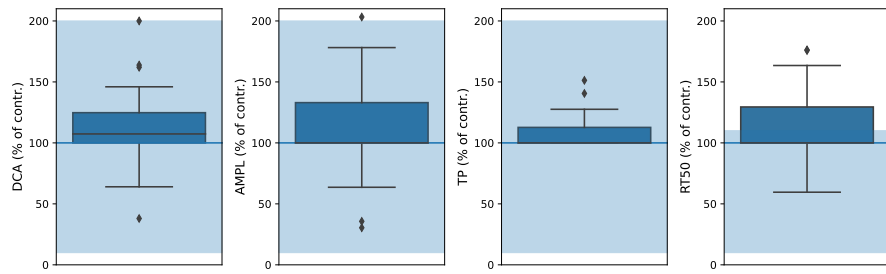


Figure 7.2: Calcium transient parameters' experimental percentage variations' distributions in heart failure rat models (blue boxes). The chosen *in silico* variability for the same parameters is also shown as blue shaded areas.

For the rest of the mechanics-regulating parameters ( $\text{Ca}_{50}$ ,  $\beta_1$ ,  $k_{\text{off}}$ ,  $n_{\text{trpn}}$ ,  $k_{\text{xb}}$ ,  $n_{\text{xb}}$ ,  $\text{TRPN}_{50}$ ,  $T_{\text{ref}}$ ,  $p$ ,  $p_{\text{ao}}$ ,  $Z$ ,  $C_1$ ) the adopted range was [50 %, 150 %] of the respective control values. This ensured that parameter values were consistent with the variability observed in both literature modelling and experimental studies on both healthy and diastolic heart failure rat models (Tables 4.3–4.4), while being symmetric around the baseline value (100 %). Additional information from local sensitivity analysis studies was used to adjust the  $\beta_1$  parameter range to be almost twice as big ([10 %, 200 %] of reference value), as LV features had a limited sensitivity to  $\beta_1$  in the narrower range. The adopted ranges for the full set of simulator/emulator 16 input parameters are reported in Table 7.5.

### 7.3.3 Training dataset, emulators, global sensitivity analysis

We sampled 14,848 points from a LHD over the input parameter space  $X$  defined in Section 7.3.2. The simulator was run at these points, and the successfully completed simulations were collected to form the training dataset (1,299 points). As the percentage of viable points out of the totally simulated points was low (~ 8.7 %), we visually and quantitatively inspected the training dataset input parameter space to search for regions that could have been not well represented after training the emulators.

Figure 7.3 shows that indeed there are regions of the input parameter space which are not covered by the training dataset due to simulator failures at points from these regions. In particular, AMPL,  $n_{\text{xb}}$  and  $\text{TRPN}_{50}$  parameters could not take values below 0.2, 2.8 and 0.195, respectively (simulated values were > 0.1, > 2.5 and > 0.175, respectively). This is consistently observed no matter the value of the other parameter points' components, concluding that there are

PARAMETER	UNITS	RANGE
DCA	$\mu\text{m}$	[0.0463, 0.9264]
AMPL	$\mu\text{m}$	[0.1034, 2.0681]
TP	$\text{ms}$	[2.5947, 51.8947]
RT <sub>50</sub>	$\text{ms}$	[4.0081, 44.0888]
Ca <sub>50</sub>	$\mu\text{M}$	[1.0861, 3.2584]
$\beta_1$	—	[-3.00, -0.15]
k <sub>off</sub>	$\text{ms}^{-1}$	[0.0257, 0.0772]
n <sub>trpn</sub>	—	[1.0, 3.0]
k <sub>xb</sub>	$\text{ms}^{-1}$	[0.0086, 0.0258]
n <sub>xb</sub>	—	[2.5, 7.5]
TRPN <sub>50</sub>	—	[0.1750, 0.5250]
T <sub>ref</sub>	$\text{kPa}$	[78.03, 234.10]
p	$\text{kPa}$	[0.1561, 0.4683]
p <sub>ao</sub>	$\text{kPa}$	[3.5568, 10.6704]
Z	$\text{mmHg s mL}^{-1}$	[2.8117, 8.4351]
C <sub>1</sub>	$\text{kPa}$	[0.4571, 1.3712]

Table 7.5: Parameters' ranges used for describing the healthy rat model 16D input parameter space.

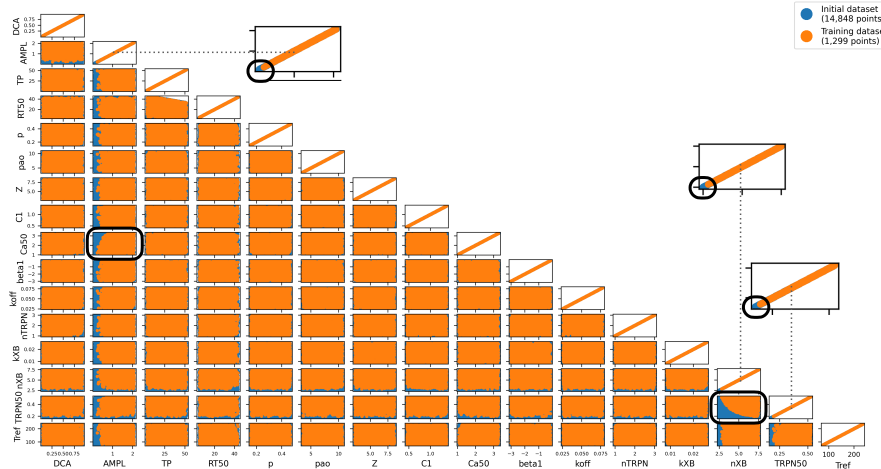


Figure 7.3: Training dataset visual exploration. The GPEs' training dataset 16D input parameter space is plotted as a 2D projection for each pair of parameters (orange dots). The initial space (blue dots) simulated for building the training dataset is plotted in the same manner to highlight regions which are not covered by the training dataset.

1-dimensional portions of the space which were not covered by the training dataset. 2-dimensional portions of the space which were not

covered are also present. These involve AMPL-vs-Ca<sub>50</sub> and n<sub>xb</sub>-vs-TRPN<sub>50</sub> parameters' interactions. Specifically, low AMPL values could not co-exist with high Ca<sub>50</sub> values. This is because high thin filament Ca<sup>2+</sup> sensitivities rapidly activate the myofilament, but the small amount of available intracellular Ca<sup>2+</sup> during systole is not enough to sustain contraction. Also, low n<sub>xb</sub> values could not co-exist with low TRPN<sub>50</sub> values. This is because they decrease the cross-bridges steady-state degree of cooperativity and sensitivity to bound Ca<sup>2+</sup>-TnC complexes, making it hard for cross-bridges to form and generate enough tension for the heart to contract.

In order to provide an estimate of the percentage area out of the total initial space area which was covered by the training dataset, we calculated for each parameter the percentage of the final covered portion of its initial 1D interval. We then multiplied all the percentage values obtained across the complete set of input parameters, resulting in parameters covering > 80 % of the whole parameter space.

Univariate GPEs, defined as in Section 3.4, were used to predict each of the 16 LV output features, and the GPE model hyperparameters were jointly optimised during training by maximisation of the model log marginal likelihood (equation (3.41)). For each of the 16 trained GPEs, we used the R<sup>2</sup>-score to check the regression accuracy and the ISE<sub>2</sub> to assess the adequacy of being used as a surrogate model (Section 3.4.1). The GPE implementation and training were performed using GPERks [142].

To study the input parameters' impact on the output LV features' total variance, we performed a GSA using the trained GPEs. Model outputs' sensitivity to model inputs was characterised by Sobol' first-order and total effects. These were estimated using SALib [78]. GPERks [142] was used to incorporate GPEs' full posterior distribution samples to account for emulators' uncertainty in Sobol' indices estimates, by following the second emulation-based approach of equations (3.90)–(3.91), presented in Section 3.6.2. Parameters whose Sobol' indices' distributions' expectation was below the threshold 0.01 were determined to have negligible effects.

#### 7.3.4 Building a model of the 20-week-old obese ZSF1 rat

To create a model of the ZSF1 rat, we re-fitted SHAM model parameters using HM technique (Section 3.5), using the maximum implausibility measure (equation (3.52)) across multiple target features, with the model discrepancy term (and its corresponding variance) set to zero in equation (3.51). HM was run using Historia tool [140].

We first applied the experimental percentage variability observed in the ZSF1 rat studies when going from control to diseased rats (Table 7.1) to the SHAM rat model corresponding features' baseline

values (Table 4.11). We then tried to match the resulting experimental variability during HM. As EF did not change significantly in any experiment, we matched for this feature an experimental variability of  $100\% \pm 0\%$  (i.e. no change).

To understand which of the 16 model parameters (Table 7.2) could undergo re-fitting, we collected evidence for changing each of them from literature studies. In ZSF1 rats, the intracellular  $\text{Ca}^{2+}$  transient was shown to have increased diastolic concentrations and decreased/unaltered amplitudes at multiple frequencies (1-4 Hz-paced cells) [2, 159], so we fitted DCA and AMPL parameters. As the observed changes in time to peak  $\text{Ca}^{2+}$  and time to  $\text{Ca}^{2+}$  half-relaxation could not be extrapolated at physiological pacing rates, TP and RT<sub>50</sub> parameters were kept fixed. Also, end-diastolic pressure [1, 30, 74, 83, 113, 125–127, 200, 209] and cardiac tissue stiffness [1, 53, 74, 127, 162, 200, 209, 234] were consistently shown to be increased w.r.t control, so we fitted p and C<sub>1</sub> parameters. Furthermore, there was evidence for an increase in systolic arterial pressure [51] and aortic characteristic impedance [127]; therefore, parameters p<sub>ao</sub>, Z were selected for optimisation as well. As there were no statistically significant changes in the reported values of myocardial active contraction in ZSF1 rats [56, 79, 155], we assumed that sarcomere properties remained unchanged (i.e. Ca<sub>50</sub>, β<sub>1</sub>, k<sub>off</sub>, n<sub>trpn</sub>, k<sub>xb</sub>, n<sub>xb</sub>, TRPN<sub>50</sub>, T<sub>ref</sub> parameters were not fitted). Although the ZSF1 rats all developed LV hypertrophy as shown by increased cardiac fibrosis, collagen type III fibres and cardiomyocyte size (increased LV mass and indexes of LV mass such as LV + IVS weights / tibial length), this was not always (e.g. [209, 234]) accompanied by an increase in LV wall thickness in male ZSF1 rats. Moreover, half of the ZSF1 rat studies [1, 74, 113, 125–127, 162, 234] showed no LV dilation as appraised by indexed end-diastolic volumes (preserved EDVi), which we translated into a no-change in the biventricular size/shape. To summarise, 6 out of 16 SHAM rat model parameters were re-fitted to build the ZSF1 rat model while keeping the other parameters fixed to reference values.

We therefore sampled 400,000 NROY points from a LHD in the input parameter space X (Section 7.3.2), which was *a priori* constrained according to the above-mentioned literature evidence. This means that for parameters that were observed to significantly vary in one specific direction, the corresponding 1D slice of the full hypercube was cut in two equal parts, and only the half which corresponded to the correct direction of change from the reference parameter value was used to generate the initial hypercube. Parameters not selected for optimisation (no significant change when going from control to diseased ZSF1 rats) had their 1D slices fixed to a single value instead (the SHAM rat reference value), effectively reducing the initial hypercube of 1 dimension for each of them. The resulting sampled NROY

space was hence a 6-dimensional space. The NROY points were then tested against an implausibility criterion with  $I_{\text{cutoff}} = 3.0$ .

### 7.3.5 *In silico* recovering the ZSF1 rat towards healthy conditions

The ZSF1 rat model we are building will constitute a virtual platform to understand better the pathophysiological mechanisms of a diseased HFP EF animal model. We aim at using this platform to identify cellular properties that can be manipulated to recover the ZSF1 rat towards a healthy condition. By the word “recover”, we mean to bring the altered LV features’ values of the ZSF1 rat model back to the values of the SHAM rat model. We will do so by explicitly targeting different subsets of model parameters to *in silico* represent different possible pharmacological compounds’ mechanisms of action.

For this purpose, starting from the built ZSF1 rat model, we refitted model parameters to go back to the initial, healthy state of the SHAM rat model, matching the *in silico* variability observed for the LV function in the SHAM rat model (Section 4.4.3, Figure 4.14), summarised in Table 7.6. A preliminary sketch of the recovery process is provided in Figure 7.4.

LV FEATURE	UNITS	SYNTHETIC VARIABILITY
EDV	$\mu\text{L}$	$498.22 \pm 13.21$
ESV	$\mu\text{L}$	$185.12 \pm 4.08$
PeakP	kPa	$16.14 \pm 0.49$
maxdP	$\text{kPa ms}^{-1}$	$0.95 \pm 0.04$
Tau	ms	$6.52 \pm 0.40$

Table 7.6: SHAM rat model *in silico* variability for the LV features used as targets for ZSF1 rat model recovery. Target mean and standard deviation LV features’ values to be matched for recovering the ZSF1 rat.

The LV features we aimed to recover were EDV, ESV, PeakP, maxdP, Tau. The groups of parameters selected for optimisation were:  $\text{Ca}^{2+}$  transient (DCA, AMPL, TP, RT50), thin filament ( $\text{Ca}_{50}$ ,  $\beta_1$ ,  $k_{\text{off}}$ ,  $n_{\text{trpn}}$ ), thick filament ( $k_{\text{xb}}$ ,  $n_{\text{xb}}$ , TRPN<sub>50</sub>,  $T_{\text{ref}}$ ) and the three groups combined, labelled, respectively, as “Ca”, “TNF”, “TKF” and “CaMYO”. We performed a separate HM for each group. This required to build a specific set of emulators to be used each time.

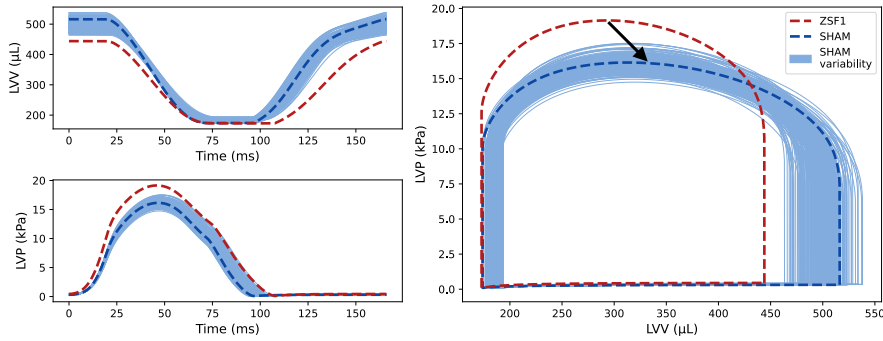


Figure 7.4: ZSF1 rat model recovery towards SHAM rat model. ZSF1 rat (red) and SHAM rat (blue) models' LV pressure and volume transients and PV loops are plotted with dashed lines. SHAM model *in silico* variability is also represented by a cloud of thin blue full lines. Black arrow represents the direction of recovery.

For each group of D parameters  $\mathbf{p} = (p_1, \dots, p_D)$ , we trained one univariate GPE for each of the target LV features to replace the deterministic map

$$f: \mathbb{R}^D \rightarrow \mathbb{R} \quad (7.2)$$

$$\mathbf{p} \mapsto f_{\text{simul}}(\mathbf{p}, (p_{D+1}^{\text{ZSF1}}, \dots, p_{16}^{\text{ZSF1}})) = y \quad (7.3)$$

with a probabilistic surrogate to predict the LV feature value  $y \in \mathbb{R}$  for a given parameter set  $\mathbf{p} \in \mathbb{R}^D$ . The training datasets were built by sampling points (512 for Ca, TNF, TKF groups and 2048 for CaMYO group) from a LHD over the restricted, D-dimensional parameter space and by running the full simulator  $f_{\text{simul}}$  (equation (7.1)) at these points while keeping all the remaining parameters ( $p_{D+1}^{\text{ZSF1}}, \dots, p_{16}^{\text{ZSF1}}$ ) fixed to the ZSF1 reference values.

## 7.4 RESULTS

### 7.4.1 Model emulators and output sensitivities

The GPEs' cross-validation mean accuracy is reported in Table 7.7. The mean  $R^2$  score was  $> 0.9$  for 4 out of 14 emulated features, while for all the other features (10 out of 14), it was ranging between 0.45 and 0.9. The lowest values were obtained for features representing timings (0.51, 0.50, 0.49 for IVCT, Tdiast, Tpeak, respectively) but not for features representing magnitudes (lowest was 0.76 for EF). On the other hand, the  $ISE_2$  was  $> 0.9$  for all the features. This suggested that the GPEs' posterior distributions' variance correctly increased to account for greater uncertainty in the point-wise predictions coming from less accurate emulators.

In Figure 7.6, the calculated Sobol' first-order effects are reported for all the 14 LV features. In Section 7.3.5, we have identified groups

LV FEATURE	R <sup>2</sup>	ISE <sub>2</sub> (%)
EDV	0.9437 ± 0.0089	98.38 ± 0.61
ESV	0.8344 ± 0.0227	98.92 ± 0.75
SV	0.7937 ± 0.0228	98.92 ± 0.66
EF	0.7627 ± 0.0051	98.77 ± 0.45
IVCT	0.5190 ± 0.0579	93.46 ± 1.19
ET	0.7900 ± 0.0248	97.15 ± 1.49
IVRT	0.7467 ± 0.0480	97.54 ± 1.02
Tdiast	0.5047 ± 0.0226	94.53 ± 1.07
PeakP	0.8942 ± 0.0114	98.61 ± 0.79
Tpeak	0.4921 ± 0.0362	94.30 ± 1.15
ESP	0.9556 ± 0.0074	98.07 ± 0.69
maxdP	0.9448 ± 0.0087	98.46 ± 0.81
mindP	0.9008 ± 0.0121	97.84 ± 1.10
Tau	0.8213 ± 0.0168	96.69 ± 0.72

Table 7.7: GPEs' accuracy. The GPEs' accuracy was evaluated using the average R<sup>2</sup> score and ISE<sub>2</sub> obtained with a 5-fold cross-validation. Values are reported as mean±std.

of parameters that regulate a specific cellular component (Ca<sup>2+</sup> transient, thin filament, thick filament) and which we will re-fit to mimic possible pharmacological interventions at the cell level to *in silico* treat rat HFpEF. To determine which of these parameter sets has the greatest impact overall on whole-heart cardiac mechanics, we ranked the parameters according to their total effects from the one that affected the highest number (and by the highest amount) to the one that affected the lowest number (and by the lowest amount) of LV features. The obtained ranking is presented in Table 7.8. We thus divided the 16 parameters into 4 sub-categories according to which specific part of the multi-scale model they regulated, the first three being the above-mentioned parameter groups while the last group describing passive material and boundary conditions properties (labelled as "BC"), with 4 parameters in each category. By summation of the parameters' individual ranks within each category, we were able to classify the groups according to how important they are in explaining the variance across output variables: the lower the sum, the higher the importance. We found that the Ca<sup>2+</sup> transient is the most important input of the multi-scale model, immediately followed by the thin filament and the thick filament. The boundary conditions were found not to play an important role in this model (ranked fourth). To summarise, altering preload and afterload were predicted to have a secondary

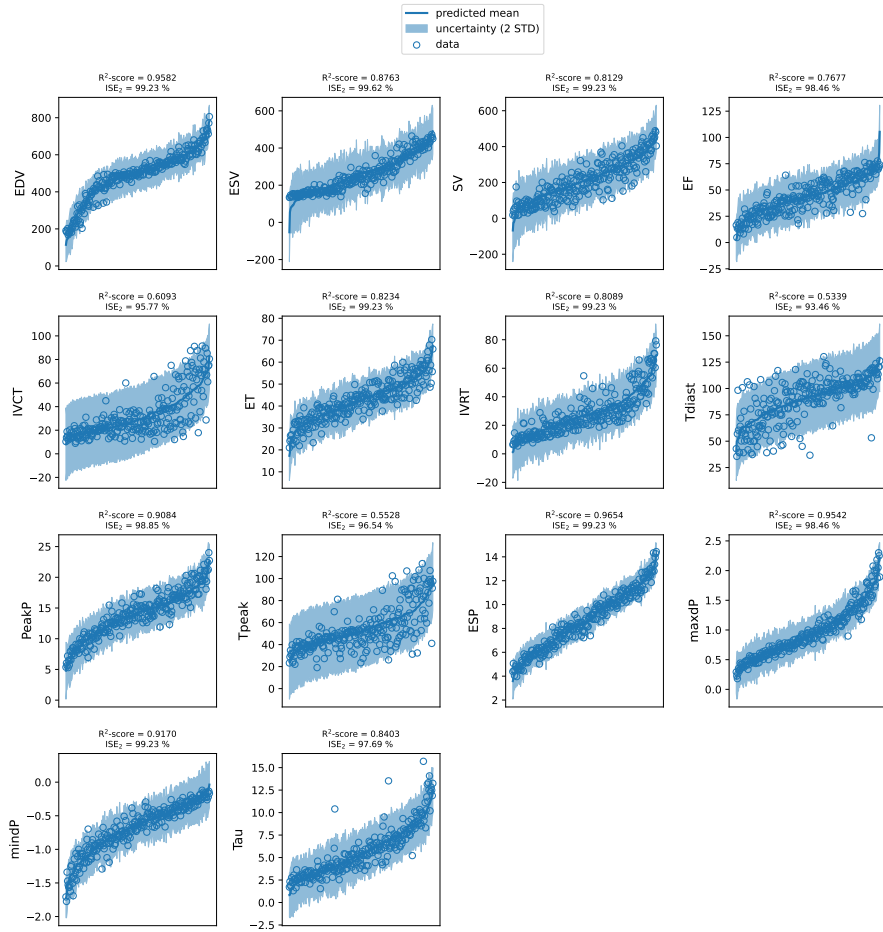


Figure 7.5: For each LV feature, the GPE with the highest  $R^2$  split test score is used to make predictions at the respective left-out subset of test points. Predictions are sorted in ascending order for the sake of better visualisation and joined with a thick blue line, and the respective observations (empty dots) are sorted accordingly. 2 STD confidence intervals (shaded regions) are also plotted around predicted mean lines.

impact on the overall cardiac function, with cellular properties being the dominant regulators of cardiac function.

#### 7.4.2 Personalised healthy rat heart model validation using emulators

Having available trained emulators that can map  $\text{Ca}^{2+}$  transient properties to LV function allowed us to validate further the SHAM rat model against experimentally observed CiPA compounds' effects by following the same approach of Section 6.3. However, in this case, we replaced the simulator with the emulator in the last validation step when LV features' dose-response curves are calculated. In particular, the perturbed  $\text{Ca}^{2+}$  transients, obtained when simulating the compounds' effects at the cellular level, were first encoded by the

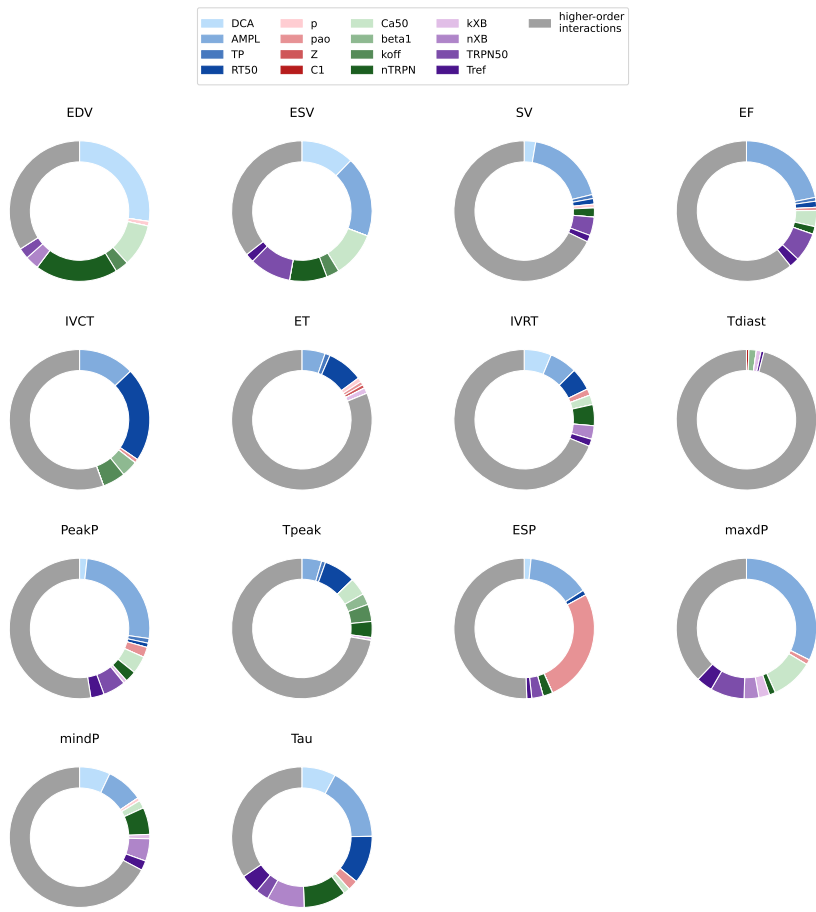


Figure 7.6: The impact of calcium dynamics, sarcomere, tissue and boundary conditions properties on organ-scale LV features in the healthy rat. The contribution of each parameter is represented by its Sobol' main effect. For each LV feature, higher-order interactions (coloured in grey) are represented by the sum of all total effects minus the sum of all main effects.

4 parameters. Then these parameters were mapped to LV features' values using the emulators while fixing the other 12 parameters of the input vector to the healthy baseline values. Predicted LV pressure features' dose-response curves are shown in Figure 7.7.

In Figure 7.7, we can see that the emulators correctly predict the same LV features' percentage variation from reference trends observed when using the simulator (Figure 6.6). Therefore, the same conclusions about the simulator matching qualitative/quantitative experimental observations can also be extended to the emulators.

#### 7.4.3 The ZSF1 rat model

The first wave of the HM procedure for building the ZSF1 rat model is displayed in Figure 7.8. 47,097 points (corresponding to 11.77 % of

GROUP	PARAMETER	RANK	SCORE
Calcium transient (Ca)	DCA	1	22
	AMPL	3	
	TP	10	
	RT <sub>50</sub>	8	
Thin filament (TNF)	Ca <sub>50</sub>	2	26
	β <sub>1</sub>	14	
	k <sub>off</sub>	6	
	n <sub>trpn</sub>	4	
Thick filament (TKF)	k <sub>xb</sub>	12	33
	n <sub>xb</sub>	7	
	TRPN <sub>50</sub>	5	
	T <sub>ref</sub>	9	
Boundary conditions (BC)	p	13	55
	p <sub>ao</sub>	11	
	Z	16	
	C <sub>1</sub>	15	

Table 7.8: Parameters ranking according to their influence on the model output total variance. A rank is assigned to each parameter according to how much it impacts the model output total variance. Parameter groups are assigned a score given by the sum of the ranks of their member parameters. This score reflects the importance of the group as an input for the multi-scale model.

all the points tested against the implausibility criterion) were deemed non-imausible. The simulator (equation (7.1)) was then run at a subset of 1024 XNIMP points to see if the respective simulation output was correctly matching the experimentally observed value for each LV feature under study. This is illustrated in Figure 7.9. Since all the simulated features' values already fell between 3 standard deviations from the respective experimental mean values, we concluded the HM.

In order to have a representative ZSF1 rat model to be used as a virtual platform for testing rat HFP EF-treating strategies, we selected one candidate represented by the best-fit according to a weighted L<sub>1</sub> norm where the last three LV features (PeakP, maxdP and Tau) which were shown to significantly change in the ZSF1 rat had double the weight of the first feature (EF) which showed no significant change, and with all the weights summing up to 1. The obtained representative ZSF1 rat model Ca<sup>2+</sup> transient and PV loop are depicted in Figure 7.10 and are compared with the reference SHAM rat model. The complete

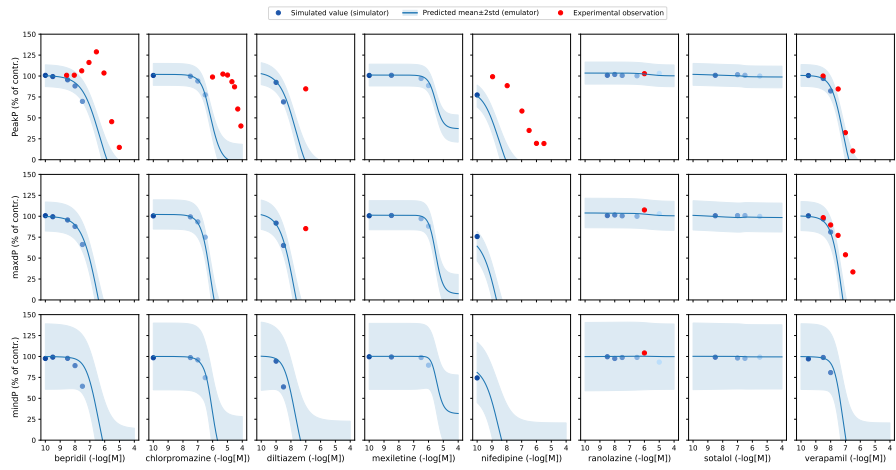


Figure 7.7: LV pressure features' dose-response curves for the eight CiPA compounds. Simulated (dots in blue variants, colour-coded with the compound doses), emulated (full lines and shaded areas in blue) and experimentally observed (dots in red) PeakP, maxdP and mindP features' values are given as percentages of the respective control values. Experimental data taken from [5] (bepridil and verapamil – PeakP), [122] (chlorpromazine, PeakP), [109] (diltiazem – PeakP and maxdP), [206] (nifedipine – PeakP), [241] (ranolazine – PeakP, maxdP and mindP), [108] (verapamil – maxdP).

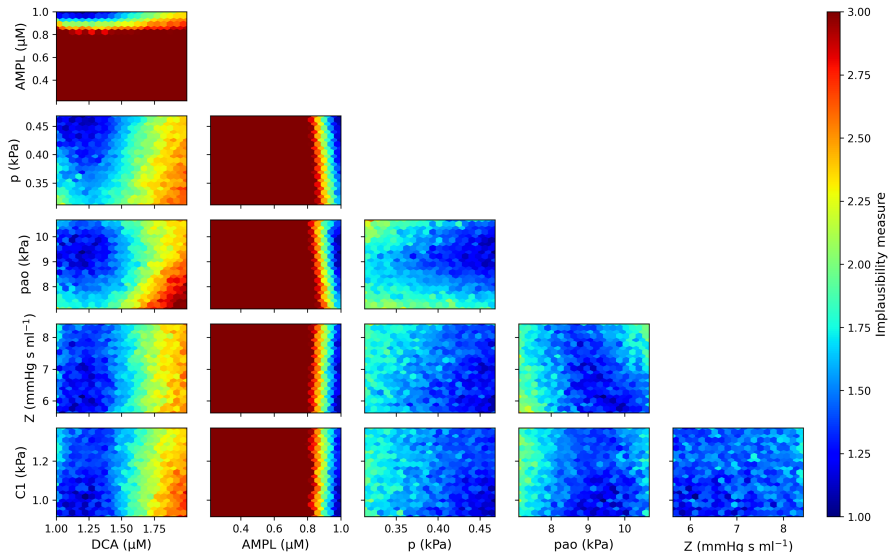


Figure 7.8: First wave of history matching. The space represented by the parameters selected for optimisation is constrained according to an implausibility criterion which evaluates how plausible is a point to yield model predictions that are matching experimental observations.

sets of re-fitted and fixed model parameters and corresponding LV features for both the reference, control SHAM rat model and the newly

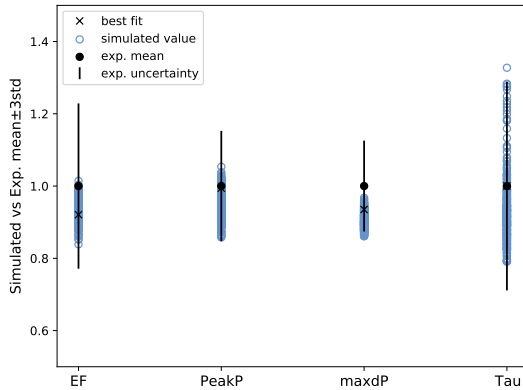


Figure 7.9: Matching experimental LV features' values. Simulator runs at input parameter points from the HM first (and also last) wave's non-imausible space. Obtained LV features' (empty, blue dots) distributions around experimental mean values (filled, black dots) are all within 3 STD confidence intervals (vertical straight lines centred in their respective mean value). The best fit in weighted L<sub>1</sub> norm is also displayed (black cross). All the values including confidence intervals have been normalised by the respective experimental mean values.

obtained, representative ZSF1 rat model are reported in Table 7.9 and Table 7.10, respectively.

#### 7.4.4 Recovered LV function in ZSF1 rats

The new training datasets had dimensions of 104, 129, 114 and 326 points for the Ca, TNF, TKF and CaMYO groups, respectively. The GPEs' accuracy for each group are reported in Tables 7.11–7.12–7.13–7.14.

Information about performed waves, used cutoff values and percentages of space reduction are summarised in Table 7.15. In Figure 7.11 the HM waves progression is shown. For each LV feature we aimed to match, its values obtained when simulating parameter points from a specific wave's non-imausible region are plotted as a distribution, possibly overlapping to the experimental variability (red band) observed for the same feature. This is done at every wave run so that the HM is represented as a sequence of LV features' values' distributions over consecutive waves.

For each parameter group, we can distinguish whether a specific LV feature has been recovered by looking at the last wave' distribution. Specifically, a feature was determined to be recovered if this distribution median was within the uncertainty region for that feature. We can see that we were able to recover the maxdP feature in all 4 cases. EDV and Tau features were only recovered in the CaMYO group. ESV feature was harder to recover, being very close to the uncertainty region

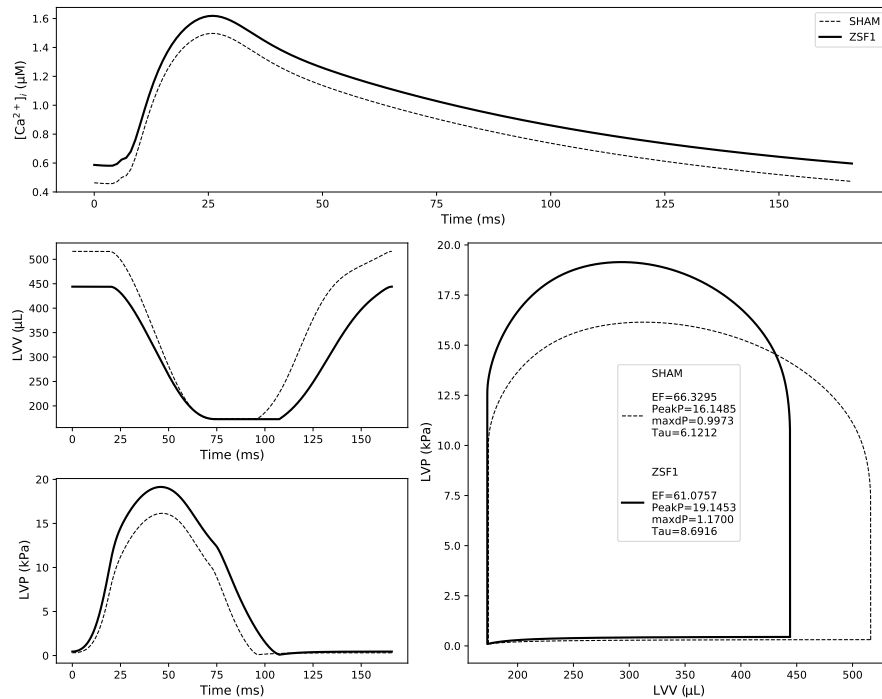


Figure 7.10: Representative SHAM and ZSF1 rat models calcium transients and pressure-volume loops. The ZSF1 rat model is created by perturbing the SHAM (healthy) state. LV features which significantly changed from control to diseased animal are highlighted at the centre of the PV loops sub-plot. EF showed no significant change.

in all the 4 cases although never meeting the median-based criterion. PeakP was never recovered, although it moved in the correct direction of recovery (decreasing) in all 4 cases. For each group, we selected (according to an  $L_2$ -norm best-fit criterion) a reference recovered rat model which we labelled as “RECOV”, and we plotted the respective LV pressure and volume transients and PV loops (Figure 7.12), compared with the reference SHAM rat and ZSF1 rat models.

By relaxing the median-based recovery criterion, we also looked at whether the last wave’ distribution of a specific LV feature  $i$  had a median value  $y_i^{\text{RECOV}}$  which was moving towards the healthy experimental mean value  $y_i^{\text{SHAM}}$  starting from the reference, diseased state value  $y_i^{\text{ZSF1}}$ . For each parameter group, we computed the percentage of recovery  $R_{\text{perc}}$  for each LV feature as described by the ratio:

$$R_{\text{perc}} = \left| \frac{y_i^{\text{RECOV}} - y_i^{\text{ZSF1}}}{y_i^{\text{SHAM}} - y_i^{\text{ZSF1}}} \right| \quad (7.4)$$

A value of  $R_{\text{perc}} = 1$  indicates that the feature has been recovered fully. When the median of a given LV feature’s distribution was not moving towards the correct direction of recovery, its corresponding  $R_{\text{perc}}$  value was set to 0. When the median was moving towards the

PARAMETER	UNITS	VALUE	
		SHAM	ZSF1
DCA	$\mu\text{M}$	0.4632	0.5870
AMPL	$\mu\text{M}$	1.0341	1.0317
TP	$\text{ms}$	25.9474	25.9474
RT <sub>50</sub>	$\text{ms}$	40.0807	40.0807
Ca <sub>50</sub>	$\mu\text{M}$	2.1723	2.1723
$\beta_1$	—	-1.5	-1.5
k <sub>off</sub>	$\text{ms}^{-1}$	0.0515	0.0515
n <sub>trpn</sub>	—	2.0	2.0
k <sub>xb</sub>	$\text{ms}^{-1}$	0.0172	0.0172
n <sub>xb</sub>	—	5.0	5.0
TRPN <sub>50</sub>	—	0.35	0.35
T <sub>ref</sub>	$\text{kPa}$	156.067	156.067
p	$\text{kPa}$	0.3122	0.4481
p <sub>ao</sub>	$\text{kPa}$	7.1136	10.3887
Z	$\text{mmHg s mL}^{-1}$	5.6234	7.4031
C <sub>1</sub>	$\text{kPa}$	0.9141	1.0670

Table 7.9: Representative SHAM and ZSF1 rat models' input parameters' values.

correct direction of recovery but surpassed the healthy value, its corresponding R<sub>perc</sub> value was set to 1 instead. R<sub>perc</sub> values for each LV feature for each group are summarised in Table 7.16. We can see that the highest degree of recovery (39 %) can be achieved when manipulating both the sarcomere kinetics and the Ca<sup>2+</sup> dynamics at the same time. It is worth noticing that the different degrees of recovery achieved by targeting the first three groups of parameters, namely 34 %, 28 % and 24 % for Ca, TNF and TKF groups, respectively, match the relative importance these groups have into explaining the total variance of the considered LV features (Table 7.8).

We further inspected the parameter space which the HM converged to in the last wave for each parameter group, and we compared this with the ZSF1 rat model reference parameter set (see Figure 7.13). The distribution's median trend over consecutive waves of each parameter within each group provides an indication on which direction the parameter has undergone a perturbation from the reference ZSF1 rat same parameter value in order to recover the LV function. This is summarised in Table 7.17 for the last waves' perturbations.

LV FEATURE	UNITS	VALUE	
		SHAM	ZSF1
EDV	$\mu\text{L}$	516.23	444.02
ESV	$\mu\text{L}$	173.82	172.83
SV	$\mu\text{L}$	342.42	271.19
EF	%	66.33	61.08
IVCT	ms	19.3	19.7
ET	ms	52.9	54.6
IVRT	ms	23.8	33.0
Tdiast	ms	93.5	91.4
PeakP	kPa	16.15	19.15
Tpeak	ms	46.6	45.9
ESP	kPa	10.04	12.55
maxdP	$\text{kPa ms}^{-1}$	0.9973	1.1700
mindP	$\text{kPa ms}^{-1}$	-0.5712	-0.5276
Tau	ms	6.1212	8.6916

Table 7.10: Representative SHAM and ZSF1 rat models' output LV features' values.

LV FEATURE	R <sup>2</sup>	ISE <sub>2</sub> (%)
EDV	0.9984 $\pm$ 0.0009	90.42 $\pm$ 6.70
ESV	0.9868 $\pm$ 0.0105	98.09 $\pm$ 3.80
PeakP	0.9940 $\pm$ 0.0045	93.33 $\pm$ 5.71
maxdP	0.9965 $\pm$ 0.0008	95.23 $\pm$ 4.25
Tau	0.9419 $\pm$ 0.0367	90.42 $\pm$ 6.70

Table 7.11: GPEs' accuracy for the Ca parameter group.

LV FEATURE	R <sup>2</sup>	ISE <sub>2</sub> (%)
EDV	0.9725 $\pm$ 0.0182	92.24 $\pm$ 4.86
ESV	0.9810 $\pm$ 0.0083	93.07 $\pm$ 5.65
PeakP	0.9557 $\pm$ 0.0235	89.93 $\pm$ 4.58
maxdP	0.9766 $\pm$ 0.0203	96.89 $\pm$ 2.88
Tau	0.9378 $\pm$ 0.0225	86.73 $\pm$ 11.97

Table 7.12: GPEs' accuracy for the TNF parameter group.

LV FEATURE	R <sup>2</sup>	ISE <sub>2</sub> (%)
EDV	0.9802 ± 0.0159	92.13 ± 6.36
ESV	0.9952 ± 0.0024	92.09 ± 7.49
PeakP	0.9937 ± 0.0020	92.13 ± 4.22
maxdP	0.9588 ± 0.0296	97.39 ± 3.47
Tau	0.8079 ± 0.1413	90.31 ± 7.53

Table 7.13: GPEs' accuracy for the TKF parameter group.

LV FEATURE	R <sup>2</sup>	ISE <sub>2</sub> (%)
EDV	0.9040 ± 0.0074	91.40 ± 4.42
ESV	0.6910 ± 0.0214	94.79 ± 1.81
PeakP	0.6986 ± 0.0639	94.47 ± 1.85
maxdP	0.9009 ± 0.0232	92.64 ± 3.54
Tau	0.7994 ± 0.0515	89.54 ± 4.72

Table 7.14: GPEs' accuracy for the CaMYO parameter group.

We can see that in order to recover the LV function by only perturbing the  $\text{Ca}^{2+}$  transient (4 parameters), DCA and TP increased, while AMPL and RT<sub>50</sub> decreased. This resulted in a  $\text{Ca}^{2+}$  transient signal which was shifted upwards, flatter and delayed in time with fast recovery. By only perturbing the thin filament properties (4 parameters), the LV function could be recovered when  $\text{Ca}_{50}$  increased at a constant  $n_{\text{trpn}}$ , with decreased  $\beta_1$  and  $k_{\text{off}}$ . This resulted in TnC- $\text{Ca}^{2+}$  bound complexes saturating at lower  $[\text{Ca}^{2+}]_i$  and to a slower dissociation of the TnC- $\text{Ca}^{2+}$  bound state, which made the actin binding sites available for longer. By only perturbing the thick filament properties (4 parameters), the LV function could be recovered when  $n_{\text{xb}}$  and  $k_{\text{xb}}$  decreased with increased TRPN<sub>50</sub> and  $T_{\text{ref}}$ . This resulted in an overall slower force generation with increased maximal generated force. Lastly, when manipulating both the  $\text{Ca}^{2+}$  transient and the whole sarcomere at the same time (12 parameters) to recover the LV function, AMPL and TP were increased at a constant DCA and decreased RT<sub>50</sub>;  $k_{\text{off}}$  and  $n_{\text{trpn}}$  were decreased at a constant  $\text{Ca}_{50}$  and  $\beta_1$ ;  $n_{\text{xb}}$  and TRPN<sub>50</sub> were increased at a constant  $T_{\text{ref}}$  and decreased  $k_{\text{xb}}$ .

To interpret these changes in terms of intact muscle experimental measurements, we used the contraction model [118] to estimate the corresponding changes in steady-state force-calcium relationship and field stimulated isometric tension transient predicted by the model to recover cardiac function in the ZSF1 model. This is illustrated in Figure 7.14. Common patterns can be observed in how the four different

	WAVE		PARAMETER GROUP							
	CA		TNF		TKF		CaMYO			
	I <sub>cutoff</sub>	NIMP (%)								
1	4.5	0.08	4.0	0.01	4.0	0.07	4.0	13.75		
2	4.5	0.18	4.0	0.33	4.0	0.14	4.0	73.78		
3	4.2	6.53	4.0	0.80	—	—	3.5	55.03		
4	4.2	92.79	—	—	—	—	3.5	84.39		
5	—	—	—	—	—	—	3.0	55.98		
6	—	—	—	—	—	—	3.0	84.43		
7	—	—	—	—	—	—	2.5	47.94		
8	—	—	—	—	—	—	2.5	83.97		
9	—	—	—	—	—	—	2.0	34.12		
10	—	—	—	—	—	—	2.0	75.03		

Table 7.15: Details of history matching progression. HM is run for each parameter group in order to re-fit the specific parameters within the group. Parameter points (400,000 at Wave 1 and 100,000 at the next Waves) are tested against an implausibility criterion using the reported cutoff values, and only a percentage of these points resulted to be non-imausible (NIMP).

LV FEATURE	PARAMETER GROUP			
	Ca	TNF	TKF	CaMYO
EDV	0.01	0.04	0.05	0.40
ESV	0.00	0.00	0.00	0.00
PeakP	0.33	0.36	0.35	0.20
maxdP	1.00	0.85	0.82	0.73
Tau	0.34	0.17	0.00	0.61
<b>Mean recovery</b>	0.34	0.28	0.24	0.39

Table 7.16: LV features' percentages of recovery. For each LV feature we aimed to recover, the distance between its median recovered value and the respective healthy value is divided by the distance between the initial, diseased value and the healthy value. This ratio describes the percentage of recovery for the examined feature.

simulated strategies of recovery act on the sarcomere. They all cause a none-to-rightwards shift of the F-pCa curve, thereby desensitising the myofilament to intracellular  $\text{Ca}^{2+}$  concentrations, and they all cause a

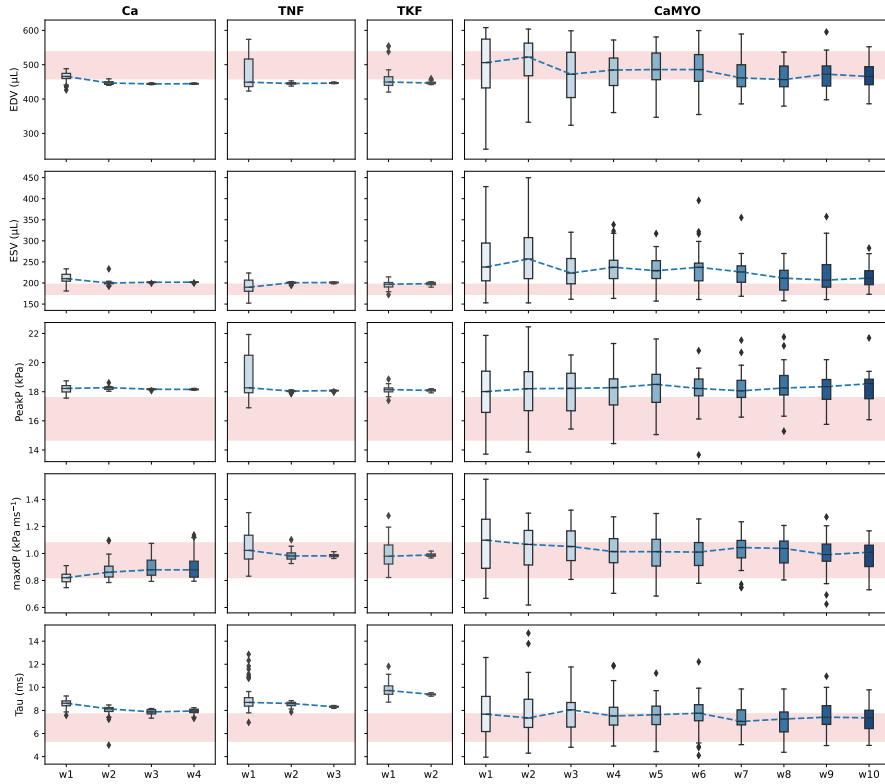


Figure 7.11: History matching waves progression. At each wave, 128 points are simulated from the current non-implausible parameter region and the features' values from the converging simulations are plotted as box plots coloured in blue variants for different consecutive waves. The median trend of these distributions is represented by a dashed blue line. Mean  $\pm$  3 standard deviations target intervals are represented in light red-coloured shaded areas for each LV feature.

no-change-to-decrease in the same curve's Hill coefficient, resulting in an overall reduced affinity for calcium. Maximum generated active tension is always decreased apart from when the recovery is carried out via  $\text{Ca}^{2+}$  transient modulation (Ca parameter group). Maximum rates of tension development and decay are always slowed down (less pronouncedly for the Ca strategy), which promotes the sarcomere to stay for longer in the force-generating state.

## 7.5 DISCUSSION

In this study, we proposed that  $\text{Ca}^{2+}$  dynamics, thin and thick filaments kinetics are all potential pharmacological targets for HFP EF, based on simulations in the ZSF1 rat model. The found recovered rat model parameter space, when interpreted in terms of muscle experimental measurements, also suggested that HFP EF-treating compounds should possibly act as direct sarcomere modulators by desensitising

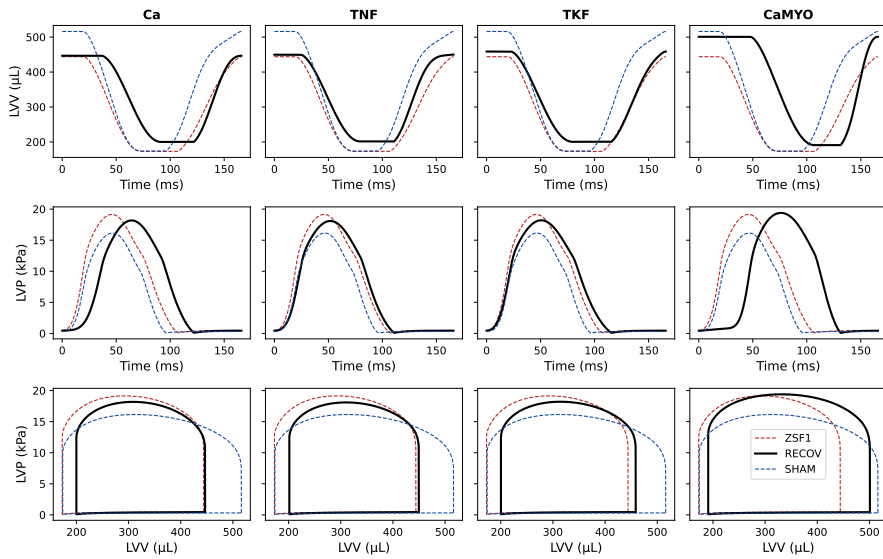


Figure 7.12: Best fit recovered rat heart models. For each parameter group, the last wave fitted models are compared against the target mean, which the history matching aimed to match, and the best-fit model is selected according to the  $L_2$ -norm. This best-fit rat model (RECOV, black thick line) is compared with the reference ZSF1 rat model (red dashed line) and with the reference SHAM rat model (blue dashed line).

the myofilament and reducing the affinity to intracellular  $\text{Ca}^{2+}$ , and decreasing the maximum generated active force while slowing down active force generation and relaxation in the intact muscle.

The targets identified in this study (Figure 7.13) are consistent with the common endpoint of the two example pharmacotherapies for HFpEF treatment presented in Section 1.3.2. Specifically, both the Ca and the CaMYO strategies of recovery proposed a decrease (of  $\sim 30 - 50\%$  from the diseased animal reference value) in the half-maximal  $\text{Ca}^{2+}$  relaxation time, making less calcium available during the cardiac cycle. However, if this is accompanied by only a slight increase ( $\sim 5 - 10\%$ ) in the diastolic  $\text{Ca}^{2+}$  concentration, a very prolonged ( $\sim 40 - 60\%$ ) time to peak  $\text{Ca}^{2+}$  concentration is present as well, although this affects mostly the tension development and duration, rather than relaxation. We have seen that the Ca and CaMYO strategies have proposed a  $\text{Ca}^{2+}$  transient which is slower to rise and faster to decline, corresponding to a delayed and more symmetric  $\text{Ca}^{2+}$  transient. This causes a far greater delay between activation and contraction and delayed systole, also visible in the left- and right-most panels in Figure 7.12. However, as more time is spent in isovolumetric contraction with unaltered ejection times, this results in negligible negative effects on the cardiac output. At the same time, this is accompanied by shorter diastole, which in the case of HFpEF pathology constitutes an improvement for cardiac relaxation.

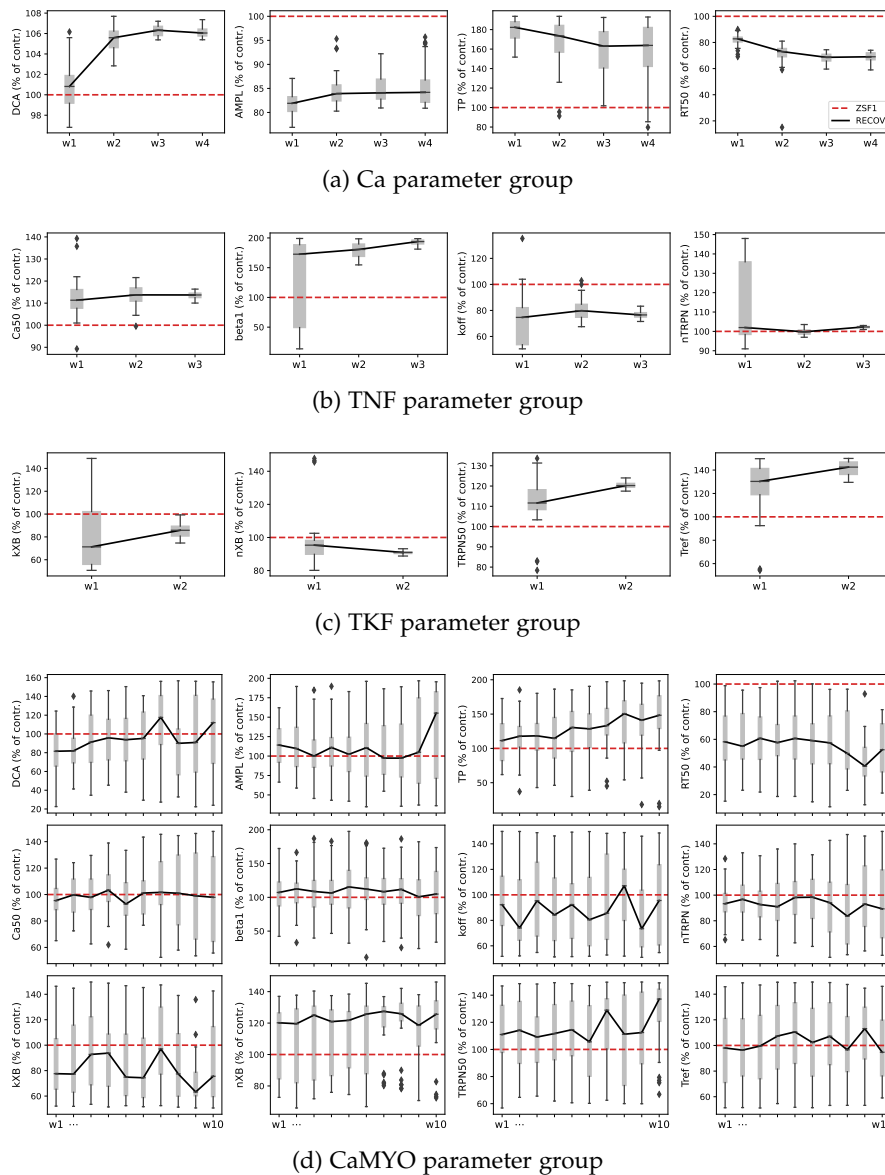


Figure 7.13: Parameter distributions across progressing waves for the four different parameter groups. Each parameter distribution is represented as a grey box plot at each wave. Its median trend during multiple waves is highlighted in a solid black line and is compared with the ZSF1 rat model reference value for the same parameter highlighted in a dashed red line. All the plotted RECOV parameter values are given as percentages of the respective baseline ZSF1 parameter values.

Although  $\text{Ca}^{2+}$  dynamics and sarcomere modulators are already subject of ongoing clinical trials (Section 1.3.2), the strategies of recovery proposed in this study by the TNF, TKF and CaMYO parameter groups cannot be directly compared to what is currently being tested experimentally. Therefore, they still miss thorough validation. Nevertheless, in Chapter 5 we have shown that single compounds' effects

GROUP	PARAMETER	ZSF1	RECOV	CHANGE (%)
Ca	DCA	1.2674	1.3440	6.05
	AMPL	0.9977	0.8399	-15.82
	TP	1.0000	1.6379	63.79
	RT <sub>50</sub>	1.0000	0.6906	-30.95
TNF	Ca <sub>50</sub>	2.1723	2.4699	13.70
	β <sub>1</sub>	-1.50	-2.91	-93.91
	k <sub>off</sub>	0.0515	0.0394	-23.47
	n <sub>trpn</sub>	2.00	2.05	2.28
TKF	k <sub>xb</sub>	0.0172	0.0147	-14.18
	n <sub>xb</sub>	5.00	4.55	-9.07
	TRPN <sub>50</sub>	0.35	0.42	20.24
	T <sub>ref</sub>	156.067	222.420	42.52
CaMYO	DCA	1.2674	1.4200	12.04
	AMPL	0.9977	1.5486	55.22
	TP	1.0000	1.4828	48.28
	RT <sub>50</sub>	1.0000	0.5247	-47.53
	Ca <sub>50</sub>	2.1723	2.1268	-2.10
	β <sub>1</sub>	-1.50	-1.57	-4.86
	k <sub>off</sub>	0.0515	0.0492	-4.44
	n <sub>trpn</sub>	2.00	1.79	-10.69
	k <sub>xb</sub>	0.0172	0.0130	-24.44
	n <sub>xb</sub>	5.00	6.28	25.61
	TRPN <sub>50</sub>	0.35	0.48	37.12
	T <sub>ref</sub>	156.067	147.785	-5.31

Table 7.17: Percentage perturbations of cardiac cellular properties resulting from the last waves' parameter spaces. For each parameter last wave distribution, its median value is given as a ± percentage perturbation from the corresponding ZSF1 reference value. Ca<sup>2+</sup> transient parameters are reported as coefficients used to scale the corresponding SHAM rat baseline real parameter values.

can be quantitatively validated using mathematical models. As previous works (e.g. [61]) have demonstrated how models could be used for transferring findings between species, we don't exclude the possibility for this framework to be scaled to human scale models in order to potentially help the designing and developing of future diagnostic and therapeutic strategies.

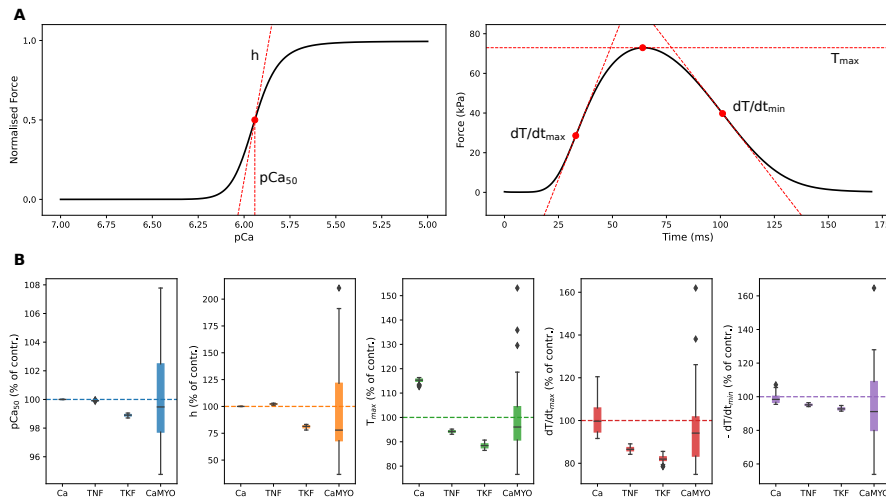


Figure 7.14: Isometric force-calcium relationship and generated active tension properties from the recovered rat model parameter space. (A) Calcium sensitivity ( $p\text{Ca}_{50}$ ) and Hill coefficient ( $h$ ) features are extracted from the F-pCa curve, while peak tension ( $T_{\text{max}}$ ) and maximum rates of tension development ( $dT/dt_{\text{max}}$ ) and decay ( $dT/dt_{\text{min}}$ ) are extracted from the twitch transient. (B) Distributions of extracted  $p\text{Ca}_{50}$  (blue),  $h$  (orange),  $T_{\text{max}}$  (green),  $dT/dt_{\text{max}}$  (red),  $dT/dt_{\text{min}}$  (purple) values are compared with the respective ZSF1 rat model baseline values (dashed lines).

### 7.5.1 Limitations

The performed GSA showed that altering preload and afterload has a secondary impact on the overall LV function. However, we modelled these two factors as fixed boundaries, and in more sophisticated closed loops heart systems, the situation might change. The GSA also highlighted that parameters  $k_{\text{xb}}$  and  $T_{\text{ref}}$  related to cross-bridge dynamics had a limited impact on haemodynamic features such as SV or EF. This may be in part due to the length dependence of tension, where decreased  $T_{\text{ref}}$  or  $k_{\text{xb}}$  will lead to slower tension development, which will lead to the muscle remaining at higher sarcomere lengths for longer, and hence having higher  $\text{Ca}^{2+}$  sensitivity, which in turn will recover contraction.

Considering the high sensitivity of EF to  $T_{\text{ref}}$  reported in other uncertainty quantification of LV cardiac function studies (e.g. [37]), we further investigated this apparently controversial finding by performing an additional *one-at-a-time* sensitivity analysis. We selected 5 parameters that were identified as the most important by the GSA, namely DCA, AMPL,  $\text{Ca}_{50}$ ,  $n_{\text{trpn}}$ ,  $\text{TRPN}_{50}$ , and we further selected the  $k_{\text{xb}}$  and  $T_{\text{ref}}$  parameters which were shown to have a limited impact instead. The SHAM rat model was then run at a fixed, reference parameter set (Table 7.9) with only one parameter taking equally-spaced values in the  $\pm 50\%$  range of perturbation from its baseline value. The

converging mechanics simulations' output PV loops were analysed to extract the corresponding EDV, ESV, SV and EF features' values, given as percentages from their baseline values (Table 7.10). The process was repeated separately for each of the 7 model parameters considered. In this way, each output LV feature response to each input parameter could be obtained.

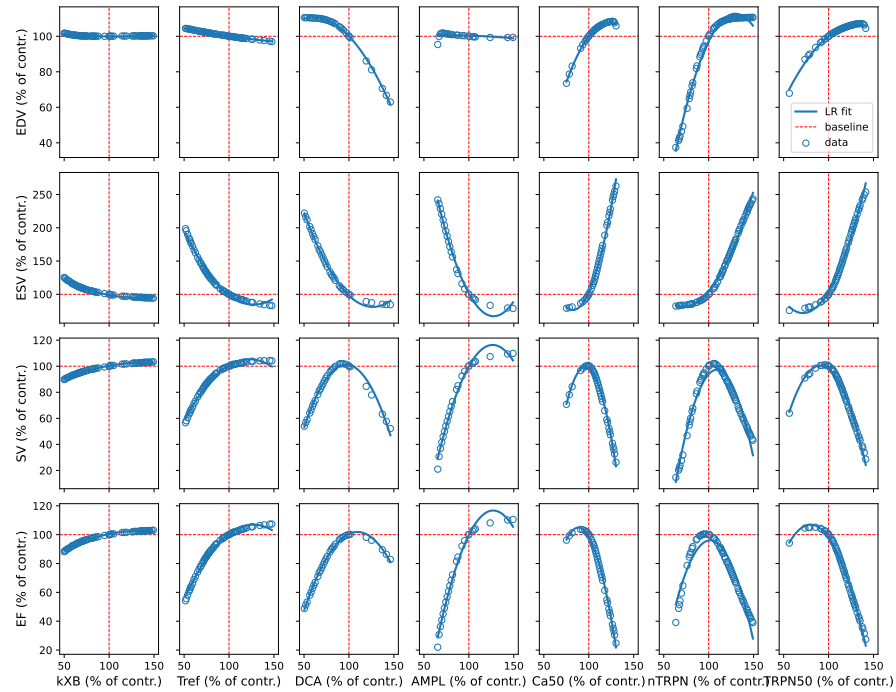


Figure 7.15: Personalised healthy rat heart contraction model LV volume features' response to model parameters' one-at-a-time variation. Both input parameters and output features are given as percentages of their baseline values (vertical and horizontal red dashed lines, respectively). Simulated features' values are displayed as open blue dots. A linear regression (LR) model with second-order degree polynomials is fitted to the data (blue lines) to facilitate the visualisation of non-linear and non-monotonic relationships between the features and each parameter.

Although the  $k_{xb}$  and  $T_{ref}$  parameters resulted in a non-negligible impact on the considered LV features, we can state that the results from this sensitivity analysis are consistent with the GSA results (Section 7.4.1). In Figure 7.15, we can see that the relationship between the considered input parameters and output features is non-linear and non-monotonic. Moreover, we can see that the parameters identified as the most important by the GSA are operating at a maximum with their reference values, where a small change can cause a sharp variation in the slope of LV features' variation, whereas  $k_{xb}$  and  $T_{ref}$  are operating on a stable slope where their impact is saturating.

In Section 7.4.2 we have seen that the emulators were able to predict with high accuracy the same quantitative compounds' effects on the examined LV features as the ones obtained using the simulator. However, the accuracy notably decreased, and uncertainties increased when predicting high compound concentration values. We know that high concentrations of  $\text{Ca}^{2+}$  channel blockers are associated with vanishing  $\text{Ca}^{2+}$  transients. Since vanishing  $\text{Ca}^{2+}$  transients also made the simulator fail due to small  $\text{Ca}^{2+}$  signal amplitudes (Section 7.3.3), the training dataset consequently did not contain parameter points encoding this kind of  $\text{Ca}^{2+}$  transient shape. Therefore, predicting high compound concentration regions resulted in performing extrapolation outside the emulators' training space boundaries, which can explain the observed reduction in prediction accuracy.

Building a ZSF1 rat model by perturbing the SHAM model is a pragmatic choice. Ideally, one would want to start from MRI images of the obese ZSF1 rat and its related control (lean ZSF1 rat), create an *in silico* representation of both by fitting model parameters to haemodynamic measurements (possibly obtained from the same experimental rats' cohorts) and then attempt to "virtually" recover the obese rat (diseased state) towards the lean rat (healthy state). The calculated percentages of recovery pointed out that all the parameter groups are able to recover the cardiac function to similar degrees. Since every parameter group represents a strategy of recovery, this results in weighting all the types of recovery equally, and in real life situations, each of them might have a different weight of clinical importance. However, this information can potentially be included in our analysis by weakening or strengthening the implausibility criterion for parameters that have to be more important than others.

More general limitations of the adopted modelling framework can be found in Chapter 9, Section 9.2.

## 7.6 SUMMARY

We have used a validated biophysically detailed computational model of 3D biventricular rat heart mechanics and a Bayesian probabilistic framework to provide an indication of potential cellular pharmacological targets to evaluate the recovery of the LV function in an animal model of HFP EF. This combination of forward deterministic modelling with machine learning techniques proved crucial to carry out analyses that are usually too computationally intensive to be performed within reasonable timescales. Furthermore, the developed framework can easily be adapted to solve many other different systems biology problems and could potentially aid the drug discovery and development process at preclinical stages.

## IN SILICO QUANTITATIVE MAPPING OF FORCE-PCA CURVES TO WHOLE HEART CONTRACTION AND RELAXATION

### OUTLINE

In this chapter, we focus on the assessment of the steady-state F-pCa relationship (this is traditionally used to assess the myofilament  $\text{Ca}^{2+}$  sensitivity) and its quantitative mapping to the LV contractile function. We start by investigating the F-pCa curve using the cell contraction sub-model of our full personalised SHAM rat heart contraction model (Section 8.2.1). Next, using a combination of simulators and emulators (Section 8.2.3), we show that changes in key features of the F-pCa curve cannot be uniquely described by changes in the sarcomere properties (Sections 8.3.2–8.3.3). At the same time, we show that changes in the LV function (e.g. ejection fraction, isovolumetric relaxation time, peak pressure) cannot be uniquely described by changes in the sarcomere properties (Section 8.3.4). By coupling these two pieces of information, we demonstrate that the mapping from the F-pCa curve to the LV function and the corresponding inverse mapping are non-unique (Section 8.3.5). We then include a discussion of results and address specific limitations (Section 8.4), and we conclude with a brief summary (Section 8.5).

### 8.1 MOTIVATION

One potential assessment for sarcomere modulators is their impact on the F-pCa [238], which is a technique that is widely used in many HF diseases including rare/genetic diseases such as dilated and hypertrophic cardiomyopathies [15, 70, 75, 106, 157], as well as for HF with reduced and preserved ejection fraction [13, 98, 103, 151, 160, 221]. The impact on the F-pCa curve is often examined in terms of observed shifts in the curve half-maximal activation ( $\text{pCa}_{50}$ ), which is used as an index of  $\text{Ca}^{2+}$  sensitivity. Leftward shifts in the  $\text{pCa}_{50}$  are expected to improve contractility, whereas rightward shifts to decrease contractility. Sometimes there is an assumption that changes in  $\text{Ca}^{2+}$  sensitivity are a surrogate for changes in whole heart function and that these changes are monotonic in that, for instance, an increase in myofilament  $\text{Ca}^{2+}$  sensitivity (i.e. a leftward shift) would improve the whole heart cardiac output. In this case study, whose related manuscript is currently in submission [138], we discuss the limitations of such an

assumption and demonstrate why the dynamic whole heart behaviour cannot be predicted or assessed with a shift in the F-pCa curve alone.

We use a mathematical model of active tension generation at the sarcomere level in LV rat myocytes to elucidate the relationship between sarcomere properties and the steady-state F-pCa curve. We next use our previously developed multi-scale model of SHAM rat heart, which integrates the cell tension model within a 3D biventricular rat heart contraction model (Section 7.3.1) and provides a quantitative link between sarcomere properties and whole heart contractile function to investigate the mapping from F-pCa curves to the LV function. In particular, using our framework, we are able to quantitatively link changes in the F-pCa curve to/from changes in the LV function for the first time to the best of our knowledge. Previously, shifts in the F-pCa curve were linked to changes in cellular tension [42] but not to the whole-organ dynamic contractile behaviour and without investigating the inverse mapping. We use our modelling framework to show that observations made at the sarcomere level (e.g. a leftward shift in the F-pCa curve) do not uniquely map to desired effects at the whole-organ level (e.g. an increase in EF or improved relaxation). We also show that the opposite holds: given a change in LV function, there exist many ways this could have been achieved through sarcomeric modulation, and thus the same change in LV function can correspond to different shifts in the F-pCa curve. The implications of these phenomena on using F-pCa curves to interpret whole heart dynamics are discussed in Section 8.4.

## 8.2 METHODS

### 8.2.1 Cellular contraction model

We employed the Land et al. [119] myocyte contraction model (Section 2.2) to simulate active tension generation at the sarcomere level and isometric steady-state F-pCa relationship in the rat heart. Parameters were all set to the personalised SHAM rat model values (Table 7.9) when applicable, or to the Land et al. [119] model baseline values when otherwise.

We recall that an experimentally derived F-pCa curve can be described by a Hill-type relationship between the force ( $F$ ) and the negative logarithm of the  $\text{Ca}^{2+}$  concentration (pCa) [238]:

$$\frac{F}{F_0} = \frac{1}{1 + 10^{h(p\text{Ca}_{50} - p\text{Ca})}} \quad (8.1)$$

where  $F_0$  is the maximal reference force and  $p\text{Ca}_{50}$  and  $h$  are, respectively, the negative logarithm of the half-maximal effective  $\text{Ca}^{2+}$  concentration and the Hill coefficient of this relationship. It immediately follows that F-pCa curves are uniquely determined by the  $p\text{Ca}_{50}$

and  $h$  values. We have also seen that the steady-state force solution of the Land et al. [119] model can be derived analytically, where both the  $p\text{Ca}_{50}$  and  $h$  features are expressed in terms of model parameters. In particular, we recall that the  $p\text{Ca}_{50}$  was given as:

$$p\text{Ca}_{50}(\mathbf{p}) = -\log \left[ \text{Ca}_{50} \left( \frac{k_{\text{off}}}{k_{\text{on}}} \frac{\text{TRPN}_{50}}{1 - \text{TRPN}_{50}} \right)^{1/n_{\text{trpn}}} \right], \quad \text{with} \quad (8.2)$$

$$\mathbf{p} := (\text{Ca}_{50}, k_{\text{on}}, k_{\text{off}}, \text{TRPN}_{50}, n_{\text{trpn}}) \quad (8.3)$$

In the next section, we shall make use of equations (8.2)–(8.3) to investigate on F-pCa curve shifts.

### 8.2.2 Non-unique mapping of changes in $p\text{Ca}_{50}$ to changes in sarcomere properties

A given change ( $\Delta$ ) in the  $p\text{Ca}_{50}$  feature value of the F-pCa curve can be written as:

$$\Delta = p\text{Ca}_{50}^{\text{new}} - p\text{Ca}_{50} \quad (8.4)$$

where  $p\text{Ca}_{50}^{\text{new}}$  is the feature value characterising the newly observed F-pCa curve. We tested whether a shift of  $\Delta$  units in the  $p\text{Ca}_{50}$  could be the result of unique changes in sarcomere properties. Testing for non-unique changes was carried out analytically and numerically (as visualised in Figure 8.4) in the case where the change was driven by perturbations in one model parameter (Section 8.3.2), and numerically (as visualised in Figure 8.5) in the case where this was driven by perturbations in two model parameters (Section 8.3.3).

In the one-parameter case, it sufficed to prove that for each parameter  $p_i$ ,  $i = 1, \dots, 5$  of equation (8.3) there exists a scaling coefficient  $\alpha_i \in \mathbb{R}$  such that

$$\mathbf{p}^{\text{new}} := (p_1, \dots, p_{i-1}, \alpha_i \times p_i, p_{i+1}, \dots, p_5) \quad (8.5)$$

is such that

$$p\text{Ca}_{50}^{\text{new}} = p\text{Ca}_{50}(\mathbf{p}^{\text{new}}) \quad (8.6)$$

We computed this scaling coefficient for each parameter  $p_i$  by solving for  $\alpha_i$  equation (8.4) for a given  $\Delta$ .

In the two-parameter case, we proceeded as follows. We allowed 2 parameters to take equally-spaced values within a  $\pm 50\%$  perturbation around their baseline values (Table 7.9). We then generated a 2D uniform grid from all the combinations of 2 parameter values and used the Land et al. [119] cell contraction model to calculate the  $p\text{Ca}_{50}$

value at each parameter point of the grid. By plotting the resulting  $p\text{Ca}_{50}$  values across the grid as a heat map, we could discern regions in the 2D parameter space that share the same  $p\text{Ca}_{50}$  value (isolines). The same process was repeated for pairs of parameters coming from vector  $\mathbf{p}$  (equation (8.3)), which was shown to regulate the  $p\text{Ca}_{50}$  feature of the F-pCa curve (equation (8.2)).

### 8.2.3 The relationship between sarcomere properties and LV function

To quantitatively link sarcomere properties to the LV function, we employed the personalised model of 3D biventricular healthy (SHAM) rat heart contraction derived in Chapter 4 and extended in Chapter 7. This model integrates the Land et al. [119] cell contraction model in the context of whole-organ simulations.

We have seen (Section 7.3.1) that this model can be represented as a multi-scale function (simulator) that maps a 16D vector of input parameters  $\mathbf{x}$  to a scalar quantity of interest  $y_j$  (e.g.  $y_1 = \text{EDV}$ ,  $y_2 = \text{ESV}$ , etc.):

$$\begin{aligned} f_{\text{simul}}: \mathbb{R}^{16} &\rightarrow \mathbb{R} \times \mathbb{R} \times \dots \\ \mathbf{x} &\mapsto (y_1, y_2, \dots) \end{aligned} \tag{8.7}$$

At the same time, we have replaced (Section 7.3.3) the simulator with a fast-evaluating surrogate model (emulator), based on Gaussian process emulation.

We used the simulator to investigate the dependence of LV volume features, namely EDV, ESV, SV, and EF, on model parameters. Specifically, we were interested in the dependence of the features on the  $\text{Ca}_{50}$ ,  $k_{\text{off}}$ ,  $n_{\text{trpn}}$  and  $\text{TRPN}_{50}$  parameters as these directly modulated the  $p\text{Ca}_{50}$  feature of the F-pCa curve (equation (8.2)). For each parameter, we performed the following operations. First, the simulator was run at 128 input points  $\mathbf{x}_i$ ,  $i = 1, \dots, 128$ , which had all their 16 components fixed to baseline values (Table 7.9) but the component corresponding to the examined parameter, which instead was set to 128 equally-spaced values between  $-50\%$  and  $50\%$  of perturbation values from baseline. The LV volume features were then extracted from the simulated 128 LV volume transients so that we could plot the variation of each feature as a function of the parameter variations around its baseline value.

We then used the emulator to perform a GPE-based GSA. We calculated the Sobol' first-order, second-order and total effects (Section 3.6) as a measure of model outputs' sensitivity to model inputs. We evaluated the impact of  $\text{Ca}_{50}$ ,  $k_{\text{off}}$ ,  $n_{\text{trpn}}$ ,  $\text{TRPN}_{50}$  parameters into affecting the total variance of EDV, ESV, SV, EF features. Parameters whose Sobol' indices' distributions' expectation was below the threshold 0.01 were determined to have negligible effects.

#### 8.2.4 Non-unique mapping of changes in LV function to changes in sarcomere properties

Left ventricular EF can be continuously monitored noninvasively as an index of LV systolic function in patients enrolled for clinical trials investigating HF treating drugs. However, it is important to discern whether detected changes in the EF value directly result from a specific cellular modulation caused by the administered drug or not. From a modelling perspective and in the context of sarcomere modulators, we can test whether changes observed in the LV function at the whole-organ level, as described by the EF feature, can be uniquely explained in terms of sarcomere properties' changes.

We therefore proceeded as in Section 8.2.2 by generating a 2D uniform grid of parameter values for each considered pair of parameters modulating the F-pCa curve (equation (8.2)). We then used the emulator to predict the EF value at each parameter point of the grid. By plotting the resulting EF values across the grid as a heat map, we could again discern regions in the 2D parameter space that share the same EF value (isolines).

#### 8.2.5 Non-unique mapping of F-pCa curve to LV function and of LV function to F-pCa curve

In order to test if the mapping from the F-pCa curve to LV function is not unique, we considered all the parameter points of the 2D grids generated in Section 8.2.2 that produced the same shift in the reference  $p\text{Ca}_{50}$  feature value. As mentioned previously, these points all belong to isolines of the local 2D parameter space. We then used the emulator to map the points to the corresponding organ-level EF value.

We also tested if the inverse mapping from the LV function to the F-pCa curve is not unique. For this purpose, we considered all the parameter points of the 2D grids generated in Section 8.2.4 that produced the same shift in the reference EF feature value. We then used the cellular contraction sub-model of the full simulator to map the points to the corresponding cell-level  $p\text{Ca}_{50}$  value.

### 8.3 RESULTS

#### 8.3.1 Non-monotonic relationship between sarcomere parameters and LV function

The variations of EDV, ESV, SV and EF features as a function of the 4 considered F-pCa curve-modulating parameters (equation (8.2)) are non-linear and non-monotonic, as shown in Figure 8.1. An example of

full simulator outputs comprising LV volume and pressure transients and PV loops is provided in Figure 8.2 for the EF-vs- $k_{\text{off}}$  case.

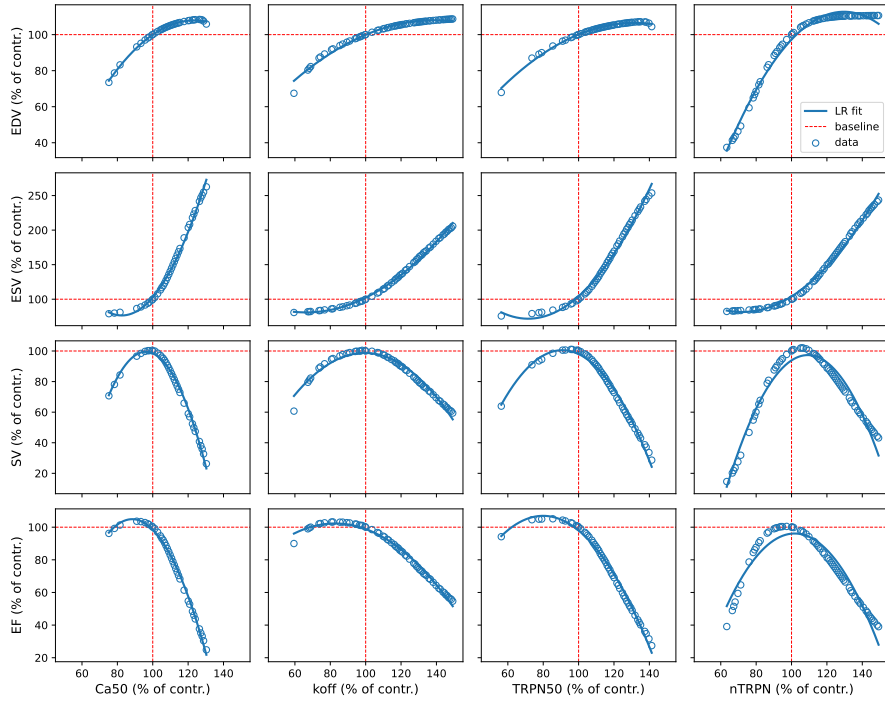


Figure 8.1: The full 3D biventricular rat heart contraction model is run at a fixed parameter set with only one parameter taking equally-spaced values in the  $\pm 50\%$  range of perturbation from its baseline value (vertical red dashed lines). The converging mechanics simulations' output PV loops are analysed to extract the corresponding EDV, ESV, SV and EF features' values (open blue dots), given as percentages from their baseline values (horizontal red dashed lines). The process is repeated separately for each parameter regulating the  $\text{pCa}_{50}$  feature of the F-pCa curve. A linear regression (LR) model with second-order degree polynomials is fitted to the data (blue lines) to facilitate the visualisation of non-linear and non-monotonic relationships between the features and each of the parameters considered.

The obtained GSA Sobol' sensitivity indices are displayed as donut charts in Figure 8.3. We can see that the reference thin filament  $\text{Ca}^{2+}$  sensitivity ( $\text{Ca}_{50}$ ) is the most important parameter in explaining the total variance of EDV, ESV, SV and EF features. The second most important parameter is the degree of cooperativity of  $\text{Ca}^{2+}$  binding to TnC ( $n_{\text{trpn}}$ ), followed by the fraction of bound  $\text{Ca}^{2+}$ -TnC complexes for half-maximal cross-bridges activation ( $\text{TRPN}_{50}$ ) and the unbinding rate of  $\text{Ca}^{2+}$  from TnC ( $k_{\text{off}}$ ).

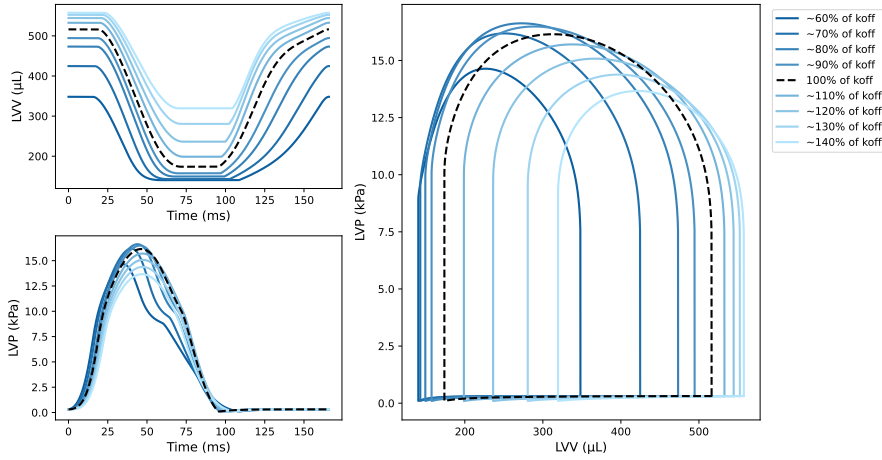


Figure 8.2: The full 3D biventricular rat heart contraction model is run at a fixed parameter set with only one parameter varying around its baseline value. The resulting LV volume and pressure transients and corresponding PV loops are plotted for some of the parameter values (full lines in blue variants) and compared to the reference parameter set mechanics solution (dashed black line). Example showing  $k_{off}$  parameter variation in the range obtained as a  $\pm 40\%$  perturbation of its baseline value.

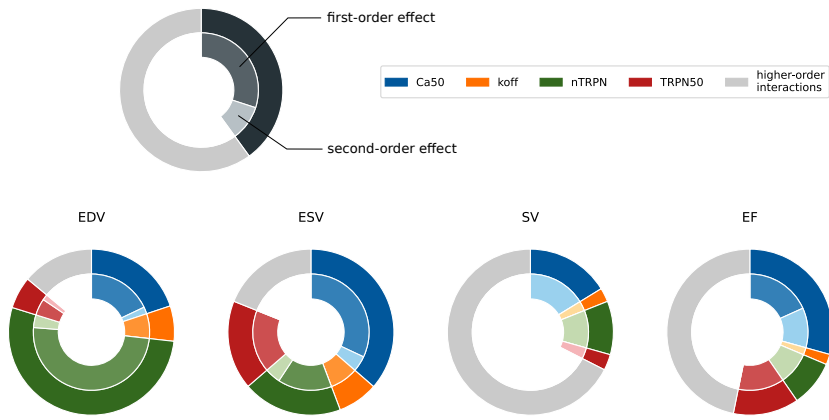


Figure 8.3: The impact of  $pCa_{50}$ -modulating, sarcomere parameters on EDV, ESV, SV and EF organ-scale LV feature. The contribution of each parameter is represented by the sum of its first- and second-order effects. For each LV feature, higher-order interactions (up to the fourth order) are represented by the sum of all total effects minus the sum of all first- and second-order effects.

### 8.3.2 $pCa_{50}$ changes are non-uniquely explained by sarcomere alterations: the one-parameter case

We show that an observed change in  $pCa_{50}$  can be caused by multiple different changes in sarcomere proprieties represented by model parameters. For each parameter  $p_i$ ,  $i = 1, \dots, 5$  of equation (8.3), we re-

port in Table 8.1 the corresponding scaling coefficient  $\alpha_i$ ,  $i = 1, \dots, 5$  that would yield a shift of exactly  $\Delta$  units in the  $p\text{Ca}_{50}$  value. This proves that an observed change in the F-pCa cannot be uniquely explained by a change in a specific sarcomere property. An example of  $\pm 2\%$  shift from a reference  $p\text{Ca}_{50}$  value is displayed in Figure 8.4.

PARAMETER	SCALING COEFFICIENT $\alpha$
$\text{Ca}_{50}$	$10^\Delta$
$k_{\text{on}}$	$10^{-\Delta \cdot n_{\text{trpn}}}$
$k_{\text{off}}$	$10^{\Delta \cdot n_{\text{trpn}}}$
$\text{TRPN}_{50}$	$\frac{10^{\Delta \cdot n_{\text{trpn}}}}{\text{TRPN}_{50}(10^{\Delta \cdot n_{\text{trpn}}} - 1) + 1}$
$n_{\text{trpn}}$	$\frac{\log\left(\frac{k_{\text{off}}}{k_{\text{on}}} \frac{\text{TRPN}_{50}}{1-\text{TRPN}_{50}}\right)}{\Delta \cdot n_{\text{trpn}} + \log\left(\frac{k_{\text{off}}}{k_{\text{on}}} \frac{\text{TRPN}_{50}}{1-\text{TRPN}_{50}}\right)}$

Table 8.1: The mapping of sarcomere properties to F-pCa variations is non-unique. By scaling each parameter  $p_i$  by the corresponding  $\alpha_i$  coefficient, the cellular contraction model simulates a  $p\text{Ca}_{50}$  value which is shifted by exactly  $\Delta$  units from the reference value.

### 8.3.3 $p\text{Ca}_{50}$ changes are non-uniquely explained by sarcomere alterations: the two-parameter case

$p\text{Ca}_{50}$  evaluation on 2-parameter grids highlighted the presence of isolines, whose parameter points induce the same  $p\text{Ca}_{50}$  feature value (Figure 8.5A). This means that moving between any two points on two isolines will result in the same shift in  $p\text{Ca}_{50}$ , demonstrating also in the two-parameter case the non-uniqueness of changes in the half-activation of the F-pCa curve and a change in sarcomere properties.

#### 8.3.3.1 Non-unique mapping of F-pCa curve to LV function

Parameter points inducing the same shifts in the  $p\text{Ca}_{50}$  feature value (isolines of Figure 8.5A) are quantitatively linked to different EF feature values (Figure 8.5B), showing that the mapping from F-pCa curve to LV function is not unique.

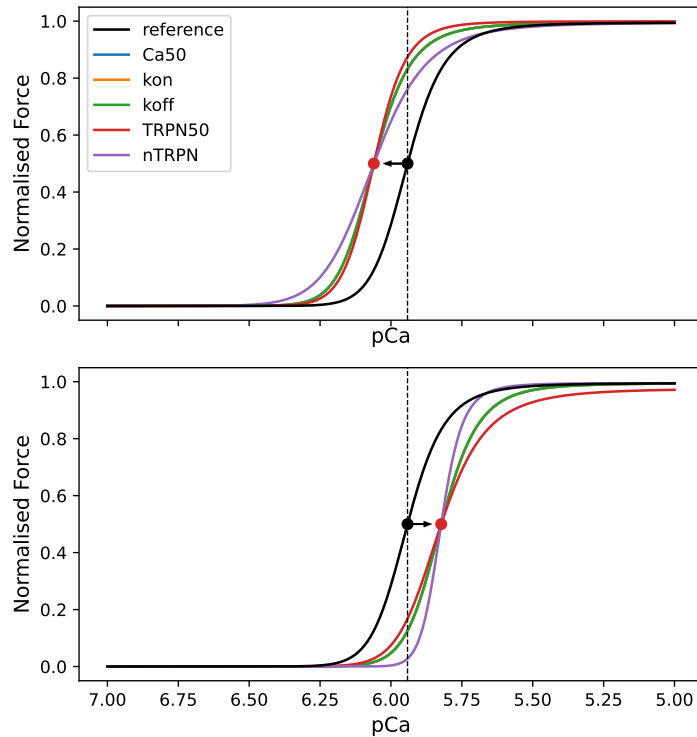


Figure 8.4: Different parameters can be individually perturbed to achieve the very same shift in the force-calcium relationship. Example showing 2 % leftwards (upper plot) and rightwards (bottom plot) shifts of the reference  $p\text{Ca}_{50}$  value. As  $\text{TRPN}_{50}$  and  $n_{\text{trpn}}$  also regulate the F-pCa curve's Hill coefficient (equation (2.19)), notice that for these two parameters the shift in the  $p\text{Ca}_{50}$  value is also affecting the curve's slope.

### 8.3.4 LV function changes are non-uniquely explained by sarcomere alterations

EF evaluation on 2-parameter grids highlighted the presence of isolines, where all parameter combinations along these lines result in the same predicted EF (Figure 8.6A). This means that moving between any two points on each isoline will result in the same EF, demonstrating the non-uniqueness of the LV function and sarcomere properties.

#### 8.3.4.1 Non-unique mapping of LV function to F-pCa curve

Parameter points that give rise to the same predicted EF value (isolines of Figure 8.6A) are quantitatively linked to different  $p\text{Ca}_{50}$  values (Figure 8.6B), showing that the mapping from LV function to the F-pCa curve is not unique.

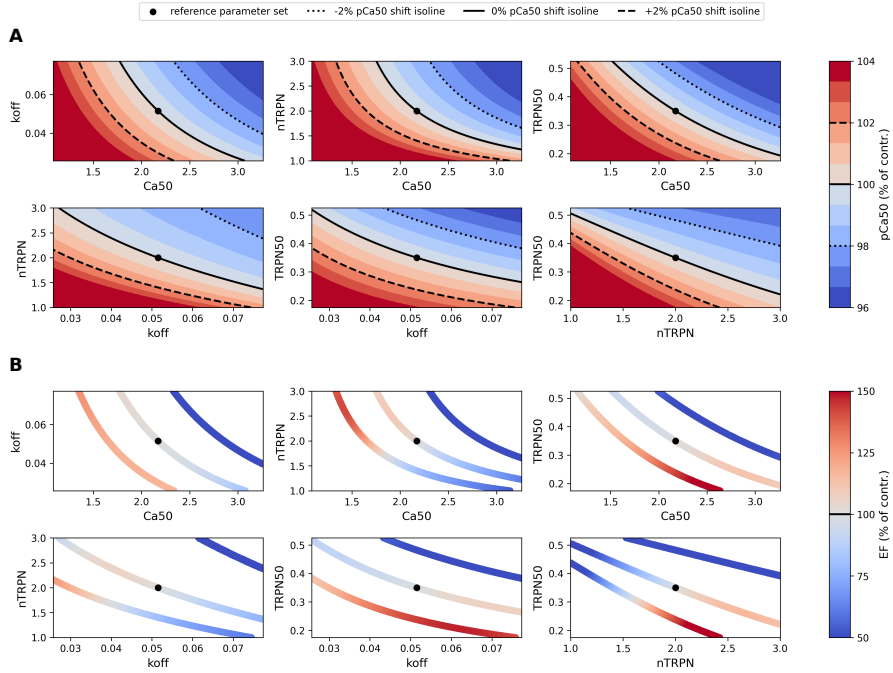


Figure 8.5: For each pair of parameters regulating the pCa<sub>50</sub> feature of the F-pCa curve, a 2D uniform grid is constructed using a ±50 % perturbation around the reference parameter set values (black dots). (A) The cell contraction model is then used to calculate the pCa<sub>50</sub> feature value at every parameter point of the grid, and each grid is plotted as a heat map with values given as percentages from the control pCa<sub>50</sub> value. Contour plots are finally added to highlight the presence of isolines, whose many different parameter sets induce the same shift (-2 % dotted, 0 % full, +2 % dashed black lines) in the control pCa<sub>50</sub> value. (B) Parameter points from the obtained isolines are mapped by the emulator into EF feature values. These values (given as percentages of the control EF value) are represented by different colour intensities used to colour each parameter point in the isolines, showing that parameters that share the same pCa<sub>50</sub> values are linked to different EF values.

### 8.3.5 Non-unique mapping from/to F-pCa curve to/from LV function

In Sections 8.3.2–8.3.3, we proved that changes in the pCa<sub>50</sub> value are not uniquely caused by changes in sarcomere properties. In Section 8.3.3.1, we also showed that changes in the EF value are not uniquely caused by changes in the pCa<sub>50</sub> value. Because of these two findings, we can state that observed changes in the F-pCa curve cannot be uniquely mapped to changes in the LV function.

At the same time, in Section 8.3.4 we proved that changes in the EF feature value are not uniquely caused by changes in sarcomere properties. In Section 8.3.4.1, we also showed that changes in the pCa<sub>50</sub> feature value are not uniquely caused by changes in the EF value. Because of these two other findings, we can state that observed

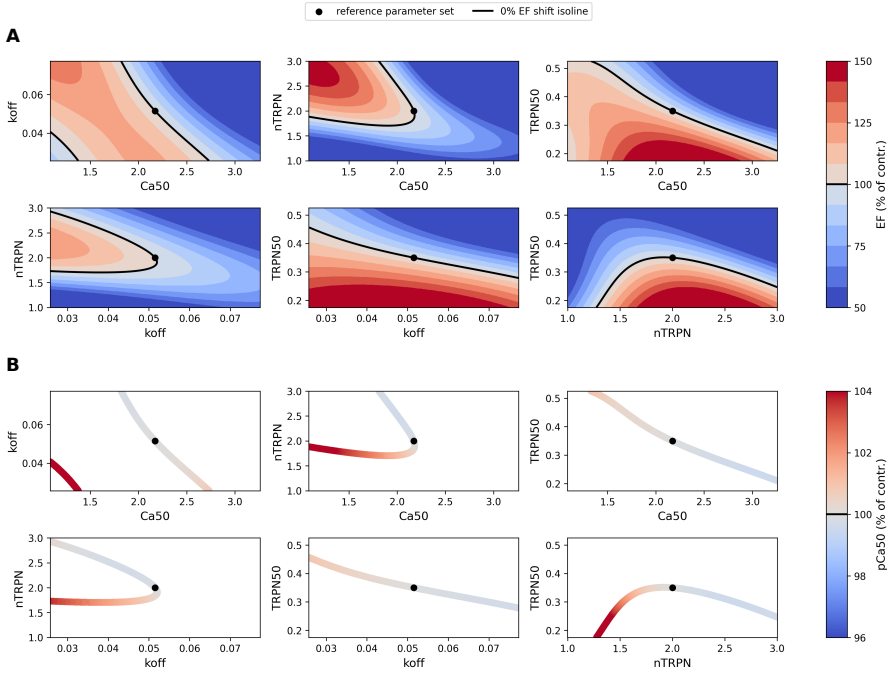


Figure 8.6: For each pair of parameters regulating the  $p\text{Ca}_{50}$  feature of the F-pCa curve, a 2D uniform grid is constructed using a  $\pm 50\%$  perturbation around the reference parameter set values (black dots). (A) A trained emulator is then used to predict the EF feature value at every parameter point of the grid, and each grid is plotted as a heat map with values given as percentages from the control EF value. Contour plots are finally added to highlight the presence of isolines (full black lines), whose many different parameter sets induce the same 0 % shift in the control EF value. (B) Parameter points from the obtained isolines are mapped by the cell contraction model into  $p\text{Ca}_{50}$  feature values. These values (given as percentages of the control  $p\text{Ca}_{50}$  value) are represented by different colour intensities used to colour each parameter point in the isolines, showing that parameters that share the same EF values are linked to different  $p\text{Ca}_{50}$  values.

changes in the LV function cannot be uniquely mapped to changes in the F-pCa curve.

#### 8.4 DISCUSSION

In this study, we have made use of mathematical models to characterise the relationship between sarcomere properties and the LV contractile function in the healthy rat heart. We have highlighted the presence of complex nonlinearities; in particular, we have demonstrated that the relationship between myofilaments' features (e.g.  $\text{Ca}_{50}$ ) and PV loop characteristics (e.g. EF) is non-monotonic. As these sarcomere properties also define the steady-state F-pCa relationship in the cardiac muscle, we extended this result in terms of shifts in the F-pCa

curve that are often examined when experimentally assessing the effect of sarcomere-targeting pharmacological compounds. Therefore, we have provided both analytical and simulation study evidence that alterations in the F-pCa curve can cause very different changes in whole heart function. At the same time, we have shown that observed changes in the LV function cannot be attributed to a unique modification in sarcomere properties. Although in the previous sections we have characterised the LV function using EF, the obtained results generally hold for many other clinically relevant indexes of LV systolic and diastolic function, e.g. IVRT and PeakP, as visualised in Figures 8.7–8.8. To design new treatment strategies, solely looking at the induced shift in the  $p\text{Ca}_{50}$  feature value of the F-pCa curve on its own is therefore not enough to predict or to understand predictions of how this will be translated into whole-organ function changes.

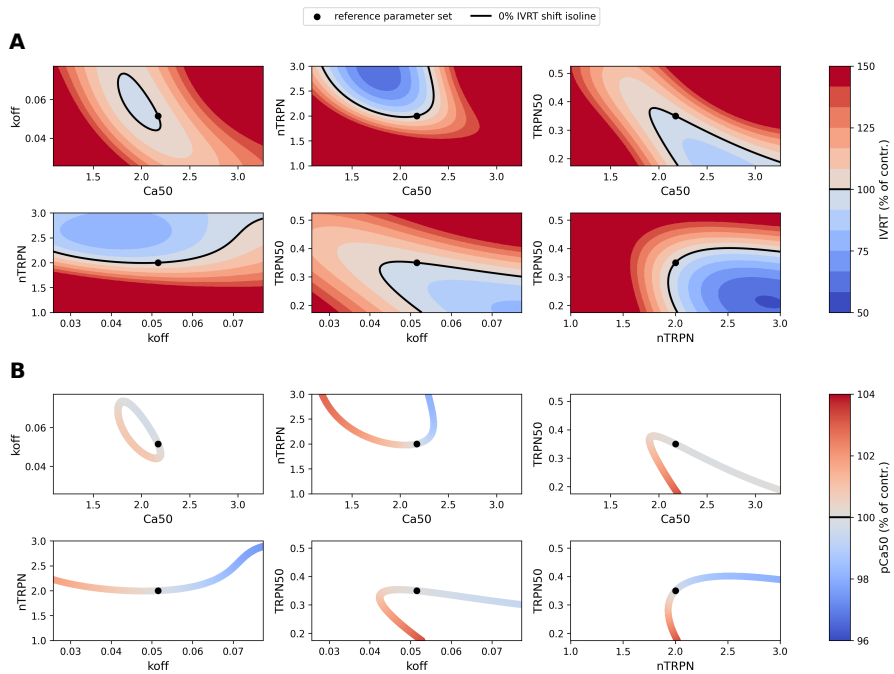


Figure 8.7: The same IVRT value (A) can be linked to different  $p\text{Ca}_{50}$  values (B) (i.e. to differently shifted F-pCa curves).

Also, when studying myofilament  $\text{Ca}^{2+}$  sensitivity using F-pCa curves, simply considering the  $p\text{Ca}_{50}$  value as a stand-alone measurement is not sufficient for translation into dynamic contraction and relaxation. This concept was previously shown for single-cell dynamics by Chung et al. [42] who highlighted the importance of biophysical measures of  $k_{\text{off}}$  and  $k_{\text{on}}$  to help predict tension dynamics at the cellular level. However, in this work, we expand this concept further to the whole heart level by analysing LV features and exploring the inverse mapping from LV features to F-pCa curves, highlighting the non-uniqueness of both forward and inverse mapping between F-pCa

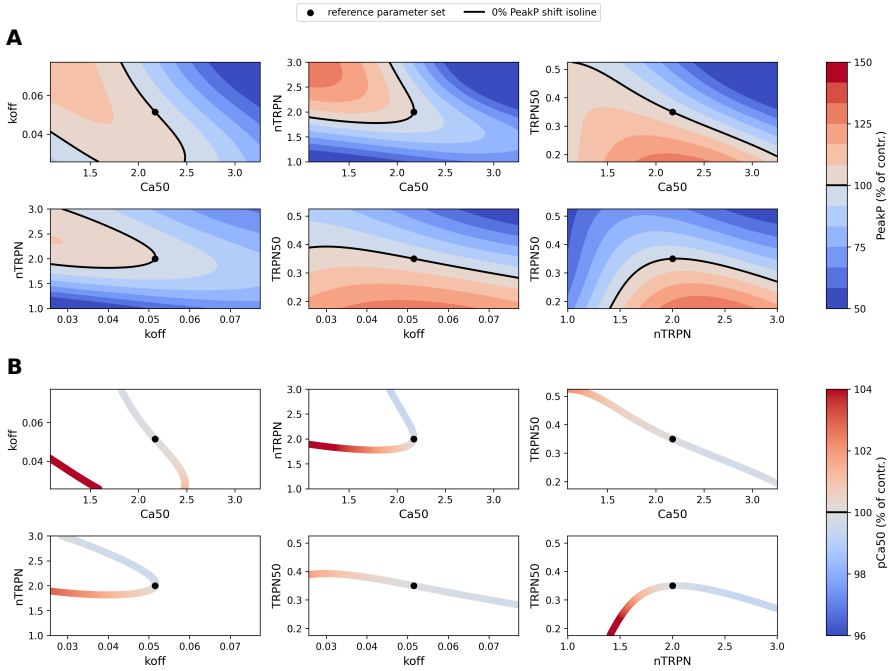


Figure 8.8: The same PeakP value (A) can be linked to different  $p\text{Ca}_{50}$  values (B) (i.e. to differently shifted F-pCa curves).

and LV features. We emphasise that, for instance, an increase in  $\text{Ca}^{2+}$  sensitivity, i.e. a leftward shift in the F-pCa curve, will have two effects. First, it will increase residual tension, decreasing EDV; second, it will increase end-systolic tension, decreasing ESV. The balance of these two effects will impact the change in SV and EF for a given change in  $\text{Ca}^{2+}$  sensitivity. This impact of changes in  $p\text{Ca}_{50}$  depends on the starting F-pCa curve, the  $\text{Ca}^{2+}$  transient, cardiac material properties and boundary conditions. Determining these multi-scale relationships from experimental preparations remains challenging.

The performed GSA interpreted the variability of EDV, ESV, SV and EF in terms of the uncertainty in F-pCa curve-modulating sarcomere parameters, and it emphasised the importance of the  $\text{Ca}^{2+}$  sensitivity in affecting these PV loop characteristics. Deeper insight can be gained if we look at higher-order interactions' effects. Although these are present for all the four LV features considered, they are remarkably high only for the SV and EF features, explaining more than half of the total variance for SV and almost half of the total variance for EF. We can notice that for the EDV and ESV features, higher-order interactions' effects are instead small, and dominating effects are mostly of the first-order type. Conversely, for the SV and EF features where higher order interactions' effects are high, dominating lower-order effects are mostly of the second-order type. All these considerations can be summarised by stating that although it is possible to interpret changes in terms of the individual contribution of parameters for the EDV and

ESV features, this is not the case for SV and EF features. In this sense, it is more the combined effect of the whole sarcomere to determine the LV function rather than single myofilament components.

Indications from the GSA coupled with the information of F-pCa curve vs LV function non-monotonicity shed new light on the problem of interpreting pharmacological interventions' effects on the F-pCa curve in terms of the desired effects on whole-heart function. This concept is illustrated via the schematic in Figure 8.9, which highlights existing feedback mechanisms that regulate contraction in the heart. Modulation of the  $\text{Ca}^{2+}$  transient can directly affect the active tension which is generated within the sarcomere, and alteration of the sarcomere generated force will eventually affect the PV loop. As the force-volume relationships at the end-diastolic and end-systolic pressures are fixed, sarcomere interventions that aim at shifting the F-pCa might result in no change in LV contractile function. For this reason, treatment strategies should aim at altering both the end-systolic and end-diastolic force-volume relationships or altering one while maintaining the other to yield an effect on EF.

#### 8.4.1 *Limitations*

The limitations of this study mainly concern the adopted modelling/emulation framework, and are presented fully in Chapter 9, Section 9.2.

## 8.5 SUMMARY

We have used a biophysically detailed mathematical model of a healthy rat heart contraction to quantitatively map sarcomere properties to whole heart function. Using this mapping, we demonstrated that the relationship between the F-pCa curve and LV function is non-linear and non-monotonic. This results in the non-interpretability of observed changes in the LV function in terms of unique sarcomere modulations, which highlights the need for muscle experimental findings to be put into a broader context where not only the  $\text{pCa}_{50}$  and Hill coefficient but also active and passive force, length and velocity dependencies, calcium transient and boundary conditions are analysed.

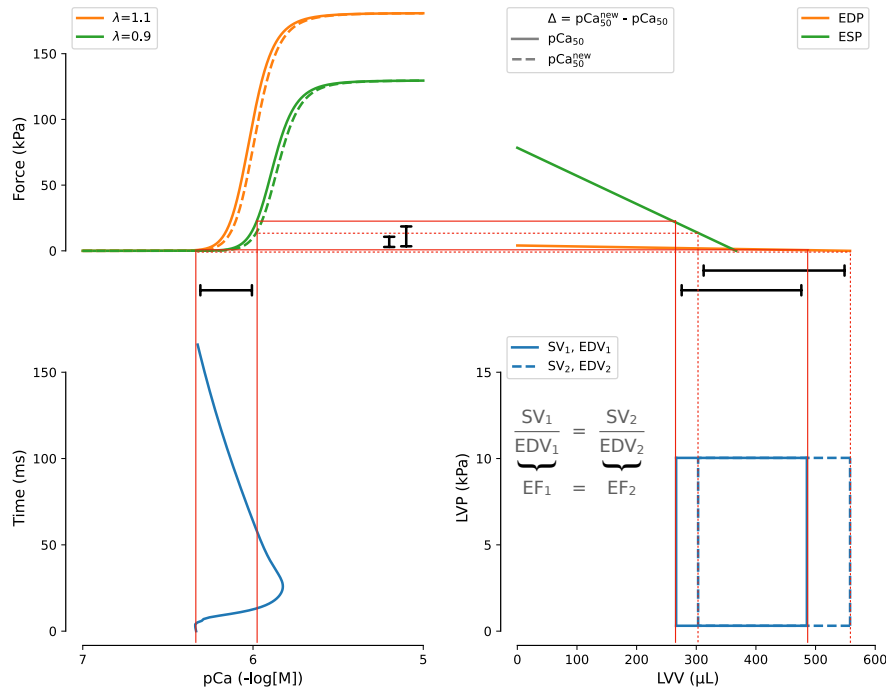


Figure 8.9: Force-LV volume curves at the end-diastolic and end-systolic pressures (top right, orange and green lines) can be separately manipulated to modulate the LV contractile function. However, interventions on calcium transient (bottom left, blue line) and sarcomeric generated force (top left, orange and green full lines) both manifest as modifications of the former curves, which in turn causes modification of the PV loop (bottom right, blue full line). In addition, pharmacological modulations on the sarcomere might cause a shift of the force-calcium relationship (top left, orange and green dashed lines). However, this will preserve the EF (bottom right, blue dashed line) without improving LV contractile function, which was the desired outcome of the performed sarcomeric intervention.

Part IV

THE END

## CONCLUSION

---

### 9.1 CONTRIBUTION

The main contribution of this thesis is to have shown the feasibility of incorporating pre-existing probabilistic tools into pre-existing complex deterministic cardiac models, thus improving our understanding of the models themselves and enhancing their capabilities in terms of real-world applications. The developed framework can be easily extended/adapted to model differently complex/different biological systems. Specifically for the cardiac modelling community, this thesis constitutes an important step towards application to the more complex human heart for personalised medicine. Example applications of this framework can already be found for cardiac statistical shape analysis models [189], cardiac tissue electrophysiology models [60], cardiac four-chamber haemodynamics models [99].

### 9.2 LIMITATIONS

This thesis work has a number of limitations which can be grouped under three main topics: (1) rat heart model, (2) experimental data and (3) model emulation, fitting and uncertainty quantification. We shall discuss each of these separately in the next sections.

#### 9.2.1 *Rat heart model*

We have developed a 3D biophysically-detailed model of rat heart contraction mechanics. This model is inherently a simplification of the underlying real biological system, which we are aiming to represent *in silico*.

Firstly, the model is a two-chamber simplification of a real heart (no atria), and spatial boundary conditions do not account for the pericardium. Furthermore, this is not a closed-loop system, with pressure boundary conditions modelled using a three-element Windkessel model. Because of these boundary conditions, this virtual rat heart is closer to an *ex vivo* preparation rather than to an *in vivo* heart. All these factors (missing atria and pericardium, no closed-loop system) could play a role in constraining the cardiac mechanics [12, 224].

We have also not accounted for potential spatial variations in cellular properties and  $\text{Ca}^{2+}$  transient, and the latter homogeneously activates contraction throughout ventricular walls. In the case of single-

cell contractile function, both thin and thick filament dynamics were modelled using a simplified representation of the sarcomere, without a detailed mechanistic description of its components. Specifically, the cross-bridge kinetics is described by a two-state model where the strongly-/weakly-/un-bound states are collapsed into a single state. While more detailed models exist [117], their parameters are not necessarily constrained using experimental data due to difficulties in measuring subcellular processes and are not easily integrable into multi-scale whole-organ simulations. The used model is still able to recapitulate all the main sarcomere processes, including the length and velocity dependencies.

The simulator resulting by coupling all these models across multiple biological scales enabled us to quantitatively link single cell to whole heart function, yet it has shown in all the presented application results to be very sensitive to random parameter perturbations and prone to convergence failure. The model failure rate (non-converging points, given as a percentage of all the simulated points) was clearly dependent on and increasing with the number of input parameters being varied in each case, e.g. ~ 70.9 %, ~ 89.7 % and ~ 91.2 %, when varying 4 (Chapter 5), 8 (Chapter 4) and 16 (Chapter 7) parameters, respectively. This was expected, since the more parameters undergo variation at the same time, the higher the chance of generating a combination of parameter values which are incompatible with the physiological function they encode in the model. However, high model failure rates (~ 74.2 % and ~ 82.6 % for the SHAM and AB rat models, respectively) were also observed when simulating parameter sets coming from regions in the high-dimensional space which were supposed to be physiologically relevant, being these associated with the generation of non-imausible models for matching the whole-organ function variability observed experimentally (Chapter 4). As this poses a large limitation, we preliminary investigated the matter further by visually exploring the non-imausible parameter space to spot regions associated with non-converging simulations.

Figures 9.1–9.2 display all the simulated parameter points from the non-imausible space while highlighting which specific points led to a successfully completed simulator run. We can immediately notice that there are portions of each 1-dimensional slice of the space (commonly located at the boundaries of the known non-imausible space) where single parameters make the model independently fail, regardless of the other parameters' values. In other words, the model is incompatible with specific parameters taking values at the extremes of the space, which we recall was previously determined to be non-imausible by the emulators at the end of the HM procedure. 2-dimensional portions of the space where the model fails are also visible, meaning that the model is also incompatible with specific pairs of parameter values. The same argument will hold more in general for specific higher-

order combinations parameter values. Determining the sources of this parameter-model incompatibility is complex. As mentioned previously, model failure could be linked to unphysiological single parameter values and/or unphysiological combinations of parameters' values. However, the possibility of model failing due to a more stiff parameter region to solve despite the parameter values being physiologically relevant cannot be ruled out since the emulators smoothly interpolate the whole input parameter space and are not subject to numerical stability issues. To dissect out the possible sources of incompatibility, a more refined and robust mechanics solver might be needed, along with an improved emulator to deem implausible a bigger portion of the input parameter space where the simulator is likely going to fail because of numerical instabilities.

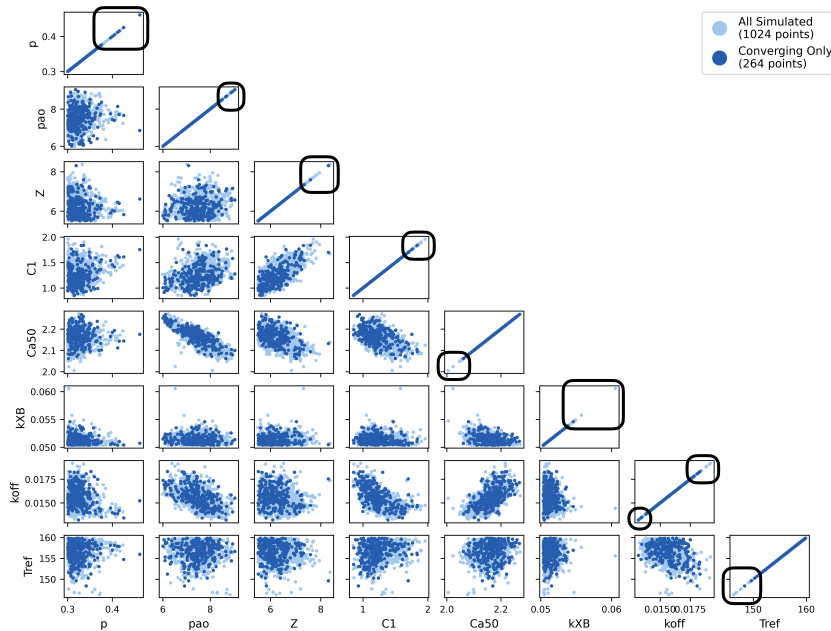


Figure 9.1: Non-implausible parameter space visual exploration for the SHAM rat model. The 8D simulated input parameter space is plotted as a 2D projection for each pair of parameters (light blue dots). The specific parameter sets leading to a converging mechanics simulation are further highlighted (dark blue dots) to spot regions of non-convergence. 1D slices of the full space where a single parameter might have independently led to model failure are additionally marked with a black rectangular box.

To conclude, it is worth mentioning that the developed rat heart contraction mechanics model is the combined result of different sub-modelling choices and assumptions, e.g. anatomy, fibre orientation, passive material properties, cell electrophysiology, tissue electrical activation, cell contraction, tissue contraction, spatial and haemodynamic boundary conditions (Chapter 2). This means that the inferences become conditional on all of those assumptions being true, which could

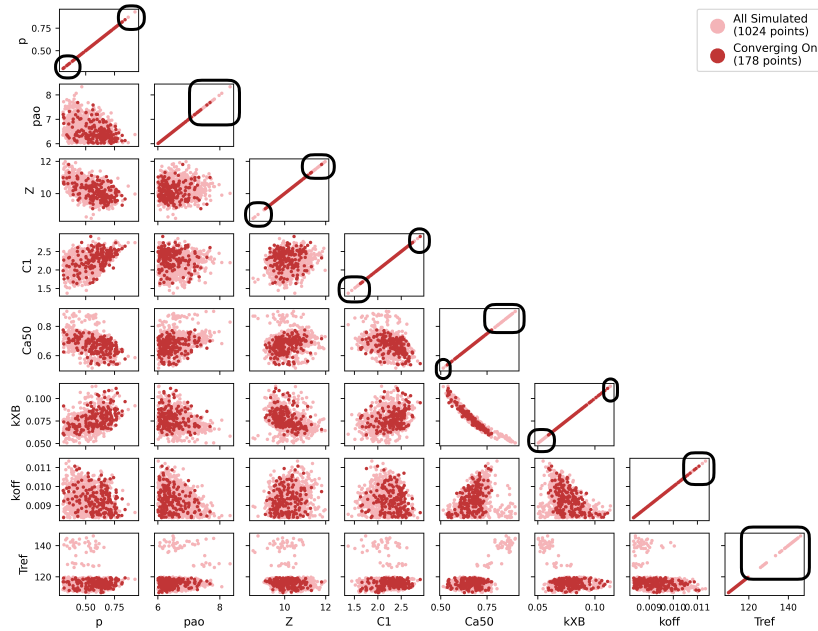


Figure 9.2: Non-implausible parameter space visual exploration for the AB rat model. The 8D simulated input parameter space is plotted as a 2D projection for each pair of parameters (light red dots). The specific parameter sets leading to a converging mechanics simulation are further highlighted (dark red dots) to spot regions of non-convergence. 1D slices of the full space where a single parameter might have independently led to model failure are additionally marked with a black rectangular box.

be a major source of discrepancy and therefore error in the final conclusions of any study we have presented within this thesis. Quantifying this discrepancy could go from looking for alternative modelling approaches i.e., different mathematical formulations for the same biological phenomena, through to simulating virtual populations of models.

### 9.2.2 Experimental data

Throughout the entire thesis, we have made extensive use of experimental data from different sources. However, we were never able to obtain a consistent dataset of measurements coming from experiments all performed within the same laboratory and thus under the same conditions and following the same protocols.

For the first study, when fitting the healthy and diseased rat models (Chapter 4), we had both the anatomy, cell electrophysiology and volumetric data coming from the same rat cohorts (SHAM and AB rats), although pressure data were taken from literature. In the second study for modelling the OM mechanisms of action (Chapter 5), all the data used were collected from literature studies and for different

species (rats for F-pCa data, pigs for LV haemodynamics data). For the third study, when performing model validation (Chapter 6), we used literature data of very different rat heart preparations, which were examined under different experimental conditions, protocols and studies. Finally, in the fourth study for identifying possible pharmacological compounds' targets for treating rat HFpEF (Chapter 7), we used ZSF1 rat data which came from many different literature studies.

The common strategy adopted in each of these studies was to project experimental observations into our current "system space" by means of averaging and percentages-of-variation calculation. Specifically, when the information about a specific feature value was provided in different studies, mean and standard deviation values for that feature were averaged to obtain the average mean and the average standard deviation for the feature across all the examined studies. This was a pragmatic choice; however, more formal approaches that make use of unbiased estimators of the sample mean and standard deviation could have been adopted to compute these statistics for a sample obtained as the combination of many samples, which also takes into account the dimension of each sample. Similarly, when the feature values could not be directly compared to our system values because the animal model was different or measurements were taken under different protocols, percentages of variation were first computed. These were then averaged as described above and finally applied to our system reference values.

### 9.2.3 *Model emulation, fitting and uncertainty quantification*

The use of emulators adds a layer of uncertainty in modelling the whole heart behaviour (LV contraction and relaxation). This is because emulators are probabilistic surrogates of the simulator, which is already an *in silico* representation/approximation of the real world biological system. However, the speed-up that we gain by using emulators, which enables efficient model fitting and global sensitivity analysis, by far outweighs the loss in quantitative accuracy when making predictions. Unlike other supervised machine learning techniques used for regression such as nearest neighbours, linear/logistic regression, decision trees or neural networks, Gaussian process regression still relies on Bayesian statistics, providing confidence interval estimates on the predictions, which makes it the preferred choice to quantify uncertainty in the models.

For both HM and GSA, we used independent GPEs for each output. This univariate approach provided us with the flexibility to tune the hyperparameters and choose basis functions for each output independently. However, it did not account for potential correlations in outputs, which could be accounted for with a multivariate strategy

(e.g. [47]), although this assumes common hyperparameters across all outputs. The GPEs trained in Chapters 4– 5–7 not always had their  $\text{ISE}_2$  scores  $\sim 95\%$  (which would correspond to a  $\pm 2$  standard deviations on a Normal probability density function). Cases of  $\text{ISE}_2$  score greater/lower than 95 % correspond to under-/over-confidence in emulator predictions, which could have affected the size of the ruled-out implausible and non-implausible spaces during HM. The GPE under-/over- confidence could point to its hyperparameters being assigned an inaccurate value during training. For this reason, alternative metrics [17] should be evaluated as well to help discerning whether the trained emulator is adequate as the simulator surrogate model for practical applications.

The HM technique provides a bounded region of non-implausible parameter sets. Parameter bounds do not define parameter distributions. Including an MCMC parameter fit using the HM bounds as priors would extend this method to estimate likely parameter distributions as opposed to parameter bounds. In the used implausibility measure (equation (3.51)) calculation, we omitted the model discrepancy term (its variance was set to zero), for which we did not have any estimate available. However, to completely replace animal models with virtual representations of them, further experts knowledge will be needed to quantify the difference between the *in silico* model and the real-world system that it represents.

Neglecting the model discrepancy was a pragmatic choice, mainly dictated by research time constraints, and we fully acknowledge the need for investing more energies towards a better characterisation of it, rather than mere neglect. In the context of HM, the poor representation (or, as in this case, no representation at all) of the model discrepancy can lead to biased and over-confident non-implausible input parameter values that cannot be used to generate trustworthy model predictions [237]. A first approach to address this issue would be to assign a weak prior information to the model discrepancy as initially proposed in [102]. However, although this approach can be suitable for accurate interpolation, it could still not be enough to perform extrapolation or learn about physical model parameters, and a strong and meaningful prior information to specify the discrepancy distribution might be needed [33]. There are formal ways of eliciting more realistic priors on the model discrepancy, and these in general aim at mathematically encoding modellers' knowledge about the underlying physical system in the form of constraints on prior distributions, as done in [33] with constraints on a Gaussian process prior's derivatives. Other non-Bayesian approaches can be used, for example in [246] a frequentist approach is employed to explicitly account for all potentially important sources of uncertainty including the structural one (model discrepancy). As computer simulators grow in complexity, their corresponding emulators introduce

other sources of uncertainty, making the characterisation of model discrepancy nowadays still challenging.

### 9.3 NEXT STEPS

The next steps will go towards improving the methodology this thesis is heavily based on.

The first matter we want to address is the optimal collection of training dataset points via simulator evaluations. As more complex simulators will require more computational resources, or when predictions will have to be derived almost in real-time scenarios, we might not afford to simulate a whole parameter sweep (sampled with a space-filling design) anymore to construct the emulator training dataset. Space-filling designs assume that the samples provide information equally across the entire input space. Therefore, they perform exploration of the whole input space [250]. However, these designs are not adaptive to the information from the response surface (input-output relationship). Identifying the nature of input-output relationships to subsequently choose design points one at a time is already possible through different *acquisition functions* available in the literature for *active learning* tasks (e.g. [94, 179, 210]). For example, points can be selected such that they maximise an *expected improvement* on a given objective function. This approach indeed realises a trade-off between exploration and exploitation. We aim to systematically incorporate an active learning component in our emulation framework to drastically reduce the number of simulator evaluations needed to build emulators for accurate regression.

The second topic of further investigation is the emulator structure we adopted. Specifically, we chose to use univariate emulators to map model input parameters to each of the LV scalar features independently. In future studies, we aim at investigating whether a multivariate approach can provide better model predictions. Building a multivariate GPE requires prescribing the covariance structure between the output components [27, 48, 192], and it is not a trivial task. However, the output features we considered were extracted from two specific curves, namely the LVV and the LVP. This fact can be used to infer the correlations between output features belonging to the same curve. For example, in the case of the timing magnitudes ET, IVCT, IVRT, Tdiast we already know that their sum cannot exceed the cardiac cycle length. This information, along with other physiologically-derived arguments on LV volume and pressure transient morphologies, could be potentially used to prescribe the multivariate GPE covariance structure. Furthermore, a multivariate implausibility measure could be constructed from multivariate GPEs, and potentially assist in ruling out more implausible parameter space.

The third improvement we have in mind concerns the variance-based sensitivity analysis. We have seen that when using emulators to estimate the Sobol' sensitivity indices, the numerical error coming from having estimated expectations' and variances' integrals using quadrature formulae was not taken into account, but capturing the emulator uncertainty in the estimates was prioritised instead. In future work, we aim at quantifying how uncertainty in the emulator can propagate in the numerical error of the Sobol' indices calculation. We also aim at comparing Sobol' sensitivity analysis with other variance-based techniques where the underlying function is replaced by a surrogate model as in this case.

#### 9.4 FINAL REMARKS

Calibrating complex multi-scale cardiac models to biological data, incorporating experimental measurements' uncertainty and propagating this forward into model predictions remains a challenge. However, these are all necessary features to incorporate if we want our virtual heart representation to be a reliable platform for testing hypotheses and aiding drug discovery and development. In this view, we have empathised the need for further research on better techniques towards a more synergic coupling between probabilistic tools and deterministic modelling. In this thesis, we have showcased this coupling in several applications, aligning with the currently increasing number of research outputs on this topic from the whole scientific community.

Part V  
APPENDIX

# A

## VALIDATION OF GPE-BASED GSA AND HM TECHNIQUES

---

### A.1 GPE-BASED GSA TECHNIQUE VALIDATION USING ANALYTIC SOLUTIONS FOR SOBOL' INDICES OF TEST FUNCTIONS

We validated the GPE-based GSA technique used throughout the entire work (second emulation-based approach presented in equations (3.90)–(3.91), Section 3.6.2) by emulating test functions whose Sobol' sensitivity indices could be calculated analytically. After training, the emulators were used to estimate the Sobol' indices and the estimates were compared with the corresponding known theoretical values.

#### A.1.1 Ishigami function

The Ishigami function [90] is commonly used in sensitivity analysis and uncertainty quantification studies [203], because it exhibits strong nonlinearity and nonmonotonicity. This function is regulated by a vector of  $D = 3$  input variables  $\mathbf{X} = (X_1, X_2, X_3)$ , which are assumed to be independent and uniformly distributed in  $[-\pi, \pi]$ :

$$Y = \sin X_1 + a \sin^2 X_2 + b X_3^4 \sin X_1, \quad \text{with} \quad (\text{A.1})$$

$$X_i \sim \mathcal{U}([-\pi, \pi]) \quad \text{for } i = 1, 2, 3 \quad \text{and} \quad a, b > 0 \quad (\text{A.2})$$

The function output total variance is given in terms of the  $a$  and  $b$  parameters:

$$V = \frac{1}{2} + a^2 \frac{1}{8} + b \frac{\pi^4}{5} + b^2 \frac{\pi^8}{18} \quad (\text{A.3})$$

Sobol' sensitivity indices are then calculated by dividing the partial variances (which are also given in terms of the  $a$  and  $b$  parameters) by the total variance of equation (A.3):

$$S_1 = \frac{V_1}{V}, \quad V_1 = \frac{1}{2} \left( 1 + b \frac{\pi^4}{5} \right)^2 \quad (\text{A.4})$$

$$S_2 = \frac{V_2}{V}, \quad V_2 = a^2 \frac{1}{8} \quad (\text{A.5})$$

$$S_3 = \frac{V_3}{V}, \quad V_3 = 0 \quad (\text{A.6})$$

$$S_{T1} = \frac{V_1}{V}, \quad V_{T1} = \frac{1}{2} \left( 1 + b \frac{\pi^4}{5} \right)^2 + b^2 \frac{8\pi^8}{225} \quad (\text{A.7})$$

$$S_{T2} = \frac{V_{T2}}{V}, \quad V_{T2} = V_2 \quad (\text{A.8})$$

$$S_{T3} = \frac{V_{T3}}{V}, \quad V_{T3} = b^2 \frac{8\pi^8}{225} \quad (\text{A.9})$$

### A.1.2 $G^*$ -function

The  $G^*$ -function proposed by Saltelli [204] is a modified version of the classic Sobol' G-function [10] which is commonly used for sensitivity analysis and uncertainty quantification purposes as its input variables' importance can be directly controlled by tuning specific function parameters (along with being strongly nonlinear and non-monotonic). Saltelli's  $G^*$ -function is a shifted and curved G-function, and overcomes the issue when low-discrepancy quasi-random Sobol' sequences (whose initial sequence point is 1/2) are used to estimate the Sobol' sensitivity indices, since the classic G-function has got a singularity in each  $i$ -th dimension exactly at the point  $X_i = 1/2$ . The  $G^*$ -function is regulated by an arbitrary positive integer number  $D$  of input variables  $\mathbf{X} = (X_1, \dots, X_D)$ , assumed to be independent and uniformly distributed in  $[0, 1]$ :

$$Y = \prod_{i=1}^D g_i(X_i), \quad \text{with} \quad (\text{A.10})$$

$$g_i(X_i) = \frac{(1 + \alpha_i)|2(X_i + \delta_i - I[X_i + \delta_i]) - 1|^{\alpha_i} + a_i}{1 + a_i} \quad \text{and} \quad (\text{A.11})$$

$$X_i \sim \mathcal{U}([0, 1]), \quad \alpha_i > 0, \quad \delta_i \in [0, 1], \quad a_i > 0 \quad \text{for } i = 1, \dots, D \quad (\text{A.12})$$

where  $I[X_i + \delta_i]$  indicates the integer part of  $X_i + \delta_i$ . Parameter  $a_i$  controls the importance of input factor  $X_i$  into affecting the total variance of the function output. A low  $a_i$  means an important  $X_i$  factor, while a high  $a_i$  indicates a negligible  $X_i$  effect. If more than one  $a_i$  parameters is low, higher order interaction effects will be present as well.  $\delta_i$  is the parameter through which the classic G-function is shifted, while the  $\alpha_i$  parameter changes the curvature of the function. The choice of  $\delta_i = 0$  and  $\alpha_i = 1, \forall i = 1, \dots, D$  gives back the original G-function formulation.

The partial variances of the first order are given in terms of the  $a_i$ s parameters and of the curvature parameters  $\alpha_i$ s, while the partial total variances are calculated as a function of the first-order ones:

$$V_i = \frac{\alpha_i^2}{(1 + 2\alpha_i)(1 + a_i)^2}, \quad \text{for } i = 1, \dots, D \quad (\text{A.13})$$

$$V_{Ti} = V_i \prod_{j=1, j \neq i}^D (1 + V_j), \quad \text{for } i = 1, \dots, D \quad (\text{A.14})$$

Sobol' sensitivity indices are then calculated by dividing the partial variances of equations (A.13)–(A.14) by the total variance, which is again given as a function of the first-order partial variances as:

$$S_i = \frac{V_i}{V} \quad \text{and} \quad S_{Ti} = \frac{V_{Ti}}{V} \quad \text{for } i = 1, \dots, k, \quad \text{with} \quad (\text{A.15})$$

$$V = -1 + \prod_{i=1}^k (1 + V_i) \quad (\text{A.16})$$

### A.1.3 Simulator estimates

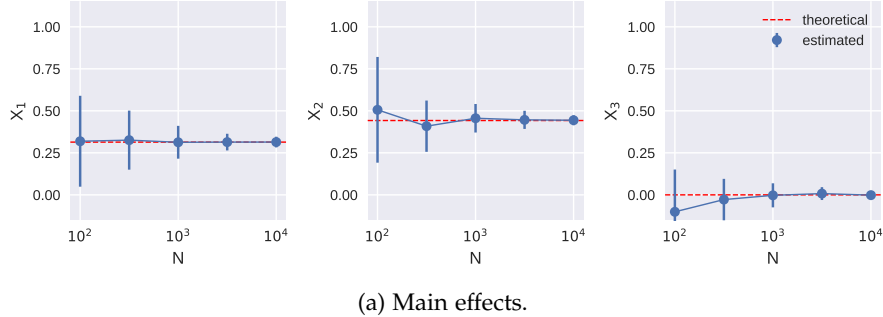
We first calculated the Sobol' first-order and total sensitivity indices using the forward models (the functions themselves, or simulators) and the estimators presented in equations (3.80)–(3.83), Section 3.6.1. In particular, we used the Ishigami function (equation (A.1)) with  $a = 7$ ,  $b = 0.1$ , and we used the G\*-function (equation (A.10)) with  $D = 10$  and  $\alpha_i = 1$ ,  $\delta_i \sim \mathcal{U}([0, 1])$ ,  $a_i = i - 1$ , for  $i = 1, \dots, D$ . This particular choice of the  $a_i$  coefficients coupled with the chosen problem dimension of  $D = 10$  ensured that at least one “very-important” and one “non-important” input factors were present [152, 204], modelled using parameter values  $a_1 = 0$  and  $a_{10} = 9$ , respectively. We calculated the Sobol' sensitivity indices by testing 5 different values (spaced evenly on a log scale) in the range  $[10^2, 10^4]$  for the number of samples  $N$  (introduced in Section 3.6.1) to be used when approximating the partial and total variances' integrals. We recall that the cost of calculating all the main and total effects is  $N \times (D + 2)$  model evaluations.

The theoretical Sobol' indices' values are summarised in Tables A.1–A.2 for the Ishigami and G\*-functions, respectively. In Figures A.1–A.2, the estimated Sobol' sensitivity indices are compared with the respective theoretical values. Bootstrap (number of resamples = 100) 95 % confidence intervals for the estimates are also provided. We can see that the estimates perfectly match the theoretical values, with better matching as the number of quadrature formulae samples increases. Although an absolute statement cannot be derived about the optimal choice of  $N$  by simply looking at the two presented example test

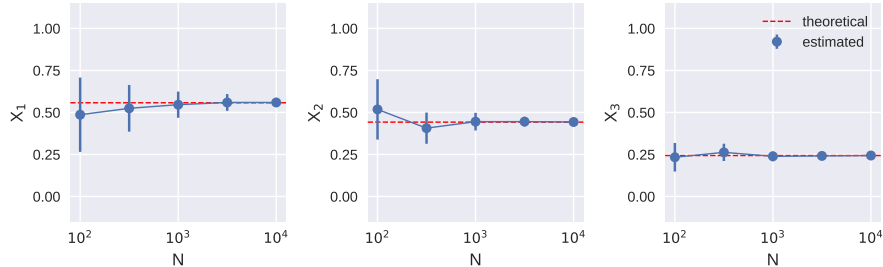
functions, we decided to fix  $N = 10^3$  in the next analysis for emulation-based estimates, to have a balance between small enough bootstrap confidence intervals, good match in the theoretical values and not too high number of model evaluations to be performed (although the latter will not be an issue anymore when using emulators).

INPUT FACTOR	SOBOL' SENSITIVITY INDEX	
	$S_i$	$S_{Ti}$
$X_1$	0.3139	0.5576
$X_2$	0.4424	0.4424
$X_3$	0.0000	0.2437

Table A.1: Ishigami function Sobol' first-order and total effects' theoretical values for  $a = 7$ ,  $b = 0.1$ .



(a) Main effects.

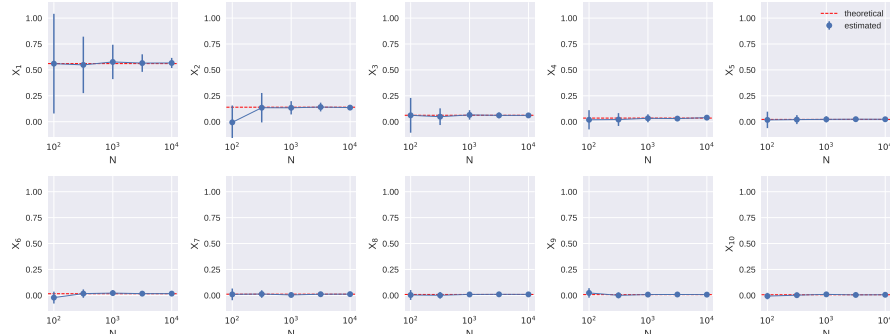


(b) Total effects.

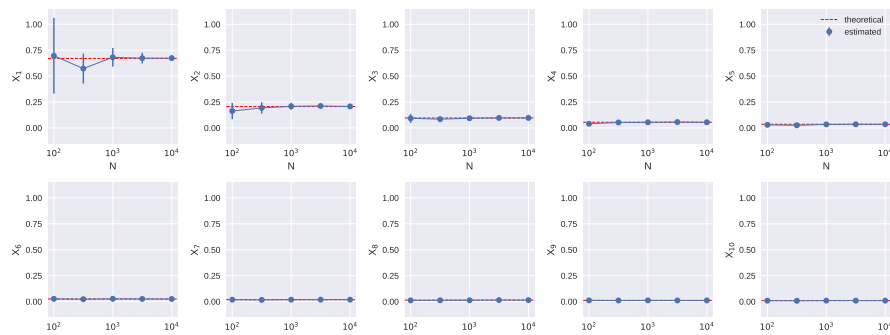
Figure A.1: Ishigami function Sobol' first-order (main) and total sensitivity indices estimated using the simulator. Indices are given as pointwise estimates with bootstrap 95 % confidance intervals.

INPUT FACTOR	SOBOL' SENSITIVITY INDEX	
	$S_i$	$S_{Ti}$
$X_1$	0.5607	0.6705
$X_2$	0.1402	0.2063
$X_3$	0.0623	0.0958
$X_4$	0.0350	0.0547
$X_5$	0.0224	0.0353
$X_6$	0.0156	0.0246
$X_7$	0.0114	0.0181
$X_8$	0.0088	0.0139
$X_9$	0.0069	0.0110
$X_{10}$	0.0056	0.0089

Table A.2: G\*-function Sobol' first-order and total effects' theoretical values for  $D = 10$  and  $\alpha_i = 1$ ,  $\delta_i \sim \mathcal{U}([0, 1])$ ,  $a_i = i - 1$ , for  $i = 1, \dots, D$ .



(a) Main effects.



(b) Total effects.

Figure A.2: G\*-function Sobol' first-order (main) and total sensitivity indices estimated using the simulator. Indices are given as pointwise estimates with bootstrap 95 % confidence intervals.

#### A.1.4 Emulator estimates

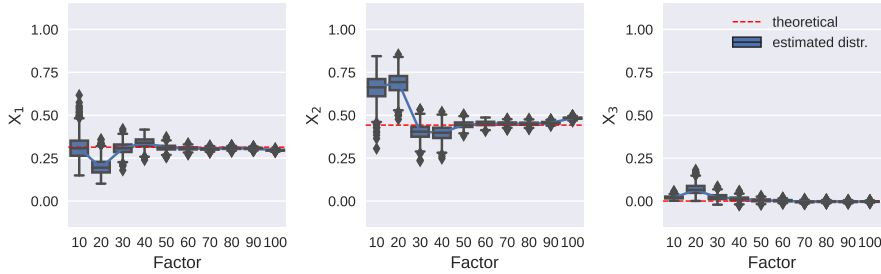
We wanted to test whether we could obtain reliable estimates of the Sobol' sensitivity indices this time by using emulators of the above presented test functions.

For this purpose, we sampled points  $\mathbf{X}$  from a LHD over the hypercubes  $[-\pi, \pi]^3$  and  $[0, 1]^{10}$  for the Ishigami and the G\*-functions, respectively. We then simulated these points  $\mathbf{Y} = f_{\text{simul}}(\mathbf{X})$  to form a dataset  $(\mathbf{X}, \mathbf{Y})$  to be used as learning sample. The learning sample size was given by  $|\mathbf{X}| = \text{factor} \times D$ , being  $D$  the problem dimension ( $D = 3$  and  $D = 10$  for the Ishigami and G\*-functions, respectively). Common practice for computer model experiments is to take at least  $10 \times D$  learning samples in Gaussian process regression settings [187]. In this study, we tested different multiplicative factors, taken from the set  $\{10, 20, 30, \dots, 100\}$ . We also simulated an additional set of points (size = 20 % of the biggest learning sample used) to be used as a testing dataset for evaluating each of the trained emulators predictivity, as described by the coefficient of determination ( $R^2$  score). After training and for each emulator, 1,000 emulator posterior distribution's samples were used to obtain Sobol' sensitivity indices' distributions as described in Section 3.6.2. In this case, we only investigated the uncertainty in the estimates arising from the use of the emulators, while the quadrature formulae numerical errors were neglected (and not estimated using the bootstrap technique as done in Section A.1.3).

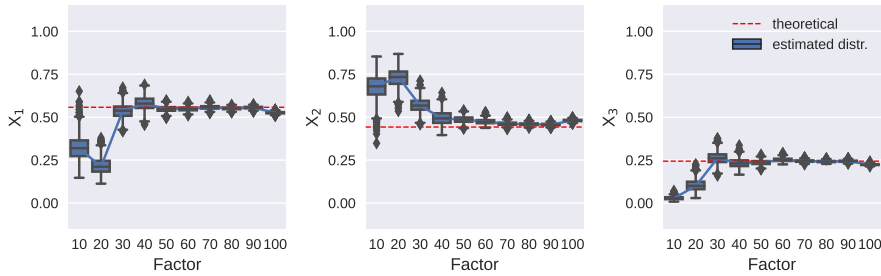
The obtained  $R^2$  scores are summarised in Tables A.3–A.4 for the Ishigami and G\*-functions, respectively. We can see that the emulator predictivity generally increases as the number of learning samples increases, although this behaviour eventually saturates, meaning that “the more points” does not always imply “the better accuracy”. In Figures A.3–A.4, the estimated Sobol' sensitivity indices are compared with the respective theoretical values. The estimated values are given as distributions, and each distribution is plotted against the multiplicative factor used to build the training dataset of the corresponding emulator which was used to obtain the distribution itself. We can see that the distributions progressively center around (i.e. their mean values match) the theoretical values as the number of learning samples used to train the emulator increases. In particular, for both the Ishigami and G\*-functions we can see that at least  $40 \times D$  learning samples were necessary to achieve a satisfactory match with theoretical values. Again, we cannot derive absolute statements concerning what is the optimal choice of the multiplicative factor, and investigating this goes beyond the scope of the project. Nevertheless, we have demonstrated the feasibility of estimating Sobol' sensitivity indices with good accuracy by using emulators of both example 3D and 10D nonlinear and nonmonotonic computer codes.

FACTOR	R <sup>2</sup> SCORE
10×	0.3796
20×	0.5187
30×	0.5438
40×	0.8563
50×	0.9526
60×	0.9770
70×	0.9806
80×	0.9862
90×	0.9876
100×	0.9941

Table A.3: Ishigami function emulators' predictivity as described by the R<sup>2</sup> score. Predictivity is tested against the same set of points for each of emulators trained on differently large training datasets.



(a) Main effects.

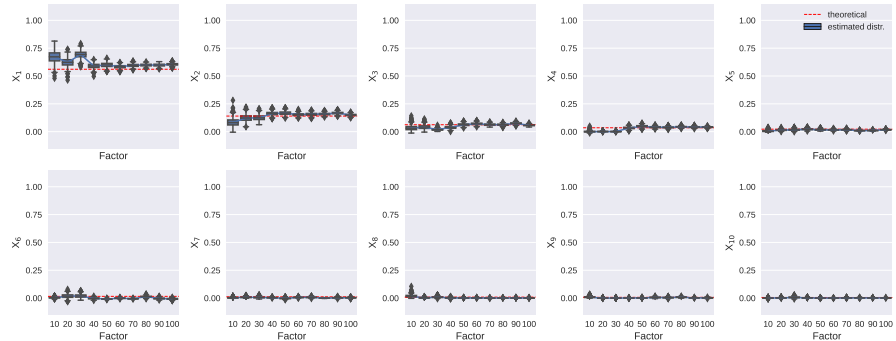


(b) Total effects.

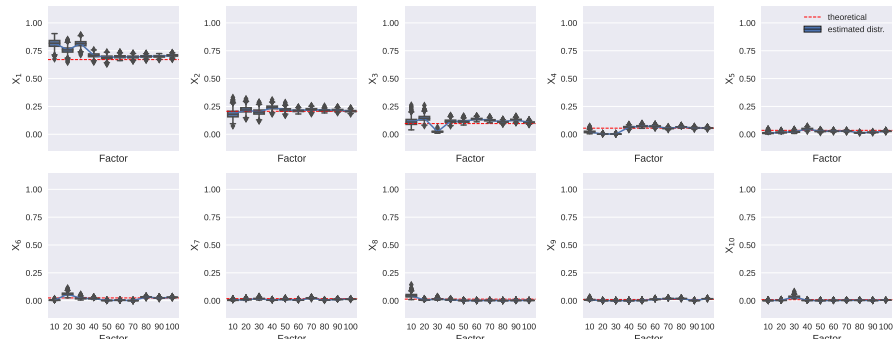
Figure A.3: Ishigami function Sobol' first-order (main) and total sensitivity indices estimated using the emulator. Indices are given as different estimates (forming entire distributions) corresponding to different samples from the full emulators' posterior distributions.

FACTOR	R <sup>2</sup> SCORE
10×	0.6470
20×	0.7689
30×	0.7534
40×	0.7881
50×	0.8332
60×	0.8396
70×	0.8427
80×	0.8569
90×	0.8805
100×	0.8896

Table A.4: G\*-function emulators' predictivity as described by the R<sup>2</sup> score. Predictivity is tested against the same set of points for each of emulators trained on differently large training datasets.



(a) Main effects.



(b) Total effects.

Figure A.4: G\*-function Sobol' first-order (main) and total sensitivity indices estimated using the emulator. Indices are given as different estimates (forming entire distributions) corresponding to different samples from the full emulators' posterior distributions.

## A.2 HM VALIDATION USING SYNTHETIC DATA

We validated HM technique against *synthetic data*, generated using the *in silico* model of SHAM rat heart contraction mechanics (Section 4.3.1).

For this purpose, we started from the performed HM on the SHAM model (Section 4.4.3, Figure 4.11). We selected an intermediate wave, specifically wave 4, among the total 8 waves the full process took to complete (Figure A.7a). We then sampled 256 points in wave 4 that did not belong to the final wave, namely wave 8 (Figures A.7b–A.7c). We then simulated all these points and computed the LV features' mean and standard deviation values for the ones that led to a converging simulation (48 points). We further used these mean and standard deviation values as synthetic data to be matched. The LV features' synthetic variability is summarised in Table A.5.

LV FEATURE	UNITS	SYNTHETIC VARIABILITY
EDV*	$\mu\text{L}$	$493.10 \pm 16.85$
ESV*	$\mu\text{L}$	$204.29 \pm 7.93$
EF	%	$58.54 \pm 1.74$
IVCT	ms	$140.86 \pm 0.78$
ET*	ms	$56.77 \pm 1.53$
IVRT*	ms	$20.03 \pm 2.43$
Tdiast	ms	$94.07 \pm 1.11$
PeakP*	kPa	$18.56 \pm 1.14$
Tpeak	ms	$39.39 \pm 1.36$
ESP	kPa	$8.74 \pm 0.21$
maxdP*	$\text{kPa ms}^{-1}$	$1.08 \pm 0.06$
mindP*	$\text{kPa ms}^{-1}$	$-0.54 \pm 0.06$

Table A.5: Synthetic data LV features' variability given as mean  $\pm$  standard deviation values to match for HM validation. Only the LV features with an asterisk (\*) were used as targets for HM.

We started the HM process from the same initial space-filling design (lightest blue variant coloured points in Figure 4.11) used for the SHAM model HM, this time trying to match the synthetic data instead of the experimental data. To replicate exactly the same process, we tried to match the same 7 features out of the total 12 features of interest, although we had mean and standard deviation values for all the LV features. Figure A.5 shows that all the LV features were perfectly matched at the end of the HM process (which took 9 waves to complete), including the 5 features we did not directly selected as targets for HM.

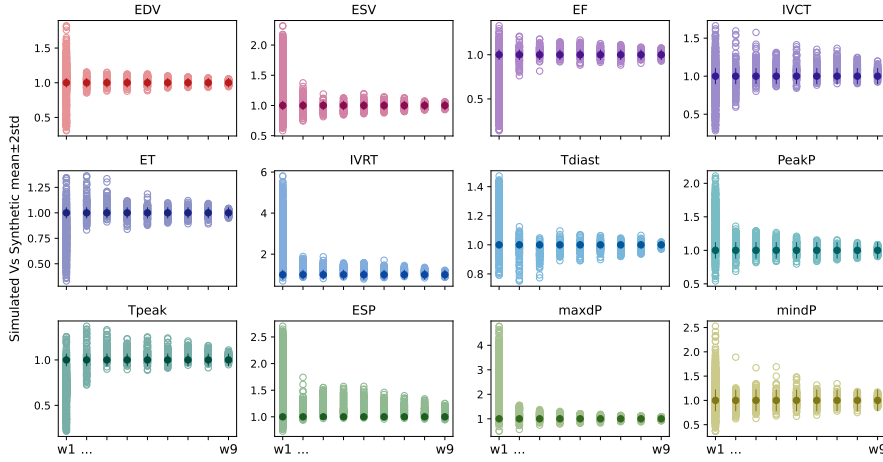


Figure A.5: Simulated LV features' distributions around synthetic mean values. These are obtained by evaluating the simulator at input parameter points belonging to the first (w1) up to the last (w9) waves of HM performed on synthetic data. Simulated features are shown as empty dots, while the related synthetic mean values are displayed as full dots. 2 STD confidence intervals are also shown as vertical straight lines centred around synthetic mean values. All the displayed values (including confidence intervals) are normalised by their respective synthetic mean values.

Moreover, we can see that the input parameters' ranges characterising the non-imausible  $X_{NIMP}$  space of the last HM wave were most of the time restricted to ranges which have non-empty intersection with the ranges where the synthetic data were sampled from (Figure A.6). This shows that HM technique not only matched the target features' values but also recovered the initial sample space.

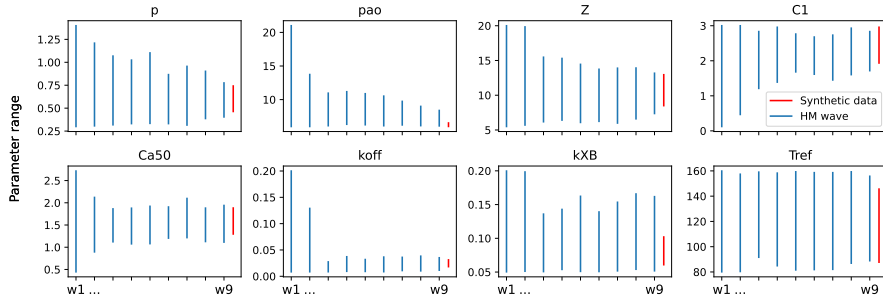


Figure A.6: Input parameters' ranges at each wave during SHAM rat heart model HM on synthetic data (blue). The parameters' ranges where the synthetic data were sampled from are also shown (red).

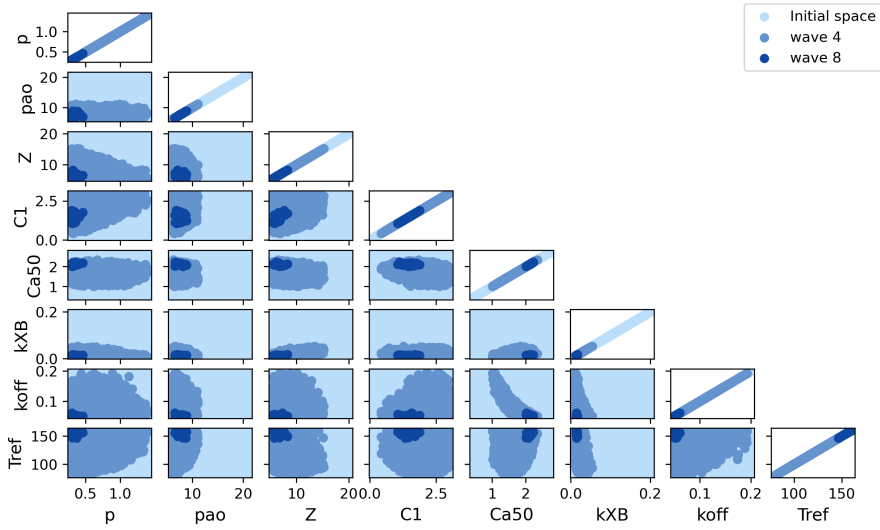
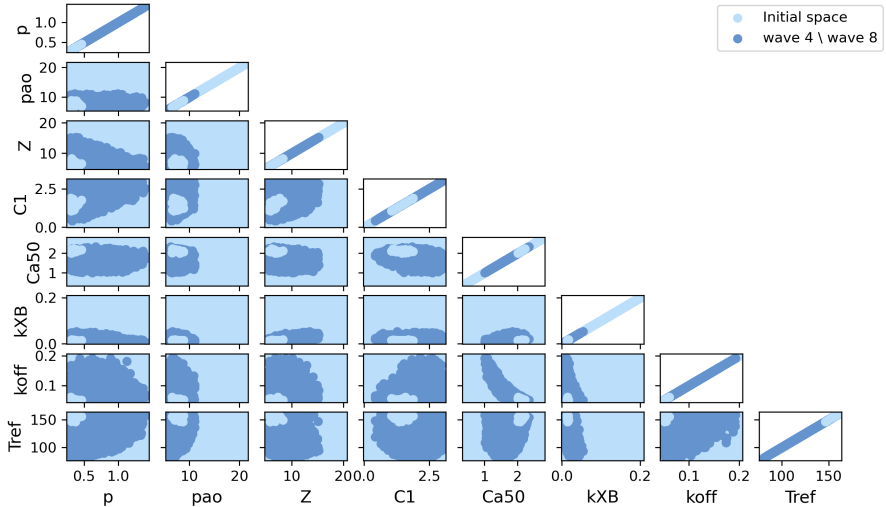
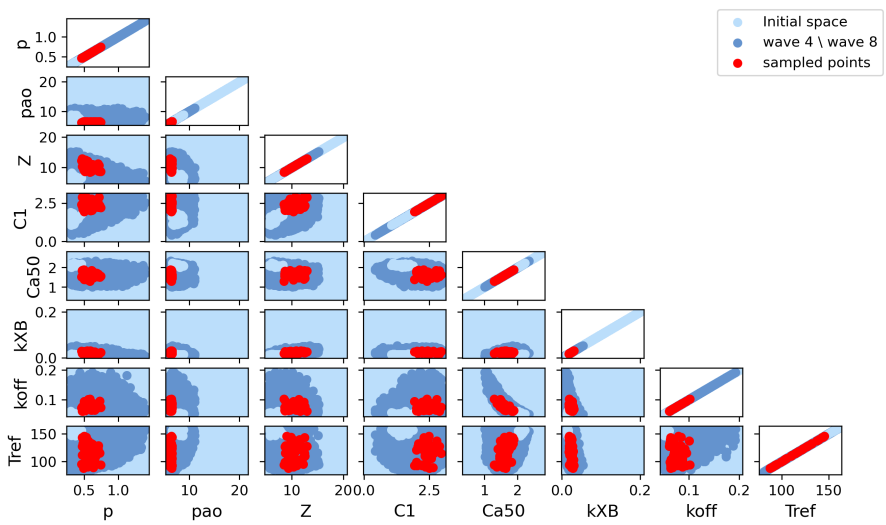
(a) The initial space with wave 4 and wave 8  $X_{NIMP}$  spaces is highlighted.(b) Wave 8  $X_{NIMP}$  space is cut out of the full space.(c) Points are sampled within wave 4  $X_{NIMP}$  but not within wave 8  $X_{NIMP}$  space.

Figure A.7: The process of points' selection for synthetic data generation to be used for HM technique validation.

## BIBLIOGRAPHY

---

- [1] M. Abdellatif, S. Leite, M. Alaa, J. Oliveira-Pinto, M. Tavares-Silva, D. Fontoura, I. Falcão-Pires, A. F. Leite-Moreira, and A. P. Lourenço. "Spectral transfer function analysis of respiratory hemodynamic fluctuations predicts end-diastolic stiffness in preserved ejection fraction heart failure." In: *Am. J. Physiol. - Hear. Circ. Physiol.* 310.1 (2016), H4–H13. doi: [10.1152/ajpheart.00399.2015](https://doi.org/10.1152/ajpheart.00399.2015).
- [2] M. Abdellatif et al. "Nicotinamide for the treatment of heart failure with preserved ejection fraction." In: *Sci. Transl. Med.* 13.580 (2021), eabd7064. doi: [10.1126/scitranslmed.abd7064](https://doi.org/10.1126/scitranslmed.abd7064).
- [3] Daria M Adamczak, Mary-tiffany Oduah, Thomas Kiebalo, Sonia Nartowicz, B Marcin, Mateusz Pochylski, Aleksandra Ciep, Adrian Gwizda, Maciej Lesiak, and Ewa Straburzy. "Heart Failure with Preserved Ejection Fraction — a Concise Review." In: *Curr. Cardiol. Rep.* 22.9 (2020), p. 82.
- [4] Kasper Adelborg, Szimonetta Szépligeti, Jens Sundbøll, Erzsébet Horváth-Puhó, Victor W. Henderson, Anne Ording, Lars Pedersen, and Henrik Toft Sørensen. "Risk of Stroke in Patients with Heart Failure: A Population-Based 30-Year Cohort Study." In: *Stroke* 48.5 (2017), pp. 1161–1168. doi: [10.1161/STROKEAHA.116.016022](https://doi.org/10.1161/STROKEAHA.116.016022).
- [5] Frank T. M. van Amsterdam and Johan Zaagsma. "Stereoisomers of calcium antagonists discriminate between coronary vascular and myocardial sites." In: *Naunyn Schmiedebergs Arch Pharmacol.* 337.2 (1988), pp. 213–219.
- [6] Shimin An, Nimra Gilani, Yuan Huang, Adam Muncan, Youhua Zhang, Yi Da Tang, A. Martin Gerdes, and Kaie Ojamaa. "Adverse transverse-tubule remodeling in a rat model of heart failure is attenuated with low-dose triiodothyronine treatment." In: *Mol. Med.* 25.1 (2019), pp. 1–14. doi: [10.1186/s10020-019-0120-3](https://doi.org/10.1186/s10020-019-0120-3).
- [7] Mads J. Andersen and Barry A. Borlaug. "Heart failure with preserved ejection fraction: Current understandings and challenges." In: *Curr. Cardiol. Rep.* 16.7 (2014). doi: [10.1007/s11886-014-0501-8](https://doi.org/10.1007/s11886-014-0501-8).
- [8] Ioannis Andrianakis and Peter G. Challenor. "The effect of the nugget on Gaussian process emulators of computer models." In: *Comput. Stat. Data Anal.* 56.12 (2012), pp. 4215–4228. doi: [10.1016/j.csda.2012.04.020](https://doi.org/10.1016/j.csda.2012.04.020). URL: <http://dx.doi.org/10.1016/j.csda.2012.04.020>.

- [9] Ioannis Andrianakis, Ian R. Vernon, Nicky McCreesh, Trevelyan J. McKinley, Jeremy E. Oakley, Rebecca N. Nsubuga, Michael Goldstein, and Richard G. White. "Bayesian History Matching of Complex Infectious Disease Models Using Emulation: A Tutorial and a Case Study on HIV in Uganda." In: *PLoS Comput. Biol.* 11.1 (2015). Ed. by Hulin Wu, e1003968. doi: [10.1371/journal.pcbi.1003968](https://doi.org/10.1371/journal.pcbi.1003968). URL: <http://dx.plos.org/10.1371/journal.pcbi.1003968>.
- [10] G. E.B. Archer, A. Saltelli, and I. M. Sobol. "Sensitivity measures, anova-like techniques and the use of bootstrap." In: *J. Stat. Comput. Simul.* 58.2 (1997), pp. 99–120. doi: [10.1080/00949659708811825](https://doi.org/10.1080/00949659708811825).
- [11] *Assessing Credibility of Computational Modeling through Verification & Validation*. URL: <https://www.asme.org/codes-standards/find-codes-standards/v-v-40-assessing-credibility-computational-modeling-verification-validation-application-medical-devices>.
- [12] Christoph M. Augustin, Matthias A.F. Gsell, Elias Karabelas, Erik Willemen, Frits W. Prinzen, Joost Lumens, Edward J. Vigmond, and Gernot Plank. "A computationally efficient physiologically comprehensive 3D-oD closed-loop model of the heart and circulation." In: *Computer Methods in Applied Mechanics and Engineering* 386 (2021), p. 114092. ISSN: 0045-7825. doi: [10.1016/j.cma.2021.114092](https://doi.org/10.1016/j.cma.2021.114092). URL: <http://dx.doi.org/10.1016/j.cma.2021.114092>.
- [13] Peter O. Awinda, Marissa Watanabe, Yemeserach Bishaw, Anna M. Huckabee, Keinan B. Agonias, Katarzyna Kazmierczak, Danuta Szczesna-Cordary, and Bertrand C.W. Tanner. "Mavacamten decreases maximal force and  $\text{Ca}^{2+}$  sensitivity in the N47K-myosin regulatory light chain mouse model of hypertrophic cardiomyopathy." In: *Am. J. Physiol. - Hear. Circ. Physiol.* 320.2 (2021), H881–H890. doi: [10.1152/AJPHEART.00345.2020](https://doi.org/10.1152/AJPHEART.00345.2020).
- [14] Peter H. Backx, Wei Dong Gao, Michelle D. Azan-Backx, and Eduardo Marban. "The relationship between contractile force and intracellular  $[\text{Ca}^{2+}]$  in intact rat cardiac trabeculae." In: *J. Gen. Physiol.* 105.1 (1995), pp. 1–19. doi: [10.1085/jgp.105.1.1](https://doi.org/10.1085/jgp.105.1.1).
- [15] Fan Bai, Hannah M. Caster, Jose R. Pinto, and Masataka Kawai. "Analysis of the molecular pathogenesis of cardiomyopathy-causing cTnT mutants I79N, Δe96, and Δk210." In: *Biophys. J.* 104.9 (2013), pp. 1979–1988. doi: [10.1016/j.bpj.2013.04.001](https://doi.org/10.1016/j.bpj.2013.04.001).
- [16] Jens Petter Bakkehaug, Anders Benjamin Kildal, Erik Torgersen Engstad, Neoma Boardman, Torvind Næsheim, Leif Rønning, Ellen Aasum, Terje Steinar Larsen, Truls Myrmel, and Ole Jakob How. "Myosin activator omecamtiv mecarbil increases myocardial oxygen consumption and impairs cardiac efficiency

- mediated by resting myosin ATPase activity." In: *Circ. Hear. Fail.* 8.4 (2015), pp. 766–775. doi: [10.1161/CIRCHEARTFAILURE.114.002152](https://doi.org/10.1161/CIRCHEARTFAILURE.114.002152).
- [17] Leonardo S. Bastos and Anthony O'hagan. "Diagnostics for gaussian process emulators." In: *Technometrics* 51.4 (2009), pp. 425–438. doi: [10.1198/TECH.2009.08019](https://doi.org/10.1198/TECH.2009.08019).
  - [18] J. D. Bayer, R. C. Blake, G. Plank, and N. A. Trayanova. "A novel rule-based algorithm for assigning myocardial fiber orientation to computational heart models." In: *Ann. Biomed. Eng.* 40.10 (2012), pp. 2243–2254. doi: [10.1007/s10439-012-0593-5](https://doi.org/10.1007/s10439-012-0593-5).
  - [19] E. J. Benjamin et al. "Heart disease and stroke statistics - 2018 update: A report from the American Heart Association." In: *Circulation* 137.12 (2018), E67–E492. doi: [10.1161/CIR.0000000000000558](https://doi.org/10.1161/CIR.0000000000000558).
  - [20] Roberta Berni, Monia Savi, Leonardo Bocchi, Francesca Delucchi, Ezio Musso, Christine Chaponnier, Giulio Gabbiani, Sophie Clement, and Donatella Stilli. "Modulation of actin isoform expression before the transition from experimental compensated pressure-overload cardiac hypertrophy to decompensation." In: *Am. J. Physiol. - Hear. Circ. Physiol.* 296.5 (2009), pp. 1625–1632. doi: [10.1152/ajpheart.01057.2008](https://doi.org/10.1152/ajpheart.01057.2008).
  - [21] Bhf.org.uk. (2021). *Heart and Circulatory Diseases Statistics 2021*. <https://www.bhf.org.uk/what-we-do/our-research/heart-statistics/heart-statistics-publications/cardiovascular-disease-statistics-2021>. Accessed 4th October 2021.
  - [22] Christian Binggeli, Roberto Corti, Isabella Sudano, Thomas F. Luscher, and Georg Noll. "Effects of chronic calcium channel blockade on sympathetic nerve activity in hypertension." In: *Hypertension* 39.4 (2002), pp. 892–896. doi: [10.1161/01.HYP.0000013264.41234.24](https://doi.org/10.1161/01.HYP.0000013264.41234.24).
  - [23] E Blanchard, C Seidman, J G Seidman, M LeWinter, and D Maughan. "Altered crossbridge kinetics in the alphaMHC403/+ mouse model of familial hypertrophic cardiomyopathy." In: *Circ. Res.* 84.4 (1999), pp. 475–83. doi: [10.1161/01.res.84.4.475](https://doi.org/10.1161/01.res.84.4.475).
  - [24] David Bode, Yan Wen, Niklas Hegemann, Uwe Primessnig, Abdul Parwani, Leif Hendrik Boldt, Burkert M. Pieske, Frank R. Heinzel, and Felix Hohendanner. "Oxidative stress and inflammatory modulation of Ca<sup>2+</sup> handling in metabolic HFPEF-related left atrial cardiomyopathy." In: *Antioxidants* 9.9 (2020), pp. 1–13. doi: [10.3390/antiox9090860](https://doi.org/10.3390/antiox9090860).

- [25] David Bode et al. "Dual SGLT-1 and SGLT-2 inhibition improves left atrial dysfunction in HFpEF." In: *Cardiovasc. Diabetol.* 20.1 (2021), pp. 1–14. DOI: [10.1186/s12933-020-01208-z](https://doi.org/10.1186/s12933-020-01208-z). URL: <https://doi.org/10.1186/s12933-020-01208-z>.
- [26] Javier Bonet and Richard D. Wood. *Nonlinear Continuum Mechanics for Finite Element Analysis*. 2nd ed. Cambridge University Press, 2008. DOI: [10.1017/CBO9780511755446](https://doi.org/10.1017/CBO9780511755446).
- [27] Edwin V Bonilla, Kian Chai, and Christopher Williams. "Multi-task Gaussian Process Prediction." In: *Advances in Neural Information Processing Systems*. Ed. by J. Platt, D. Koller, Y. Singer, and S. Roweis. Vol. 20. Curran Associates, Inc., 2008. URL: <https://proceedings.neurips.cc/paper/2007/file/66368270ffd51418ec58bd793f2d9b1b-Paper.pdf>.
- [28] Barry A. Borlaug, Carolyn S.P. Lam, Véronique L. Roger, Richard J. Rodeheffer, and Margaret M. Redfield. "Contractility and Ventricular Systolic Stiffening in Hypertensive Heart Disease. Insights Into the Pathogenesis of Heart Failure With Preserved Ejection Fraction." In: *J. Am. Coll. Cardiol.* 54.5 (2009), pp. 410–418. DOI: [10.1016/j.jacc.2009.05.013](https://doi.org/10.1016/j.jacc.2009.05.013).
- [29] Peter H.M. Bovendeerd, Wilco Kroon, and Tammo Delhaas. "Determinants of left ventricular shear strain." In: *Am. J. Physiol. - Hear. Circ. Physiol.* 297.3 (2009), pp. 1058–1068. DOI: [10.1152/ajpheart.01334.2008](https://doi.org/10.1152/ajpheart.01334.2008).
- [30] T. Scott Bowen et al. "Exercise training reveals inflexibility of the diaphragm in an animal model of patients with obesity-driven heart failure with a preserved ejection fraction." In: *J. Am. Heart Assoc.* 6.10 (2017), pp. 1–16. DOI: [10.1161/JAHA.117.006416](https://doi.org/10.1161/JAHA.117.006416).
- [31] T. Scott Bowen, Christian Herz, Natale P.L. Rolim, Anne Marie Ormbostad Berre, Martin Halle, Angela Kricke, Axel Linke, Gustavo Justo da Silva, Ulrik Wisloff, and Volker Adams. "Effects of Endurance Training on Detrimental Structural, Cellular, and Functional Alterations in Skeletal Muscles of Heart Failure With Preserved Ejection Fraction." In: *J. Card. Fail.* 24.9 (2018), pp. 603–613. DOI: [10.1016/j.cardfail.2018.08.009](https://doi.org/10.1016/j.cardfail.2018.08.009). URL: <https://doi.org/10.1016/j.cardfail.2018.08.009>.
- [32] Maarten M. Brandt, Isabel T.N. Nguyen, Merle M. Krebber, Jens van de Wouw, Michal Mokry, Maarten J. Cramer, Dirk J. Duncker, Marianne C. Verhaar, Jaap A. Joles, and Caroline Cheng. "Limited synergy of obesity and hypertension, prevalent risk factors in onset and progression of heart failure with preserved ejection fraction." In: *J. Cell. Mol. Med.* 23.10 (2019), pp. 6666–6678. DOI: [10.1111/jcmm.14542](https://doi.org/10.1111/jcmm.14542).

- [33] Jenni Brynjarsdóttir and Anthony Ohagan. "Learning about physical parameters: The importance of model discrepancy." In: *Inverse Probl.* 30.11 (2014). DOI: [10.1088/0266-5611/30/11/114007](https://doi.org/10.1088/0266-5611/30/11/114007).
- [34] Brad S. Burlew and Karl T. Weber. "Cardiac fibrosis as a cause of diastolic dysfunction." In: *Herz* 27.2 (2002), pp. 92–98. DOI: [10.1007/s00059-002-2354-y](https://doi.org/10.1007/s00059-002-2354-y).
- [35] Eileen M C Call, Kenneth S Ginsburg, Rosana a Bassani, Thomas R Shannon, Ming Qi, Allen M Samarel, Donald M Bers, Rosana A, and Allen M Sa. "Coupling in Hypertrophic Rat Ventricular Myocytes." In: *Test* (1998).
- [36] Paula Camacho, Huimin Fan, Zhongmin Liu, and Jia-Qiang He. "Small mammalian animal models of heart disease." In: *Am. J. Cardiovasc. Dis.* 6.3 (2016), pp. 70–80. URL: <http://www.ncbi.nlm.nih.gov/pubmed/27679742> <http://www.ncbi.nlm.nih.gov/articlerender.fcgi?artid=PMC5030387>.
- [37] J. O. Campos, J. Sundnes, R. W. Dos Santos, and B. M. Rocha. "Uncertainty quantification and sensitivity analysis of left ventricular function during the full cardiac cycle: UQ and SA in cardiac mechanics." In: *Philos. Trans. R. Soc. A Math. Phys. Eng. Sci.* 378.2173 (2020). DOI: [10.1098/rsta.2019.0381](https://doi.org/10.1098/rsta.2019.0381).
- [38] Kelly Chang and Zhihua Li. *FDA/CiPA*. [https://github.com/FDA/CiPA/blob/Model-Validation-2018/AP\\_simulation/data/newCiPA.csv](https://github.com/FDA/CiPA/blob/Model-Validation-2018/AP_simulation/data/newCiPA.csv). 2018.
- [39] Kevin C. Chang, Vincent M. Figueiredo, Joop H.M. Schreur, Ken Ichi Kariya, Michael W. Weiner, Paul C. Simpson, and S. Albert Camacho. "Thyroid hormone improves function and Ca<sup>2+</sup> handling in pressure overload hypertrophy. Association with increased sarcoplasmic reticulum Ca<sup>2+</sup>-ATPase and  $\alpha$ -myosin heavy chain in rat hearts." In: *J. Clin. Invest.* 100.7 (1997), pp. 1742–1749. DOI: [10.1172/JCI119699](https://doi.org/10.1172/JCI119699).
- [40] Ru Wen Chang, Chun Yi Chang, Ming Shiou Wu, Hsi Yu Yu, Jian Ming Luo, Yih Sharng Chen, Fang Yue Lin, Liang Chuan Lai, Chih Hsien Wang, and Kuo Chu Chang. "Systolic aortic pressure-time area is a useful index describing arterial wave properties in rats with diabetes." In: *Sci. Rep.* 5.October (2015), pp. 1–10. DOI: [10.1038/srep17293](https://doi.org/10.1038/srep17293).
- [41] Hui Hua Chen et al. "Stachydrine hydrochloride alleviates pressure overload-induced heart failure and calcium mishandling on mice." In: *J. Ethnopharmacol.* 248.October 2019 (2020), p. 112306. DOI: [10.1016/j.jep.2019.112306](https://doi.org/10.1016/j.jep.2019.112306). URL: <https://doi.org/10.1016/j.jep.2019.112306>.

- [42] Jae Hoon Chung, Brandon J. Biesiadecki, Mark T. Ziolo, Jonathan P. Davis, and Paul M.L. Janssen. "Myofilament calcium sensitivity: Role in regulation of in vivo cardiac contraction and relaxation." In: *Front. Physiol.* 7.DEC (2016), pp. 1–9. DOI: [10.3389/fphys.2016.00562](https://doi.org/10.3389/fphys.2016.00562).
- [43] R. H. Clayton, O. Bernus, E. M. Cherry, H. Dierckx, F. H. Fenton, L. Mirabella, A. V. Panfilov, F. B. Sachse, G. Seemann, and H. Zhang. "Models of cardiac tissue electrophysiology: Progress, challenges and open questions." In: *Prog. Biophys. Mol. Biol.* 104.1-3 (2011), pp. 22–48. DOI: [10.1016/j.pbiomolbio.2010.05.008](https://doi.org/10.1016/j.pbiomolbio.2010.05.008).
- [44] John G.F. Cleland, Pierpaolo Pellicori, and Riet Dierckx. "Clinical Trials in Patients with Heart Failure and Preserved Left Ventricular Ejection Fraction." In: *Heart Fail. Clin.* 10.3 (2014), pp. 511–523. DOI: [10.1016/j.hfc.2014.04.011](https://doi.org/10.1016/j.hfc.2014.04.011). URL: <http://dx.doi.org/10.1016/j.hfc.2014.04.011>.
- [45] Jon Cockayne, Chris J. Oates, T. J. Sullivan, and Mark Girolami. "Bayesian probabilistic numerical methods." In: *SIAM Rev.* 61.4 (2019), pp. 756–789. DOI: [10.1137/17M1139357](https://doi.org/10.1137/17M1139357). arXiv: [1702.03673](https://arxiv.org/abs/1702.03673).
- [46] G. Conceição, I. Heinonen, A. P. Lourenço, D. J. Duncker, and I. Falcão-Pires. "Animal models of heart failure with preserved ejection fraction." In: *Netherlands Hear. J.* 24.4 (2016), pp. 275–286. DOI: [10.1007/s12471-016-0815-9](https://doi.org/10.1007/s12471-016-0815-9).
- [47] S. Conti, J. P. Gosling, J. E. Oakley, and A. O'Hagan. "Gaussian process emulation of dynamic computer codes." In: *Biometrika* 96.3 (2009), pp. 663–676. DOI: [10.1093/biomet/asp028](https://doi.org/10.1093/biomet/asp028).
- [48] Stefano Conti and Anthony O'Hagan. "Bayesian emulation of complex multi-output and dynamic computer models." In: *Journal of Statistical Planning and Inference* 140.3 (2010), pp. 640–651. ISSN: 0378-3758. DOI: <https://doi.org/10.1016/j.jspi.2009.08.006>. URL: <https://www.sciencedirect.com/science/article/pii/S0378375809002559>.
- [49] Cesare Corrado, Adelisa Avezzù, Angela W.C. Lee, Caroline Mendoca Costa, Caroline H. Roney, Marina Strocchi, Martin Bishop, and Steven A. Niederer. "Using cardiac ionic cell models to interpret clinical data." In: *Wiley Interdiscip. Rev. Syst. Biol. Med.* May 2020 (2020), pp. 1–16. DOI: [10.1002/wsbm.1508](https://doi.org/10.1002/wsbm.1508).
- [50] Sam Coveney and Richard H. Clayton. "Fitting two human atrial cell models to experimental data using Bayesian history matching." In: *Prog. Biophys. Mol. Biol.* 139 (2018), pp. 43–58. DOI: [10.1016/J.PBIOMOLBIO.2018.08.001](https://doi.org/10.1016/J.PBIOMOLBIO.2018.08.001). URL: <https://www.sciencedirect.com/science/article/pii/S0079610718300154>.

- [51] I. Cuijpers, P. Carai, P. Mendes-Ferreira, S. J. Simmonds, P. Mulder, D. Miranda-Silva, D. De Giorgio, P. Pokreisz, S. Heymans, and E. A. V. Jones. "The effect of different anaesthetics on echocardiographic evaluation of diastolic dysfunction in a heart failure with preserved ejection fraction model." In: *Sci. Rep.* 10.1 (2020), pp. 1–12. DOI: [10.1038/s41598-020-72924-5](https://doi.org/10.1038/s41598-020-72924-5). URL: <https://doi.org/10.1038/s41598-020-72924-5>.
- [52] Claire L. Curl et al. "Cardiomyocyte functional etiology in heart failure with preserved ejection fraction is distinctive—a new preclinical model." In: *J. Am. Heart Assoc.* 7.11 (2018). DOI: [10.1161/JAHA.117.007451](https://doi.org/10.1161/JAHA.117.007451).
- [53] Alec Davila et al. "Adenosine kinase inhibition augments conducted vasodilation and prevents left ventricle diastolic dysfunction in heart failure with preserved ejection fraction." In: *Circ. Hear. Fail.* 12.8 (2019), pp. 1–12. DOI: [10.1161/CIRCHEARTFAILURE.118.005762](https://doi.org/10.1161/CIRCHEARTFAILURE.118.005762).
- [54] Jonathan P. Davis, Catalina Norman, Tomoyoshi Kobayashi, R. John Solaro, Darl R. Swartz, and Svetlana B. Tikunova. "Effects of thin and thick filament proteins on calcium binding and exchange with cardiac troponin C." In: *Biophys. J.* 92.9 (2007), pp. 3195–3206. DOI: [10.1529/biophysj.106.095406](https://doi.org/10.1529/biophysj.106.095406).
- [55] Agnieszka Dębska-Kozłowska, Marcin Książczyk, and Małgorzata Lelonek. "Where are we in 2021 with heart failure with reduced ejection fraction?—current outlook and expectations from new promising clinical trials." In: *Heart Fail. Rev.* 0123456789 (2021). DOI: [10.1007/s10741-021-10120-x](https://doi.org/10.1007/s10741-021-10120-x). URL: <https://doi.org/10.1007/s10741-021-10120-x>.
- [56] Elza D. van Deel, Aref Najafi, Dulce Fontoura, Erik Valent, Max Goebel, Kim Kardux, Inês Falcão-Pires, and Jolanda van der Velden. "In vitro model to study the effects of matrix stiffening on Ca<sup>2+</sup> handling and myofilament function in isolated adult rat cardiomyocytes." In: *J. Physiol.* 595.14 (2017), pp. 4597–4610. DOI: [10.1113/JP274460](https://doi.org/10.1113/JP274460).
- [57] Socrates Dokos and Nigel H. Lovell. "Parameter estimation in cardiac ionic models." In: *Prog. Biophys. Mol. Biol.* 85.2-3 (2004), pp. 407–431. DOI: [10.1016/j.pbiomolbio.2004.02.002](https://doi.org/10.1016/j.pbiomolbio.2004.02.002).
- [58] Hui Dong, Mary L. Earle, Yanfen Jiang, Kathy A. Loutzenhisler, and Christopher R. Triggle. "Cardiovascular effects of CPU-23, a novel L-type calcium channel blocker with a unique molecular structure." In: *Br. J. Pharmacol.* 122.7 (1997), pp. 1271–1278. DOI: [10.1038/sj.bjp.0701508](https://doi.org/10.1038/sj.bjp.0701508).
- [59] FDA. "Treatment for heart failure: endpoints for drug development." In: *Guid. Ind.* June (2019).

- [60] Damiano Fassina, Caroline M. Costa, Stefano Longobardi, Elias Karabelas, Gernot Plank, Sian E. Harding, and Steven A. Niederer. "Modelling the interaction between stem cells derived cardiomyocytes patches and host myocardium to aid non-arrhythmic engineered heart tissue design." In: *PLOS Comput. Biol.* 18.4 (2022), e1010030. DOI: [10.1371/journal.pcbi.1010030](https://doi.org/10.1371/journal.pcbi.1010030). URL: <http://dx.doi.org/10.1371/journal.pcbi.1010030>.
- [61] M. Fernandez-Chas, M. J. Curtis, and S. A. Niederer. "Mechanism of doxorubicin cardiotoxicity evaluated by integrating multiple molecular effects into a biophysical model." In: *Br. J. Pharmacol.* 175.5 (2018), pp. 763–781. DOI: [10.1111/bph.14104](https://doi.org/10.1111/bph.14104).
- [62] Martin Fink and Denis Noble. "Markov models for ion channels: Versatility versus identifiability and speed." In: *Philos. Trans. R. Soc. A Math. Phys. Eng. Sci.* 367.1896 (2009), pp. 2161–2179. DOI: [10.1098/rsta.2008.0301](https://doi.org/10.1098/rsta.2008.0301).
- [63] Matthew A Fisher, Chris J Oates, Catherine Powell, and Aretha Teckentrup. "A Locally Adaptive Bayesian Cubature Method." In: *1* (2019), pp. 1–47. arXiv: [1910.02995](https://arxiv.org/abs/1910.02995). URL: <http://arxiv.org/abs/1910.02995>.
- [64] Mona Fiuzat et al. "Endpoints in Heart Failure Drug Development: History and Future." In: *JACC Hear. Fail.* 8.6 (2020), pp. 429–440. DOI: [10.1016/j.jchf.2019.12.011](https://doi.org/10.1016/j.jchf.2019.12.011).
- [65] Stephen F. Flaim and Robert Zelis. "Effects of diltiazem on total cardiac output distribution in conscious rats." In: *J. Pharmacol. Exp. Ther.* 222.2 (1982), pp. 359–366.
- [66] Wei Dong Gao, Dan Atar, Peter H. Backx, and Eduardo Marban. "Relationship Between Intracellular Calcium and Contractile Force in Stunned Myocardium." In: *Circ. Res.* 76.6 (1995), pp. 1036–1048. DOI: [10.1161/01.res.76.6.1036](https://doi.org/10.1161/01.res.76.6.1036).
- [67] Jacob R. Gardner, Geoff Pleiss, David Bindel, Kilian Q. Weinberger, and Andrew Gordon Wilson. *GPyTorch: Blackbox Matrix-Matrix Gaussian Process Inference with GPU Acceleration*. 2019. arXiv: [1809.11165 \[cs.LG\]](https://arxiv.org/abs/1809.11165).
- [68] Sara Gattoni, Åsmund Treu Røe, Michael Frisk, William E. Louch, Steven A. Niederer, and Nicolas P. Smith. "The calcium–frequency response in the rat ventricular myocyte: an experimental and modelling study." In: *J. Physiol.* 594.15 (2016), pp. 4193–4224. DOI: [10.1113/JP272011](https://doi.org/10.1113/JP272011).
- [69] Sara Gattoni, Åsmund Treu Røe, Jan Magnus Aronsen, Ivar Sjaastad, William E. Louch, Nicolas P. Smith, and Steven A. Niederer. "Compensatory and decompensatory alterations in cardiomyocyte Ca<sup>2+</sup> dynamics in hearts with diastolic dysfunction following aortic banding." In: *J. Physiol.* 595.12 (2017), pp. 3867–3889. DOI: [10.1113/JP273879](https://doi.org/10.1113/JP273879).

- [70] Marcel Groen, Alfredo Jesus López-Dávila, Stefan Zitrich, Gabriele Pfitzer, and Robert Stehle. "Hypertrophic and Dilated Cardiomyopathy-Associated Troponin T Mutations R130C and  $\Delta K_{210}$  Oppositely Affect Length-Dependent Calcium Sensitivity of Force Generation." In: *Front. Physiol.* 11.June (2020), pp. 1–9. doi: [10.3389/fphys.2020.00516](https://doi.org/10.3389/fphys.2020.00516).
- [71] Willemijn Groenendaal, Francis A. Ortega, Armen R. Kherlopian, Andrew C. Zygmunt, Trine Krogh-Madsen, and David J. Christini. "Cell-Specific Cardiac Electrophysiology Models." In: *PLoS Comput. Biol.* 11.4 (2015), pp. 1–22. doi: [10.1371/journal.pcbi.1004242](https://doi.org/10.1371/journal.pcbi.1004242).
- [72] J. M. Guccione, A. D. McCulloch, and L. K. Waldman. "Passive material properties of intact ventricular myocardium determined from a cylindrical model." In: *J. Biomech. Eng.* 113.1 (1991), pp. 42–55. doi: [10.1115/1.2894084](https://doi.org/10.1115/1.2894084).
- [73] John E. Hall and Michael E. Hall. *Guyton and Hall Textbook of Medical Physiology*. 14th Edition. Philadelphia, PA: Elsevier, 2021. ISBN: 9780323597128.
- [74] N. Hamdani et al. "Myocardial titin hypophosphorylation importantly contributes to heart failure with preserved ejection fraction in a rat metabolic risk model." In: *Circ. Hear. Fail.* 6.6 (2013), pp. 1239–1249. doi: [10.1161/CIRCHEARTFAILURE.113.000539](https://doi.org/10.1161/CIRCHEARTFAILURE.113.000539).
- [75] Samantha P. Harris, Christopher R. Bartley, Timothy A. Hacker, Kerry S. McDonald, Pamela S. Douglas, Marion L. Greaser, Patricia A. Powers, and Richard L. Moss. "Hypertrophic cardiomyopathy in cardiac myosin binding protein-C knockout mice." In: *Circ. Res.* 90.5 (2002), pp. 594–601. doi: [10.1161/01.RES.0000012222.70819.64](https://doi.org/10.1161/01.RES.0000012222.70819.64).
- [76] Danielle M. Henkel, Margaret M. Redfield, Susan A. Weston, Yariv Gerber, and Véronique L. Roger. "Death in heart failure: a community perspective." In: *Circ. Heart Fail.* 1.2 (2008), pp. 91–97. doi: [10.1161/CIRCHEARTFAILURE.107.743146](https://doi.org/10.1161/CIRCHEARTFAILURE.107.743146).
- [77] Philipp Hennig, Michael A. Osborne, and Mark Girolami. "Probabilistic numerics and uncertainty in computations." In: *Proc. R. Soc. A Math. Phys. Eng. Sci.* 471.2179 (2015). doi: [10.1098/rspa.2015.0142](https://doi.org/10.1098/rspa.2015.0142). arXiv: [1506.01326](https://arxiv.org/abs/1506.01326).
- [78] Jon Herman and Will Usher. "SALib: An open-source Python library for Sensitivity Analysis." In: *J. Open Source Softw.* 2.9 (2017), p. 97. doi: [10.21105/joss.00097](https://doi.org/10.21105/joss.00097).
- [79] N. Hersch, B. Wolters, G. Dreissen, R. Springer, N. Kirchgessner, R. Merkel, and B. Hoffmann. "The constant beat: cardiomyocytes adapt their forces by equal contraction upon environ-

- mental stiffening." In: *Biol. Open* 2.3 (2013), pp. 351–361. DOI: [10.1242/bio.20133830](https://doi.org/10.1242/bio.20133830).
- [80] Louise M. Hesketh, Catherine D.E. Wilder, Niraja N. Ranadive, Georgia Lytra, Patricia Qazimi, Jade S. Munro, Nakita Ahdi, and Michael J. Curtis. "Characterisation of mexiletine's translational therapeutic index for suppression of ischaemia-induced ventricular fibrillation in the rat isolated heart." In: *Sci. Rep.* 10.1 (2020), pp. 1–11. DOI: [10.1038/s41598-020-65190-y](https://doi.org/10.1038/s41598-020-65190-y).
- [81] A. L. Hodgkin and A. F. Huxley. "A quantitative description of membrane current and its application to conduction and excitation in nerve." In: *J. Physiol.* 117.4 (1952), pp. 500–544. DOI: [10.1113/jphysiol.1952.sp004764](https://doi.org/10.1113/jphysiol.1952.sp004764).
- [82] H. M. Hoffmeister and L. Seipel. "Comparison of the hemodynamics effects of D-sotalol and D,L-sotalol." In: *Klin Wochenschr.* 66.10 (1988), pp. 451–454.
- [83] F. Hohendanner et al. "Cellular mechanisms of metabolic syndrome-related atrial decompensation in a rat model of HFpEF." In: *J. Mol. Cell. Cardiol.* 115.November 2017 (2018), pp. 10–19. DOI: [10.1016/j.yjmcc.2017.12.012](https://doi.org/10.1016/j.yjmcc.2017.12.012). URL: <https://doi.org/10.1016/j.yjmcc.2017.12.012>.
- [84] Balázs Horváth, Norbert Szentandrásy, Roland Veress, János Almássy, János Magyar, Tamás Bányász, Attila Tóth, Zoltán Papp, and Péter P. Nánási. "Frequency-dependent effects of omecamtiv mecarbil on cell shortening of isolated canine ventricular cardiomyocytes." In: *Naunyn Schmiedebergs Arch. Pharmacol.* 390.12 (2017), pp. 1239–1246. DOI: [10.1007/s00210-017-1422-z](https://doi.org/10.1007/s00210-017-1422-z).
- [85] Shu Ting Hu, Ying Tang, Ya Feng Shen, Hai Hang Ao, Jie Bai, Yong Liang Wang, and Yong Ji Yang. "Protective effect of oxymatrine on chronic rat heart failure." In: *J. Physiol. Sci.* 61.5 (2011), pp. 363–372. DOI: [10.1007/s12576-011-0154-y](https://doi.org/10.1007/s12576-011-0154-y).
- [86] T. Huizer, JW de Jong, and PW Achterberg. "Protection by bepridil against myocardial ATP-catabolism is probably due to negative inotropy." In: *J Cardiovasc Pharmacol.* 10.1 (1987), pp. 55–61.
- [87] Hyosook Hwang, Joseph M. Arcidi, Sharon L. Hale, Boris Z. Simkhovich, Luiz Belardinelli, Arvinder K. Dhalla, John C. Shryock, and Robert A. Kloner. "Ranolazine as a cardioplegia additive improves recovery of diastolic function in isolated rat hearts." In: *Circulation* 120.SUPPL. 1 (2009), pp. 16–21. DOI: [10.1161/CIRCULATIONAHA.108.844167](https://doi.org/10.1161/CIRCULATIONAHA.108.844167).

- [88] Ronald L. Iman, Jon C. Helton, and James E. Campbell. "An Approach to Sensitivity Analysis of Computer Models: Part I—Introduction, Input Variable Selection and Preliminary Variable Assessment." In: *Journal of Quality Technology* 13.3 (1981), pp. 174–183. DOI: [10.1080/00224065.1981.11978748](https://doi.org/10.1080/00224065.1981.11978748).
- [89] Christos V. Ioannou, Denis R. Morel, Asterios N. Katsamouris, Sofia Katranitsa, Irena Startchik, Afksentios Kalangos, Nico Westerhof, and Nikos Stergiopoulos. "Left ventricular hypertrophy induced by reduced aortic compliance." In: *J. Vasc. Res.* 46.5 (2009), pp. 417–425. DOI: [10.1159/000194272](https://doi.org/10.1159/000194272).
- [90] T. Ishigami and T. Homma. "An importance quantification technique in uncertainty analysis for computer models." In: [1990] *Proceedings. First International Symposium on Uncertainty Modeling and Analysis*. 1990, pp. 398–403. DOI: [10.1109/ISUMA.1990.151285](https://doi.org/10.1109/ISUMA.1990.151285).
- [91] Nobuhiko Ito, Yutaka Kagaya, Ellen O. Weinberg, William H. Barry, and Beverly H. Lorell. "Endothelin and angiotensin II stimulation of Na<sup>+</sup>-H<sup>+</sup> exchange is impaired in cardiac hypertrophy." In: *J. Clin. Invest.* 99.1 (1997), pp. 125–135. DOI: [10.1172/JCI119123](https://doi.org/10.1172/JCI119123).
- [92] Michiel J.W. Jansen. "Analysis of variance designs for model output." In: *Computer Physics Communications* 117.1 (1999), pp. 35–43. DOI: [https://doi.org/10.1016/S0010-4655\(98\)00154-4](https://doi.org/10.1016/S0010-4655(98)00154-4).
- [93] R. H. Johnstone, E. T. Y. Chang, R. Bardenet, T. P. de Boer, D. J. Gavaghan, P. Pathmanathan, R. H. Clayton, and G. R. Mirams. "Uncertainty and variability in models of the cardiac action potential: Can we build trustworthy models?" In: *J. Mol. Cell. Cardiol.* 96 (July 2016), pp. 49–62.
- [94] Donald R. Jones, Matthias Schonlau, and William J. Welch. "Efficient Global Optimization of Expensive Black-Box Functions." In: *J. Glob. Optim.* 13.4 (1998), pp. 455–492. DOI: [10.1023/A:1008306431147](https://doi.org/10.1023/A:1008306431147).
- [95] Yutaka Kagaya, Ellen O. Weinberg, Nobuhiko Ito, Takatoshi Mochizuki, William H. Barry, and Beverly H. Lorell. "Glycolytic inhibition: Effects on diastolic relaxation and intracellular calcium handling in hypertrophied rat ventricular myocytes." In: *J. Clin. Invest.* 95.6 (1995), pp. 2766–2776. DOI: [10.1172/JCI117980](https://doi.org/10.1172/JCI117980).
- [96] Yutaka Kagaya, Roger J. Hajjar, Judith K. Gwathmey, William H. Barry, and Beverly H. Lorell. "Long-term angiotensin-converting enzyme inhibition with fosinopril improves depressed responsiveness to Ca<sup>2+</sup> in myocytes from aortic-banded rats." In: *Circulation* 94.11 (1996), pp. 2915–2922. DOI: [10.1161/01.CIR.94.11.2915](https://doi.org/10.1161/01.CIR.94.11.2915).

- [97] Toru Kamiyama, Kouichi Tanonaka, Hideaki Harada, Kat-suhiko Nakai, and Satoshi Takeo. "Mexiletine and lidocaine reduce post-ischemic functional and biochemical dysfunction of perfused hearts." In: *Eur. J. Pharmacol.* 272.2-3 (1995), pp. 151–158. DOI: [10.1016/0014-2999\(94\)00640-S](https://doi.org/10.1016/0014-2999(94)00640-S).
- [98] Thomas Kampourakis, Xuemeng Zhang, Yin Biao Sun, and Malcolm Irving. "Omecamtiv mercabil and blebbistatin modulate cardiac contractility by perturbing the regulatory state of the myosin filament." In: *J. Physiol.* 596.1 (2018), pp. 31–46. DOI: [10.1113/JP275050](https://doi.org/10.1113/JP275050).
- [99] Elias Karabelas, Stefano Longobardi, Jana Fuchsberger, Orod Razeghi, Cristobal Rodero, Marina Strocchi, Ronak Rajani, Gundolf Haase, Gernot Plank, and Steven Niederer. "Global Sensitivity Analysis of Four Chamber Heart Hemodynamics Using Surrogate Models." In: *IEEE Trans. Biomed. Eng.* PP.Xx (2021), p. 1. DOI: [10.1109/TBME.2022.3163428](https://doi.org/10.1109/TBME.2022.3163428). arXiv: [2111.08339](https://arxiv.org/abs/2111.08339). URL: <http://arxiv.org/abs/2111.08339>.
- [100] M. Katsuoka and S. T. Ohnishi. "Pharmacologic protection of perfused rat heart against global ischemia." In: *Prostaglandins, Leukot. Essent. Fat. Acids* 38.3 (1989), pp. 151–156. DOI: [10.1016/0952-3278\(89\)90064-1](https://doi.org/10.1016/0952-3278(89)90064-1).
- [101] David Kennedy, Eiad Omran, Sankaridrug M. Periyasamy, Jalaa Nadoor, Anumeet Priyadarshi, James C. Willey, Deepak Malhotra, Zijian Xie, and Joseph I. Shapiro. "Effect of chronic renal failure on cardiac contractile function, calcium cycling, and gene expression of proteins important for calcium homeostasis in the rat." In: *J. Am. Soc. Nephrol.* 14.1 (2003), pp. 90–97. DOI: [10.1097/01.ASN.0000037403.95126.03](https://doi.org/10.1097/01.ASN.0000037403.95126.03).
- [102] Marc C Kennedy and Anthony O'hagan. *Bayesian calibration of computer models*. Tech. rep. 2001, pp. 425–464.
- [103] Thinh T. Kieu, Peter O. Awinda, and Bertrand C.W. Tanner. "Omecamtiv Mecarbil Slows Myosin Kinetics in Skinned Rat Myocardium at Physiological Temperature." In: *Biophys. J.* 116.11 (2019), pp. 2149–2160. DOI: [10.1016/j.bpj.2019.04.020](https://doi.org/10.1016/j.bpj.2019.04.020).
- [104] Peter J. Kilfoil, Sabine Lotteau, Rui Zhang, Xin Yue, Stephan Aynaszyan, Ryan E. Solymani, Eugenio Cingolani, Eduardo Marbán, and Joshua I. Goldhaber. "Distinct features of calcium handling and  $\beta$ -adrenergic sensitivity in heart failure with preserved versus reduced ejection fraction." In: *J. Physiol.* 598.22 (2020), pp. 5091–5108. DOI: [10.1113/JP280425](https://doi.org/10.1113/JP280425).
- [105] Tae Yun Kim et al. "SK channel enhancers attenuate  $\text{Ca}^{2+}$ -dependent arrhythmia in hypertrophic hearts by regulating mito-ROS-dependent oxidation and activity of RyR." In: *Cardiovasc. Res.* 113.3 (2017), pp. 343–353. DOI: [10.1093/cvr/cvx005](https://doi.org/10.1093/cvr/cvx005).

- [106] Sebastian E. Kirschner et al. "Hypertrophic cardiomyopathy-related  $\beta$ -myosin mutations cause highly variable calcium sensitivity with functional imbalances among individual muscle cells." In: *Am. J. Physiol. - Hear. Circ. Physiol.* 288.3 57-3 (2005), pp. 1242–1251. DOI: [10.1152/ajpheart.00686.2004](https://doi.org/10.1152/ajpheart.00686.2004).
- [107] S Kobayashi, M Yano, M Kohno, M Obayashi, Y Hisamatsu, T Ryoke, T Ohkusa, K Yamakawa, and M Matsuzaki. "Influence of aortic impedance on the development of pressure-overload left ventricular hypertrophy in rats." In: *Circulation* 94.12 (1996), pp. 3362–8. DOI: [10.1161/01.cir.94.12.3362](https://doi.org/10.1161/01.cir.94.12.3362).
- [108] F. Kolář, B. Ošt'ádal, and F. Papoušek. "Effect of verapamil on contractile function of the isolated perfused rat heart during postnatal ontogeny." In: *Basic Res. Cardiol.* 85.5 (1990), pp. 429–434. DOI: [10.1007/BF01931488](https://doi.org/10.1007/BF01931488).
- [109] Matyas Koltai, Arpad Tosaki, David Hosford, and Pierre Brquet. "Ginkgolide B protects isolated hearts against arrhythmias induced by ischemia but not reperfusion." In: *Eur. J. Pharmacol.* 164.2 (1989), pp. 293–302. DOI: [10.1016/0014-2999\(89\)90470-6](https://doi.org/10.1016/0014-2999(89)90470-6).
- [110] Attila Kovács et al. "Strain and strain rate by speckle-tracking echocardiography correlate with pressure-volume loop-derived contractility indices in a rat model of athlete's heart." In: *J Physiol Hear. Circ Physiol* 308 (2015), pp. 743–748. DOI: [10.1152/ajpheart.00828.2014.-Contractile](https://doi.org/10.1152/ajpheart.00828.2014.-Contractile). URL: [www.ajpheart.org](http://www.ajpheart.org).
- [111] Karen L. Kreutziger, Nicoletta Piroddi, Jonathan T. McMichael, Chiara Tesi, Corrado Poggesi, and Michael Regnier. "Calcium binding kinetics of troponin C strongly modulate cooperative activation and tension kinetics in cardiac muscle." In: *J. Mol. Cell. Cardiol.* 50.1 (2011), pp. 165–174. DOI: [10.1016/j.yjmcc.2010.10.025](https://doi.org/10.1016/j.yjmcc.2010.10.025). URL: <http://dx.doi.org/10.1016/j.yjmcc.2010.10.025>.
- [112] Hui Chun Ku and Ming Jai Su. "DPP4 deficiency preserved cardiac function in abdominal aortic banding rats." In: *PLoS One* 9.1 (2014). DOI: [10.1371/journal.pone.0085634](https://doi.org/10.1371/journal.pone.0085634).
- [113] Yen Chun Lai et al. "SIRT3-AMP-Activated Protein Kinase Activation by Nitrite and Metformin Improves Hyperglycemia and Normalizes Pulmonary Hypertension Associated with Heart Failure with Preserved Ejection Fraction." In: *Circulation* 133.8 (2016), pp. 717–731. DOI: [10.1161/CIRCULATIONAHA.115.018935](https://doi.org/10.1161/CIRCULATIONAHA.115.018935).
- [114] Pablo Lamata, Steven Niederer, David Nordsletten, David C. Barber, Ishani Roy, D. Rod Hose, and Nic Smith. "An accurate, fast and robust method to generate patient-specific cubic

- Hermite meshes." In: *Med. Image Anal.* 15.6 (2011), pp. 801–813. doi: [10.1016/j.media.2011.06.010](https://doi.org/10.1016/j.media.2011.06.010).
- [115] Pablo Lamata et al. "An automatic service for the personalization of ventricular cardiac meshes." In: *J. R. Soc. Interface* 11.91 (2014). doi: [10.1098/rsif.2013.1023](https://doi.org/10.1098/rsif.2013.1023).
- [116] D. Lamontagne, L. Rochette, M. Vermeulen, N. Yamaguchi, R. Nadeau, and J. De Champlain. "Effect of sotalol against reperfusion-induced arrhythmias in Sprague-Dawley and Wistar rats." In: *Fundamental & Clinical Pharmacology* 3.6 (1989), pp. 671–685. doi: <https://doi.org/10.1111/j.1472-8206.1989.tb00468.x>.
- [117] Sander Land and Steven A. Niederer. "A Spatially Detailed Model of Isometric Contraction Based on Competitive Binding of Troponin I Explains Cooperative Interactions between Tropomyosin and Crossbridges." In: *PLoS Comput. Biol.* 11.8 (2015). doi: [10.1371/journal.pcbi.1004376](https://doi.org/10.1371/journal.pcbi.1004376).
- [118] Sander Land, Steven A. Niederer, and Nicolas P. Smith. "Efficient computational methods for strongly coupled cardiac electromechanics." In: *IEEE Trans. Biomed. Eng.* 59.5 (2012), pp. 1219–1228. doi: [10.1109/TBME.2011.2112359](https://doi.org/10.1109/TBME.2011.2112359).
- [119] Sander Land, Steven A. Niederer, Jan Magnus Aronsen, Emil K.S. Espe, Lili Zhang, William E. Louch, Ivar Sjaastad, Ole M. Sejersted, and Nicolas P. Smith. "An analysis of deformation-dependent electromechanical coupling in the mouse heart." In: *J. Physiol.* 590.18 (2012), pp. 4553–4569. doi: [10.1113/jphysiol.2012.231928](https://doi.org/10.1113/jphysiol.2012.231928).
- [120] Sander Land, Steven A Niederer, Pablo Lamata, and Nicolas P Smith. "Improving the stability of cardiac mechanical simulations." In: *IEEE Trans. Biomed. Eng.* 62.3 (2015), pp. 939–947. doi: [10.1109/TBME.2014.2373399.Improving](https://doi.org/10.1109/TBME.2014.2373399.Improving).
- [121] Sander Land et al. "Verification of cardiac mechanics software: Benchmark problems and solutions for testing active and passivematerial behaviour." In: *Proc. R. Soc. A Math. Phys. Eng. Sci.* 471.2184 (2015). doi: [10.1098/rspa.2015.0641](https://doi.org/10.1098/rspa.2015.0641).
- [122] Asbjørn Langslet and Morten Ryg. "Effects of Chlorpromazine and Propranolol on Left Ventricular Systolic Pressure, ECG, and K<sup>+</sup> Efflux in the Isolated Perfused Rat Heart." In: *Acta Pharmacol. Toxicol. (Copenh.)*. 29.5-6 (1971), pp. 533–541. doi: [10.1111/j.1600-0773.1971.tb00627.x](https://doi.org/10.1111/j.1600-0773.1971.tb00627.x).
- [123] Kyuho Lee, Hye Jeong Hwang, Ok Soo Kim, and Young Jun Oh. "Assessment of dexmedetomidine effects on left ventricular function using pressure–volume loops in rats." In: *J. Anesth.* 31.1 (2017), pp. 18–24. doi: [10.1007/s00540-016-2278-y](https://doi.org/10.1007/s00540-016-2278-y).

- [124] J. de Leiris, D. P. Harding, and S. Pestre. "The isolated perfused rat heart: A model for studying myocardial hypoxia or ischaemia." In: *Basic Res. Cardiol.* 79.3 (1984), pp. 313–321. DOI: [10.1007/BF01908032](https://doi.org/10.1007/BF01908032).
- [125] Sara Leite et al. "Afterload-induced diastolic dysfunction contributes to high filling pressures in experimental heart failure with preserved ejection fraction." In: *Am. J. Physiol. - Hear. Circ. Physiol.* 309.10 (2015), H1648–H1654. DOI: [10.1152/ajpheart.00397.2015](https://doi.org/10.1152/ajpheart.00397.2015).
- [126] Sara Leite, José Oliveira-Pinto, Marta Tavares-Silva, Mahmoud Abdellatif, Dulce Fontoura, Inês Falcão-Pires, Adelino F. Leite-Moreira, and André P. Lourenço. "Echocardiography and invasive hemodynamics during stress testing for diagnosis of heart failure with preserved ejection fraction: An experimental study." In: *Am. J. Physiol. - Hear. Circ. Physiol.* 308.12 (2015), H1556–H1563. DOI: [10.1152/ajpheart.00076.2015](https://doi.org/10.1152/ajpheart.00076.2015).
- [127] Sara Leite et al. "Arterial Remodeling and Dysfunction in the ZSF1 Rat Model of Heart Failure With Preserved Ejection Fraction." In: *Circ. Hear. Fail.* 12.7 (2019), pp. 1–12. DOI: [10.1161/CIRCHEARTFAILURE.118.005596](https://doi.org/10.1161/CIRCHEARTFAILURE.118.005596).
- [128] Rodney J. Levick. *An Introduction to Cardiovascular Physiology*. 5th ed. CRC Press, 2009.
- [129] B. I. Levy, J. B. Michel, J. L. Salzmann, M. Azizi, P. Poitevin, M. Safar, and J. P. Camilleri. "Effects of chronic inhibition of converting enzyme on mechanical and structural properties of arteries in rat renovascular hypertension." In: *Circ. Res.* 63.1 (1988), pp. 227–239. DOI: [10.1161/01.RES.63.1.227](https://doi.org/10.1161/01.RES.63.1.227).
- [130] Alexandre Lewalle, Sander Land, Eric Carruth, Lawrence R. Frank, Pablo Lamata, Jeffrey H. Omens, Andrew D. McCulloch, Steven A. Niederer, and Nicolas P. Smith. "Decreasing compensatory ability of concentric ventricular hypertrophy in aortic-banded rat hearts." In: *Front. Physiol.* 9.FEB (2018). DOI: [10.3389/fphys.2018.00037](https://doi.org/10.3389/fphys.2018.00037).
- [131] Zhihua Li et al. "Assessment of an In Silico Mechanistic Model for Proarrhythmia Risk Prediction Under the CiPA Initiative." In: *Clin. Pharmacol. Ther.* 105.2 (2019), pp. 466–475. DOI: [10.1002/cpt.1184](https://doi.org/10.1002/cpt.1184).
- [132] Yi-Tsen Lin, Yung-Zu Tseng, and Kuo-Chu Chang. "Aminoguanidine Prevents Fructose-Induced Arterial Stiffening in Wistar Rats: Aortic Impedance Analysis." In: *Exp. Biol. Med.* 229.10 (2004), pp. 1038–1045. DOI: [10.1177/153537020422901008](https://doi.org/10.1177/153537020422901008).

- [133] Jiaming Liu, Pengfei Han, Ying Xiao, Jian Li, Y James Kang, Liu Jm, and Liu Jn. "A novel knot method for individually measurable aortic constriction in rats." In: *Am J Physiol Hear. Circ Physiol* 307 (2014), pp. 987–995. doi: [10.1152/ajpheart.00990.2013](https://doi.org/10.1152/ajpheart.00990.2013). -A. URL: [www.ajpheart.org](http://www.ajpheart.org).
- [134] J. P. Loennechen, U. Wisløff, G. Falck, and Ellingsen. "Cardiomyocyte contractility and calcium handling partially recover after early deterioration during post-infarction failure in rat." In: *Acta Physiol. Scand.* 176.1 (2002), pp. 17–26. doi: [10.1046/j.1365-201X.2002.01011.x](https://doi.org/10.1046/j.1365-201X.2002.01011.x).
- [135] Jan P. Loennechen, Ulrik Wisløff, Geir Falck, and Øyvind Ellingsen. "Effects of cariporide and losartan on hypertrophy, calcium transients, contractility, and gene expression in congestive heart failure." In: *Circulation* 105.11 (2002), pp. 1380–1386. doi: [10.1161/hc1102.105258](https://doi.org/10.1161/hc1102.105258).
- [136] S. Longobardi, A. Sher, and S. A. Niederer. "In Silico Mapping of the Omecamtiv Mecarbil Effects from the Sarcomere to the Whole-Heart and Back Again." In: *Functional Imaging and Modeling of the Heart*. Ed. by Daniel B. Ennis, Luigi E. Perotti, and Vicky Y. Wang. Cham: Springer International Publishing, June 2021, pp. 406–415. ISBN: 978-3-030-78710-3. doi: [10.1007/978-3-030-78710-3\\_39](https://doi.org/10.1007/978-3-030-78710-3_39).
- [137] S. Longobardi, A. Sher, and S. A. Niederer. "In silico identification of potential calcium dynamics and sarcomere targets for recovering left ventricular function in rat heart failure with preserved ejection fraction." In: *PLoS Comput. Biol.* 17.12 (Dec. 2021), pp. 1–22. doi: [10.1371/journal.pcbi.1009646](https://doi.org/10.1371/journal.pcbi.1009646).
- [138] S. Longobardi, A. Sher, and S. A. Niederer. "Quantitative mapping of force-pCa curves to whole heart contraction and relaxation." In: *J. Physiol.* o (July 2022), pp. 1–20. doi: [10.1113/jp283352](https://doi.org/10.1113/jp283352).
- [139] S. Longobardi, A. Lewalle, S. Coveney, I. Sjaastad, E. K.S. Espe, W. E. Louch, C. J. Musante, A. Sher, and S. A. Niederer. "Predicting left ventricular contractile function via Gaussian process emulation in aortic-banded rats." In: *Philos. Trans. A. Math. Phys. Eng. Sci.* 378.2173 (June 2020), p. 20190334. doi: [10.1098/rsta.2019.0334](https://doi.org/10.1098/rsta.2019.0334).
- [140] Stefano Longobardi. *Historia: A set of more or less powerful tools I developed during my PhD for more or less generic scientific computing purposes.* <https://github.com/stelong/Historia>. 2018–2021.
- [141] Stefano Longobardi, Anna Sher, and Steven Niederer. *In silico identification of potential calcium dynamics and sarcomere targets for recovering left ventricular function in rat heart failure with pre-*

*served ejection fraction.* Version 1.0.0. Oct. 2021. DOI: [10.5281/zenodo.5595066](https://doi.org/10.5281/zenodo.5595066). URL: <https://doi.org/10.5281/zenodo.5595066>.

- [142] Stefano Longobardi and Gianvito Taneburgo. *GPErks: a Python library to (bene)fit Gaussian Process Emulators.* <https://github.com/stelong/GPErks>. 2021.
- [143] Annemarieke Elisabeth Loot. “Therapeutic perspectives of Angiotensin-(1-7) in heart failure.” PhD thesis. University of Groningen, 2005.
- [144] Reginald I. Low, Patricia Takeda, Dean T. Mason, and Anthony N. DeMaria. “The effects of calcium channel blocking agents on cardiovascular function.” In: *Am. J. Cardiol.* 49.3 (1982), pp. 547–553. DOI: [10.1016/S0002-9149\(82\)80010-6](https://doi.org/10.1016/S0002-9149(82)80010-6).
- [145] Alexander R. Lyon, Ken T. MacLeod, Yanjun Zhang, Edwin Garcia, Gaelle Kikonda Kanda, Max J. Lab, Yuri E. Korchev, Sian E. Harding, and Julia Gorelik. “Loss of T-tubules and other changes to surface topography in ventricular myocytes from failing human and rat heart.” In: *Proc. Natl. Acad. Sci. U. S. A.* 106.16 (2009), pp. 6854–6859. DOI: [10.1073/pnas.0809777106](https://doi.org/10.1073/pnas.0809777106).
- [146] Alexander R. Lyon et al. “SERCA2a gene transfer decreases sarcoplasmic reticulum calcium leak and reduces ventricular arrhythmias in a model of chronic heart failure.” In: *Circ. Arrhythmia Electrophysiol.* 4.3 (2011), pp. 362–372. DOI: [10.1161/CIRCEP.110.961615](https://doi.org/10.1161/CIRCEP.110.961615).
- [147] Michał Maćzewski and Urszula Mackiewicz. “Effect of metoprolol and ivabradine on left ventricular remodelling and Ca<sup>2+</sup> handling in the post-infarction rat heart.” In: *Cardiovasc. Res.* 79.1 (2008), pp. 42–51. DOI: [10.1093/cvr/cvn057](https://doi.org/10.1093/cvr/cvn057).
- [148] Charles Mackin, Elizabeth S. DeWitt, Katherine J. Black, Xiaoli Tang, Brian D. Polizzotti, Sarah J. van den Bosch, Mark E. Alexander, and John N. Kheir. “Intravenous Amiodarone and Sotalol Impair Contractility and Cardiac Output, but Procainamide Does Not: A Langendorff Study.” In: *J. Cardiovasc. Pharmacol. Ther.* 24.3 (2019), pp. 288–297. DOI: [10.1177/1074248418810811](https://doi.org/10.1177/1074248418810811).
- [149] Lars S. Maier, Rolf Brandes, Burkert Pieske, and Donald M. Bers. “Effects of left ventricular hypertrophy on force and Ca<sup>2+</sup> handling in isolated rat myocardium.” In: *Am. J. Physiol. - Hear. Circ. Physiol.* 274.4 H3-H4 (1998). DOI: [10.1152/ajpheart.1998.274.4.h1361](https://doi.org/10.1152/ajpheart.1998.274.4.h1361).
- [150] F. I. Malik et al. “Cardiac Myosin Activation: A Potential Therapeutic Approach for Systolic Heart Failure.” In: *Science (80- ).* 331.6023 (2011). DOI: [10.1126/science.1200113](https://doi.org/10.1126/science.1200113).

- [151] Ranganath Mamidi, Jiayang Li, Chang Yoon Doh, Sujeeet Verma, and Julian E. Stelzer. "Impact of the myosin modulator mavacamten on force generation and cross-bridge behavior in a murine model of hypercontractility." In: *J. Am. Heart Assoc.* 7.17 (2018), pp. 1–15. DOI: [10.1161/JAHA.118.009627](https://doi.org/10.1161/JAHA.118.009627).
- [152] Amandine Marrel, Bertrand Iooss, François Van Dorpe, and Elena Volkova. "An efficient methodology for modeling complex computer codes with Gaussian processes." In: *Comput. Stat. Data Anal.* 52.10 (2008), pp. 4731–4744. DOI: [10.1016/j.csda.2008.03.026](https://doi.org/10.1016/j.csda.2008.03.026). arXiv: [0802.1099](https://arxiv.org/abs/0802.1099).
- [153] Amandine Marrel, Bertrand Iooss, Béatrice Laurent, and Olivier Roustant. "Calculations of Sobol indices for the Gaussian process metamodel." In: *Reliab. Eng. Syst. Saf.* 94.3 (2009), pp. 742–751. DOI: [10.1016/j.ress.2008.07.008](https://doi.org/10.1016/j.ress.2008.07.008). arXiv: [0802.1008](https://arxiv.org/abs/0802.1008).
- [154] R J Marshall, A W Muir, and E Winslow. "Mexiletine and Org 6001 in the Anaesthetized Rat." In: *Br. J. Pharmacol.* 74 (1981), pp. 381–388.
- [155] Megan L. McCain, Hongyan Yuan, Francesco S. Pasqualini, Patrick H. Campbell, and Kevin Kit Parker. "Matrix elasticity regulates the optimal cardiac myocyte shape for contractility." In: *Am. J. Physiol. - Hear. Circ. Physiol.* 306.11 (2014), pp. 1525–1539. DOI: [10.1152/ajpheart.00799.2013](https://doi.org/10.1152/ajpheart.00799.2013).
- [156] Achim Meissner, Jiang Yong Min, and Rüdiger Simon. "Effects of angiotensin II on inotropy and intracellular Ca<sup>2+</sup> handling in normal and hypertrophied rat myocardium." In: *J. Mol. Cell. Cardiol.* 30.11 (1998), pp. 2507–2518. DOI: [10.1006/jmcc.1998.0813](https://doi.org/10.1006/jmcc.1998.0813).
- [157] John Jeshurun Michael, Sampath K. Gollapudi, and Murali Chandra. "Interplay between the effects of a Protein Kinase C phosphomimic (T204E) and a dilated cardiomyopathy mutation (K211Δ or R206W) in rat cardiac troponin T blunts the magnitude of muscle length-mediated crossbridge recruitment against the β-myosin heavy cha." In: *J. Muscle Res. Cell Motil.* 37.3 (2016), pp. 83–93. DOI: [10.1007/s10974-016-9448-2](https://doi.org/10.1007/s10974-016-9448-2).
- [158] Jiang-Yong Min, Achim Meissner, and James P. Morgan. "Mibepradil Improves β-drenergic Responsiveness and Intracellular Ca<sup>2+</sup> Handling in Hypertrophied Rat Myocardium." In: *Exp. Biol. Med.* 227.5 (2002), pp. 336–344. DOI: [10.1177/153537020222700506](https://doi.org/10.1177/153537020222700506).
- [159] Daniela Miranda-Silva et al. "Disturbed cardiac mitochondrial and cytosolic calcium handling in a metabolic risk-related rat model of heart failure with preserved ejection fraction." In: *Acta Physiol.* 228.3 (2020), pp. 1–17. DOI: [10.1111/apha.13378](https://doi.org/10.1111/apha.13378).

- [160] L. Nagy, Kovács, B. Bődi, E. T. Pásztor, G. Fülöp, A. Tőth, I. Édes, and Z. Papp. "The novel cardiac myosin activator omecamtiv mecarbil increases the calcium sensitivity of force production in isolated cardiomyocytes and skeletal muscle fibres of the rat." In: *Br. J. Pharmacol.* 172.18 (2015), pp. 4506–4518. DOI: [10.1111/bph.13235](https://doi.org/10.1111/bph.13235).
- [161] Balázs Tamás Németh et al. "Cinaciguat prevents the development of pathologic hypertrophy in a rat model of left ventricular pressure overload." In: *Sci. Rep.* 6 (2016). DOI: [10.1038/srep37166](https://doi.org/10.1038/srep37166).
- [162] Isabel T.N. Nguyen et al. "Both male and female obese ZSF1 rats develop cardiac dysfunction in obesity-induced heart failure with preserved ejection fraction." In: *PLoS One* 15.5 (2020), pp. 1–16. DOI: [10.1371/journal.pone.0232399](https://doi.org/10.1371/journal.pone.0232399). URL: <http://dx.doi.org/10.1371/journal.pone.0232399>.
- [163] S. A. Niederer, P. J. Hunter, and N. P. Smith. "A quantitative analysis of cardiac myocyte relaxation: A simulation study." In: *Biophys. J.* 90.5 (2006), pp. 1697–1722. DOI: [10.1529/biophysj.105.069534](https://doi.org/10.1529/biophysj.105.069534).
- [164] Steven A. Niederer, Kenneth S. Campbell, and Stuart G. Campbell. "A short history of the development of mathematical models of cardiac mechanics." In: *J. Mol. Cell. Cardiol.* 127.November 2018 (2019), pp. 11–19. DOI: [10.1016/j.yjmcc.2018.11.015](https://doi.org/10.1016/j.yjmcc.2018.11.015). URL: <https://doi.org/10.1016/j.yjmcc.2018.11.015>.
- [165] Steven A. Niederer and Nicolas P. Smith. "The Role of the Frank–Starling Law in the Transduction of Cellular Work to Whole Organ Pump Function: A Computational Modeling Analysis." In: *PLoS Comput. Biol.* 5.4 (2009). Ed. by Martyn Nash, e1000371. DOI: [10.1371/journal.pcbi.1000371](https://doi.org/10.1371/journal.pcbi.1000371). URL: <https://doi.org/10.1371/journal.pcbi.1000371>.
- [166] H Nishimura, J Kubota, M Okabe, M Ueyama, and K Kawamura. "Nifedipine in divided doses does not reverse left ventricular hypertrophy in spontaneously hypertensive rats." In: *Jpn Circ J* 56.3 (1992), pp. 256–261. URL: [https://www.jstage.jst.go.jp/article/bpb1993/17/11/17{\\\_}11{\\\_}1460/{\\\_}pdf/-char/ja](https://www.jstage.jst.go.jp/article/bpb1993/17/11/17{\_}11{\_}1460/{\_}pdf/-char/ja).
- [167] D. Noble. "A modification of the Hodgkin–Huxley equations applicable to Purkinje fibre action and pacemaker potentials." In: *The Journal of Physiology* 160.2 (1962), pp. 317–352. DOI: [10.1113/jphysiol.1962.sp006849](https://doi.org/10.1113/jphysiol.1962.sp006849).
- [168] Øyvind Nordbø et al. "A computational pipeline for quantification of mouse myocardial stiffness parameters." In: *Comput. Biol. Med.* 53 (2014), pp. 65–75. DOI: [10.1016/j.combiomed.2014.07.013](https://doi.org/10.1016/j.combiomed.2014.07.013).

- [169] Jeremy E. Oakley and Anthony O'Hagan. "Probabilistic sensitivity analysis of complex models: a Bayesian approach." In: *J. R. Stat. Soc. Ser. B (Statistical Methodol.)* 66.3 (2004), pp. 751–769. DOI: [10.1111/j.1467-9868.2004.05304.x](https://doi.org/10.1111/j.1467-9868.2004.05304.x).
- [170] Chris J. Oates, Steven Niederer, Angela Lee, François Xavier Briol, and Mark Girolami. "Probabilistic models for integration error in the assessment of functional cardiac models." In: *Adv. Neural Inf. Process. Syst.* 2017-Decem.1 (2017), pp. 110–118. arXiv: [1606.06841](https://arxiv.org/abs/1606.06841).
- [171] Attila Oláh et al. "Cardiac effects of acute exhaustive exercise in a rat model." In: *Int. J. Cardiol.* 182.C (2015), pp. 258–266. DOI: [10.1016/j.ijcard.2014.12.045](https://doi.org/10.1016/j.ijcard.2014.12.045).
- [172] Iacopo Olivotto et al. "Mavacamten for treatment of symptomatic obstructive hypertrophic cardiomyopathy (EXPLORER-HCM): a randomised, double-blind, placebo-controlled, phase 3 trial." In: *Lancet* 396.10253 (2020), pp. 759–769. DOI: [10.1016/S0140-6736\(20\)31792-X](https://doi.org/10.1016/S0140-6736(20)31792-X).
- [173] Jeffrey H. Omens, Deidre A. MacKenna, and Andrew D. McCulloch. "Measurement of strain and analysis of stress in resting rat left ventricular myocardium." In: *J. Biomech.* 26.6 (1993), pp. 665–676. DOI: [10.1016/0021-9290\(93\)90030-I](https://doi.org/10.1016/0021-9290(93)90030-I). URL: <https://www.sciencedirect.com/science/article/pii/002192909390030I?via%20Dihub>.
- [174] Theophilus E. Owan, David O. Hodge, Regina M. Herges, Steven J. Jacobsen, Veronique L. Roger, and Margaret M. Redfield. "Trends in Prevalence and Outcome of Heart Failure with Preserved Ejection Fraction." In: *N. Engl. J. Med.* 355.3 (2006), pp. 251–259. DOI: [10.1056/NEJMoa052256](https://doi.org/10.1056/NEJMoa052256).
- [175] A. O'Hagan. "Bayesian analysis of computer code outputs: A tutorial." In: *Reliability Engineering & System Safety* 91.10 (2006). The Fourth International Conference on Sensitivity Analysis of Model Output (SAMO 2004), pp. 1290–1300. ISSN: 0951-8320. URL: <https://doi.org/10.1016/j.ress.2005.11.025>.
- [176] Bradley M Palmer, David E Fishbaugher, Joachim P Schmitt, Yuan Wang, Norman R Alpert, Christine E Seidman, J G Seidman, Peter Vanburen, and David W Maughan. "Differential cross-bridge kinetics of FHC myosin mutations R403Q and R453C in heterozygous mouse myocardium." In: *Am J Physiol Hear. Circ Physiol* 287 (2004), pp. 91–99. DOI: [10.1152/ajpheart.01015.2003](https://doi.org/10.1152/ajpheart.01015.2003). -The. URL: [www.ajpheart.org](http://www.ajpheart.org).
- [177] Jin-sol Park, Ji-young Jeon, Ji-ho Yang, and Min-gul Kim. "Introduction to in silico model for proarrhythmic risk assessment under the CiPA initiative." In: *Transl Clin Pharmacol* 27.1 (2019), pp. 12–18.

- [178] Sin Hee Park et al. "Empagliflozin improved systolic blood pressure, endothelial dysfunction and heart remodeling in the metabolic syndrome ZSF<sub>1</sub> rat." In: *Cardiovasc. Diabetol.* 19.1 (2020), pp. 1–14. DOI: [10.1186/s12933-020-00997-7](https://doi.org/10.1186/s12933-020-00997-7). URL: <https://doi.org/10.1186/s12933-020-00997-7>.
- [179] Edoardo Pasolli and Farid Melgani. "Gaussian process regression within an active learning scheme." In: *2011 IEEE International Geoscience and Remote Sensing Symposium*. 2011, pp. 3574–3577. DOI: [10.1109/IGARSS.2011.6049994](https://doi.org/10.1109/IGARSS.2011.6049994).
- [180] Ravi B. Patel and Sanjiv J. Shah. "Drug targets for heart failure with preserved ejection fraction: A mechanistic approach and review of contemporary clinical trials." In: *Annu. Rev. Pharmacol. Toxicol.* 59 (2019), pp. 41–63. DOI: [10.1146/annurev-pharmtox-010818-021136](https://doi.org/10.1146/annurev-pharmtox-010818-021136).
- [181] Pras Pathmanathan, Jonathan M. Cordeiro, and Richard A. Gray. "Comprehensive uncertainty quantification and sensitivity analysis for cardiac action potential models." In: *Front. Physiol.* 10.JUN (2019), pp. 1–20. DOI: [10.3389/fphys.2019.00721](https://doi.org/10.3389/fphys.2019.00721).
- [182] Richard D. Patten and Monica R. Hall-Porter. "Small Animal Models of Heart Failure." In: *Circ. Hear. Fail.* 2.2 (2009), pp. 138–144. DOI: [10.1161/CIRCHEARTFAILURE.108.839761](https://doi.org/10.1161/CIRCHEARTFAILURE.108.839761).
- [183] F. Pedregosa et al. "Scikit-learn: Machine Learning in Python." In: *Journal of Machine Learning Research* 12 (2011), pp. 2825–2830.
- [184] Marc A. Pfeffer, Amil M. Shah, and Barry A. Borlaug. "Heart Failure with Preserved Ejection Fraction in Perspective." In: *Circ. Res.* 124.11 (2019), pp. 1598–1617. DOI: [10.1161/CIRCRESAHA.119.313572](https://doi.org/10.1161/CIRCRESAHA.119.313572).
- [185] Friedrich Pukelsheim. "The Three Sigma Rule." In: *Am. Stat.* 48.2 (1994), pp. 88–91. URL: <http://www.jstor.org/stable/2684253>.
- [186] Herschel Rabitz, Ömer F. Aliş, Jeffrey Shorter, and Kyurhee Shim. "Efficient input-output model representations." In: *Comput. Phys. Commun.* 117.1 (1999), pp. 11–20. DOI: [10.1016/S0010-4655\(98\)00152-0](https://doi.org/10.1016/S0010-4655(98)00152-0).
- [187] Carl Edward Rasmussen and Christopher K. I. Williams. *Gaussian processes for machine learning*. Adaptive computation and machine learning. MIT Press, 2006, pp. I–XVIII, 1–248. ISBN: 026218253X.
- [188] John Jeremy Rice, Fei Wang, Donald M. Bers, and Pieter P. De Tombe. "Approximate model of cooperative activation and crossbridge cycling in cardiac muscle using ordinary differential equations." In: *Biophys. J.* 95.5 (2008), pp. 2368–2390. DOI: [10.1529/biophysj.107.119487](https://doi.org/10.1529/biophysj.107.119487).

- [189] Cristobal Rodero et al. "Linking statistical shape models and simulated function in the healthy adult human heart." In: *PLOS Computational Biology* 17.4 (Apr. 2021), pp. 1–28. DOI: [10.1371/journal.pcbi.1008851](https://doi.org/10.1371/journal.pcbi.1008851). URL: <https://doi.org/10.1371/journal.pcbi.1008851>.
- [190] Åsmund T. Røe, Jan Magnus Aronsen, Kristine Skårdal, Nazha Hamdani, Wolfgang A. Linke, Håvard E. Danielsen, Ole M. Sejersted, Ivar Sjaastad, and William E. Louch. "Increased passive stiffness promotes diastolic dysfunction despite improved Ca<sup>2+</sup> handling during left ventricular concentric hypertrophy." In: *Cardiovasc. Res.* 113.10 (2017), pp. 1161–1172. DOI: [10.1093/cvr/cvx087](https://doi.org/10.1093/cvr/cvx087).
- [191] S S Rosenfeld and E W Taylor. "Kinetic studies of calcium binding to regulatory complexes from skeletal muscle." In: *J. Biol. Chem.* 260.1 (1985), pp. 252–61.
- [192] Jonathan Rougier. "Efficient Emulators for Multivariate Deterministic Functions." In: *Journal of Computational and Graphical Statistics* 17.4 (2008), pp. 827–843. DOI: [10.1198/106186008X384032](https://doi.org/10.1198/106186008X384032).
- [193] Sarah Rouhana et al. "Early calcium handling imbalance in pressure overload-induced heart failure with nearly normal left ventricular ejection fraction." In: *Biochim. Biophys. Acta - Mol. Basis Dis.* 1865.1 (2019), pp. 230–242. DOI: [10.1016/j.bbadis.2018.08.005](https://doi.org/10.1016/j.bbadis.2018.08.005). URL: <https://doi.org/10.1016/j.bbadis.2018.08.005>.
- [194] Sebastian Ruder. "An overview of gradient descent optimization algorithms." In: *CoRR* abs/1609.04747 (2016). URL: <http://arxiv.org/abs/1609.04747>.
- [195] Mihály Ruppert et al. "Myocardial reverse remodeling after pressure unloading is associated with maintained cardiac mechanoenergetics in a rat model of left ventricular hypertrophy." In: *Am J Physiol Hear. Circ Physiol* 311 (2016), pp. 592–603. DOI: [10.1152/ajpheart.00085.2016](https://doi.org/10.1152/ajpheart.00085.2016). - Pressure. URL: [www.ajpheart.org](http://www.ajpheart.org).
- [196] Mihály Ruppert et al. "Pressure-volume analysis reveals characteristic sex-related differences in cardiac function in a rat model of aortic banding-induced myocardial hypertrophy." In: *Am J Physiol Hear. Circ Physiol* 315 (2018), pp. 502–511. DOI: [10.1152/ajpheart.00202.2018](https://doi.org/10.1152/ajpheart.00202.2018). - Sex. URL: [www.ajpheart.org](http://www.ajpheart.org).
- [197] Mani Sadredini, Tore Kristian Danielsen, Jan Magnus Aronsen, Ravinea Manotheepan, Karina Hougen, Ivar Sjaastad, and Mathis Korseberg Stokke. "Beta-adrenoceptor stimulation reveals Ca<sup>2+</sup> waves and sarcoplasmic reticulum Ca<sup>2+</sup> depletion in left ventricular cardiomyocytes from post-infarction rats with

- and without heart failure." In: *PLoS One* 11.4 (2016), pp. 1–18. DOI: [10.1371/journal.pone.0153887](https://doi.org/10.1371/journal.pone.0153887).
- [198] K. Sagawa, R. K. Lie, J. Schaefer, and O. Frank. "Translation of Otto Frank's paper "Die Grundform des Arteriellen Pulses" *Zeitschrift für Biologie* 37: 483-526 (1899)." In: *J Mol Cell Cardiol* 22.3 (1990), pp. 253–254.
- [199] Arisa Sakai and Katsuhisa Sunada. "Effects of adrenaline on circulatory dynamics and cardiac function in rats administered chlorpromazine." In: *Odontology* 105.1 (2017), pp. 103–107. DOI: [10.1007/s10266-016-0241-x](https://doi.org/10.1007/s10266-016-0241-x).
- [200] Eman M. Salah, Sheldon I. Bastacky, Edwin K. Jackson, and Stevan P. Tofovic. "Captopril Attenuates Cardiovascular and Renal Disease in a Rat Model of Heart Failure with Preserved Ejection Fraction." In: *J. Cardiovasc. Pharmacol.* 71.4 (2018), pp. 205–214. DOI: [10.1097/FJC.0000000000000561](https://doi.org/10.1097/FJC.0000000000000561).
- [201] Shaul Salomon, Gideon Avigad, Alex Goldvard, and Oliver Schütze. "PSA – A New Scalable Space Partition Based Selection Algorithm for MOEAs." In: *EVOLVE - A Bridge between Probability, Set Oriented Numerics, and Evolutionary Computation II*. Ed. by Oliver Schütze, Carlos A. Coello Coello, Alexandru-Adrian Tantar, Emilia Tantar, Pascal Bouvry, Pierre Del Moral, and Pierrick Legrand. Berlin, Heidelberg: Springer Berlin Heidelberg, 2013, pp. 137–151. ISBN: 978-3-642-31519-0. DOI: [10.1007/978-3-642-31519-0\\_9](https://doi.org/10.1007/978-3-642-31519-0_9).
- [202] Andrea Saltelli. *Making best use of model evaluations to compute sensitivity indices*. Tech. rep. 2002, pp. 280–297. URL: [www.elsevier.com/locate/cpc](http://www.elsevier.com/locate/cpc).
- [203] Andrea Saltelli, Marco Ratto, Terry Andres, Francesca Campolongo, Jessica Cariboni, Debora Gatelli, Michaela Saisana, and Stefano Tarantola. "Variance-Based Methods." In: *Global Sensitivity Analysis. The Primer*. John Wiley & Sons, Ltd, 2007. Chap. 4, pp. 155–182. ISBN: 9780470725184. DOI: <https://doi.org/10.1002/9780470725184.ch4>.
- [204] Andrea Saltelli, Paola Annoni, Ivano Azzini, Francesca Campolongo, Marco Ratto, and Stefano Tarantola. "Variance based sensitivity analysis of model output. Design and estimator for the total sensitivity index." In: *Comput. Phys. Commun.* 181.2 (2010), pp. 259–270. DOI: [10.1016/j.cpc.2009.09.018](https://doi.org/10.1016/j.cpc.2009.09.018).
- [205] James M. Salter and Daniel Williamson. "A comparison of statistical emulation methodologies for multi-wave calibration of environmental models." In: *Environmetrics* 27.8 (2016), pp. 507–523. DOI: [10.1002/env.2405](https://doi.org/10.1002/env.2405).

- [206] Simona Saponara, Antonella Ferrara, Beatrice Gorelli, Anamik Shah, Masami Kawase, Noboru Motohashi, Joseph Molnar, Giampietro Sgaragli, and Fabio Fusi. “3,5-Dibenzoyl-4-(3-phenoxyphenyl)-1,4-dihydro-2,6-dimethylpyridine (DP7): A new multidrug resistance inhibitor devoid of effects on Langendorff-perfused rat heart.” In: *Eur. J. Pharmacol.* 563.1-3 (2007), pp. 160–163. DOI: [10.1016/j.ejphar.2007.02.001](https://doi.org/10.1016/j.ejphar.2007.02.001).
- [207] Amrita X. Sarkar and Eric A. Sobie. “Regression analysis for constraining free parameters in electrophysiological models of cardiac cells.” In: *PLoS Comput. Biol.* 6.9 (2010). DOI: [10.1371/journal.pcbi.1000914](https://doi.org/10.1371/journal.pcbi.1000914).
- [208] F Sato, S Isoyama, and T Takishima. “Normalization of impaired coronary circulation in hypertrophied rat hearts.” In: *Hypertension* 16.1 (1990), pp. 26–34. DOI: [10.1161/01.hyp.16.1.26](https://doi.org/10.1161/01.hyp.16.1.26). URL: <http://www.ncbi.nlm.nih.gov/pubmed/2142125>.
- [209] Zelia Schmederer, Natale Rolim, T. Scott Bowen, Axel Linke, Ulrik Wisloff, and Volker Adams. “Endothelial function is disturbed in a hypertensive diabetic animal model of HFpEF: Moderate continuous vs. high intensity interval training.” In: *Int. J. Cardiol.* 273 (2018), pp. 147–154. DOI: [10.1016/j.ijcard.2018.08.087](https://doi.org/10.1016/j.ijcard.2018.08.087). URL: <https://doi.org/10.1016/j.ijcard.2018.08.087>.
- [210] Jens Schreiter, Duy Nguyen-Tuong, Mona Eberts, Bastian Bischoff, Heiner Markert, and Marc Toussaint. “Safe exploration for active learning with gaussian processes.” In: *Lect. Notes Comput. Sci. (including Subser. Lect. Notes Artif. Intell. Lect. Notes Bioinformatics)* 9286.i (2015), pp. 133–149. DOI: [10.1007/978-3-319-23461-8\\_9](https://doi.org/10.1007/978-3-319-23461-8_9).
- [211] H Schunkert, V J Dzau, S S Tang, A T Hirsch, C S Apstein, and B H Lorell. “Increased rat cardiac angiotensin converting enzyme activity and mRNA expression in pressure overload left ventricular hypertrophy. Effects on coronary resistance, contractility, and relaxation.” In: *J. Clin. Invest.* 86.6 (1990), pp. 1913–1920. DOI: [10.1172/JCI114924](https://doi.org/10.1172/JCI114924).
- [212] H Schunkert, E O Weinberg, G Bruckschlegel, A J Rieger, and B H Lorell. “Alteration of growth responses in established cardiac pressure overload hypertrophy in rats with aortic banding.” In: *J. Clin. Invest.* 96.6 (1995), pp. 2768–2774. DOI: [10.1172/JCI118346](https://doi.org/10.1172/JCI118346).
- [213] Amil M. Shah and Marc A. Pfeffer. “Heart failure: The many faces of heart failure with preserved ejection fraction.” In: *Nat. Rev. Cardiol.* 9.10 (2012), pp. 555–556. DOI: [10.1038/nrccardio.2012.123](https://doi.org/10.1038/nrccardio.2012.123).

- [214] Anna A. Sher, Ken Wang, Andrew Wathen, Philip John Maybank, Gary R. Mirams, David Abramson, Denis Noble, and David J. Gavaghan. “A local sensitivity analysis method for developing biological models with identifiable parameters: Application to cardiac ionic channel modelling.” In: *Futur. Gener. Comput. Syst.* 29.2 (2013), pp. 591–598. doi: [10.1016/j.future.2011.09.006](https://doi.org/10.1016/j.future.2011.09.006). URL: <http://dx.doi.org/10.1016/j.future.2011.09.006>.
- [215] Ying Tung Sia et al. “Beneficial effects of long-term use of the antioxidant probucol in heart failure in the rat.” In: *Circulation* 105.21 (2002), pp. 2549–2555. doi: [10.1161/01.CIR.0000016721.84535.00](https://doi.org/10.1161/01.CIR.0000016721.84535.00).
- [216] Nina Simonovic, Vladimir Jakovljevic, Jovana Jeremic, Zarko Finderle, Ivan Srejovic, Tamara Nikolic Turnic, Isidora Milosavljevic, and Vladimir Zivkovic. “Comparative effects of calcium and potassium channel modulators on ischemia/reperfusion injury in the isolated rat heart.” In: *Mol. Cell. Biochem.* 450.1-2 (2019), pp. 175–185. doi: [10.1007/s11010-018-3384-y](https://doi.org/10.1007/s11010-018-3384-y). URL: <http://dx.doi.org/10.1007/s11010-018-3384-y>.
- [217] I.M Sobol’. “On the distribution of points in a cube and the approximate evaluation of integrals.” In: *USSR Computational Mathematics and Mathematical Physics* 7.4 (1967), pp. 86–112. doi: [https://doi.org/10.1016/0041-5553\(67\)90144-9](https://doi.org/10.1016/0041-5553(67)90144-9).
- [218] I.M Sobol. “Global sensitivity indices for nonlinear mathematical models and their Monte Carlo estimates.” In: *Math. Comput. Simul.* 55.1-3 (2001), pp. 271–280. doi: [10.1016/S0378-4754\(00\)00270-6](https://doi.org/10.1016/S0378-4754(00)00270-6).
- [219] Ilya M. Sobol. “Theorems and examples on high dimensional model representation.” In: *Reliab. Eng. Syst. Saf.* 79 (2003), pp. 187–193.
- [220] R. John Solaro and Helen M. Rarick. “Troponin and tropomyosin: Proteins that switch on and tune in the activity of cardiac myofilaments.” In: *Circ. Res.* 83.5 (1998), pp. 471–480. doi: [10.1161/01.RES.83.5.471](https://doi.org/10.1161/01.RES.83.5.471).
- [221] Alexander J. Sparrow, Hugh Watkins, Matthew J. Daniels, Charles Redwood, and Paul Robinson. “Mavacamten rescues increased myofilament calcium sensitivity and dysregulation of Ca<sup>2+</sup> flux caused by thin filament hypertrophic cardiomyopathy mutations.” In: *Am. J. Physiol. Heart Circ. Physiol.* 318.3 (2020), H715–H722. doi: [10.1152/ajpheart.00023.2020](https://doi.org/10.1152/ajpheart.00023.2020).
- [222] Isidora Stojic, Ivan Srejovic, Vladimir Zivkovic, Nevena Jeremic, Marko Djuric, Ana Stevanovic, Tamara Milanovic, Dragan Djuric, and Vladimir Jakovljevic. “The effects of verapamil and its combinations with glutamate and glycine on cardio-

- dynamics, coronary flow and oxidative stress in isolated rat heart." In: *J. Physiol. Biochem.* 73.1 (2017), pp. 141–153. DOI: [10.1007/s13105-016-0534-0](https://doi.org/10.1007/s13105-016-0534-0). URL: <http://dx.doi.org/10.1007/s13105-016-0534-0>.
- [223] Marina Stolina et al. "The evolving systemic biomarker milieu in obese ZSF1 rat model of human cardiometabolic syndrome: Characterization of the model and cardioprotective effect of GDF15." In: *PLoS One* 15.8 August (2020), pp. 1–25. DOI: [10.1371/journal.pone.0231234](https://doi.org/10.1371/journal.pone.0231234).
- [224] Marina Strocchi et al. "Simulating ventricular systolic motion in a four-chamber heart model with spatially varying robin boundary conditions to model the effect of the pericardium." In: *J. Biomech.* 101 (2020), p. 109645. DOI: [10.1016/j.jbiomech.2020.109645](https://doi.org/10.1016/j.jbiomech.2020.109645). URL: <https://doi.org/10.1016/j.jbiomech.2020.109645>.
- [225] Linda B. Stull, Michelle K. Leppo, Eduardo Marbán, and Paul M.L. Janssen. "Physiological Determinants of Contractile Force Generation and Calcium Handling in Mouse Myocardium." In: *J. Mol. Cell. Cardiol.* 34.10 (2002), pp. 1367–1376. DOI: [10.1006/jmcc.2002.2065](https://doi.org/10.1006/jmcc.2002.2065).
- [226] Bruno D. Stuyvers, Andrew D. McCulloch, Jiqing Guo, Henry J. Duff, and Henk E.D.J. Ter Keurs. "Effect of stimulation rate, sarcomere length and Ca<sup>2+</sup> on force generation by mouse cardiac muscle." In: *J. Physiol.* 544.3 (2002), pp. 817–830. DOI: [10.1113/jphysiol.2002.024430](https://doi.org/10.1113/jphysiol.2002.024430).
- [227] Anja M. Swenson, X. Wanjian Tang, Cheavar A. Blair, Christopher M. Fetrow, William C. Unrath, Michael J. Previs, Kenneth S. Campbell, and Christopher M. Yengo. "Omecamtiv mecarbil enhances the duty ratio of human β-cardiac myosin resulting in increased calcium sensitivity and slowed force development in cardiac muscle." In: *J. Biol. Chem.* 292.9 (2017), pp. 3768–3778. DOI: [10.1074/jbc.M116.748780](https://doi.org/10.1074/jbc.M116.748780).
- [228] John R. Teerlink et al. "Dose-dependent augmentation of cardiac systolic function with the selective cardiac myosin activator, omecamtiv mecarbil: A first-in-man study." In: *Lancet* 378.9792 (2011), pp. 667–675. DOI: [10.1016/S0140-6736\(11\)61219-1](https://doi.org/10.1016/S0140-6736(11)61219-1).
- [229] John R. Teerlink et al. "Chronic Oral Study of Myosin Activation to Increase Contractility in Heart Failure (COSMIC-HF): a phase 2, pharmacokinetic, randomised, placebo-controlled trial." In: *Lancet* 388.10062 (2016), pp. 2895–2903. DOI: [10.1016/S0140-6736\(16\)32049-9](https://doi.org/10.1016/S0140-6736(16)32049-9).

- [230] John R. Teerlink et al. "Cardiac Myosin Activation with Ome-camtil Mecarbil in Systolic Heart Failure." In: *N. Engl. J. Med.* 384.2 (2021). DOI: [10.1056/NEJMoa2025797](https://doi.org/10.1056/NEJMoa2025797).
- [231] Svetlana B. Tikunova and Jonathan P. Davis. "Designing calcium-sensitizing mutations in the regulatory domain of cardiac troponin C." In: *J. Biol. Chem.* 279.34 (2004), pp. 35341–35352. DOI: [10.1074/jbc.M405413200](https://doi.org/10.1074/jbc.M405413200).
- [232] Camilo Toledo et al. "Cardiac diastolic and autonomic dysfunction are aggravated by central chemoreflex activation in heart failure with preserved ejection fraction rats." In: *J. Physiol.* 595.8 (2017), pp. 2479–2495. DOI: [10.1113/JP273558](https://doi.org/10.1113/JP273558).
- [233] Osamu Tsukamoto. "Direct sarcomere modulators are promising new treatments for cardiomyopathies." In: *Int. J. Mol. Sci.* 21.1 (2020). DOI: [10.3390/ijms21010226](https://doi.org/10.3390/ijms21010226).
- [234] Christian G.M. Van Dijk et al. "Distinct endothelial cell responses in the heart and kidney microvasculature characterize the progression of heart failure with preserved ejection fraction in the obese ZSF1 rat with cardiorenal metabolic syndrome." In: *Circ. Hear. Fail.* 9.4 (2016), pp. 1–13. DOI: [10.1161/CIRCHEARTFAILURE.115.002760](https://doi.org/10.1161/CIRCHEARTFAILURE.115.002760).
- [235] Ian Vernon, Michael Goldsteiny, and Richard G. Bowerz. "Galaxy formation: A Bayesian uncertainty analysis." In: *Bayesian Anal.* 5.4 (2010), pp. 619–670. DOI: [10.1214/10-BA524](https://doi.org/10.1214/10-BA524).
- [236] Ian Vernon, Junli Liu, Michael Goldstein, James Rowe, Jen Topping, and Keith Lindsey. "Bayesian uncertainty analysis for complex systems biology models: emulation, global parameter searches and evaluation of gene functions." In: *BMC Syst. Biol.* 12.1 (2018), p. 1. DOI: [10.1186/s12918-017-0484-3](https://doi.org/10.1186/s12918-017-0484-3).
- [237] Victoria Volodina and Peter Challenor. "The importance of uncertainty quantification in model reproducibility." In: *Philos. Trans. R. Soc. A Math. Phys. Eng. Sci.* 379.2197 (2021). DOI: [10.1098/rsta.2020.0071](https://doi.org/10.1098/rsta.2020.0071).
- [238] John S. Walker, Xiaotao Li, and Peter M. Buttrick. "Analysing force-pCa curves." In: *J. Muscle Res. Cell Motil.* 31.1 (2010), pp. 59–69. DOI: [10.1007/s10974-010-9208-7](https://doi.org/10.1007/s10974-010-9208-7).
- [239] G. T. Wang, H. Li, Z. Q. Yu, and X. N. He. "Effects of ranolazine on cardiac function in rats with heart failure." In: *Eur. Rev. Med. Pharmacol. Sci.* 23.21 (2019), pp. 9625–9632. DOI: [10.26355/eurrev\\_201911\\_19456](https://doi.org/10.26355/eurrev_201911_19456).
- [240] L. Wang et al. "Treatment with Treprostinil and Metformin Normalizes Hyperglycemia and Improves Cardiac Function in Pulmonary Hypertension Associated with Heart Failure with Preserved Ejection Fraction." In: *Arterioscler. Thromb. Vasc. Biol.* June (2020), pp. 1543–1558. DOI: [10.1161/ATVBAHA.119.313883](https://doi.org/10.1161/ATVBAHA.119.313883).

- [241] Peipei Wang, Heather Fraser, Steven G. Lloyd, Jeffrey J. McVeigh, Luiz Belardinelli, and John C. Chatham. "A comparison between ranolazine and CVT-4325, a novel inhibitor of fatty acid oxidation, on cardiac metabolism and left ventricular function in rat isolated perfused heart during ischemia and reperfusion." In: *J. Pharmacol. Exp. Ther.* 321.1 (2007), pp. 213–220. DOI: [10.1124/jpet.106.115519](https://doi.org/10.1124/jpet.106.115519).
- [242] Vicky Y. Wang, H. I. Lam, Daniel B. Ennis, Brett R. Cowan, Alistair A. Young, and Martyn P. Nash. "Modelling passive diastolic mechanics with quantitative MRI of cardiac structure and function." In: *Med. Image Anal.* 13.5 (2009), pp. 773–784. DOI: [10.1016/j.media.2009.07.006](https://doi.org/10.1016/j.media.2009.07.006).
- [243] Wei Dong Gao, P. H. Backx, M. Azan-Backx, and E. Marban. "Myofilament Ca<sub>2+</sub> sensitivity in intact versus skinned rat ventricular muscle." In: *Circ. Res.* 74.3 (1994), pp. 408–415. DOI: [10.1161/01.res.74.3.408](https://doi.org/10.1161/01.res.74.3.408).
- [244] N. Westerhof and G. Elzinga. "Normalized input impedance and arterial decay time over heart period are independent of animal size." In: *Am. J. Physiol. Integr. Comp. Physiol.* 261.1 (1991), R126–R133. DOI: [10.1152/ajpregu.1991.261.1.R126](https://doi.org/10.1152/ajpregu.1991.261.1.R126).
- [245] N. Westerhof, G. Elzinga, and P. Sipkema. "An artificial arterial system for pumping hearts." In: *J. Appl. Physiol.* 31.5 (1971), pp. 776–781. DOI: [10.1152/jappl.1971.31.5.776](https://doi.org/10.1152/jappl.1971.31.5.776).
- [246] Raymond K.W. Wong, Curtis B. Storlie, and Thomas C.M. Lee. "A frequentist approach to computer model calibration." In: *J. R. Stat. Soc. Ser. B Stat. Methodol.* 79.2 (2017), pp. 635–648. DOI: [10.1111/rssb.12182](https://doi.org/10.1111/rssb.12182). arXiv: [1411.4723](https://arxiv.org/abs/1411.4723).
- [247] R. S. Wymore, G. A. Gintant, R. T. Wymore, J. E. Dixon, D. McKinnon, and I. S. Cohen. "Tissue and species distribution of mRNA for the IKr-like K<sup>+</sup> channel, erg." In: *Circ. Res.* 80.2 (1997), pp. 261–268. DOI: [10.1161/01.res.80.2.261](https://doi.org/10.1161/01.res.80.2.261).
- [248] Jiahe Xi et al. "The estimation of patient-specific cardiac diastolic functions from clinical measurements." In: *Med. Image. Anal.* 17.2 (2013), pp. 133–146. DOI: <https://doi.org/10.1016/j.media.2012.08.001>.
- [249] F. C.P. Yin, H. A. Spurgeon, M. L. Weisfeldt, and E. G. Lakatta. "Mechanical properties of myocardium from hypertrophied rat hearts. A comparison between hypertrophy induced by senescence and by aortic banding." In: *Circ. Res.* 46.2 (1980), pp. 292–300. DOI: [10.1161/01.RES.46.2.292](https://doi.org/10.1161/01.RES.46.2.292).
- [250] Xiaowei Yue, Yuchen Wen, Jeffrey H. Hunt, and Jianjun Shi. "Active Learning for Gaussian Process Considering Uncertainties with Application to Shape Control of Composite Fuse-

- lage." In: *IEEE Trans. Autom. Sci. Eng.* 18.1 (2021), pp. 36–46. DOI: [10.1109/TASE.2020.2990401](https://doi.org/10.1109/TASE.2020.2990401).
- [251] P. A. Yushkevich, J. Piven, H. C. Hazlett, R. G. Smith, S. Ho, J. C. Gee, and G. Gerig. "User-guided 3D active contour segmentation of anatomical structures: Significantly improved efficiency and reliability." In: *Neuroimage* 31.3 (2006), pp. 1116–1128. DOI: [10.1016/j.neuroimage.2006.01.015](https://doi.org/10.1016/j.neuroimage.2006.01.015).
- [252] Luisa Zanolla and Piero Zardini. "Selection of endpoints for heart failure clinical trials." In: *Eur. J. Heart Fail.* 5.6 (2003), pp. 717–723. DOI: [10.1016/S1388-9842\(03\)00101-6](https://doi.org/10.1016/S1388-9842(03)00101-6).
- [253] Michael R. Zile, Catalin F. Baicu, and William H. Gaasch. "Diastolic Heart Failure — Abnormalities in Active Relaxation and Passive Stiffness of the Left Ventricle." In: *N. Engl. J. Med.* 350.19 (2004), pp. 1953–1959. DOI: [10.1056/nejmoa032566](https://doi.org/10.1056/nejmoa032566).
- [254] B. D. Zuckerman and F. C.P. Yin. "Aortic impedance and compliance in hypertensive rats." In: *Am. J. Physiol. - Hear. Circ. Physiol.* 257.2 (1989). DOI: [10.1152/ajpheart.1989.257.2.h553](https://doi.org/10.1152/ajpheart.1989.257.2.h553).